Some problems in low Reynolds number environmental flows

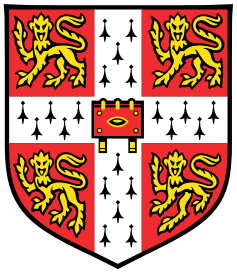

Edward M. Hinton

Department of Earth Sciences
University of Cambridge

This dissertation is submitted for the degree of
Doctor of Philosophy

Clare College

February 2020

Declaration

This thesis is the result of my own work and includes nothing which is the outcome of work done in collaboration except as declared in the Preface and specified in the text. It is not substantially the same as any that I have submitted, or, is being concurrently submitted for a degree or diploma or other qualification at the University of Cambridge or any other University or similar institution except as declared in the Preface and specified in the text. I further state that no substantial part of my thesis has already been submitted, or, is being concurrently submitted for any such degree, diploma or other qualification at the University of Cambridge or any other University or similar institution except as declared in the Preface and specified in the text. It does not exceed the prescribed word limit for the relevant Degree Committee. This thesis contains fewer than 275 numbered pages of which not more than 225 pages are text, appendices, illustrations and bibliography.

The material contained in chapters 2, 3, 4, 5, 6 and 7 has been published or submitted for publication, as noted at the start of each chapter.

Edward M. Hinton
February 2020

Abstract

Some problems in low Reynolds number environmental flows
Edward M. Hinton

This thesis investigates some problems in environmental fluid dynamics in which the role of inertia is negligible relative to viscous stresses and buoyancy forces. Simple models are developed to provide insight into the physics governing the flows and to determine the dependencies on a few parameters. We study the fluid dynamics of carbon dioxide storage in heterogeneous aquifers, the migration of tracers in such flows and the interaction of lava flows with barriers.

First, in chapter 2, we examine the injection of fluid of one viscosity and density into a horizontal permeable aquifer initially saturated with a second fluid of different viscosity and density. The novel feature of the analysis is that we allow the permeability to vary vertically across the aquifer so that there is a shear in the flow. This leads to recognition that the interface may evolve as either a rarefaction wave that grows at a rate proportional to time, a shock-like front of fixed length or a mixture of shock-like regions and rarefaction-wave-type regions.

In chapter 3, we study the migration of a tracer within the flows described in chapter 2. Owing to the shear flow, tracer in the high permeability regions moves substantially faster than the mean flow and eventually enters the interface region. The tracer may either remain in this region or cycle through it and be left behind. We then proceed to consider the role of diffusion of the tracer in the case that the interface has fixed extent (chapter 4). Cross-aquifer diffusion homogenises the tracer distribution, which becomes independent of depth but spreads longitudinally in this shear dispersion regime. This leads to much faster spreading than by diffusion alone. The shear dispersion of tracer in a growing interface (chapter 5) is more complicated because the tracer migrates into thin regions where the shear becomes dominated by the lateral spreading owing to the growth of the interface.

In the second part of the thesis, we consider the flow of lava down a slope with an obstruction. We assume that the lava is a low Reynolds number gravity-driven flow and we

study the free-surface deformation owing to the obstruction. For small smooth mounds, it is shown in chapter 6 that the flow surmounts the obstacles, but for larger mounds the flow is deflected around it and can form dry zones in its wake into which fluid does not flow. In chapter 7, we theoretically and experimentally investigate the interaction of free-surface flows with cylinders of various cross-sections on an inclined plane. The cylinders are oriented with their axis perpendicular to the plane and are sufficiently tall so that they are not overtopped. For relatively shallow flows, there is a 'pond' of nearly stationary fluid upstream of the cylinder and a 'dry' region in which there is no fluid downstream of the cylinder. The investigation has direct relevance to the deflection of lava flows by barriers and buildings and the theory is employed to deduce simplified asymptotic expressions of the force exerted on the cylinders.

Acknowledgements

I have thoroughly enjoyed studying for a PhD and my supervisor, Andy Woods, has been a major part of this. I am very grateful for his interest, insights and encouragement, which have been invaluable. It has always been a pleasure to discuss ideas with Andy and learn from his passion for science and its effective communication. I also want to thank Andrew Hogg and Herbert Huppert, who supervised the last two chapters of this thesis. They have been very generous to me with their time and energy. It was a privilege to get to work with them both.

The BP Institute has been a lovely place to work for the past three and a half years. The staff: Patrick, Lotty, Chris, Catherine, Andrew and Caroline make it such a welcoming community to be a part of and have helped me enormously, for example in the laboratory and with numerical simulations. Sharing an office with Jeffrey Poon for three years was a joy and he has been sorely missed since he moved to Germany. I also want to thank Neeraja Bhamidipati, Martin Lippert and Fin Allen for lots of laughter and camaraderie during our studies. Pete Baddoo, Zika Muwowo and Peter Asimov have been wonderful friends to me in Cambridge; I am sad to be moving away from them.

To my family I owe more than I can say. Mum and Dad have provided constant support and encouragement. I feel very blessed to have them as parents. Finally, I want to thank Clemency for being the best companion who has taught me so much. I am excited for the next chapter together.

Table of contents

List of figures

List of tables

Chapter 1

Introduction

This thesis considers two problems in environmental fluid dynamics; flow in a vertically heterogeneous porous medium and the interaction of viscous flows with obstructions on an inclined plane. The two settings are quite different but are related by some important common features concerning the modelling approach. Both flows typically occur at low Reynolds number; they are driven primarily by gravity and resisted by viscous stresses. In addition, the longitudinal lengthscale is much greater than the thickness of the flow. These features enable simplifications of the models for the two problems. Since viscous stresses dominate, we neglect inertia so that the motion is governed by the equations for Stokes flow (see chapter 4 of Batchelor [14]) or Darcy's law [17]. Secondly, owing to the large longitudinal lengthscale, the vertical velocities may be neglected (the lubrication approximation) and the pressure is assumed to be hydrostatic [89, 86]. With these assumptions, we derive governing equations for the flows, which depend on just a few parameters. The reduced models enable the characterisation of the flow with a few variables and therefore provides understanding of the underlying physical processes. The equations are studied analytically and through numerical integration to identify how the flow depends on the parameters. This in turn provides key insights and an improved physical understanding of the underlying engineering or environmental problem, which can be used to inform high level decisions.

The first part of the thesis investigates flow in porous aquifers. There has been much previous modelling of flow in the subsurface owing to its importance in geothermal power generation, aquifer cleanup, enhanced oil recovery and geological CO_2 storage. Many of these models consider the subsurface to have a vertically uniform permeability structure and there have been studies investigating the evolution of a fluid-fluid displacement. It has been shown that when the injected fluid is of relatively high viscosity, as in the context of enhanced oil recovery, the interface advances at a constant velocity with a fixed shape[111].

If instead the injected fluid is of relatively low viscosity as is relevant for CO_2 storage, the interface extends in time. However, rocks often have a very complex structure and in this thesis we show that vertical heterogeneities within a porous layer can substantially alter the flow behaviour and the shape of the interface (figure 1.1a and figure 1.1b).

Tracers are often added to the flows in porous rocks to understand fluid-rock interactions and to assist in quantifying the flow velocity [132]. The tracer arrival times at an observation well may help to constrain parameters such as the permeability and aquifer thickness. Accurately interpreting the results of tracer tests is challenging owing to the rock heterogeneity and the complex interactions with the interface region. We describe and quantify the processes that control the migration of tracer within fluid-fluid displacements. In the case that the permeability varies vertically, the tracer is sheared and interacts with the interface region of the flow (figure 1.1c, 1.1d). We then generalise the analysis to incorporate molecular diffusion of the tracer.

In the second part of the thesis, we turn our attention to lava flows and their interaction with obstacles and topography on a slope. We discuss the design of lava flow barriers, which are used to protect homes and infrastructure. This is another environmental problem in which models that neglect inertia can accurately quantify the evolution of the flow.

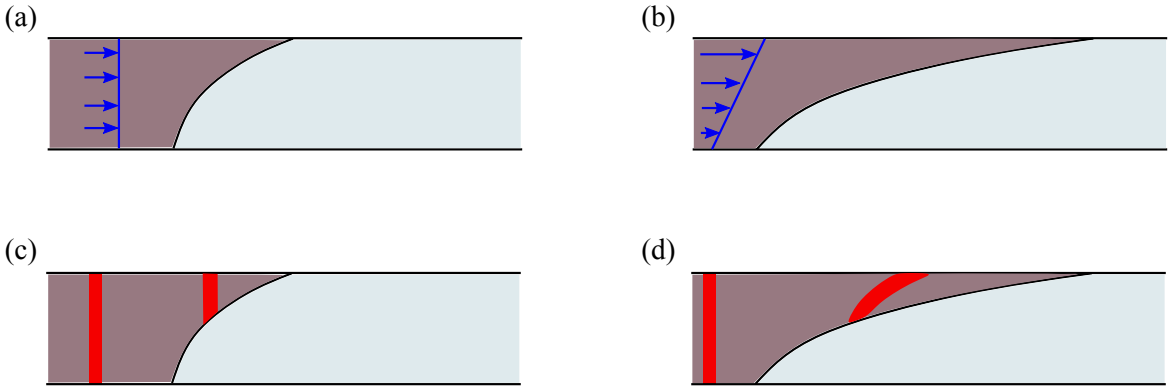

Fig. 1.1 (a, b) Schematic of the influence of vertically varying permeability, and the associated shear flow, on the evolution of the fluid-fluid interface. The interface is extended in the case that the permeability increases towards the top of the aquifer. (c, d) The migration of tracer within the injected fluid in the case of a uniform aquifer and an aquifer in which the permeability increases towards the top.

1.1 Flow in a heterogeneous porous medium

The migration of a fluid through porous rocks has received considerable interest over many decades [33, 65, 19, 110]. Such flows are of concern in many industrial and environmental applications including radioactive waste disposal, the flow of contaminants in freshwater aquifers, enhanced oil recovery and the sequestration of CO_2 within geological storage reservoirs [99, 112, 87, 144]. It is important to understand where fluid flows, at what speed and how this depends on the properties of the fluid and the rock.

Often the porous layers into which fluid is injected are bounded above and below by much less permeable rock and the layer is initially saturated with an ambient fluid. The flow of the injected fluid is then rate-limited by the displacement of the ambient fluid [89, 121, 144]. At first, an injected buoyant fluid spreads in a thin region beneath the upper seal rock and the displacement of the ambient fluid is unimportant and the current behaves as unconfined. However, at later times the injected fluid fills the aquifer and confinement plays a key role [111, 146]. Leakage of fluid through the seal layers can significantly reduce the extent of the current [116].

The shape of the interface between the fluids is highly sensitive to the viscosity ratio [98, 92, 55]. The injection of a high viscosity fluid, which is relevant to enhanced oil recovery, leads to the interface advancing as a fixed travelling wave in a confined aquifer. In the case of a low viscosity input fluid, which is relevant to CO_2 storage, the interface grows in proportion to time [111, 146]. In the special case of equal viscosity fluids, which is an important problem in hydrology, the interface migrates downstream with constant velocity and extends at a rate proportional to the square root of time [89].

Much of the research on fluid-fluid displacements in porous media uses the approximation that the two fluids are separated by a sharp interface. Models have also been developed to account for two-phase flow effects [53]. It has been shown theoretically and experimentally that miscibility can be neglected during the injection-phase of a CO_2 project but the dissolution of the CO_2 plays a key role at later times [108, 103, 111]. The effects of the gradual dissolution of the CO_2 and capillary trapping of the CO_2 have been shown to cause the currents to gradually wane [119, 66, 78].

The majority of the models mentioned hitherto have assumed that the formation is of uniform permeability. This leads to the simplifying result that the speed of the current is uniform with depth. However, real geological strata are more complicated. They exhibit many heterogeneous features including folding, inclusions of different permeability and cross-bedding. There are often multiple layers of different permeability. Reservoirs are

typically made up of sedimentary rock that is very inhomogeneous and the contrasts in permeability can totally dominate fluid flow [22]. Also within single geological flow units, such as are produced from massive turbidite flows on the sea-floor, the grain size is expected to gradually change with depth in the deposit as the parent turbulent flow either waxes or wanes [141, 25, 120]. While some of the effects of layering which can lead to the dispersion of buoyant plumes and gravity currents in a geological stratum have been examined [47, 69, 56, 46], there has been much less analysis of the effects of permeability gradients across an individual flow unit.

In **chapter 2**, we propose a novel model to account for permeability variations within a confined layer. Our results identify that if the permeability increases towards the top of the aquifer, the buoyant lateral spreading beneath the seal is enhanced as the flow speed increases towards the top seal (see figure 1.1). In contrast, if the permeability decreases towards the top of the aquifer, there is a competition between buoyancy driving the less dense input fluid up and the rock structure through which flow is faster near the bottom. This leads to a blunted and shortened current and hence a much greater proportion of the rock is accessed. This has significant implications for the efficacy of CO_2 storage, which we discuss. We assume that the buoyant injected fluid always lies above the dense ambient fluid even when the permeability increases strongly towards the bottom of the aquifer. This has been shown to be a valid assumption experimentally and numerically in a two-layer system provided that the rate of injection is sufficiently slow relative to the characteristic buoyancy velocity [88, 39].

1.2 Tracer tests

A significant challenge to determining flow in a heterogeneous aquifer is the uncertainty in the knowledge of the rock structure. One way to learn about the unknown and often very complex rock structure is to add tracers to the injected fluid and observe them downstream [134, 25, 21, 105, 94, 132, 73]. It is also possible to use naturally occurring isotopes to monitor the sequestration of CO_2 [58]. In this thesis, we study how the interface between the fluids and the shear flow associated with vertically varying permeability controls the migration of tracer. These two effects have a profound influence on the evolution of a pulse of tracer but the combination has received little previous attention. We develop the results of chapter two to derive a simplified model for tracer migration. Our idealised model assists in understanding the processes that govern the dispersion, rather than providing an engineering tool to interpret specific data.

Much of the previous work on tracer migration has focused on the effect of heterogeneity on the dispersion in a pressure-driven flow [33, 43, 112]. However, Farcas and Woods [46] showed that longitudinal dispersion is possible in flow in a layered porous medium, even if the layers have constant permeability. Porous rocks often have low permeability baffles which act as a barrier to the vertical migration of a buoyant fluid such as CO_2. Hesse and Woods [69] illustrated how the lateral spreading beneath these baffles can lead to longitudinal dispersion. Many models have been built assuming that the permeability is a random function of position and it has been shown that this leads to longitudinal dispersion at a rate proportional to $t^{1/2}$, where t represents time [50, 43, 19].

Dispersal of the tracer may also arise from large-scale systematic heterogeneity. If there is a systematic variation in the permeability in the cross-flow direction, this can lead to development of a large-scale shear in which case the longitudinal extent of a finite pulse of tracer grows linearly with distance in the absence of pore-scale dispersion or diffusion. Such advection-driven dispersion is controlled by the geometry and length scale of the formation.

In addition to the effects of micro-scale and large-scale heterogeneity, in a two-phase fluid-fluid displacement, the interface zone between the two fluids has an important influence on the path taken by tracer and this can significantly alter the character of the dispersion, especially if the tracer is soluble only in the injected fluid and not the displaced fluid as assumed herein. The presence and evolution of this flow front leads to very different patterns of evolution of the tracer depending on whether the intrusion grows or is of fixed size. The effect of the growing intrusion on tracer tests in CO_2 sequestration is a significant new result.

The migration of a tracer is complex, with many of the discussed processes playing a key role in different contexts. To simplify the analysis, we unravel the problem. We first consider the advection-driven migration of a tracer added to the injected fluid in a confined aquifer in **chapter 3**. We neglect pore-scale dispersion and molecular diffusion, which are added back into the analysis in **chapter 4** and **chapter 5**. The role of diffusion may be negligible provided that the aquifer is thick and the work in chapter 3 pertains to this context. The tracer migration is controlled by the shear flow associated with permeability variations and the interaction with the nose of the flow. We show that the migration in a shear flow is fundamentally different to the migration in a uniform aquifer owing to the linear dispersion of tracer. We use our results for the interface structure to understand how tracer interacts with the nose. The different regimes for the evolution of tracer demonstrate the difficulty which arises when inverting tracer data from production wells to constrain aquifer properties.

In thinner layers or at much longer timescales, dispersion is controlled by both advection and molecular diffusion [121, 110, 139]. There are two mechanisms for dispersion on

the micro-scale within a porous medium; molecular diffusion and pore-scale mechanical dispersion which results from the different pathways followed by particles as they pass around solid grains [42, 144]. The experiments of Bear [16] showed that at low flow rates, molecular diffusion is the dominant contribution to dispersion whilst at higher flow rates dispersion is controlled by the tortuous path taken through the matrix [see also 40]. Indeed, De Josselin De Jong [38] showed that the dispersion associated with the pore geometry has the character of diffusion with coefficient $D \sim \delta v_0$ where δ is a characteristic pore size and v_0 is the flow velocity.

In **chapter 4**, we incorporate the effects of molecular diffusion. In the case that the nose has fixed extent, tracer spreads towards the nose which provides a no-flux boundary and the concentration profile transitions from a Gaussian to a half-Gaussian. The rate of along-channel diffusion is enhanced owing to Taylor dispersion [see 137]. The combination of large-scale shear and micro-scale dispersion creates large cross-layer concentration gradients, which are eventually homogenised by cross-layer diffusion. The longitudinal extent of the tracer grows in proportion to $t^{1/2}$ after the homogenisation but with a significantly enhanced dispersion coefficient as compared to the pore-scale dispersion [137, 5]. The results of chapter 4 apply when the input fluid is more viscous than the ambient fluid, as may be the case in enhanced oil recovery and geothermal power generation, so that the interface has fixed extent [99, 144].

In the context of CO_2 sequestration, the viscosity ratio is much less than one and the interface grows in time. In **chapter 5**, we show how the growing nose region disperses tracer in a uniform aquifer and an aquifer in which the permeability varies with depth. Owing to the squashing and stretching of the nose, the tracer is spread laterally at a rate proportional to $t^{1/2}$ in a uniform aquifer. Molecular diffusion acts at the same rate and the combination of the two processes leads to a faster, anomalous rate of dispersion. The presence of a permeability gradient leads to a shear flow but as tracer migrates into thin regions of the growing nose, the proportion of the permeability variation that it accesses diminishes. Eventually, the shearing is dominated by the stretching but the late-time tracer extent exhibits interesting dependencies on the early-time shearing.

1.3 Diverting lava flows

Lava flows can migrate into populated areas and cause significant damage to homes and infrastructure, costing millions of dollars to local economies [142, 11]. There have been attempts to construct barriers to divert lava flows, but these have had limited success [31,

127, 83]. There has been significant progress in the related problem of the construction of avalanche defences [60, 59, 32]. This has led to new guidelines for the design of defence schemes to these inertially-controlled flows [4]; we note that there is no equivalent guidance for viscously-controlled lava or mud flows and we aim to inform this challenge. Whilst there have been some numerical simulations and laboratory studies on controlling and diverting lava flows [48, 41], there has been little theoretical analysis of how effective barriers should be designed. One of the key results we find is that deep ponds of fluid form upstream of barriers. Thus, a key challenge is how to design barriers to minimise the depth of the pond to reduce the chance of overtopping or rupturing of the defence. We focus on informing the optimal barrier shape but note that the barrier strength is also an important consideration. There is a spectrum of barrier types from smoothly varying mounds through to bluff obstructions and we analyse these in turn. In addition, real hills have mounds and undulations and we explore how these impact the flow of lava.

Lava is a complex fluid with a rheology that can change rapidly and it solidifies at its boundaries to form crust, which confines the flow [54, 95]. Over a significant range of temperatures, lava behaves as a viscoplastic fluid, with internal stresses having a significant influence on its gravity-driven flow [see 9]. A key challenge for creating simplified models of lava is determining which of its non-Newtonian properties is the most important physical process in any given situation [8]. The interaction between a lava flow and varying topography adds an extra layer of complexity to the modelling. In order to gain insight into the flow around barriers, we consider a simplified model of lava as an isothermal Newtonian fluid. We also neglect surface tension because it is insignificant at the relatively large environmental scales of interest. Viscous Newtonian flows have been studied in the absence of undulations on a horizontal plane by Huppert [85], and an inclined plane by Smith [130], Huppert [84] and Lister [101], who showed that flow from a line source on an inclined plane becomes steady far behind the contact line where it advances with constant depth. These studies have been central to improving our understanding of lava flows and they have been used extensively.

In **chapter 6**, we consider the interaction of this steady viscous flow with smooth mounds. We demonstrate, and analyse quantitatively, that smaller mounds are surmounted by the flow whilst larger mounds lead to dry regions in which there is no fluid and a build-up of fluid upstream of the mound. The results quantifying the shape of the dry zone that develops as lava flows around topographical mounds can also assist with generating lava flow hazard maps. These are vital in many regions for understanding the probability of lava inundation and the need for evacuation.

Next, in **chapter 7**, we investigate the interaction of a downslope viscous flow with cylindrical obstructions, which pertains to lava barriers that are steeper and taller than those considered in chapter 6. Such barriers were proposed in Hawaii to protect a research observatory [107] and motivated by this laboratory experiments investigating the influence of perpendicular obstructions were carried out by Dietterich *et al*. [41]. Their experiments showed that oblique barriers lead to deeper ponds and we aim to understand the physics that determines the shape and depth of such ponds.

Our work on the interaction between viscous flows and obstructions has important implications beyond informing environmental defences. Although this thesis does not consider the role of surface tension, many of the results in chapters 6 and 7 may be extended to consider its effect. There has been extensive theoretical and numerical research on thin-film flows over adhered obstacles, for which surface tension plays a key role [133, 93, 106, 23]. These studies have important applications in manufacturing and printing owing to the ubiquity of coating flows in such industries. The role of surface tension in thin film flows past cylinders has been investigated numerically [129, 128]. In addition to surface tension, inertia may play a key role in some interactions between thin films and obstructions [49, 3]. There has been extensive analysis into viscous flow over isolated and periodic topographies, which have analysed the importance of capillary effects [114, 104, 62, 100, 126]. Significant progress has also been made in the inverse problem; determining the underlying topography given a known free-surface, which is important for determining the required bottom topography for a desired free-surface profile [63, 64]. These works are primarily numerical and our asymptotic analysis provides a framework to understand the dominant physics governing the flows and their interactions with obstructions.

Chapter 2

Interface evolution for fluid injected into a confined aquifer with vertically varying permeability

The material contained in this chapter has been published in the *Journal of Fluid Mechanics*, under the title 'Buoyancy-driven flow in a confined aquifer with a vertical gradient of permeability' [81].

2.1 Introduction

The purpose of this chapter is to explore how an increase or decrease of permeability with height in a permeable layer influences the flow through that layer. The critical physical effect that this introduces is the variation of flow speed with vertical position in the layer, and we show that this can lead to some fundamentally different controls on the flow compared to a homogeneous reservoir.

In section 2.2, we introduce a model for a gravity-driven flow in a confined permeable rock in which the permeability varies with height. We then present some numerical solutions of the resulting nonlinear advection-diffusion equation for the evolution of the interface between the injected fluid and the original fluid in the system. This identifies that, under different conditions, there are rarefaction-wave-type solutions, travelling-wave-type solutions, and mixtures of these solutions at different depths in the layer. We then compare long-time asymptotic rarefaction-wave and travelling-wave solutions of the governing equation with the full numerical solutions. We discuss the implications of these results, in comparison with

the very different current structure that develops in a homogeneous porous layer, when each fluid has the same viscosity, in which the front of the flow spreads at a rate proportional to $t^{1/2}$. Detailed analysis of the early-time behaviour is omitted from this thesis but can be found in Zheng et al. [146] for a uniform aquifer and Hinton and Woods [81] for an aquifer in which the permeability varies with depth.

We conclude with a discussion focusing on the challenges of predicting the storage capacity of an aquifer by illustrating how the fraction of the pore space that may be flooded with CO_2 varies if we account for cross-layer variations in permeability, and illustrating that, with more complex vertical structure for the permeability, it is possible to have multiple shock regions separated by rarefaction-wave regions.

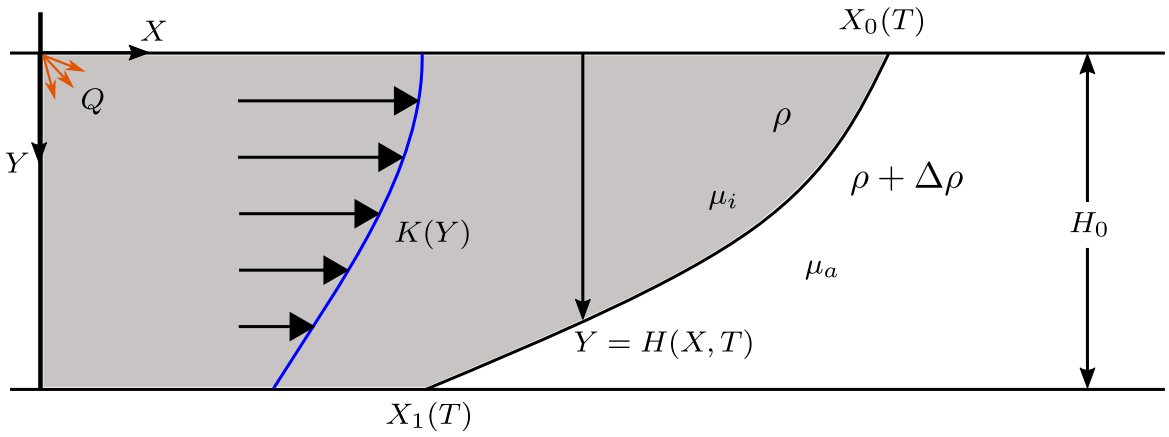

Fig. 2.1 Schematic diagram showing the model problem for constant injection into a vertically heterogeneous aquifer.

2.2 Model

We assume liquid of density ρ and viscosity μ_i is injected into a horizontal, laterally extensive aquifer initially filled with liquid of density $\rho + \Delta\rho$ and viscosity μ_a (figure 2.1). The aquifer has thickness H_0 and porosity ϕ, and fluid is injected at $X = 0$, $Y = 0$ with a flow rate Q. The vertically varying permeability $K(Y)$ is independent of horizontal position and is a smooth function of Y. In the region where the aquifer is fully flooded by the injected fluid, the flow will be pressure-driven, whilst in the slumping region between the two contact points, flow will be driven by a mixture of buoyancy and the background pressure gradient. We assume that the fluids are incompressible, that the motion is governed by Darcy's law and that the mixing between the two fluid is negligible so that there is a sharp interface between them [see

the experimental results of Pegler et al. [111]]. Once the invading fluid has spread beyond a distance $L \gg H_0$ from the well, the pressure becomes approximately hydrostatic [17, 89] and is given by

$$P(X,Y,T) = \begin{cases} P_0 + \rho g Y & 0 < Y < H \\ P_0 + (\rho + \Delta\rho) g Y - \Delta\rho g H & H < Y < H_0 \end{cases} \tag{2.1}$$

where $P_0 = P(X,0,T)$ is the unknown pressure at the top of the aquifer. Using Darcy's law for the horizontal component of the flow,

$$U_i = -\frac{k_0(Y)}{\mu_i}\frac{\partial P_0}{\partial X}, \quad U_a = -\frac{k_0(Y)}{\mu_a}\left(\frac{\partial P_0}{\partial X} - \Delta\rho g \frac{\partial H}{\partial X}\right), \tag{2.2}$$

where U_i and U_a are the transport velocities of the injectate and ambient fluid, respectively. Local mass conservation for the injected and ambient fluids may be expressed in the form

$$\phi\frac{\partial H}{\partial T} = -\frac{\partial}{\partial X}\left(\int_0^H U_i \mathrm{d}Y\right), \quad \phi\frac{\partial (H_0 - H)}{\partial T} = -\frac{\partial}{\partial X}\left(\int_H^{H_0} U_a \mathrm{d}Y\right). \tag{2.3}$$

Adding these two equations together provides an equation for the conservation of mass of the current,

$$\int_0^H U_i \mathrm{d}Y + \int_H^{H_0} U_a \mathrm{d}Y = Q. \tag{2.4}$$

This can be recast as a constraint for the global mass conservation of the injected fluid,

$$\phi \int_0^{X_0(t)} H(X,T)\mathrm{d}X = QT, \tag{2.5}$$

where $X_0(T)$ is the contact point along the top of the aquifer (see figure 2.1), and we have assumed injection begins at $T = 0$. We use the aquifer height H_0 and the vertically averaged permeability,

$$\bar{K} = \frac{1}{H_0}\int_0^{H_0} K(Y)\mathrm{d}Y \tag{2.6}$$

to introduce the dimensionless depth-integrated permeability,

$$\psi(H/H_0) = \frac{1}{H_0\bar{K}}\int_0^H K(Y)\mathrm{d}Y. \tag{2.7}$$

Note that $\psi(0) = 0$, $\psi(1) = 1$ and, in a uniform aquifer, $\psi(H/H_0) = H/H_0$. The unknown pressure P_0 can be eliminated by substituting the expressions for the Darcy velocities (2.2) into (2.4). Local mass conservation for the injectate (2.3a) then leads to the advection-

diffusion type equation for the thickness of the current,

$$\phi\frac{\partial H}{\partial T}+Q\frac{\partial}{\partial X}\left\{\frac{\psi(H/H_0)}{m+(1-m)\psi(H/H_0)}\right\}=UH_0\frac{\partial}{\partial X}\left\{\frac{m\psi(H/H_0)[1-\psi(H/H_0)]}{m+(1-m)\psi(H/H_0)}\frac{\partial H}{\partial X}\right\}, \tag{2.8}$$

where

$$U=\frac{\Delta\rho g\bar{K}}{\mu_i}, \qquad m=\frac{\mu_i}{\mu_a} \tag{2.9}$$

are the velocity associated with the buoyant slumping of the injectate, and the viscosity ratio, respectively. To complete the mathematical description, we require initial and boundary conditions. Injection begins at $T=0$ so

$$H(X,0)=0. \tag{2.10}$$

At the contact point along the top of the aquifer, $X=X_0(T)$, the boundary condition is

$$H(X_0(T),T)=0. \tag{2.11}$$

Differentiating the equation for mass conservation (2.5) with respect to time and applying the boundary condition (2.11) gives

$$\phi\int_0^{X_0(t)}\frac{\partial H}{\partial T}\mathrm{d}X=Q. \tag{2.12}$$

By integrating (2.8) between $X=0$ and $X=X_0(T)$, and applying (2.11) and (2.12) we obtain the boundary condition at $X=0$:

$$\left\{Q\frac{\psi(H/H_0)}{m+(1-m)\psi(H/H_0)}-UH_0\frac{m\psi(H/H_0)[1-\psi(H/H_0)]}{m+(1-m)\psi(H/H_0)}\frac{\partial H}{\partial X}\right\}\Bigg|_{X=0}=Q. \tag{2.13}$$

Note that the governing equation (2.8) and the boundary conditions (2.11) and (2.13) do not change when the aquifer becomes fully flooded by the injectate.

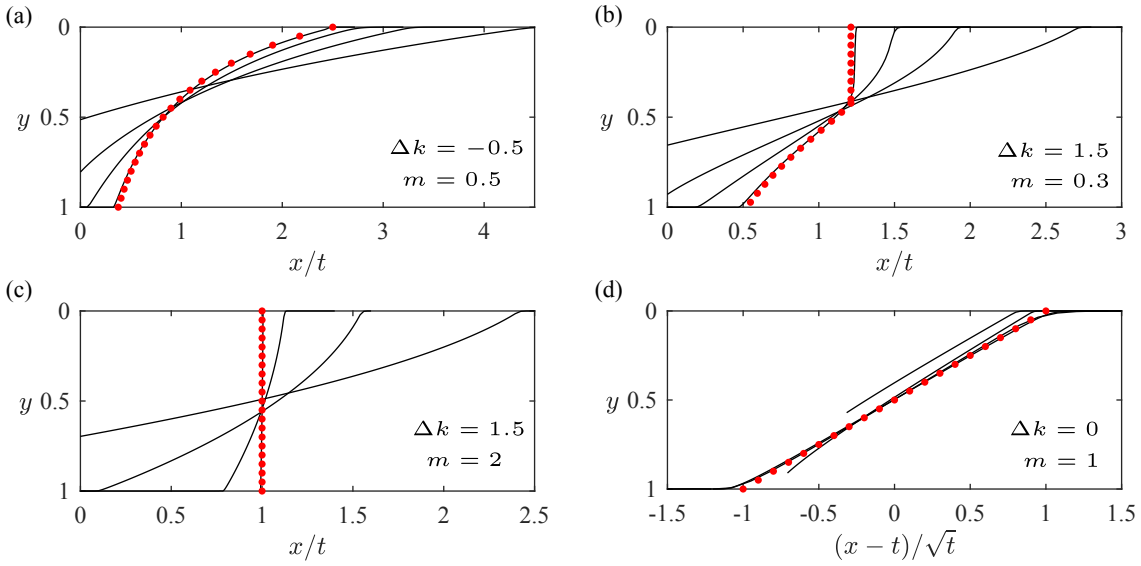

Fig. 2.2 Numerical simulations of the injection of buoyant fluid into a stratified porous medium from early to late times. The interface is shown at $t = 0.1$, 0.5, 2.5 and 62.5 in similarity coordinates for four different sets of parameter values (a-d). The late-time asymptotic solutions found in section 2.4 are shown as red dots and they agree well with the $t = 62.5$ numerical solution. (a) shows a rarefaction wave, the asymptotic shape being given by (2.26); (b) is a compound interface with shock and rarefaction regions, the shape of the shock being given by (2.38); (c) is a full shock, with shape given by (2.30); and (d) is the case of uniform permeability and equal viscosities, which leads to a front that grows in proportion to $t^{1/2}$, the shape found by Huppert and Woods [89]. These four panels characterise the four possible late time regimes, shown in parameter space in figure 2.3.

2.2.1 Non-dimensionalisation

Balancing the contributions from the net flow and the buoyant slumping in the nose region of the current leads to the scalings

$$h = \frac{H}{H_0}, \quad y = \frac{Y}{H_0}, \quad x = \frac{Q}{UH_0^2}X, \quad t = \frac{Q^2}{\phi U H_0^3}T. \tag{2.14}$$

Using these scalings and the dimensionless functions

$$k(y) = \frac{K(Y)}{\bar{K}}, \quad \psi(y) = \psi(Y/H_0), \tag{2.15}$$

we can re-express equation (2.8) in dimensionless form as

$$\frac{\partial h}{\partial t} + \frac{\partial}{\partial x}\left\{\frac{\psi(h)}{m+(1-m)\psi(h)}\right\} = \frac{\partial}{\partial x}\left\{\frac{m\psi(h)[1-\psi(h)]}{m+(1-m)\psi(h)}\frac{\partial h}{\partial x}\right\}. \tag{2.16}$$

Our choice of scalings (2.14) has removed the buoyancy parameter,

$$B = \frac{Q}{UH_0}, \tag{2.17}$$

from the governing equation so that, in dimensionless terms, buoyancy dominates for $t \ll 1$ and the net flow driven by pressure for $t \gg 1$. The initial condition is $h(x,0) = 0$. The boundary condition at the leading contact point, $x = x_0(t)$, is $h(x_0(t),t) = 0$. The dimensionless form of the $X = 0$ boundary condition (2.13) is

$$\left\{\frac{\psi(h)}{m+(1-m)\psi(h)} - \frac{m\psi(h)[1-\psi(h)]}{m+(1-m)\psi(h)}\frac{\partial h}{\partial x}\right\}\Bigg|_{x=0} = 1. \tag{2.18}$$

At early times, when the aquifer has not been fully flooded by the injectate and $h(0,t) < 1$, the boundary condition (2.18) can be rearranged. First, we multiply by $m+(1-m)\psi(h)$, the $\psi(h)$ terms then cancel, and dividing by $m[1-\psi(h)]$ yields

$$1 = \left[-\psi(h)\frac{\partial h}{\partial x}\right]\Bigg|_{x=0}. \tag{2.19}$$

At later times, $h(0,t) = 1$, and such a rearrangement is not possible because the last step was dividing by $m[1-\psi(h)]$. Instead, we observe that $h = 1$ satisfies equation (2.18) for any

value of $\partial h/\partial x$. The flooding of the aquifer implies a second contact point at the base of the aquifer with $h(x_1(t),t) = 1$, where $x_1(t) < x_0(t)$ (see figure 2.1).

2.3 Numerical simulation

The nonlinear advection-diffusion equation (2.16) with appropriate boundary conditions was integrated numerically following the approach of Zheng et al. [146] using the finite difference scheme of Kurganov and Tadmor [97]. Whilst the model in section 2.2 applies for a wide range of choices for $k(y)$, we first choose to use a linear stratification,

$$k(y) = 1 + \Delta k\left(y - \frac{1}{2}\right). \tag{2.20}$$

Here $\Delta k = k(1) - k(0)$ is the dimensionless permeability difference between the top and the base of the aquifer, and has values in the range $-2 < \Delta k < 2$.

Figure 2.2 shows the numerical results at early and late times, illustrating how the interface transitions to the late-time solution (red dots). The long-time solutions are independent of the vertical location of the injection well at $x = 0$ because the injectate has flooded the aquifer. Figure 2.2 illlustrates the four late-time regimes for the interface. Figure 2.2a is a growing rarefaction wave across the whole aquifer, which may be identified since the horizontal coordinate is x/t; figure 2.2b shows a compound interface consisting of a vertical interface in the upper region, which travels at a constant speed v_s, and a growing rarefaction wave in the lower region. In figure 2.2c, the shock extends across the entire aquifer and travels with unit velocity; figure 2.2d is the special case of uniform permeability and unit viscosity ratio, for which the interface grows proportionally to $t^{1/2}$ as found by Huppert and Woods [89]. These numerical results motivate the late-time asymptotic analysis of the four regimes in section 2.4, which suggests parameter values for which each regime occurs (see figure 2.3).

2.4 Late-time asymptotic solutions

At long times, the permeability profile across the aquifer has a significant influence on the interface evolution. We anticipate that the lateral extent of the current is very large compared to the thickness of the layer. This implies that the ratio of the buoyancy force to the pressure associated with the net flow is small. In dimensional terms, this is equivalent to assuming that the interface is much longer than the aquifer thickness [111, 146]. The diffusive term on the right-hand side of (2.16) can then be neglected. We therefore seek solutions to the

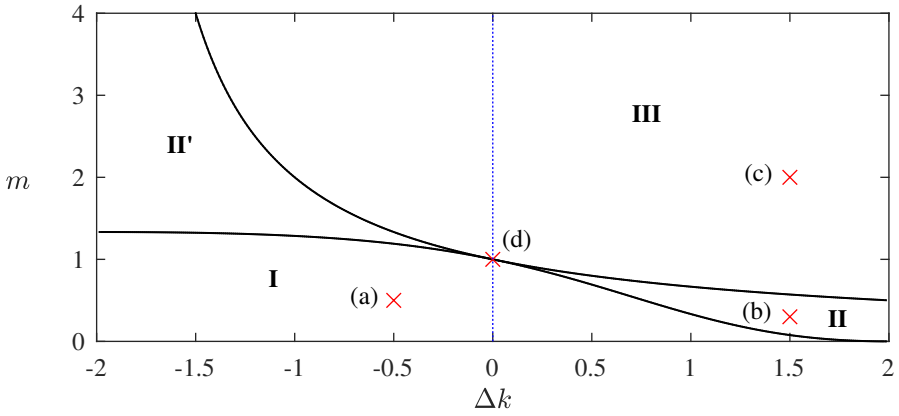

Fig. 2.3 Parameter space for the late-time solution for linear $k(y)$. For parameter values in region I, given by (2.25), the interface tends to a rarefaction wave (figure 2.2a). In region III, given by (2.28), the interface develops a shock across the entire aquifer (figure 2.2c). For regions II and II', there is a mixed solution (figure 2.2b). The blue dashed line along $\Delta k = 0$ is the region of parameter space previously studied by Pegler et al. [111] and Zheng et al. [146]; the solution at $\Delta k = 0$, $m = 1$ (see figure 2.2d) where the interface grows proportional to $t^{1/2}$ is shown to be singular by this figure. Moreover, by including heterogeneous permeability, we have found new compound solutions in II and II' which do not occur along the blue dashed line. The labelled red crosses correspond to the parameter values for the interface shapes in the panels (a-d) in figure 2.2.

equation

$$\frac{\partial h}{\partial t} + \frac{\partial}{\partial x}\left\{\frac{\psi(h)}{m+(1-m)\psi(h)}\right\} = 0, \tag{2.21}$$

with boundary conditions $h(x_0(t),t) = 0$ and $h(0,t) = 1$ since the aquifer is fully flooded. This is a scalar first-order equation with flux function [see section 4 of 92],

$$f(h) = \frac{\psi(h)}{m+(1-m)\psi(h)}. \tag{2.22}$$

The characteristics are

$$\frac{\mathrm{d}x}{\mathrm{d}t} = f'[h_0(s)] = \frac{mk[h_0(s)]}{[m+(1-m)\psi(h_0(s))]^2} \tag{2.23}$$

where $h = h_0(s)$ is the general initial condition on the line $x = s$, $t = 0$ in the (x,t) plane and $h_0(s)$ is a decreasing function. The initial conditions develop into either a shock or a rarefaction wave.

2.4.1 Rarefaction interface

If $f'(h)$ is monotonically decreasing in $(0,1)$, then the Jacobian is nowhere zero and the method of characteristics can be applied to solve equation (2.21). For the linear $k(y)$ given by equation (2.20), we wish to find values of the parameters Δk and m for which this solution method is possible and the interface is a rarefaction. The condition that $f'(h)$ is monotonically decreasing across the channel is equivalent to requiring

$$f''(h) \equiv \frac{m\Delta k[m+(1-m)\psi(h)] - 2m(1-m)k(h)^2}{[m+(1-m)\psi(h)]^3} \tag{2.24}$$

to be negative in all of $(0,1)$. The denominator is always positive across the channel and the numerator is a quadratic in h since $k(h)$ is linear. The condition for the rarefaction solution can now be found in terms of the parameters,

$$m \leq \frac{(\Delta k-2)^2}{\Delta k^2 - 2\Delta k + 4}. \tag{2.25}$$

Equation (2.21) then has self-similar solutions $h(x,t) = h(\xi)$, in terms of the similarity variable $\xi = x/t$. The solution is implicitly given by

$$\xi = \frac{x}{t} = f'(h), \tag{2.26}$$

and the contact points satisfy

$$x_0(t) = m^{-1}\big(1 - \tfrac{1}{2}\Delta k\big)t, \qquad x_1(t) = m\big(1 + \tfrac{1}{2}\Delta k\big)t, \tag{2.27}$$

at $h = 0$ and $h = 1$, respectively. Provided the inequality (2.25) is satisfied, h is a decreasing function of x and the extent of the interface grows in proportion to time, implying that the diffusive term in the governing equation (2.16) is $\mathscr{O}(t^{-2})$ whilst the advection term is $\mathscr{O}(t^{-1})$. The interface gradient is $\mathscr{O}(t^{-1})$ and the assumptions made in arriving at equation (2.21) are self-consistent. This analysis is confirmed by comparing the asymptotic solution (2.26), with numerical simulations of the full governing equation in figure 2.2a.

Figure 2.3 shows the region I in parameter space given by (2.25). If the injectate is sufficiently mobile compared to the ambient fluid ($m \ll 1$), then the current will run along a thin layer at the top, even if the permeability is much lower there (i.e. $\Delta k \approx 2$). Conversely, when Δk is close to -2, the resistance to flow is so much higher at the bottom of the aquifer that even an injectate that is slightly more viscous than the ambient fluid will spread out

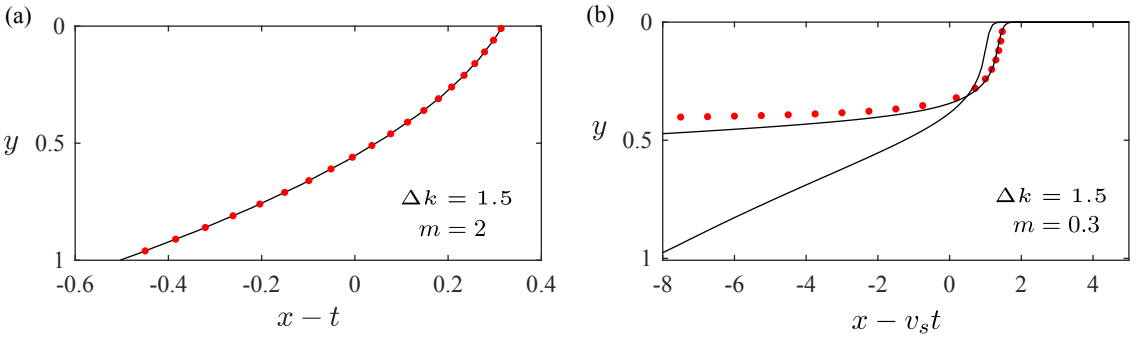

Fig. 2.4 Shocks in travelling-wave coordinates. The solid lines are the numerical results and the red dots show the shape predicted by the steady travelling wave solutions found in section 2.4.2 and 2.4.3. (a) The full shock from figure 2.2c shown at $t = 10$, which has excellent agreement with the asymptotic shape. (b) The partial shock from figure 2.2b shown at $t = 10$ and $t = 100$ in coordinates moving at the speed of the shock, given by (2.37). Convergence to the asymptotic shape is much slower for the partial shock.

along the top as a rarefaction wave. For values of Δk between these two limits, there is a balance between the resistance associated with the low permeability and the resistance associated with the high viscosity. Indeed, the boundary given by the inequality (2.25) has m as a decreasing function of Δk.

2.4.2 Full shock interface

When the parameter values do not satisfy the inequality (2.25), a shock needs to be introduced to solve the weak formulation of equation (2.21), which corresponds to a conservation law. If $f'(h)$ is monotonically increasing in $(0,1)$, then all the characteristics of the advection equation (2.21), given by (2.23), cross and a weak solution (with a discontinuity) can be sought; the solution develops a shock that extends across the whole aquifer from $h = 0$ to $h = 1$. The shock requires $f''(h)$ (equation 2.24) to be positive in $(0,1)$. For the linear variation of permeability (equation 2.20), the condition for the full shock in terms of the parameters is

$$m \geq \frac{1}{1+\Delta k/2}. \tag{2.28}$$

In the absence of gravity, this shock would not occur; instead, the buoyant injectate would be driven along the base of the aquifer by the combination of higher permeability and the low viscosity of the ambient fluid. The introduction of a shock is equivalent to assuming that buoyancy forces balance this effect and so the light injectate rises to the top of the aquifer

and the interface travels with constant shape and velocity. Mass conservation implies the shock travels with unit velocity (see figure 2.2c).

The numerical results in travelling coordinates, shown in figure 2.4a, can be used to inspect the approximately vertical interface in figure 2.2b. The shock is not in fact a vertical line; it is smoothed by the buoyancy force. We seek to find the shape of this non-vertical shock.

For parameter values such that the full shock condition given by (2.28) is satisfied, the interface moves with unit velocity, and this motivates our seeking a travelling-wave solution to the full equation (2.16), with $h(x,t) = h(\eta)$ where $\eta = x - t$. Dropping the time derivative and integrating, we find that the shape satisfies

$$h = 1 \qquad \eta \leq \eta_1 \tag{2.29}$$

$$\frac{\mathrm{d}h}{\mathrm{d}\eta} = \frac{\psi(h) - mh + (m-1)h\psi(h)}{m\psi(h)[1-\psi(h)]} \qquad \eta_1 < \eta < \eta_0 \tag{2.30}$$

$$h = 0 \qquad \eta \geq \eta_0. \tag{2.31}$$

The constant of integration is set to zero because the gradient is finite as $h \to 0$. The contact points are constants, $\eta_0 = x_0(t) - t$ and $\eta_1 = x_1(t) - t$ at the top and base of the aquifer, respectively. Note that $\eta_1 < 0$ and $\eta_0 > 0$. The separation of the contact points can be found by numerically integrating equation (2.30) across the aquifer:

$$\eta_0 - \eta_1 = \int_{h=1}^{h=0} \left(\frac{\mathrm{d}h}{\mathrm{d}\eta} \right)^{-1} \mathrm{d}h. \tag{2.32}$$

The shape of the travelling-wave interface is independent of the position of the contact points because the right-hand side of equation (2.30) is independent of η. We can find the shape by solving (2.30) numerically with an arbitrary choice of η_1. To determine the position of the contact points, we use mass conservation, which is

$$\eta_1 + A = 0, \tag{2.33}$$

where A is the area under the interface shape in the partially flooded region.

The red dots in figure 2.4a show the travelling-wave solution we have just calculated. There is good agreement with the numerical solution to the full governing equation (2.16) at $t = 10$, which is plotted as a solid black line.

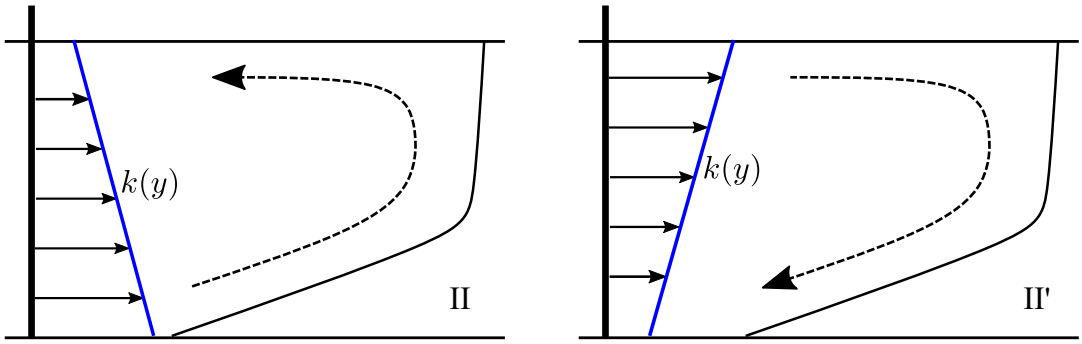

Fig. 2.5 The two different flow structures in a compound rarefaction-shock interface. For parameters in region II ($\Delta k > 0$), the shock is at the base of the shear; whilst in region II' ($\Delta k < 0$), the shock is at the top of the shear. The dashed line shows how fluid enters and then exits the nose region in each regime. The flow structure in the nose is discussed further in chapter 3.

Our model in section 2.2 used the hydrostatic pressure assumption and for this constant wave solution to be consistent, we require that the shape has a shallow gradient so that

$$B = \frac{Q}{UH_0} \ll 1. \tag{2.34}$$

This is equivalent to requiring that the injection flux is small compared to the natural buoyancy velocity. In contrast to the case of a shock, this condition can be relaxed when the interface spreads as a rarefaction wave since the gradient becomes progressively shallower at late times.

2.4.3 Compound rarefaction-shock interface

There are regions of $(\Delta k, m)$ parameter space outside that given by the inequalities (2.25) and (2.28) in which $f(h)$ is neither concave nor convex. For a linearly varying permeability (equation 2.20), $f'(h)$ has a single maximum, in $(0,1)$, for those values of m and Δk. The velocity of the interface is then faster in the middle of the aquifer than at the top and the bottom; the buoyant injectate in the middle would then lie underneath the heavy ambient fluid at the top of the aquifer. We assume that the vertical adjustment owing to buoyancy and Rayleigh-Taylor fingering is much faster than the along-channel advection of fluid driven by injection, which is accurate provided that (2.34) is satisfied [see 88]. In this limit, we expect a compound solution: a rarefaction wave in $h_s < h < 1$ and a vertical shock across $0 < h < h_s$, where h_s is the height of the shock (see figure 2.2b).

The partial shock travels with a velocity of at least 1 owing to mass conservation in order that the interface remains monotonic. In the region of parameter space outside the full shock region, the velocity of the trailing contact point $m(1+\Delta k/2)$ is less than 1 (see (2.28)) and hence travels slower than the partial shock. This confirms that, when $f'(h)$ has a single maximum in $(0,1)$, the shock does not occupy the entire thickness of the aquifer.

Assuming the partial shock is approximately vertical at late times, mass conservation implies that the speed of the shock v_s satisfies

$$v_s h_s = f(h_s) = \frac{\psi(h_s)}{m+(1-m)\psi(h_s)}, \tag{2.35}$$

which is equivalent to a Rankine-Hugoniot condition. The physical requirement that the interface must be continuous at the contact point between the wave and the shock imposes

$$v_s = f'(h_s). \tag{2.36}$$

For a linear $k(y)$, equations (2.35) and (2.36) can be solved to obtain h_s and v_s,

$$h_s = 1-\frac{2}{\Delta k} \pm \sqrt{\frac{2m}{(1-m)\Delta k}}, \quad v_s = \frac{1}{\left(1-m\right)\left(1-\frac{2}{\Delta k}\pm 2\sqrt{\frac{2m}{(1-m)\Delta k}}\right)} \tag{2.37}$$

where the positive square root is taken in $m<1, \Delta k>0$ (II in figure 2.3) and the negative root in $m>1, \Delta k<0$ (II' in figure 2.3). There are no solutions in the other two quadrants, as a compound solution is not possible there. Although II and II' both give rise to compound interface shapes, the flows are physically different, as shown in figure 2.5. In II, the buoyant injectate migrates along the high-permeability region at the base of the aquifer and then rises in the growing nose into the low-permeability region, but the interface advances more rapidly in this upper region of the system. In II', $\Delta k<0$ and the fluid at the top of the aquifer catches the front and is deflected down into the low-permeability region. A more detailed analysis of the particle paths in the nose region of the flow can be found in chapter 3.

As with the full shock, we expect the shape of the partial shock not to be a vertical line because buoyancy smoothes the interface. We adopt a similar approach to that of section 2.4.2 to find the structure of the partial shock. The shock moves with speed v_s, and to capture its dynamics we seek a travelling-wave solution in the shock region ($h<h_s$). In the rarefaction region ($h>h_s$), the interface has gradient of order t^{-1}. Assuming we are at long times, we impose the boundary condition $dh/d\eta \to 0$, as $h \to h_s$, on the shape of the shock.

We transform the full governing equation (2.16) using the travelling coordinate $\eta = x - v_s t$. We drop the time derivative and integrate to obtain

$$\frac{\mathrm{d}h}{\mathrm{d}\eta} = \frac{\psi(h) - v_s h\big[m + (1-m)\psi(h)\big]}{m\psi(h)[1-\psi(h)]} \quad \text{in} \quad h < h_s, \tag{2.38}$$

where the constant of integration is set to zero to satisfy the condition of zero gradient at $h = h_s$. The matching with the rarefaction region leads to the shape having an infinite horizontal extent in the η coordinates, and the position of the leading contact point cannot be determined using mass conservation.

Instead, we solve equation (2.38) numerically with initial condition $h(0) = 0$ and then translate the solution to fit the full numerical solution at some late time. Figure 2.4b shows the $t = 100$ interface as a black line, and the shape given by (2.38) as red dots. In figure 2.4a, the asymptotic shape is compared to the $t = 10$ interface for the full shock. We include the $t = 10$ interface in figure 2.4b to illustrate that convergence to the full shock shape is much faster than convergence to the partial shock shape. Unlike the full shock shape, the partial shock shape equation (2.38) is only valid in the limit as $t \to \infty$. This is because we imposed that the gradient at $h = h_s$ must be zero but the gradient of the rarefaction is $\mathscr{O}(t^{-1})$ at $h = h_s$.

2.4.4 Singular solution for $\Delta k = 0$, $M = 1$

We have found three different late-time regimes and the values of the viscosity ratio and permeability difference for which they occur (see figure 2.3). The four regions of parameter space, I, II, II' and III touch at the point $\Delta k = 0$, $m = 1$. The late-time solutions for this special case of injection of an equal viscosity fluid into a uniform aquifer were found by Huppert and Woods [89]. The distance between the injection well and the fluid-fluid interface is proportional to t and the extent of the front grows proportional to $t^{1/2}$ (see figure 2.2d), an altogether different result from those found for regions I, II, II' and III. This is a singular solution, since, if the aquifer is not uniform or the viscosity ratio is not exactly 1, it is invalid. In that case, the late-time regime will move to one of the cases described above.

2.5 Multiple shock solutions

Thus far in this chapter we have restricted our attention to aquifers in which the permeability increases or decreases linearly from top to bottom. Reservoir rock is typically more complicated than this. Permeabilities can vary significantly over small vertical distances and

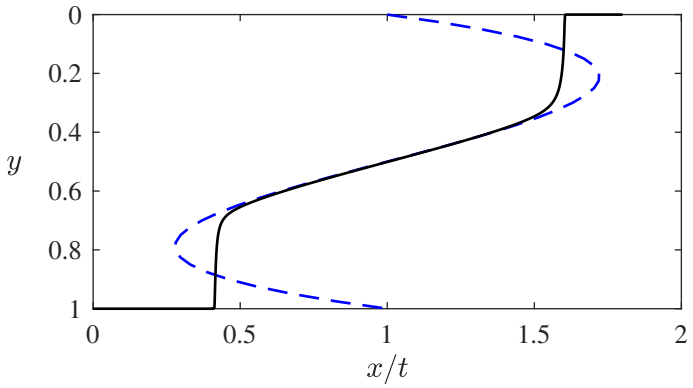

Fig. 2.6 Interface shape for a double-shock (solid black line) at $t = 100$. The governing equation has been solved numerically for $k(y)$ given by equation (2.39). The blue dashed line illustrates how the permeability varies with height and gives the characteristic speeds $f'(h) = k(h)$ for the advection equation.

we expect that there may be more complex late-time regimes as well as the three described earlier for the relatively simple linear vertical variations in permeability. It is possible to have two or more separate shocks across the aquifer moving at different speeds. In the analogous problem of viscous channel flow, a double shock has been observed [see 135] but not in a porous medium. This can have significant implications for reservoir sweep, which is important in both enhanced oil recovery and geologic CO_2 sequestration. In this section, to demonstrate the phenomenon, we consider a more complex cross-layer permeability in which there is a local minimum and local maximum of the permeability within the layer,

$$k(y) = 1 + 15\big(y-1\big)\big(y-\tfrac{1}{2}\big)y. \tag{2.39}$$

For simplicity, we take $m = 1$ so that the advection speeds of constant h are given by

$$\frac{\mathrm{d}x}{\mathrm{d}t} = f'(h) = k(h). \tag{2.40}$$

Since there is a local minimum h_- and a local maximum h_+ in the permeability with $h_- > h_+$, two shock-like regions develop (see figure 2.6).

2.6 Implications for CO_2 sequestration

When using geologic formations as a means of storing CO_2 it is important to have accurate estimates of the fraction of the pore space into which CO_2 can be stored. In particular, the critical volume fraction of interest corresponds to the fraction of pore space accessed by the

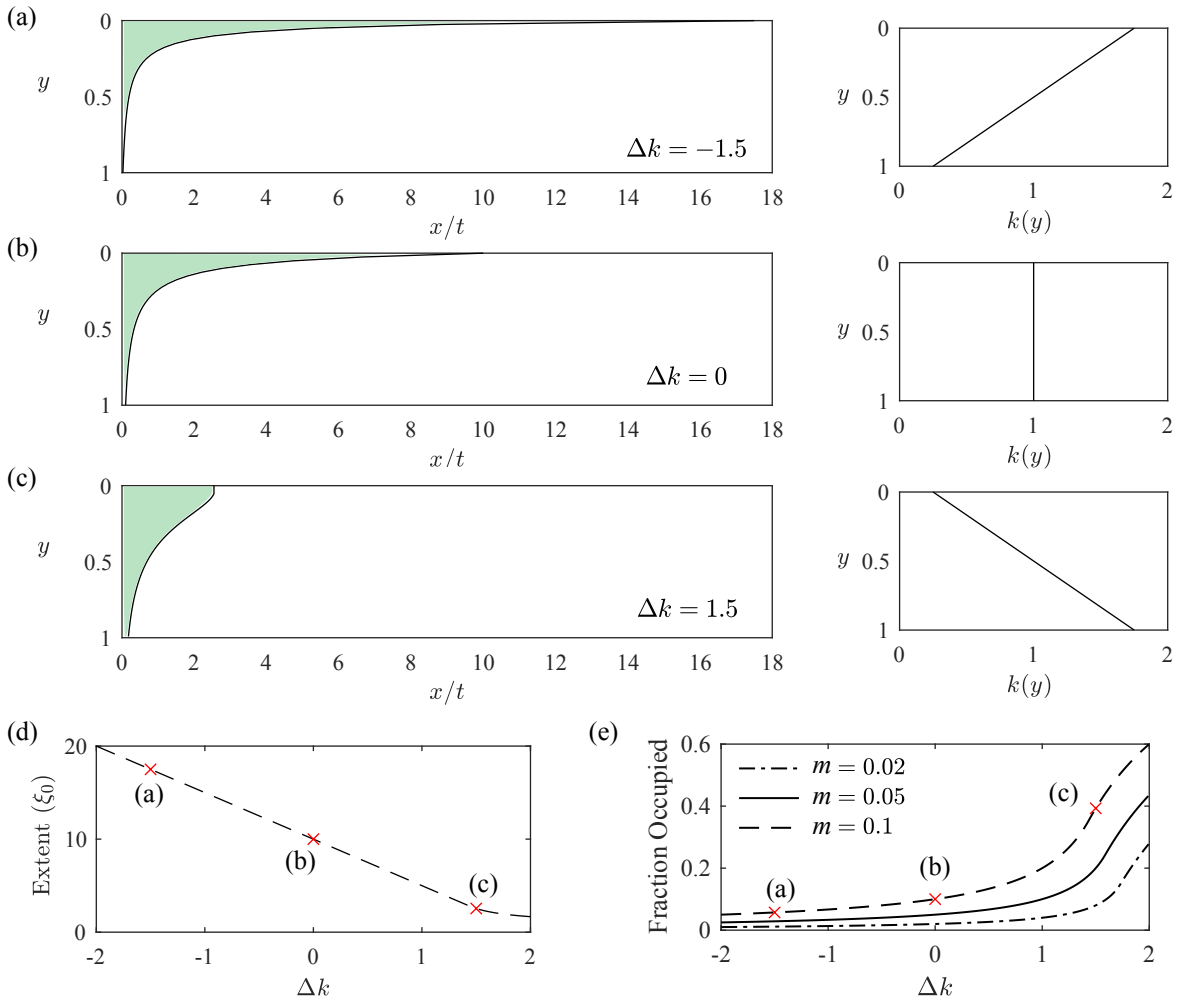

Fig. 2.7 (a-c) Shape of the interface in x/t coordinates for $m = 0.1$ and three different permeability gradients, which are shown in the right-hand column. The shapes are obtained from the numerical solutions at $t = 200$. (d) The position of the leading contact point, ξ_0, as a function of Δk for $m = 0.1$. (e) The fraction of pore space occupied as a function of the permeability gradient for three values of the viscosity ratio typical in carbon sequestration. The red crosses correspond to the interfaces in (a), (b) and (c) showing how a steeper interface (c) leads to a greater fraction of pore space invaded.

CO_2 between the injection well and the leading contact point of the CO_2 plume [28]. This is because once the leading edge of the plume reaches a particular distance from the injection well, the injection may need to cease, either for reasons of security of storage if there are faults or fractures downstream of the injection well, or, in a commercial setting, if different organisations have rights to CO_2 sequestration in adjacent regions of land. The fraction of the pore space accessed by the CO_2 plume during the injection phase will represent the maximum fraction of the pore space into which the CO_2 can be sequestered, since the subsequent motion of the CO_2 is controlled by buoyancy, and hence the plume will subsequently tend to thin and spread. The impact of the plume structure and shape at the end of injection is therefore key for estimating the efficiency of the sequestration [6].

In this chapter we have shown that the presence of a vertical permeability gradient across an aquifer plays a key role in the dynamics of the interface. Here we apply our results to illustrate how such a permeability gradient influences the fraction of pore space accessed by the CO_2.

We define the available pore space as the product of the position of the leading contact point and the thickness of the aquifer. The position of the leading contact point in the $\xi = x/t$ coordinates predicted by the long-time asymptotic solutions is a constant, $\xi_0 = x_0(t)/t$. The area invaded equals the amount of fluid injected which, in dimensionless variables, is t. The fraction of pore space invaded is the ratio of these two quantities:

$$\frac{t}{x_0(t)} = \frac{1}{\xi_0}. \tag{2.41}$$

This implies that the fraction of the pore space invaded is independent of time, as found by Guo et al. [57] for a radial, vertically homogeneous aquifer. Unlike the radial case, however, the fraction invaded is independent of the buoyancy parameter (2.17) because at late times the role of buoyancy can be neglected.

Supercritical carbon dioxide is typically much less viscous than the ambient brine in storage sites and we take the values $m = 0.1$, 0.05 and 0.02 in our examples since m varies with the depth of the aquifer because the viscosities of the brine and the CO_2 exhibit different dependencies on the pressure and temperature. In the classical model with $\Delta k = 0$, these choices of m lead to the interface following the shape of a rarefaction wave with the injectate migrating fastest at the top of the aquifer. For $\Delta k < 0$, the CO_2 migrates even faster at the top of the aquifer owing to the relatively high permeability there, causing the rarefaction to be elongated and the fraction of pore space invaded to be reduced. Conversely, for $\Delta k > 0$, the interface is steeper and the pore space occupied is greater. The interfaces for these three cases

Layer thickness (H_0)	20m
Porosity (ϕ)	0.15
Density of CO_2 (ρ_i)	$750\,\mathrm{kg\,m^{-3}}$
Viscosity of CO_2 (μ_i)	$4\times10^{-4}\,\mathrm{Pa\,s}$
Viscosity of brine (μ_a)	$4\times10^{-3}\,\mathrm{Pa\,s}$

Table 2.1 Parameter values for an example aquifer correspondint to the In Salah storage project [see 140].

are shown in figure 2.7 for $m = 0.1$ and $\Delta k = 0, \pm 1.5$. The right-hand column of figure 2.7 shows the associated permeability profiles. For sufficiently large Δk, the parameters move from region I into region II in figure 2.3 and there is a shock at the top of the aquifer, which alters the fraction stored (see figure 2.7c). The fraction occupied for each of our parameter choices is labelled (a), (b) and (c) in figure 2.7e, which illustrates how the fraction of pore space occupied depends on Δk for our three choices of m.

It is clear that the fraction of pore space invaded is highly dependent on the permeability profile; for example, when $m = 0.1$, in an aquifer with $\Delta k = 1.5$ the CO_2 invades approximately four times the pore space invaded in a uniform aquifer of the same mean permeability. For reference, $\Delta k = 1.5$ represents an aquifer in which the permeability varies by a factor of 7. Using the Kozeny-Carman relation that suggests the permeability is proportional to the grain size squared, $\Delta k = 1.5$ only requires the grain size to vary by a factor of 2.65 across the aquifer, which is within measured values for many aquifers [26]. Therefore, in making storage estimates there is an important uncertainty associated with vertical heterogeneities. Our results could be applied to find the probability distribution of the fraction of pore space occupied given a large dataset of permeability variations in aquifers.

2.6.1 CO_2 storage in a real aquifer with lenses of high and low permeability

In this subsection, we extend the analysis above to the case of a nonlinear permeability profile and we calculate how the permeability structure influences the volume of CO_2 stored in a typical project. We compare permeability profiles, each with the same mean permeability, in which there are lenses of high and low permeability. These profiles are shown in figure 2.8, where the left-hand column shows the interface shape. We assume that the aquifer and the injection well are one kilometre wide (in the direction out of the plane in figure 2.8). We can calculate the mass of CO_2 stored using the parameter values in table 2.1. We assume

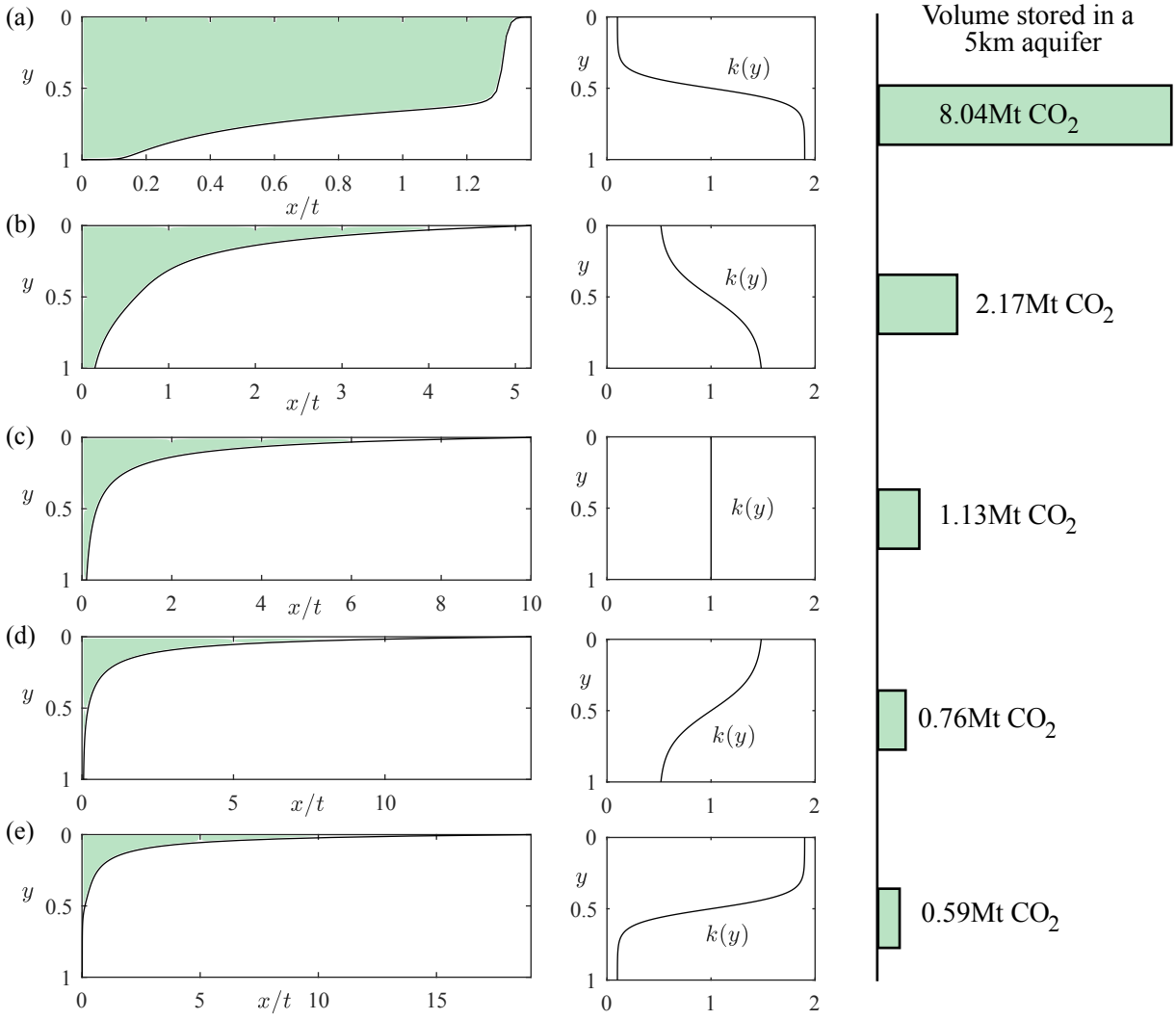

Fig. 2.8 Interface shapes and volume of CO_2 stored for nonlinear permeability profiles including lenses of high and low permeability. The first column shows the interface shape in x/t coordinates, and the corresponding permeability profile is shown in the second column. We calculate the volume of CO_2 stored for each permeability profile in an aquifer which is 20m deep and 1000m wide, assuming injection must stop when the leading edge of the plume has travelled 5000m from the injection well. The parameter values are given in table 2.1. The location of the high and low permeability lenses has a significant influence on the volume stored.

injection is required to stop when the plume reaches a point five kilometres from the injection well. These volumes are shown in figure 2.8 and demonstrate that the volume of CO_2 stored is heavily dependent on the location of the low- and high-permeability lenses.

2.7 Conclusion

We have analysed the injection of buoyant fluid into an aquifer in which the permeability varies vertically. With a permeability that varies linearly with height, we have found four late-time regimes, including a compound rarefaction-shock interface, which does not occur in a uniform porous medium. Our parameter space shows that the classic solution for equally viscous fluids in a uniform aquifer is singular and unstable to small changes in the permeability profile. Applying our results to the problem of carbon storage, we have shown that cross-aquifer permeability differences can significantly influence the volume of CO_2 that can be stored in an aquifer. When the assumption of permeability that varies only linearly with height is relaxed, we have found that it is possible to have two separate shocks that travel at different speeds in a porous medium.

Chapter 3

Advection-controlled tracer migration in a fluid-fluid displacement with vertically varying permeability

The material contained in this chapter has been published in the *Journal of Fluid Mechanics*, under the title 'The effect of vertically varying permeability on tracer dispersion' [82].

3.1 Introduction

We consider the migration of a tracer within a permeable layer in which the permeability varies linearly with height. It has previously been shown that contrasts in permeability lead to shear in the flow profile [22]. In the absence of diffusion, the migration of a tracer is controlled by the shear and the interaction with the nose of the current. In this chapter, we explore the migration of a material line of tracer in each of the regimes for the evolution of the nose described in chapter 2 in the case of linearly varying permeability. We neglect the role of diffusion, which is considered in the next chapter.

However, before launching into this analysis, it is useful for reference to describe the motion of a material line of tracer within the flow in a uniform aquifer distinguishing between the cases in which the nose is of fixed shape and volume and in which the nose gradually spreads with time. Since the flow is uniform across the depth of the aquifer, there is no dispersion associated with the flow, but the location of the tracer relative to the front of the flow does change depending on whether the volume of the fluid in the nose of the current grows in time or remains fixed. In the case that the nose forms a fixed travelling-wave

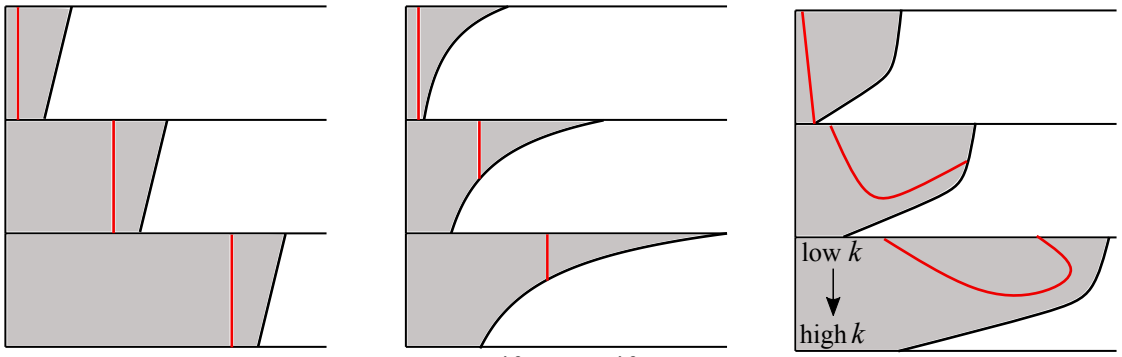

Fig. 3.1 Schematic diagram showing the interaction between injected tracer (red pulse) and the nose region of the current. For a uniform aquifer in which the nose is of fixed shape, tracer remains a constant distance behind the interface. When the nose is growing, tracer is carried into the nose. In a heterogeneous aquifer, tracer undergoes a shear and tracer in the fastest moving regions enters the nose.

structure, the tracer remains a fixed distance behind the nose (see left-hand cartoon in figure 3.1). If instead the nose region grows, the tracer is advected into continually shallower regions of the nose (see middle cartoon in figure 3.1).

In section 3.3, we consider the migration of tracer in an aquifer with a vertical gradient of permeability. The shear in these flows leads to the line of tracer extending laterally upstream of the nose and we examine how this behaviour interacts with the nose region. In section 3.4, we investigate the regime in which the nose of the flow continually grows (see right-hand cartoon in figure 3.1). We show that the tracer may migrate towards the front of the nose as in the case of a uniform aquifer, or that the tracer may initially enter the nose, but then slow down relative to the speed of the nose, and may in fact subsequently advance more slowly than the trailing edge of the nose.

In section 3.5, we explore the interaction of the shearing of the tracer with a nose of fixed shape. Now the nose is a travelling wave which moves at the mean flow speed owing to mass conservation. The cross-channel shear associated with the variation of the permeability leads to a range of heights at which the flow is faster than the mean speed. The combination of these two effects means the tracer can catch and enter the fixed nose. However, mass conservation requires that the tracer which enters the nose subsequently leaves the nose and this occurs through the migration of the tracer into lower permeability regions where it is then left behind as the nose continues to advance.

Finally, in section 3.6, we summarise our results and briefly discuss some implications for CO_2 sequestration.

3.2 Vertically uniform aquifer

In this section we consider the migration of tracer in a vertically uniform aquifer. There are three late-time regimes and we begin by recalling the interface shape from section 2.4. We then introduce a tracer into the flow, and consider how it migrates in each regime. We show that the migration of the tracer is controlled by whether the nose is growing or has fixed volume. A vertical line of tracer added to the injectate at $X = 0$ will remain vertical because there is no shear in the flow.

3.2.1 Late-time interface evolution in a uniform aquifer

In a vertically uniform aquifer, three different late-time asymptotic regimes for the evolution of the nose can emerge depending on whether m is less than, equal to or greater than 1 [see 89, 111, 146]. With a less viscous injectate ($m < 1$), the extent of the nose region increases in proportion to t and the late-time shape is then given by [111]

$$h(x,t) = \frac{\sqrt{\frac{mt}{x}} - m}{1-m}, \tag{3.1}$$

and the positions of the trailing ($h = 1$) and leading ($h = 0$) contact points are, $x_1(t) = mt$ and $x_0(t) = t/m$, respectively (see figure 3.2a).

In the case of fluids with the same viscosity ($m = 1$), the extent of the nose grows in proportion to $t^{1/2}$ and the depth is given by [89]

$$h = \tfrac{1}{2}(1-\xi), \quad \text{where } \xi = (x-t)/\sqrt{t}, \quad \text{for } -1 \le \xi \le 1, \tag{3.2}$$

and the contact points are

$$x_1(t) = t - t^{1/2}, \quad x_0(t) = t + t^{1/2} \tag{3.3}$$

(see figure 3.2b).

With a more viscous injectate ($m > 1$), a steadily travelling shock moving with the speed of the mean flow develops across the entire depth of the aquifer. To model the shock it is convenient to transform to coordinates moving with the shock. We then find the constant

shape of the nose is a straight line with gradient $(1-m)/m$ (see figure 3.2c). The equation for the depth in the nose region is

$$h(x,t) = \frac{1}{2} + \frac{1-m}{m}(x-t), \quad \text{for } x_1(t) < x < x_0(t), \tag{3.4}$$

where the contact points are

$$x_0(t) = t + \frac{m}{2(m-1)}, \quad x_1(t) = t - \frac{m}{2(m-1)}. \tag{3.5}$$

In each regime, the dimensionless Darcy velocity in the current is

$$u = \frac{1 - m(1-h)\frac{\partial h}{\partial x}}{m + (1-m)h}. \tag{3.6}$$

The second term in the numerator arises from buoyancy forces, and the first is associated with the injection pressure. The incompressibility condition for the flow, $\boldsymbol{\nabla} \cdot \boldsymbol{u} = 0$, can be used to calculate the vertical velocity from the horizontal velocity,

$$v = -\int_0^y \frac{\partial u}{\partial x} \mathrm{d}y, \tag{3.7}$$

and $v(y=0) = 0$ as there is no flux across the upper boundary. For the hydrostatic assumption to apply, we require the vertical velocity to be much smaller than the horizontal velocity, which imposes the condition (2.34) in the case of a shock interface.

3.2.2 Tracer injection

The injection of fluid begins at $t = 0$. We consider releasing a pulse of tracer across the entire depth of the aquifer at a dimensionless time t_R after the first injection of fluid. The tracer pulse has negligible lateral extent; it is a material line of particles. The dispersion of a pulse of tracer with non-zero width is analysed in the next chapter. We assume t_R is sufficiently large that the interface between the two fluids has evolved to one of the late-time regimes. We assume the tracer does not react with the injectate or the rock, the interface is gravitationally stable and we assume there is no mixing across the interface. Tracer particles are advected by the flow field (diffusion is neglected in this chapter for simplicity).

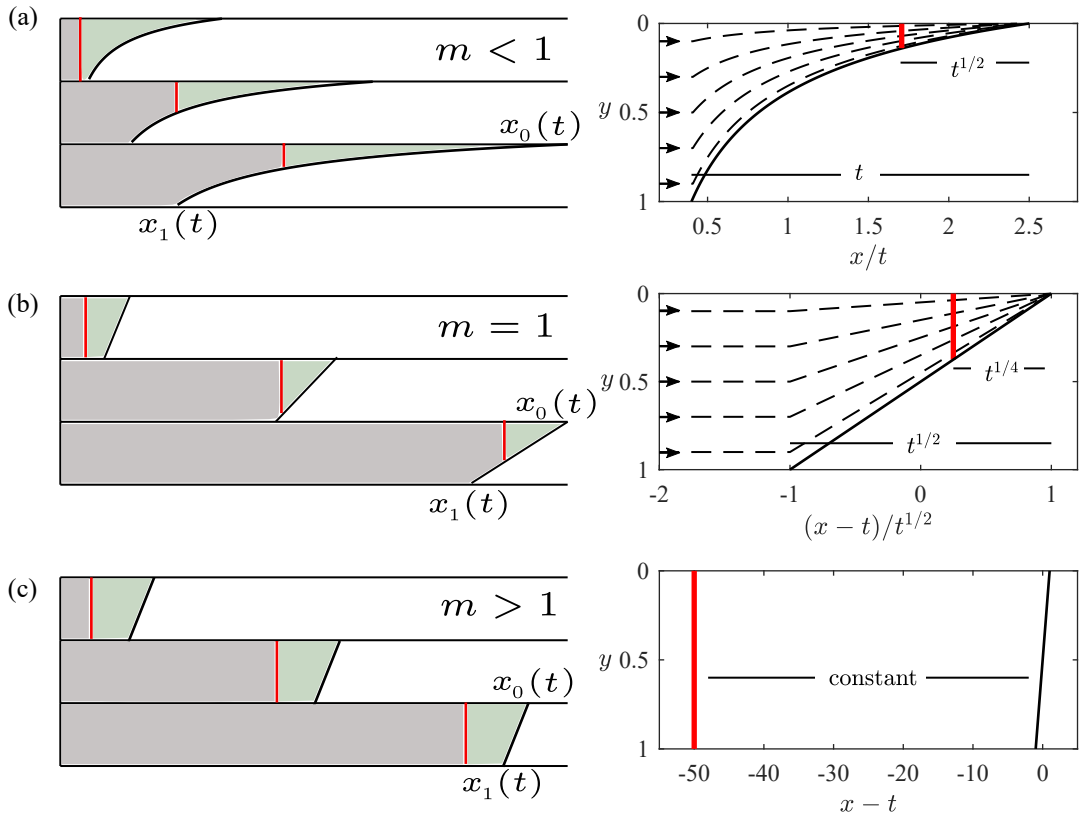

Fig. 3.2 Tracer injection into a uniform porous medium. The left-hand column shows cartoons of the position of tracer (red) relative to the nose at three times. The area of fluid ahead of the tracer (green region) is constant. The right-hand column shows the position of the red tracer in coordinates moving with the nose region, and the particle paths (dashed lines). (a) The case of a less viscous injected fluid. The extent of the nose grows in proportion to t and the distance between the tracer and the leading contact point in proportion to $t^{1/2}$. (b) Equally viscous fluids. The nose grows in proportion to $t^{1/2}$ with the tracer a distance proportional to $t^{1/4}$ from the leading contact point. (c) More viscous injected fluid. The fixed shape nose and the tracer both travel at the mean flow speed and hence the distance between them is constant.

3.2.3 Tracer migration for a less viscous injected fluid ($m < 1$)

At late times the interface is long and thin; the role of buoyancy is negligible. Behind the nose region, the along-channel velocity is 1 which is greater than m, the velocity of the trailing contact point (see figure 3.2a). Using these two velocities and the release time of tracer, $t = t_R$, we calculate that the line of tracer enters the nose region at a time,

$$t_E = \frac{t_R}{1-m}. \tag{3.8}$$

The along-channel velocity in the nose region can be calculated from equation (3.6),

$$u = \frac{1}{m+(1-m)h}, \tag{3.9}$$

where we have neglected the component of velocity owing to buoyancy, consistent with the assumption used in deriving the interface shape. Combining this with our expression for the depth, $h(x,t)$ (equation 3.1), and mass continuity (equation 3.7), we derive the equations for the particle paths in the nose region,

$$\frac{\mathrm{d}x}{\mathrm{d}t} = \left(\frac{x}{mt}\right)^{1/2}, \quad \frac{\mathrm{d}y}{\mathrm{d}t} = -\frac{y}{2(mxt)^{1/2}}. \tag{3.10}$$

We can solve equation (3.10a) for the horizontal position of a vertical line of tracer as it is advected in the nose,

$$x(t;a_0) = \left[\left(\frac{t}{m}\right)^{1/2} - a_0\right]^2 \tag{3.11}$$

where a_0 is a constant which can be found using the time, $t = t_E$ (equation 3.8), at which the line of tracer passes the trailing contact point, $x_1(t) = mt$, and enters the nose,

$$a_0 = \left(\frac{t_E}{m}\right)^{1/2} - (mt_E)^{1/2}. \tag{3.12}$$

Relative to the leading contact point, $x_0(t) = t/m$, the tracer position is

$$x_L = x_0(t) - x(t;a_0) = 2a_0\left(\frac{t}{m}\right)^{1/2} - a_0^2. \tag{3.13}$$

At late times, to leading order, equation (3.13) implies that the distance between the line of tracer and the leading contact point grows in proportion to $b_0 t^{1/2}$ where

$$b_0 = \frac{2a_0}{m^{1/2}} = 2\frac{(1-m)^{1/2}}{m} t_R^{1/2}. \tag{3.14}$$

The volume of fluid ahead of the tracer is constant (green region in figure 3.2a) and hence the line of tracer travels into continually thinner regions of the growing nose. This can also be seen by comparing the distance to the leading contact point, $t^{1/2}$, with the extent of the interface, which grows in proportional to t (see figure 3.2a).

3.2.4 Tracer migration for equally viscous fluids ($m = 1$)

The structure of the nose in the case of isoviscous fluids is singular owing to the balance between the term associated with buoyancy and the term associated with advection. The horizontal velocity upstream of the nose is 1 and hence a line of tracer released from $x = 0$ at $t = t_R$ reaches the trailing contact point, $x_1(t) = t - t^{1/2}$ (equation 3.3), and enters the nose at a time,

$$t_E = t_R^2. \tag{3.15}$$

The along-channel velocity in the nose is given by equation (3.6),

$$u = 1 - (1-h)\frac{\partial h}{\partial x}. \tag{3.16}$$

Combining this with our expression for the depth of the current, $h(x,t)$, (equation 3.2), and mass continuity (equation 3.7), we derive the equations for the velocity and hence the particle paths in the nose region,

$$\frac{\mathrm{d}x}{\mathrm{d}t} = 1 + \frac{x - (t - t^{1/2})}{4t}, \qquad \frac{\mathrm{d}y}{\mathrm{d}t} = \frac{-y}{4t}. \tag{3.17}$$

Solving equation (3.17a) for the horizontal position of the vertical line of tracer gives

$$x = t + t^{1/2} - a_1 t^{1/4}, \tag{3.18}$$

where a_1 is a constant that can be found using the time at which the line of tracer enters the nose,

$$a_1 = 2t_E^{1/4} = 2t_R^{1/2}. \tag{3.19}$$

The distance between the line of tracer and the leading contact point, $x_0(t) = t + t^{1/2}$, grows in proportion to $t^{1/4}$. The distance from the trailing contact point grows in proportion to $t^{1/2}$ because the nose grows in proportion to $t^{1/2}$ (see figure 3.2b). Using the vertical velocity (3.17b), we calculate that the height of the line of tracer decays in proportion to $t^{-1/4}$.

3.2.5 Tracer migration for a more viscous injected fluid ($m > 1$)

When the injected fluid is more viscous than the ambient fluid, the nose takes the form of a fixed travelling wave, shown as a black line in figure 3.2c. A line of tracer is released at $t = t_R$ from $x = 0$; it is initially behind the interface in the fully-flooded region. The nose and the line of tracer both travel at the injection velocity, which in dimensionless terms is unity. The tracer remains a constant distance behind the nose (see figure 3.2c). The nose of the current never influences the dynamics.

3.2.6 Summary of tracer migration in a uniform aquifer

We have found that when fluid is injected into a uniform aquifer of finite thickness and the viscosity of the injected fluid is less than or equal to the viscosity of the ambient fluid ($m \leq 1$), the nose region grows in time, supplied by fluid from behind. There is no dispersion of the tracer but it is carried into continually shallower regions of the nose. When $m > 1$, the nose has fixed shape, and all the fluid moves at the same velocity, remaining a fixed distance behind the nose.

3.3 Model for flow in an aquifer with a vertical gradient of permeability

We now extend the analysis from section 3.2, for tracer migration in a uniform aquifer, to incorporate the influence of vertical heterogeneities. We consider the migration of tracer in the case that the late-time regimes for the evolution of the interface from chapter 2 have developed and we again use a linear permeability profile. The dimensionless Darcy velocity in the current is

$$u = k(y)\frac{1 - m(1 - \psi(h))\frac{\partial h}{\partial x}}{m + (1 - m)\psi(h)}. \tag{3.20}$$

With a linear permeability profile, the interface can evolve into one of the four late-time regimes described in the previous chapter, depending on the values of the parameters Δk

and m. We consider only the migration of tracer in the case of an interface that grows in proportion to time, t and the case of a fixed travelling interface. The singular regime in which the nose grows in proportion to $t^{1/2}$ occurs only in a uniform aquifer and was described in §3.2. For details of the migration of tracer in the mixed regime in which the interface has growing and fixed regions, see Hinton and Woods [82].

The vertical shear produced when there is a vertical gradient of permeability can lead to fundamentally different regimes for the migration of tracer to those found for a uniform aquifer that were presented in section 3.2. We begin in section 3.4 with the migration of the tracer when the nose has the form of a growing rarefaction wave for which we identify three different subregimes depending on the viscosity ratio and the vertical permeability contrast. We then study the migration of the tracer in the full shock regime in section 3.5.

3.4 Tracer migration in a growing nose in a heterogeneous aquifer

In this section, we study the migration of the tracer in the case that the nose of the current grows in proportion to t and the permeability in the aquifer varies linearly with depth. We generalise the results of section 3.2.3, which analysed the migration in a growing nose in a uniform aquifer. We first analyse the structure of the nose and flow therein, and then show that this leads to three subregimes for the evolution of the tracer.

3.4.1 Interface shape and flow structure in a growing nose

In the case of a linear permeability profile, the condition for a growing nose is that $f''(h) < 0$ for all h in $(0,1)$, which is equivalent to

$$m \leq \frac{(2-\Delta k)^2}{4-2\Delta k+\Delta k^2}. \tag{3.21}$$

When this condition is satisfied, the shape of the nose is given by

$$x(h,t) = f'(h)t. \tag{3.22}$$

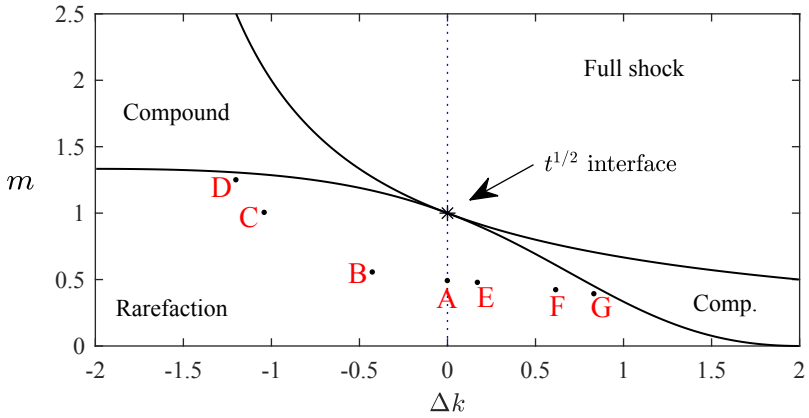

Fig. 3.3 Parameter space delineating the different regimes for the evolution of the interface in an aquifer with a permeability gradient. The vertical axis is the viscosity ratio, $m = \mu_i/\mu_a$, of the injected and ambient fluid. The left-hand side ($\Delta k < 0$) corresponds to the permeability increasing towards the top of the aquifer whilst the right-hand side corresponds to permeability decreasing towards the top of the aquifer. Four regimes can occur; a travelling wave of fixed extent ('Full shock'), a nose which grows in proportion to t (a 'Rarefaction' wave), a mixture of shock and rarefaction regions ('Compound') and the singular case of isoviscous fluids in a uniform aquifer in which the nose grows in proportion to $t^{1/2}$. The dashed blue line indicates $\Delta k = 0$, the case of uniform permeability. To understand the migration of tracer in the rarefaction regime, we consider the parameter values marked with red letters, the migration for A-D is shown in figure 3.4, and the migration of A, E-G is shown in figure 3.5.

The position of the trailing contact point, $h(x_1(t),t) = 1$, can be calculated from the equation for the shape of the nose (3.22),

$$x_1(t) = f'(1)t = mk(1)t. \tag{3.23}$$

Similarly, the leading contact point, $h(x_0(t),t) = 0$, has position given by

$$x_0(t) = f'(0)t = k(0)t/m. \tag{3.24}$$

The shape of the nose is controlled by two parameters, the viscosity ratio, m, and the permeability gradient, Δk. In the case of a uniform aquifer ($\Delta k = 0$) the position of the leading contact point was found to be t/m. As the viscosity of the injectate decreases relative to the ambient fluid, the nose becomes elongated owing to the instability which occurs when a less viscous fluid is injected into a more viscous fluid [125]. A permeability gradient across the aquifer may complement or oppose the effect of the viscosity ratio. If the permeability increases towards the top of the aquifer ($\Delta k < 0$), the injected fluid prefers to flow near the upper boundary and this enhances the effect of the viscous fingering (case B, figure 3.3). As the magnitude of the change in permeability increases, the role of the viscosity contrast becomes smaller in driving the instability (e.g. cases B and C, figure 3.3). Eventually, it is possible for the variations in permeability to dominate the spreading of the nose of the flow and in fact even if the viscosity gradient becomes weakly stabilising ($m > 1$), a sufficient gradient in the permeability can still lead to the spreading of the nose of the flow (case D, figure 3.3). In section 3.4.2, we analyse how the dispersal of tracer is influenced by this balance between the permeability gradient and the viscosity gradient, for flow regimes B-D.

In the opposite case that the permeability decreases towards the top of the aquifer ($\Delta k > 0$), we expect the extent of the finger to be reduced (case E, figure 3.3). If the permeability decreases sufficiently rapidly towards the top of the aquifer, then even with an unstable viscosity ratio the viscous fingering instability at the top of the domain may be suppressed.

To determine how tracer migrates within the nose, we calculate the horizontal and vertical velocities in the nose region from equation (3.20) and mass continuity,

$$u(x,y,t) = \frac{k(y)}{m+(1-m)\psi(h)}, \qquad v(x,y,t) = \frac{(1-m)\psi(y)f'(h)}{mf''(h)t}, \tag{3.25}$$

where $h = h(x,t)$. As before, in the long-time limit, buoyancy is neglected. The velocities upstream of the nose are $u = k(y)$ and $v = 0$. Note that at the late times considered, the

vertical velocity is much less than the horizontal velocity ($v \ll u$) and the hydrostatic pressure assumption is not violated.

In the case that the fluids have equal viscosities ($m = 1$), the vertical velocity in the nose is zero and the flow is purely horizontal. Since $f''(h) < 0$ and $f'(h) > 0$, the vertical velocity is negative when $m < 1$ and fluid migrates towards the upper boundary, whilst when $m > 1$, fluid migrates down towards the bottom boundary. This change in the flow structure is independent of the permeability gradient. Indeed, $m = 1$ is a limiting case for any general nonlinear permeability profile. The limit of purely horizontal flow in the nose is critical to understanding the migration of tracer and will be used in our discussion below.

3.4.2 Permeability increasing towards the top of the aquifer ($\Delta k < 0$)

We examine the migration of tracer in the case that the permeability increases towards the top of the aquifer ($\Delta k < 0$) corresponding to cases B-D in figure 3.3.

In a uniform aquifer the flow speed is constant with depth and fluid enters the nose at all depths with the same flux. As the nose grows in time this fluid is then distributed through the nose, and as a result, the streamlines are all tilted upwards (see figure 3.4aii). A line of tracer therefore moves into the nose and gradually enters shallower and shallower regions as the nose stretches out. If the permeability increases towards the top a small amount, this same process dominates, and the streamlines are all tilted upwards as in the uniform case. However, the speed on the higher streamlines is faster and so a line of tracer becomes stretched out laterally within the nose, with the leading part of the tracer being at the top of the aquifer (case B, figure 3.3, 3.4b).

For a larger viscosity ratio (m), the nose grows more slowly, reducing the tilting of the streamlines. A specific value is reached at which exactly the correct flux of fluid is supplied above each height to supply the growing nose region above that height, and so the streamlines are everywhere horizontal (case C, figure 3.3, 3.4c). In this special case, the tracer is sheared out, but the tracer now remains on an inclined straight line. As discussed earlier, this corresponds to $m = 1$, and occurs for any permeability gradient which increases towards the top of the aquifer.

Finally, if the permeability increases sufficiently rapidly towards the top of the aquifer, but the effect of the viscosity is stabilising ($m > 1$) then the speed of the flow upstream of the nose can exceed the speed of the head of the nose near the upper boundary of the aquifer. As a result, fluid near the top of the aquifer travels faster than the front of the nose, and hence moves into the nose. However, the upstream speed in the aquifer at lower points is now

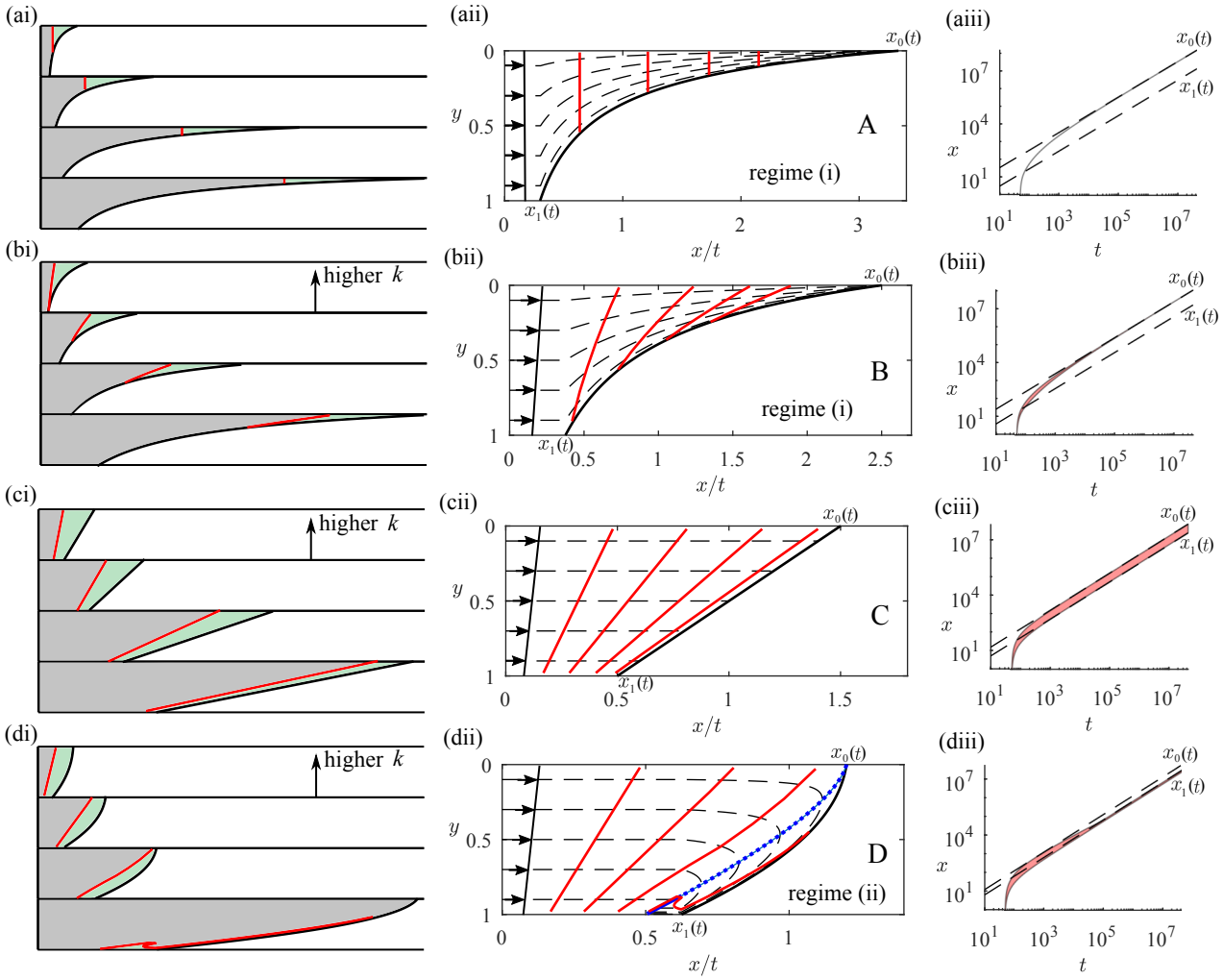

Fig. 3.4 Tracer migration in a growing nose in the case that the permeability decreases from top to bottom ($\Delta k < 0$). The first column shows how the tracer (red line) is carried into the nose in real coordinates at four times. The volume of the green fluid ahead of the tracer is constant. The middle column shows the direction of the shear, the particle paths (dashed lines) relative to the growing nose and the position of tracer at four times (red lines) corresponding to the times in the four cartoons. In the right-hand column, the shaded area shows the along-channel positions occupied by a pulse of tracer released at $t_R = 50$, and the position of the contact points (dashed lines). The rows correspond to A-D in parameter space in figure 3.3. The case of a uniform aquifer is included in the top row for comparison. The dashed blue line in (dii) distinguishes the region in which fluid travels more slowly than the nose.

smaller than the speed of the nose, and so here, the fluid at that depth cannot supply the nose region. Instead the fluid entering the nose at higher points in the aquifer moves down into the lower part of the nose region. Here, the speed is smaller than the speed of the interface, and so the fluid begins to lag behind the nose of the flow. The region in which particles travel more slowly than the interface is bounded by the interface and the dashed blue line in figure 3.4dii. The dashed blue line is the nullcline on which the flow velocity equals the interface velocity. All the tracer eventually converges to a line of points behind the nose on which $x = k(y)t$, shown as a solid blue line in figure 3.4dii. To find the equation of the nullcline, we consider points in similarity space, i.e. $(x/t, y)$ coordinates, at which the along-channel velocity is equal to the velocity of the interface,

$$u(x,y,t) = f'(h(x,t)). \tag{3.26}$$

Using our expression for u (equation 3.25), this can be rewritten as

$$\frac{k(y)}{m+(1-m)\psi(h)} = \frac{mk(h)}{[m+(1-m)\psi(h)]^2}. \tag{3.27}$$

Noting that the depth is a function only of x/t so $h(x,t) = h(x/t)$, the shape of the nullcline is given implicitly by

$$y = \frac{m\Delta k h - (1-m)\psi(h)k(0)}{m\Delta k + (1-m)\psi(h)\Delta k}, \tag{3.28}$$

where $h = h(x/t)$. Note that this line coincides with the interface in the limiting case of $m = 1$.

We have found two regimes for the migration of the tracer. We call the case in which the tracer migrates into continually shallower regions of the nose 'regime (i)' (A and B in figure 3.4), and the case in which the tracer enters the nose in the high permeability region at the top of the aquifer and subsequently lags behind the nose in the low permeability region 'regime (ii)' (D in figure 3.4). The migration towards the leading contact point in regime (i) and migration behind the trailing contact point in regime (ii) is illustrated in the right-hand column of figure 3.4, the shaded area shows the along-channel positions of the tracer and the dashed lines are the positions of the contact points.

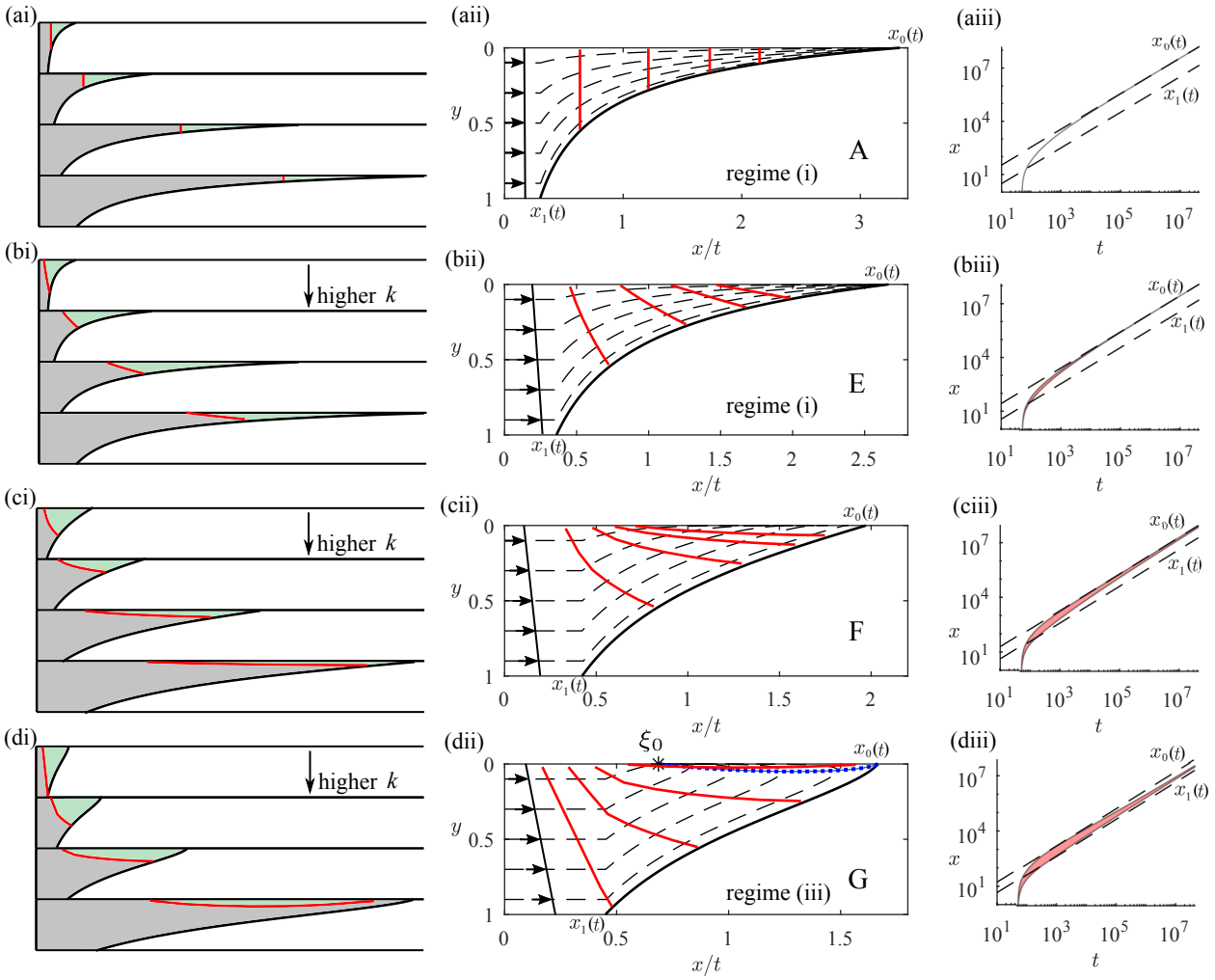

Fig. 3.5 Tracer migration in a growing nose in the case that the permeability increases towards the bottom of the aquifer ($\Delta k > 0$). The first column shows how the tracer (red line) is carried into the nose in real coordinates at four times. The volume of the green fluid ahead of the tracer is constant. The middle column shows the direction of the shear, the particle paths (dashed lines) relative to the growing nose and the position of tracer at four times (red lines) corresponding to the times in the four cartoons. In the right-hand column, the shaded area shows the along-channel positions occupied by a pulse of tracer released at $t_R = 50$, and the position of the contact points (dashed lines). The rows correspond to A, E, F and G in parameter space in figure 3.3. The case of a uniform aquifer is included in the top row for comparison. The dashed blue line in (dii) distinguishes the region in which fluid travels more slowly than the nose, and ξ_0 is the position along the upper boundary which tracer converges to in similarity coordinates.

3.4.3 Permeability increasing towards the bottom of the aquifer ($\Delta k > 0$)

We examine the migration of tracer in the case that the permeability is highest towards the bottom of the aquifer ($\Delta k > 0$) corresponding to cases E-G in figure 3.3. Note that the viscosity ratio is less than 1 in this case because the permeability gradient suppresses the viscous fingering. Hence, $v < 0$ (see equation 3.25b) and fluid in the nose always migrates upwards.

If there is a small increase in permeability from the top of the aquifer to the bottom then the streamlines are all tilted upwards as in the uniform case. However, the speed on the lower streamlines is faster and so a line of tracer becomes stretched out laterally within the nose, with the leading part of the tracer being nearest to the interface (case E, figure 3.3, 3.5b). Tracer migrates into shallower and shallower regions as the nose stretches out and hence case E lies in regime (i) (see figure 3.5biii).

In an aquifer with a larger increase in permeability from the top to the bottom, the fluid near the bottom of the aquifer travels much faster than the nose. There is a specific value (which shall be specified later in 3.30) at which the lower region provides sufficient flux that the leading portion of the nose is supplied only by fluid from the bottom of the aquifer. In this case, fluid near the top of the aquifer does not migrate into continually shallower regions of the nose; instead, particles travel towards the top boundary and subsequently slowly converge towards the leading contact point (case F, figure 3.3, 3.5c).

If the permeability increase is even larger, the flux entering the nose near the bottom boundary is greater than the flux needed to supply the growing nose. Owing to mass conservation, fluid reverses relative to the nose in a thin region near the upper boundary (case G, figure 3.3, 3.5d). The equation of the nullcline is given by (3.28). We call this 'regime (iii)'. It is fundamentally different from regime (ii) because fluid is supplied to the nose from the bottom of the aquifer, and fluid never lags behind the nose. The nullcline intersects the upper boundary at a point ξ_0 given implicitly by

$$h(\xi_0) = \frac{2m}{(1-m)k(0)} + 1 - \frac{2}{\Delta k}. \tag{3.29}$$

Tracer converges towards a region around this point, which lies within the nose, and between the two contact points (see figure 3.5dii and 3.5diii).

To find the value of the viscosity ratio at which the transition between regimes (i) and (iii) occurs, we analyse the limiting case (F in figure 3.3, 3.5c). Fluid migrates towards the

upper boundary and the nullcline just touches the upper boundary. This corresponds to the stationary point given by equation (3.29) coalescing with the leading contact point. Setting $h(\xi_0) = 0$ yields

$$m = \frac{(2-\Delta k)^2}{\Delta k^2 + 4}, \tag{3.30}$$

which is the boundary between regime (i) and regime (iii).

It is interesting to note that the regimes correspond to the convexity of the interface at the leading contact point. The interface is concave for parameter values in regime (i), and convex at the leading contact point for regimes (ii) and (iii). The limiting interface between regimes (i) and (ii) is linear and the limiting interface between regimes (i) and (iii) has an inflection point at the leading contact point (see figure 3.4cii and figure 3.5cii). This characterisation arises from the linear shear; the limiting regimes occur when the interface is linear because the volume of fluid supplied at each height upstream of the nose matches the flux at that height in the nose. If the permeability gradient was not linear, the limit between regimes would not correspond to a locally linear interface at the leading contact point.

3.5 Heterogeneous aquifer; tracer migration in a nose of fixed extent

In the present section, we consider the case in which the nose is a travelling wave of fixed extent. The shape of the travelling interface, with $\eta = x - t$, satisfies (section 2.4.2)

$$\frac{\mathrm{d}h}{\mathrm{d}\eta} = \frac{\psi(h) - mh + (m-1)h\psi(h)}{m\psi(h)(1-\psi(h))}. \tag{3.31}$$

Using the Darcy velocity (equation 3.20), and mass continuity, we can calculate the horizontal and vertical particle velocities in the nose region,

$$u = \frac{h}{\psi(h)}k(y), \qquad v = -\psi(y)\frac{\psi(h) - hk(h)}{\psi(h)^2}\frac{\mathrm{d}h}{\mathrm{d}\eta}. \tag{3.32}$$

Upstream of the nose, in the fully-flooded region, $u = k(y)$ and $v = 0$. There is a discontinuity in v at the trailing contact point. This is unphysical but the hydrostatic assumption requires that the horizontal length scale is much larger than H_0 (cf. equation 2.34) and hence in dimensional terms the vertical velocity is much less than the horizontal velocity and the discontinuity in the vertical velocity is small.

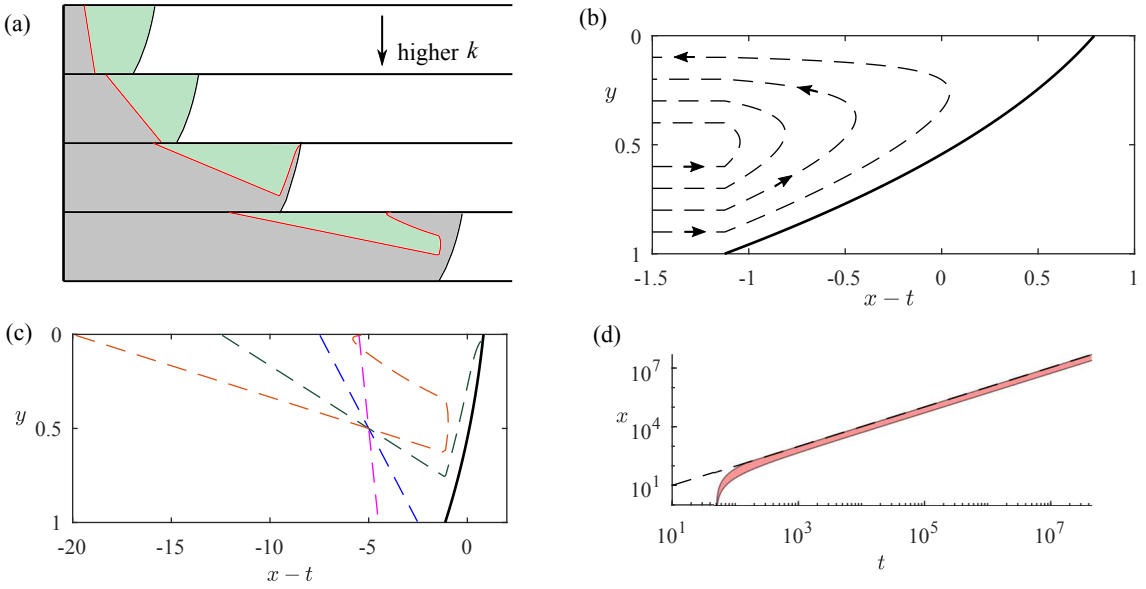

Fig. 3.6 The interaction between the shearing of tracer and a fixed nose. The permeability increases from the top of the aquifer to the bottom of the aquifer ($\Delta k > 0$). (a) is a cartoon illustrating how a red line of tracer undergoes a shear, tracer in the fast regions enters the nose and subsequently encloses the green fluid which was initially ahead of the line of tracer. (b) shows particle paths relative to the travelling nose, particles below $\frac{1}{2}$ are deflected into the upper region. (c) shows the position of a line of tracer at four times (dashed lines) relative to the position of the interface (solid line). The line of tracer is folded over itself and becomes two asymptotically parallel lines joining the top of the aquifer to the trailing edge of the nose. (d) is the position of a pulse of tracer relative to the leading contact point (dashed line) illustrating that the tracer disperses at a rate proportional to t.

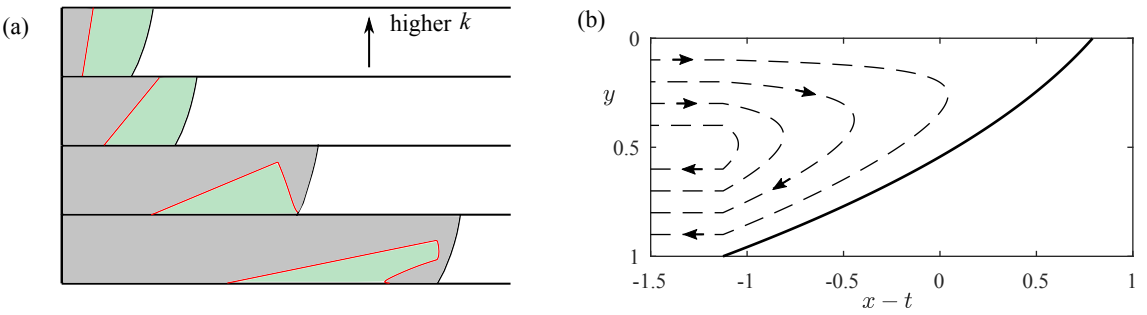

Fig. 3.7 Tracer migration for permeability increasing towards the top of the aquifer ($\Delta k < 0$), in the case of a fixed nose. (a) is a cartoon illustrating how a red line of tracer undergoes a shear, tracer in the fast regions enters the nose and subsequently encloses the green fluid which was initially ahead of the line of tracer. (b) shows particle paths relative to the travelling nose, particles above $\frac{1}{2}$ are deflected into the lower region. The late time evolution of a line of tracer is similar to the case $\Delta k > 0$ up to a reflection across $y = \frac{1}{2}$.

In section 3.2.5, we showed that in a uniform aquifer in which there is a travelling wave solution, all the fluid travels at the mean flow speed and a line of tracer remains a fixed distance behind the nose. Now, when the aquifer is not uniform, the variation of the permeability with height partitions the line of tracer into heights where the tracer travels faster than the mean speed ($k(y) > 1$) and heights where the tracer is slower ($k(y) < 1$). The vertical line of tracer is linearly sheared until the fastest particle, either $y = 1$ if $\Delta k > 0$ or $y = 0$ if $\Delta k < 0$ reaches the nose region, which travels at the mean speed. This fastest particle enters the nose, and travels across the aquifer towards the lower permeability region near the opposite boundary of the aquifer where it is left behind by the advancing nose region (see figure 3.6). After the first entry time, tracer at progressively lower (or greater if $\Delta k < 0$) heights reaches the nose region where it travels to successively higher (or lower) points in the slower half. This eventually leads to the migration of all particles which originate in the region in which $k(y) > 1$ to the region in which $k(y) < 1$, the slow half. In contrast, particles which began in the slow region never reach the nose. These particles undergo a linear shear. The particle at $y = \frac{1}{2}$ travels at the speed of the nose. At long times, there are then two regions of tracer: that which has travelled through the nose and that which has not. Both are linearly sheared and form lines joining the slow boundary of the aquifer to the point at $y = \frac{1}{2}$ behind the nose. The initial vertical line of tracer has been folded in half and linearly sheared as shown in figure 3.6 for the case of permeability decreasing towards the top of the aquifer ($\Delta k > 0$). Figure 3.7 shows the case $\Delta k < 0$. The particle paths and interface shape are calculated numerically using equations (3.31) and (3.32). Owing to mass conservation, particles that enter the nose at $y = y_0$ leave at $y = 1 - y_0$.

At times long after all the tracer is in the slow half of the aquifer, the two lines of tracer continue to be linearly sheared and become asymptotically identical straight lines with gradient $(\Delta k t)^{-1}$. The distance behind the front of the centre of mass of the tracer tends to

$$\frac{\Delta k t}{4} \tag{3.33}$$

as $t \to \infty$. Similarly, the lateral standard deviation of the tracer lines is

$$\frac{\Delta k t}{4\sqrt{3}}. \tag{3.34}$$

The extent of tracer grows in proportion to t and Δk owing to the shear, in contrast to a uniform aquifer. Molecular diffusion or pore-scale dispersion would lead to growth in the

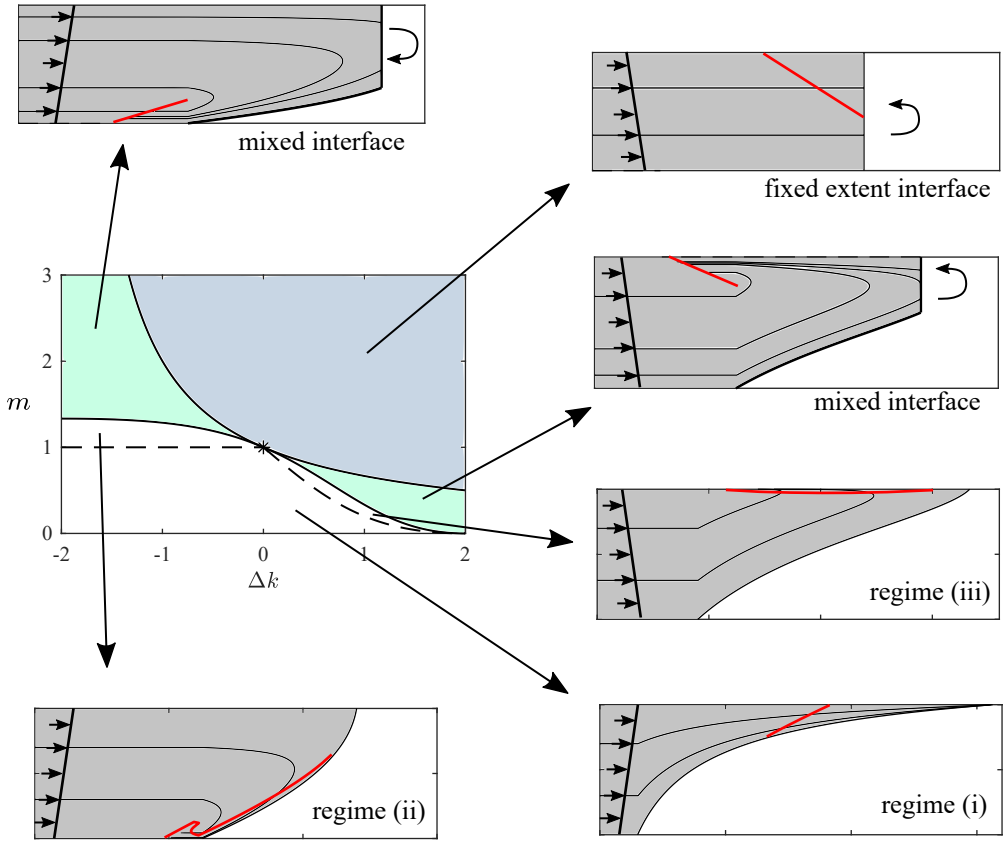

Fig. 3.8 Parameter space and corresponding plots of the interface and flow structure in x/t coordinates. The red lines show the position of tracer at a late time. The dashed lines in parameter space separate the three regimes for a growing nose, the boundary is given by $m = 1$ in $\Delta k < 0$ and equation (3.30) in $\Delta k > 0$. The curly arrows indicate the recirculation within the fixed extent regions. For details of the migration of tracer in the case of a mixed interface consisting of growing and fixed regions see Hinton and Woods [82].

extent of the tracer zone at a rate proportional to $t^{1/2}$ in a uniform flow [cf. 112]. This is discussed further in the following chapter.

3.6 Discussion and conclusion

We have analysed the migration of tracer within a flow in a confined aquifer in which the permeability varies linearly with height. In the context of CO_2 sequestration, our work focuses on the regime in which the dispersion of the tracer by the shear dominates the effects of pore-scale dispersion or molecular diffusion. In this regime, the tracer evolution is controlled by the structure of the leading interface of the CO_2 plume as well as the shear.

For reference, we have shown that in a uniform medium the nose region may either grow in time if the viscosity of the input fluid is less than the original, and it has a fixed shape if the viscosity of the input fluid is greater. If the nose region is growing, the tracer travels into increasingly shallow regions of the nose. If the nose region has fixed shape, the tracer remains a constant distance behind the interface.

When the formation has a vertical gradient of permeability, we have found three regimes for the evolution of the tracer in a growing interface; the tracer can continue to migrate into progressively shallower regions of the nose indefinitely; the tracer can enter the nose, and then circulate through the nose, so that it then reverses relative to the interface and drops out of the nose; finally, tracer may converge to a region within the nose. We have found parameter values which delineate these different regimes and explored the transitions between them.

The combination of a shear flow and a fixed-shape, shock-like interface also leads to novel results. Fluid in the high permeability regions travels faster than the interface, this fluid enters the nose and subsequently migrates out of the nose via the low permeability region. The longitudinal extent of the tracer then grows in proportion to t, rather than $\sqrt{t}$ which would be expected if small-scale dispersion or diffusion dominated.

In all regimes, the longitudinal extent of the tracer is proportional to $|\Delta k|t$ at early times before tracer enters the nose. This picture has some similarities with the review of field data by Gelhar et al. [51] who investigated an extensive range of tracer dispersal data in water saturated aquifers, for which the viscosity ratio is unity, and found that the dispersion coefficient increased linearly with the distance between the wells. However, we note that in the real rock systems studied by Gelhar et al. [51] the detailed permeability structure would be more complex than the present modelling, the flows are three dimensional and the effects of multiple layers may also play a role.

In figure 3.8, we summarise the results of this chapter and relate them to parameter space. The interface shapes in figure 3.8 are shown in x/t coordinates and hence the fixed regions have zero width and the recirculation within them is not shown.

Chapter 4

Shear dispersion in an intrusion with a nose of fixed extent in a porous medium

The material contained in this chapter has been accepted for publication in the *Journal of Fluid Mechanics*, under the title 'Shear dispersion in a porous medium. Part 1. An intrusion with a steady shape' [79].

4.1 Introduction

Determining the flow through porous rocks is an important problem in many contexts such as the contamination of freshwater aquifers, enhanced oil recovery and the sequestration of CO_2 within geological storage reservoirs [99, 112, 94]. One way to learn about the unknown and often very heterogeneous rock structure is to add tracers to the injected fluid and observe them downstream [134, 25]. Variations in the permeability within a porous layer can lead to a shear flow as well as Fickian dispersion, as discussed later in this introduction. In addition, the injected fluid may not be miscible with the ambient fluid and the interface between the fluids may evolve in a complex nonlinear fashion. The present chapter explores how the combination of the interface evolution and tracer dispersion regulates the migration of tracer. We combine knowledge about dispersion in a porous medium with knowledge about the evolution of the interface and the associated nose region. The evolution of the interface is different in the cases of a low or high viscosity injectate. The present chapter focuses on the case of a high viscosity injectate, important for enhanced oil recovery and geothermal power. In such situations, the interface advances with fixed shape and tracer remains in the fully-flooded region of the flow where it may become vertically homogenised so that shear dispersion dominates the spreading. In the next chapter, we analyse the case of a less viscous

injectate, typical in CO_2 storage, for which the interface grows in time. Tracer is quickly advected into continually thinner regions of the growing nose, leading to a very different form of dispersion because the role of the shear diminishes in time.

Dispersal of the tracer may arise from pore-scale dispersion, for example owing to molecular diffusion, and large-scale heterogeneity. A significant challenge to determining flow in a heterogeneous aquifer is the uncertainty in the rock structure. Many models have been built assuming that the permeability is a random function of position and it has been shown that this also leads to longitudinal dispersion at a rate proportional to $t^{1/2}$ [50, 33, 43]. However, if there is a systematic variation in the permeability in the cross-flow direction, this can lead to development of a large-scale shear in which case the longitudinal extent of a finite pulse of tracer grows linearly with distance in the absence of pore-scale dispersion or diffusion as analysed in the previous chapter. Such systematic heterogeneity has been observed in numerous deposits [141, 25, 120].

The combination of large-scale shear and micro-scale dispersion creates large cross-layer concentration gradients, which are eventually homogenised by cross-layer diffusion. The longitudinal extent of the tracer grows in proportion to $t^{1/2}$ after the homogenisation but with a significantly enhanced dispersion coefficient as compared to the pore-scale dispersion [137, 5]. In a porous medium, this shear dispersion may occur owing to systematic heterogeneity within a single layer.

In addition to the effects of micro-scale and large-scale dispersion, in a two-phase fluid-fluid displacement, the interface zone between the two fluids has an important influence on the path taken by tracer and this can significantly alter the character of the dispersion, especially if the tracer is soluble only in the injected fluid and not the displaced fluid as assumed herein. The evolution of the nose of the flow, where the thickness of the injected fluid is less than the thickness of the aquifer, is controlled by the injection flux, the buoyancy force, the viscosity ratio and any permeability variations (chapter 2). The evolution of this flow front leads to very different patterns of spreading of the tracer depending on whether the intrusion grows or is of fixed size.

In the previous chapter, we illustrated that in an aquifer with vertically varying permeability, the shear flow results in the maximum speed of the tracer being faster than the speed of the fixed-extent nose. In the absence of any diffusion, the tracer in the high permeability regions catches and circulates through the flow nose. At long times, diffusion becomes important, and leads to cross-layer homogenisation of the tracer. We studied the purely advective transport, as relevant to relatively thick porous layers for which the cross-layer diffusion time, H^2/D, is long compared to the time-scale of the flow (see the region below

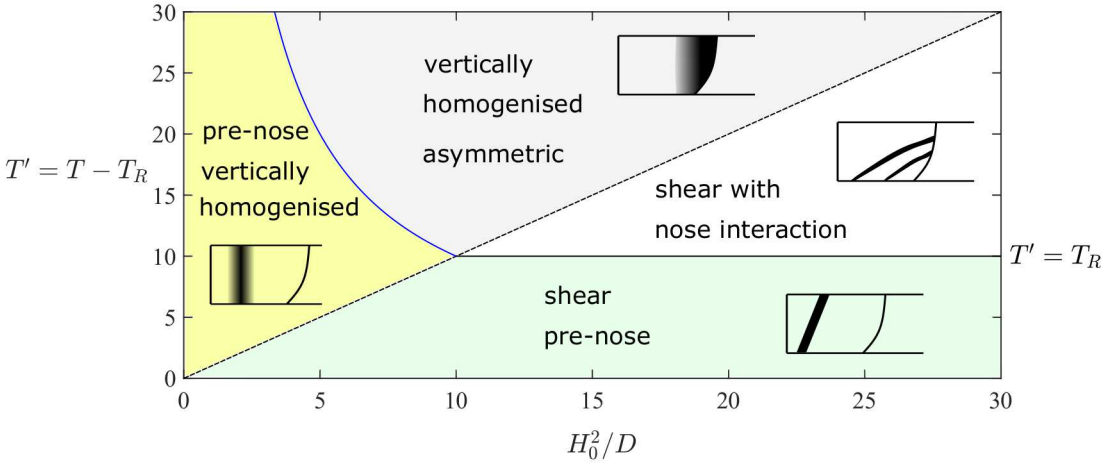

Fig. 4.1 Time regimes for the dispersion of tracer in a fixed intrusion. The horizontal axis corresponds to the timescale for vertical homogenisation (H_0^2/D) relative to the release time of the tracer, T_R, whilst the vertical axis is the dimensionless time after release of the tracer. We use illustrative values of the release time and a linear permeability structure with variation relative to the mean permeability of $\Delta k = 0.1$. The dashed line denotes the time required for vertical homogenisation of the tracer. The pre-homogenised dispersion (below the dashed line) is controlled by the shear flow and interaction with the nose, which was studied in the previous chapter. The tracer is sheared prior to interacting with the fixed nose ('advection, pre-nose'). At a time $L/(\Delta kV)$ after tracer release, where $L = VT_R$ is the distance of the nose from the initial release, the shearing tracer reaches the nose and is folded ('advection with nose interaction'). In the next regime, tracer becomes vertically homogenised and spreads from the nose ('vertically homogenised, asymmetric'). This ordering of regimes occurs in thick aquifers in which H_0^2/D is large. In thinner aquifers, vertical homogenisation occurs prior to tracer reaching the nose. Tracer spreads laterally behind the nose in its vertically homogenised regime ('pre-nose vertically homogenised'). Once homogenised, the rate of dispersion is proportional to $D_{\text{eff}} \sim \Delta k^2 V^2 H_0^2/D$ owing to shear dispersion and the tracer spreads towards the nose, interacting with the nose at a time proportional to L^2/D_{eff}. The curved solid line, corresponding to the interaction between tracer and the nose therefore has shape $\Delta k^{-2}(H_0^2/DT_R)^{-1}$. The diffusive regimes form the topic of the present paper. The case of pre-nose homogenisation is studied in §4.4.1 and the interaction with the nose in §4.4.2 and 4.4.3.

the dashed line in figure 4.1). In thinner layers, the cross-flow diffusion may be significant on the time-scale of the flow and so the dynamics of the tracer dispersal will be different from the purely advective regime described in the previous chapter. This forms the subject of the present chapter (see figure 4.1). We combine the physical ingredients of tracer diffusion, an interface zone between the injected and ambient fluid and variation of the rock permeability in the cross-flow direction, which leads to an along flow shear, which causes some of the tracer to catch up with the nose. The homogenisation owing to cross-flow diffusion occurs before or after tracer reaches the nose leading to different patterns of dispersal. In either case, the tracer eventually becomes vertically homogenised and we investigate the late-time evolution of the tracer distribution and how it is influenced by the interaction with the nose (see figure 4.1). The different transitions to the late-time vertically well-mixed regimes lead to differences in the ultimate extent of the tracer.

We first describe how a finite, vertically uniform pulse of tracer is dispersed within the flow before, during and after its interactions with the nose. We then develop the model in §4.5 to account for a non-uniform initial distribution of the tracer owing to the vertical permeability structure. Finally, in §4.6, we consider the implications of the combined action of dispersion, shear and the interface zone on inferences made about the rock structure from tracer tests.

4.2 Formulation

In the present chapter, we focus on the migration of tracer in the case that the nose has a fixed shape and extent at late times.

4.2.1 Migration of tracer

We consider the release of a pulse of passive tracer into the input fluid. The tracer undergoes diffusion with coefficient D. We assume that the tracer is immiscible in the ambient fluid. The dimensional advection-diffusion equation for the evolution of the concentration of the tracer is

$$\frac{\partial C}{\partial T} + \boldsymbol{U}\cdot\boldsymbol{\nabla} C = \boldsymbol{\nabla}\cdot\big(D\boldsymbol{\nabla} C\big), \tag{4.1}$$

where $\boldsymbol{\nabla}\cdot\boldsymbol{U} = 0$ because the injectate is incompressible. We focus on the case in which molecular diffusion is the dominant dispersive mechanism, which was found to be accurate for low flow rates by Bear [16] (i.e. $U\delta \ll D$, where δ is the typical pore size). This simplifies the problem because the diffusion coefficient, D, is everywhere a constant.

We make C dimensionless by scaling it with the total volume of tracer released. We scale the spatial and temporal coordinates as follows

$$h = H/H_0, \quad y = Y/H_0, \quad x = X/H_0, \quad t = QT/(\phi H_0^2). \tag{4.2}$$

Note that this scaling is different to that of previous chapters so that the dimensionless diffusion coefficient is isotropic (see below). The nose still advances with unit velocity in dimensionless terms. We scale the diffusion coefficient, D with the timescale from (4.2) and the thickness of the aquifer to obtain the dimensionless parameter,

$$\mathscr{D} = \frac{\phi D}{Q}. \tag{4.3}$$

Note that this is the inverse of the Peclet number, $\mathscr{D} = Pe^{-1}$.

Behind the nose, the dimensionless flow velocity is $u = k(y)$ and the vertical velocity is zero by mass continuity. In the previous chapter, we showed that in the absence of diffusion, particles in high permeability regions catch and enter the fixed-extent nose where they migrate into lower permeability regions and fall behind the nose. By considering mass conservation, we showed that particles that enter the nose at $y = y_0$ fall behind and exit the nose at $y = 1 - y_0$. In the present chapter, we assume that if the tracer is well-mixed across the vertical extent of the aquifer, then the flux of tracer into the nose at y_0 equals the flux out of the nose at $1 - y_0$. The time tracer spends in the nose is negligible compared to the time spent behind the nose. Hence, we assume the transition in the nose is instantaneous. We assume that the injection of fluid continues at a constant rate throughout the period in which we study the migration of tracer.

4.3 Numerical simulations

To simulate the migration of a pulse of tracer numerically, we consider the release of a line of particles from $x = 0$ at $t = t_R$ that subsequently undergo advection and diffusion. We use a particle-tracking numerical method, rather than solving the governing advection-diffusion equation for the concentration, because of the complex geometry of the domain associated with the moving fluid-fluid interface.

The position of a particle satisfies the following dimensionless stochastic differential equation

$$\mathrm{d}\mathbf{x} = \mathbf{u}(\mathbf{x}, t)\,\mathrm{d}t + \sqrt{2\mathscr{D}}\,\mathrm{d}\mathbf{W}(t), \tag{4.4}$$

where $\mathbf{u}$ is the flow velocity, $\mathscr{D}$ is the diffusion coefficient and $\mathbf{W}$ is a standard two-dimensional Brownian motion. The interface between the injected and ambient fluids, and the aquifer boundaries are treated as no-flux boundaries. We simulate equation (4.4) numerically using the Euler-Maruyama method [71]. The numerical method is implemented in MATLAB with timestep Δt. The Brownian motion is simulated by generating two random numbers, R_x and R_y, uniformly distributed in $[-0.5, 0.5]$, for each time step and each particle. The horizontal and vertical locations of a particle are updated from time t_n to time $t_{n+1} = t_n + \Delta t$ by

$$x_{n+1} = x_n + u(x_n, t_n)\Delta t + R_x\sqrt{24\mathscr{D}\Delta t}, \tag{4.5}$$

$$y_{n+1} = y_n + v(x_n, t_n)\Delta t + R_y\sqrt{24\mathscr{D}\Delta t}. \tag{4.6}$$

We implement the no-flux condition on the aquifer boundaries, at $y = 0$ and $y = 1$, by treating it as reflective in the numerical scheme [45]. The no-flux condition on the moving fluid-fluid interface is implemented as follows. First, the interface position is updated at each time step. Next, the position of the tracer particles are updated. If a tracer particle is outside the injected fluid, then it is reflected in the updated interface. The reflection is via the normal direction to the interface at the point on the interface nearest to the particle.

As a first check on the numerical method, the calculated mean and variance of a pulse of tracer in a single fluid flow in an aquifer with a vertical gradient of permeability was compared to Taylor's analytic results [137]. One million particles and a time step $\Delta t = 10^{-5}/\mathscr{D}$ provided predictions that were within 0.5% error at a time $t = 2/\mathscr{D}$. In the simulations incorporating the effect of a no-flux interface between the injected and ambient fluids, the method was first run with these choices for the timestep and the number of particles. The method was then repeated with half the timestep and repeated with double the number of particles. This iteration was continued until further changes led to less than 0.5% variation in the mean and variance of the tracer distribution as compared to the previous run. We typically found that this occurred with two or four million particles and a timestep of $\Delta t = 10^{-5}/\mathscr{D}$. For $\mathscr{D} \leq 10^{-4}$, we used $\Delta t = 0.1$. The initial release is either vertically uniform (§4.4) or the concentration is proportional to the permeability at each height (§4.5).

4.4 Release of a uniform pulse

We consider the release of a pulse of tracer into the flow at $x = 0$ at a time, $t = t_R$. The time after release is

$$\tau = t - t_R. \tag{4.7}$$

The concentration of tracer within the released pulse is assumed to be uniform across the vertical extent of the aquifer. We study the situation in which the aquifer heterogeneity influences the initial vertical structure of the concentration in §4.5.

4.4.1 Pre-nose migration

We first consider the migration of the tracer at times before the nose has any influence. In this regime the flow depth is $h = 1$ and the flow velocities are $u = k(y)$ and $v = 0$.

At very early times, the tracer spreading is dominated by molecular diffusion. However, this quickly becomes negligible in comparison to the shearing of the tracer pulse owing to the vertical variation of the permeability. We ignore the initial molecular diffusive regime.

In the shearing regime, the mean velocity is unity and this motivates transforming the advection-diffusion equation into the travelling frame with $\chi = x - \tau$,

$$\frac{\partial c}{\partial t} + \tilde{k}(y)\frac{\partial c}{\partial \chi} = \mathscr{D}\left(\frac{\partial^2 c}{\partial \chi^2} + \frac{\partial^2 c}{\partial y^2}\right), \tag{4.8}$$

where $\tilde{k}(y) = k(y) - 1$ is the relative velocity. Note that $\int_0^1 \tilde{k}(y)\,\mathrm{d}y = 0$.

At early times, the dispersion of tracer is dominated by the shear flow due to the permeability variation across the aquifer. The lateral extent of the tracer initially grows in proportion to time τ and the role of diffusion is negligible (see figure 4.2a). This advection-dominated dispersion was studied in the previous chapter.

At later times the role of diffusion becomes non-negligible. As the tracer is sheared, large cross-channel concentration gradients develop (see figure 4.2b). These gradients are smoothed out by diffusion over a timescale of order $1/\mathscr{D}$, which corresponds to the time taken for tracer particles to sample the entire thickness of the aquifer. At times $\tau \gg 1/\mathscr{D}$, the tracer has been sheared and has become 'well-mixed' vertically so that the concentration is independent of depth, y (see figure 4.2d). It has thus spread a much larger lateral distance than it would owing to along-flow diffusion alone, demonstrated by the two columns in figure 4.2. The combination of the shear flow and cross-channel diffusion enhances the rate of

along-flow dispersion. This effect is known as shear dispersion, first explained by Taylor [137].

To study the distribution of tracer in the along-flow direction, we calculate the moments of the distribution. We follow the method of Aris [5] and define

$$c_p(y,\tau) = \int_{-\infty}^{\infty} \chi^p c(\chi, y, \tau) \mathrm{d}\chi, \tag{4.9}$$

$$m_p(\tau) = \overline{c_p} = \int_0^1 c_p \mathrm{d}y, \tag{4.10}$$

for any integer p. We can obtain an equation for c_p by multiplying equation (4.8) by χ^p and integrating over the entire extent of the aquifer (assuming the nose is far from the zone occupied by the tracer),

$$\frac{\partial c_p}{\partial \tau} = \mathscr{D}\frac{\partial^2 c_p}{\partial y^2} + \mathscr{D}p(p-1)c_{p-2} + p\tilde{k}(y)c_{p-1}. \tag{4.11}$$

Then integrating over the thickness of the aquifer yields

$$\frac{\mathrm{d}m_p}{\mathrm{d}\tau} = \mathscr{D}p(p-1)\overline{c_{p-2}} + p\overline{c_{p-1}\tilde{k}(y)}, \tag{4.12}$$

where an overline represents the integral,

$$\overline{\phi}(\chi,\tau) = \int_0^1 \phi(\chi, y, \tau)\,\mathrm{d}y. \tag{4.13}$$

Since a vertically uniform pulse of tracer is released from $\chi = 0$ at $\tau = 0$ we obtain the following initial conditions

$$c_0(y,0) = 1 \qquad c_p(y,0) = 0 \text{ for } p \geq 1 \tag{4.14}$$

$$m_0(0) = 1 \qquad m_p(y,0) = 0 \text{ for } p \geq 1. \tag{4.15}$$

Note that $m_0(\tau) \equiv 1$ owing to conservation of tracer. We also have the boundary conditions $\partial c_p/\partial y = 0$ at $y = 0$ and $y = 1$ as there is no flux into the boundary.

The equation for c_0 is (see 4.11)

$$\frac{\partial c_0}{\partial \tau} = \mathscr{D}\frac{\partial^2 c_0}{\partial y^2}. \tag{4.16}$$

Combining equation (4.16) with the initial condition (4.14a), we obtain $c_0(y,\tau) \equiv 1$. Substituting this into the equation for the first moment (4.12) yields $m_1(\tau) \equiv 0$ i.e. the centre of mass of the tracer is at $\chi = 0$.

Before launching into the calculation for the second moment, it is useful to define the function

$$\tilde{\psi}(y) = \int_0^y \tilde{k}(s)\mathrm{d}s, \tag{4.17}$$

and $\tilde{\Psi}(y)$ is defined to be the anti-derivative of $\tilde{\psi}(y)$ where the constant of integration is chosen so that $\overline{\tilde{\Psi}(y)} = 0$.

The governing equation (4.11) for c_1 is

$$\frac{\partial c_1}{\partial \tau} = \mathscr{D}\frac{\partial^2 c_1}{\partial y^2} + \tilde{k}(y), \tag{4.18}$$

which has solution

$$c_1(y,\tau) = \sum_{n=1}^{\infty} b_n \cos(n\pi y)\exp\left[-n^2\pi^2\mathscr{D}\tau\right] - (1/\mathscr{D})\tilde{\Psi}(y), \tag{4.19}$$

where we have used the no-flux conditions and initial condition (4.14). The terms with coefficients b_n comprise the complementary function, whilst the last term is the particular integral. The initial condition (4.14) requires that the coefficients satisfy the equation

$$\sum_{n=1}^{\infty} b_n \cos(n\pi y) = (1/\mathscr{D})\tilde{\Psi}(y). \tag{4.20}$$

The equation for the evolution of the second moment is (see 4.12)

$$\frac{\mathrm{d}m_2}{\mathrm{d}\tau} = 2\mathscr{D} + 2\overline{c_1\tilde{k}(y)}. \tag{4.21}$$

Upon substituting our expression for c_1 (4.19), we obtain

$$\frac{\mathrm{d}m_2}{\mathrm{d}\tau} = 2\mathscr{D} - (2/\mathscr{D})\overline{\tilde{k}(y)\tilde{\Psi}(y)} + 2\overline{\sum_{n=1}^{\infty} b_n \cos(n\pi y)\exp\left[-n^2\pi^2\mathscr{D}\tau\right]\tilde{k}(y)}, \tag{4.22}$$

We integrate with respect to time to obtain

$$m_2(\tau) - m_2(0) = 2(\mathscr{D} + \kappa/\mathscr{D})\tau + 2\overline{\sum_{n=1}^{\infty} \frac{b_n}{n^2\pi^2\mathscr{D}}\cos(n\pi y)\left\{1 - \exp\left[-n^2\pi^2\mathscr{D}\tau\right]\right\}\tilde{k}(y)}, \tag{4.23}$$

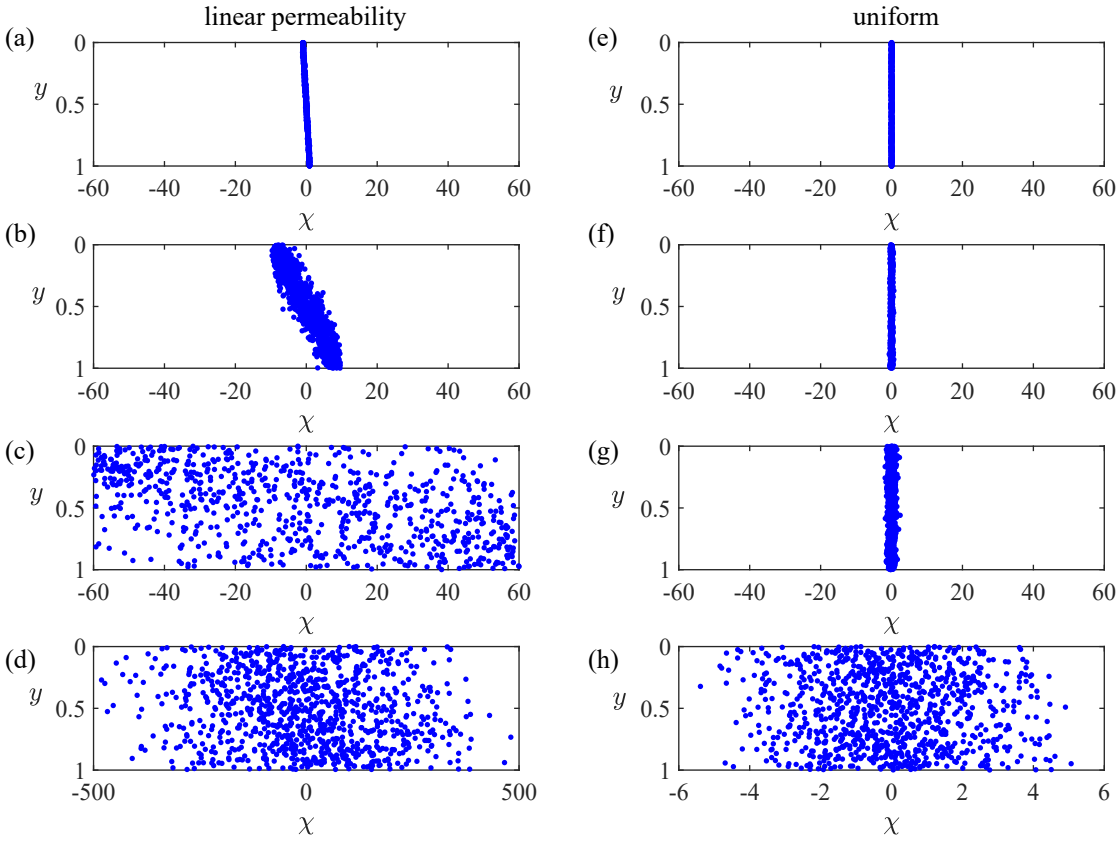

Fig. 4.2 Dispersion of 1000 particles upstream of the nose. (a-d) Dispersion in an aquifer with a vertical linear permeability variation, $\Delta k = 1$, and (e-h) in a uniform aquifer. In both cases $\mathscr{D} = 0.001$. The rows correspond to four times, in (a, e) $\tau = 0.002/\mathscr{D}$, in (b, f) $\tau = 0.02/\mathscr{D}$, in (c, g) $\tau = 0.2/\mathscr{D}$ and in (d, h) $\tau = 2/\mathscr{D}$. In a heterogeneous aquifer, the tracer is sheared by the permeability gradient (see panel a and b), which leads to large cross-channel concentration gradients. These are smoothed out by diffusion after times of order $1/\mathscr{D}$ and the tracer distribution becomes independent of cross-channel coordinate. This leads to a much higher dispersion coefficient (see equation 4.25) than in a uniform aquifer (note the different axes in d and h).

where

$$\kappa = \int_0^1 \tilde{\psi}(y)^2 \mathrm{d}y, \tag{4.24}$$

which is obtained from integrating $\overline{-\tilde{k}(y)\tilde{\Psi}(y)}$ by parts. To determine the late-time behaviour of the second moment we neglect the exponential terms in (4.23). Then we integrate by parts twice in the summand and substitute (4.20) for the coefficients to obtain the late-time expression

$$m_2(\tau) = 2\mathscr{D}_{\mathrm{eff}}\tau - \frac{2\lambda}{\mathscr{D}^2}, \tag{4.25}$$

where

$$\lambda = \overline{\tilde{\Psi}(y)^2} \tag{4.26}$$

and

$$\mathscr{D}_{\mathrm{eff}} = \mathscr{D} + \kappa/\mathscr{D} \tag{4.27}$$

is the effective diffusion coefficient, which is an enhanced rate, faster than ordinary molecular diffusion, $\mathscr{D}$, owing to shear dispersion (compare the two columns in figure 4.2). We plot the predicted variance (4.25) as a red dotted-dashed line in figure 4.3 for particular parameter values, showing excellent agreement with the numerical results at later times.

Since the centre of mass is at $\chi = 0$, equation (4.25) provides the late-time along-flow variance of the tracer distribution. Late times correspond to τ of order at least $1/\mathscr{D}$ so that the neglected terms in (4.23) are exponentially small. Physically, this is the time for tracer to diffuse across the thickness of the aquifer and the tracer distribution to become independent of y (figure 4.2).

The dispersion of tracer is symmetric about its centre of mass, provided tracer has not yet dispersed towards the nose. We analyse the interaction between the tracer and the different noses in the next subsections.

The analysis of Taylor [137] can be used to show that at late times the thickness averaged concentration of tracer, $\bar{c}(\chi,\tau)$, satisfies the diffusion equation with coefficient $\mathscr{D}_{\mathrm{eff}}$. At such times, the concentration distribution evolves as a Gaussian with mean $\chi = 0$ and variance given by equation (4.25). The constant term in (4.25) can be interpreted as an adjustment time to the y-independent, Gaussian spreading and we write

$$m_2(\tau) = 2\mathscr{D}_{\mathrm{eff}}(\tau - \tau_0) \qquad \text{where} \quad \tau_0 = \frac{\lambda}{\mathscr{D}^2\mathscr{D}_{\mathrm{eff}}}. \tag{4.28}$$

The constant τ_0 is a virtual source time for the self-similar Gaussian spreading.

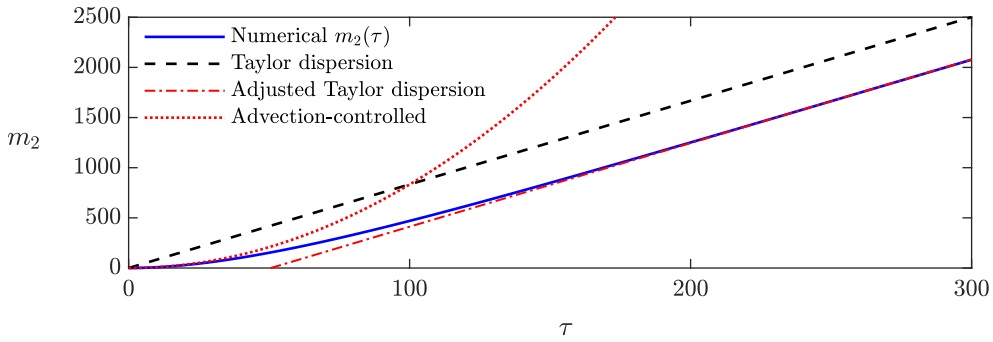

Fig. 4.3 Second moment of the tracer distribution in the along-channel direction in the case of a linear permeability gradient with $\Delta k = 1$ and diffusion coefficient, $\mathscr{D} = 0.002$. The numerical results are plotted as a solid blue line. The second moment arising from the enhanced Taylor dispersion, $2\mathscr{D}_{\text{eff}}\tau$, is plotted as a black dashed line. The adjustment owing to the early-time transition to the shear dispersion regime is $-2\lambda/\mathscr{D}^2$ (equation 4.25), which is plotted as a red dotted-dashed line showing excellent agreement with the late-time numerical results. The red dotted line represents the early-time dispersion owing to advection in which the second moment of the tracer extent is $(\Delta k\tau)^2/12$.

The reduction in the second moment from $2\mathscr{D}_{\text{eff}}\tau$ arises because of the early-time behaviour during which the role of diffusion is negligible and the lateral extent of the tracer grows more slowly driven by advection. For example, for a linear permeability gradient,

$$k(y) = 1 + \Delta k(y - 1/2), \tag{4.29}$$

the second moment evolves according to $(\Delta k\tau)^2/12$ in the absence of diffusion. This is plotted as a red dotted line in figure 4.3, and is slower than shear dispersion (dashed black line) at early times.

In order to illustrate the magnitude of shear dispersion in a typical heterogeneous layer, consider the following permeability profile

$$k(y) = 1 + \frac{\Delta k}{2}\left\{\frac{\tanh[(x-1/2)/a]}{\tanh[1/(2a)]}\right\}, \tag{4.30}$$

where Δk is the permeability difference between the top and bottom of the aquifer and a is a parameter that quantifies the linearity of the permeability profile (see figure 4.4a). In the limit $a \to \infty$ the profile (4.30) is linear, given by equation (4.29), whilst in the limit $a \to 0$

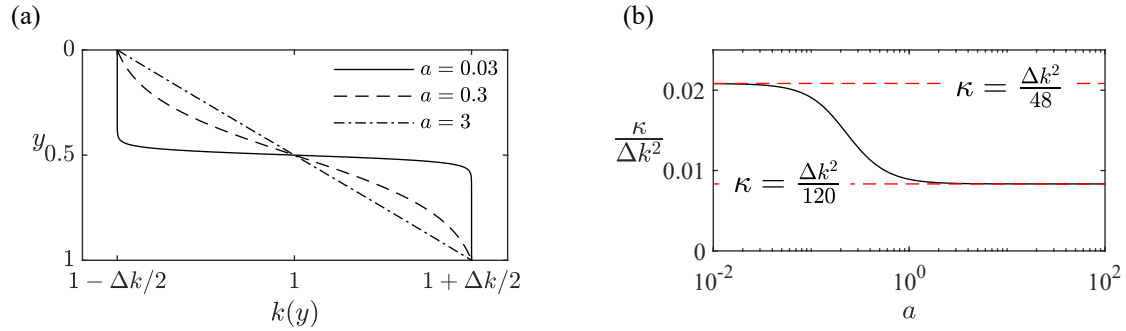

Fig. 4.4 (a) Permeability structure, $k(y)$, according to equation (4.30). The profile is linear in the limit $a \to \infty$ and is piecewise constant in the limit $a \to 0$. (b) Shear dispersion coefficient, $\kappa/\Delta k^2$ as a function of a for the permeability (4.30) (calculated from equation 4.24). A linear profile ($a \to \infty$) has coefficient $1/120$, whilst the piecewise constant profile ($a \to 0$) has coefficient $1/48$.

the profile is piecewise constant,

$$k(y) = \begin{cases} 1 - \Delta k/2 & \text{for } y < 1/2 \\ 1 + \Delta k/2 & \text{for } y > 1/2 \end{cases} \tag{4.31}$$

In figure 4.4b, the contribution, κ, to the enhanced diffusion coefficient from the shear is plotted as a function of the parameter a for the permeability profile (4.30). The coefficient κ transitions between the two limiting cases of $a \to 0$ and $a \to \infty$. For the piecewise constant profile ($a \to 0$, equation 4.31) we calculate $\kappa = \Delta k^2/48$ from (4.24). For the linear permeability profile ($a \to \infty$, equation 4.29), $\kappa = \Delta k^2/120$, which is 2.5 times smaller than for the profile (4.31).

Note that for a linear profile (4.29),

$$\lambda = \frac{17\Delta k^2}{20160}. \tag{4.32}$$

In this section, we have studied the transition from advection-dominated dispersion at early times to shear-dispersion at late times in the case that the tracer is sufficiently far away from the nose that its influence can be neglected.

4.4.2 Interaction with the nose post-homogenisation

We consider the interaction of tracer with a fixed nose in the case that the tracer is vertically homogenised before the interaction. We obtain parameter values for which this occurs in

§4.4.3. When the tracer is vertically homogenised, its concentration is independent of depth and satisfies the diffusion equation

$$\frac{\partial c}{\partial \tau} = \mathscr{D}_{\rm eff}\frac{\partial^2 c}{\partial \chi^2}, \tag{4.33}$$

where the diffusion coefficient is enhanced owing to shear dispersion.

The fixed nose spans the thickness of the aquifer and travels at the dimensionless mean flow velocity, which is 1. Tracer is released from $x = 0$ at $t = t_R$ and the lateral distance between the tracer and the nose is initially $l_R = t_R$. We showed earlier that, for a vertically uniform release of tracer, the centre of mass of tracer travels at the mean flow velocity at times when the nose influence is negligible. Thus, the distance between the nose and the centre of mass remains l_R at these times.

The nose of the current has fixed lateral extent and hence at late times the interface can be approximated as a vertical line, relative to the horizontal length scale of the tracer distribution, which grows in proportion to $(\mathscr{D}_{\rm eff}\tau)^{1/2}$. This assumption is justified further in the application in §4.6. Since the tracer is vertically homogenised, the zero-width nose acts as a no-flux boundary to the migration of tracer

$$\left.\frac{\partial c}{\partial \chi}\right|_{\chi=l_R} = 0. \tag{4.34}$$

Mass conservation of the tracer takes the form

$$\int_{-\infty}^{l_R} c(\chi,\tau)\,{\rm d}\chi = 1. \tag{4.35}$$

Before the vertically homogenised tracer distribution reaches the nose, it spreads horizontally and symmetrically as a Gaussian about $\chi = 0$,

$$c(\chi,\tau) = \left[4\pi\mathscr{D}_{\rm eff}(\tau-\tau_0)\right]^{-1/2}\exp\left[\frac{-\chi^2}{4\mathscr{D}_{\rm eff}(\tau-\tau_0)}\right]. \tag{4.36}$$

The time, τ_0 arises from the adjustment to the shear dispersion regime (described in the previous section). We write $\tau' = \tau - \tau_0$.

After times of order

$$\tau' \sim \frac{l_R^2}{\mathscr{D}_{\rm eff}}, \tag{4.37}$$

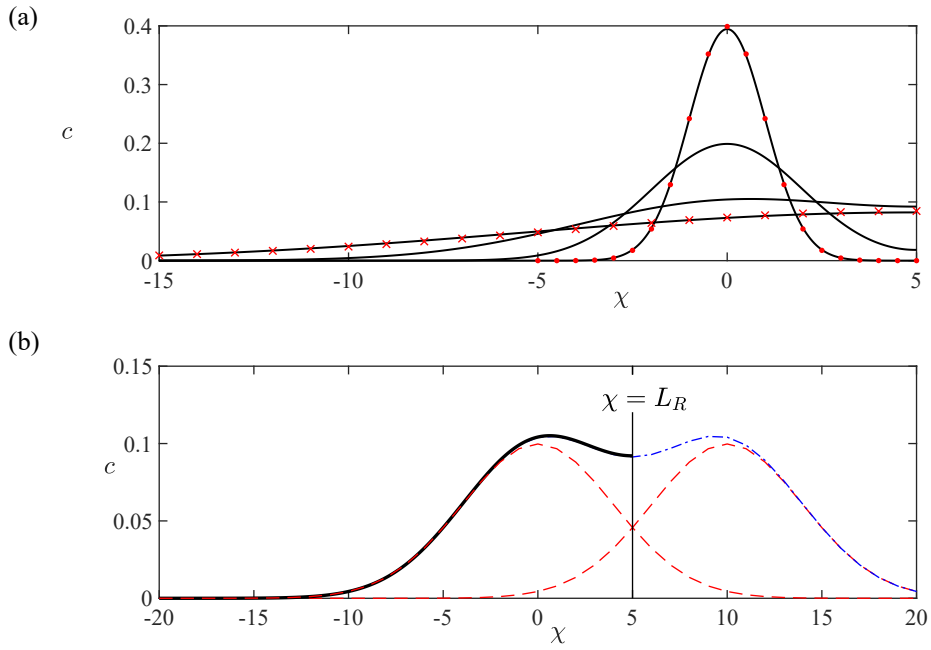

Fig. 4.5 Transition from symmetric dispersion of the vertically homogenised tracer distribution to asymmetric dispersion at late times owing to the interaction with the nose. (a) Transition from Gaussian concentration profile to half-Gaussian with diffusion coefficient $\mathscr{D}_{\text{eff}} = 0.005$. Black solid lines show the concentration profiles at four times $\tau' = 100$, 400, 1600 and 6400 calculated from the numerical solution to equation (4.33) with boundary condition (4.34). We have used $l_R = 5$, and hence there is a no-flux boundary at $\chi = 5$. The red dots show the Gaussian solution (equation 4.36) and the red crosses show the half-Gaussian solution (equation 4.38). The transition time is $\tau_1 = 2500$ (see equation 4.42). (b) Illustration of Barenblatt's technique for superposing two Gaussian solutions at $\tau' = 1600$. The red dashed lines show the Gaussian and its reflection in $\chi = 5$, the blue dashed line shows the sum of these two Gaussians and the solid black line is the numerical solution, which shows good agreement with the superposition.

the tracer reaches the nose, and subsequently the distribution changes, owing to the no-flux boundary at this front, assuming the tracer is insoluble in the original fluid in the aquifer. The nose, at $\chi = l_R$, influences the dispersion of the tracer and the concentration distribution becomes asymmetric (see figure 4.5a).

The concentration of tracer satisfies the diffusion equation (4.33) on a semi-infinite domain with a no-flux boundary condition at $\chi = l_R$. For times much longer than $\tau' = l_R^2/\mathscr{D}_{\text{eff}}$ (equation 4.37) the solution is given by the half-Gaussian profile,

$$c(\chi,\tau) = \left[\pi\mathscr{D}_{\text{eff}}(\tau'+\tau_1)\right]^{-1/2}\exp\left(\frac{-(\chi-l_R)^2}{4\mathscr{D}_{\text{eff}}(\tau'+\tau_1)}\right), \tag{4.38}$$

where τ_1 is a constant associated with the time for a transition to this similarity solution. The half-Gaussian is plotted with red crosses in figure 4.5a and shows good agreement with the late-time numerical solution at $\tau = 6400$. We determine τ_1 below by applying the technique of Barenblatt [13] for determining the heat distribution in a semi-infinite bar.

The first step in determining τ_1 is to note that our solution (4.38) for the dispersion in a semi-infinite domain for tracer released from $\chi = 0$ at time $\tau' = 0$ with no-flux boundary at $\chi = l_R$ corresponds to the superposition of the solution for tracer released from $\chi = 0$ and the solution for tracer released from $\chi = 2l_R$ in an infinite domain (see figure 4.5b). We can use (4.36) to calculate the superposed solution,

$$c = \left[4\pi\mathscr{D}_{\text{eff}}\tau'\right]^{-1/2}\left[\exp\left(\frac{-\chi^2}{4\mathscr{D}_{\text{eff}}\tau'}\right)+\exp\left(\frac{-(\chi-2l_R)^2}{4\mathscr{D}_{\text{eff}}\tau'}\right)\right], \tag{4.39}$$

which is plotted as a blue dashed line in figure 4.5b. It is straightforward, using symmetry, to show that this composite solution satisfies the no-flux condition at $\chi = l_R$ and mass conservation in $\chi < l_R$. Indeed, (4.39) is the exact solution for the migration of tracer at all times after vertical homogenisation.

We now match (4.39) at late times ($\tau' \gg l_R^2/\mathscr{D}_{\text{eff}}$) to our solution on a semi-infinite domain (4.38) to determine τ_1. Expanding (4.38) in τ_1/τ', which is small at late times, yields

$$c = \frac{e^{-(\chi-l_R)^2/4\mathscr{D}_{\text{eff}}\tau'}}{(\pi\mathscr{D}_{\text{eff}}\tau')^{1/2}}\left\{1+\left[\frac{(\chi-l_R)^2}{4\mathscr{D}_{\text{eff}}\tau'}-\frac{1}{2}\right]\frac{\tau_1}{\tau'}+\mathscr{O}\left(\frac{\tau_1^2}{\tau'^2}\right)\right\}. \tag{4.40}$$

We expand the composite solution (4.39) in $l_R/|\chi - l_R|$, which is small at late times because the extent of the tracer distribution becomes much larger than l_R. This yields

$$c = \frac{e^{-(\chi-l_R)^2/4\mathscr{D}_{\text{eff}}\tau'}}{(\pi\mathscr{D}_{\text{eff}}\tau')^{1/2}}\left\{1 + \left[\frac{-(\chi-l_R)^2}{4\mathscr{D}_{\text{eff}}\tau'} + \frac{(\chi-l_R)^4}{8\mathscr{D}_{\text{eff}}^2\tau'^2}\right]\frac{l_R^2}{(\chi-l_R)^2} + \mathscr{O}\left[\frac{l_R^4}{(\chi-l_R)^4}\right]\right\}. \quad (4.41)$$

The leading order terms in equations (4.40) and (4.41) are identical. Comparing the second order terms in (4.40) and (4.41) determines the transition time,

$$\tau_1 = \frac{l_R^2}{2\mathscr{D}_{\text{eff}}}. \quad (4.42)$$

The late-time half-Gaussian solution (4.38) is now fully determined, valid for $\tau' \gg \tau_1$. The time τ_1 is positive because tracer spreads further in the composite solution than it does if tracer were released from the nose at $\chi = l_R$ at time $\tau' = 0$. We note that $\tau' + \tau_1 = \tau + \tau_1 - \tau_0$ and hence the correction time in the late-time half-Gaussian is the adjustment time to the asymmetric spreading minus the correction time for shear dispersion.

During the symmetric spreading regime, the distance of the centre of mass of tracer behind the interface is a constant, l_R. In the half-Gaussian regime, the distance grows in time and is given by

$$\left[4\mathscr{D}_{\text{eff}}(\tau' + \tau_1)/\pi\right]^{1/2}. \quad (4.43)$$

The lateral standard deviation of the tracer concentration transitions from $(2\mathscr{D}\tau)^{1/2}$ for symmetric spreading to

$$\left[2(1-2/\pi)\mathscr{D}_{\text{eff}}(\tau' + \tau_1)\right]^{1/2} \quad (4.44)$$

for the half-Gaussian spreading.

The distance of the centre of mass behind the nose predicted by the composite solution (4.39), which is accurate at all times, is

$$\left[4\mathscr{D}_{\text{eff}}\tau'/\pi\right]^{1/2}\exp(-l_R^2/4\mathscr{D}_{\text{eff}}\tau') - l_R\,\text{erfc}[l_R/(4\mathscr{D}_{\text{eff}}\tau')^{1/2}], \quad (4.45)$$

where erfc is the complementary error function. This mean is plotted in figure 4.6a, for the case $l_R = 5$ and $\mathscr{D}_{\text{eff}} = 0.005$, where it is compared to the early-time mean position ($\chi = 0$) and the late-time mean position (4.43). The transition between the time regimes occurs at $\tau' \sim \tau_1$. In figure 4.6b, we illustrate how this transition time ($\tau' \sim \tau_1$) corresponds to tracer reaching the nose by plotting the location of the 90$^{\text{th}}$, 50$^{\text{th}}$ and 10$^{\text{th}}$ percentiles of the tracer distribution (according to equation 4.39) and the location of the nose.

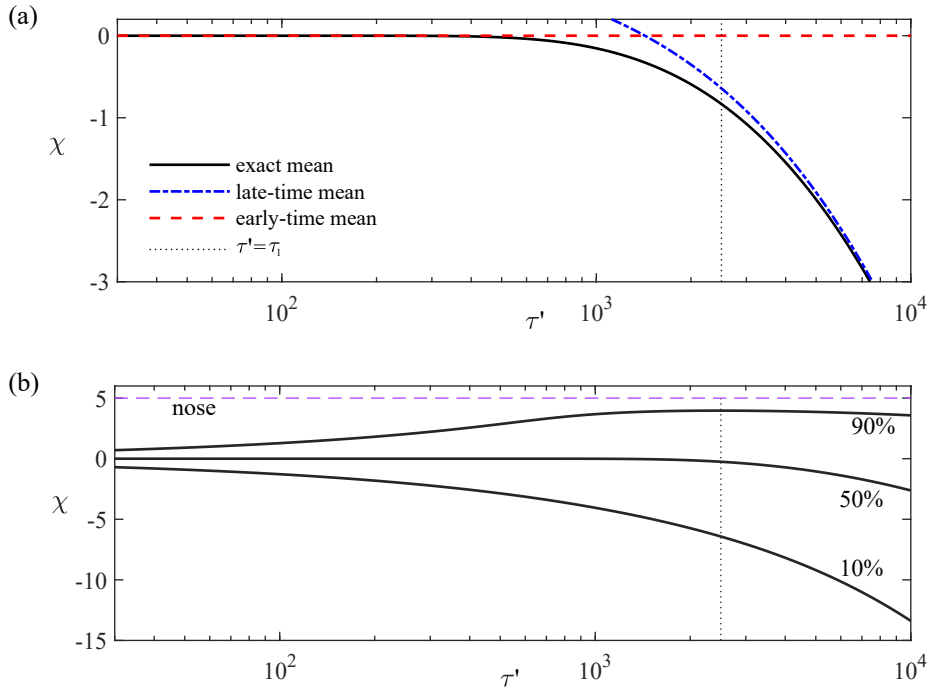

Fig. 4.6 (a) Location of the centre of mass of tracer in travelling coordinates $\chi = x - \tau$ in the case of a nose of fixed extent initially a distance $l_R = 5$ ahead of the tracer. We use diffusion coefficient $\mathscr{D}_{\text{eff}} = 0.005$. The exact position is calculated from the composite solution (4.39), whilst the early- and late-time approximations are calculated from Gaussian spreading (4.36) and half-Gaussian spreading (4.38). (b) Along-channel location of the 90$^{\text{th}}$, 50$^{\text{th}}$ and 10$^{\text{th}}$ percentiles of the tracer distribution, illustrating how the transition from the early- to late-time regimes occurs (at $\tau' \sim \tau_1$) when tracer nears the nose.

4.4.3 Interaction with the nose pre-homogenisation

We have shown how the nose influences the spreading of tracer in the case that tracer is vertically homogenised before reaching the nose. We consider presently the situation in which tracer is not vertically homogenised when it interacts with the nose.

Consider the permeability profile (4.30) with $\Delta k > 0$. The permeability is greatest at $y = 1$ and the velocity of tracer is $1 + \Delta k/2$ there. In the advection-dominated regime ($\tau \ll 1/\mathscr{D}$), diffusion is negligible and tracer at the bottom of the aquifer ($y = 1$) remains there. In the absence of diffusion, tracer reaches the nose at a time $t = 2l_R/\Delta k$ after release.

This time is a good approximation for the arrival of tracer at the nose provided that it is much smaller than the diffusive timescale i.e.

$$\Gamma = \frac{2l_R\mathscr{D}}{\Delta k} = \frac{2DT_R}{\Delta k H_0^2} \ll 1, \tag{4.46}$$

where T_R is the dimensional release time. Tracer that enters the nose at a height $y = y_0$ subsequently experiences a non-zero cross-channel velocity. Tracer within the nose migrates across the aquifer into regions of lower permeability where it travels more slowly than the advancing interface. It then lags behind the nose, and in the case of a linear permeability gradient, tracer exits the nose region at a height $1 - y_0$ in the absence of diffusion. As before, we assume that the transition in the nose happens instantaneously.

The case $\Gamma \ll 1$, corresponds to a thick layer in which the time for cross-channel diffusion is large. The transition in the nose leads to a reflection of tracer in the centreline and subsequently tracer migrates backwards relative to the nose as illustrated in figure 4.7b-4.7e (corresponding to the white region in figure 4.1). The extent of the tracer continues to grow in proportion to time, τ, until, at times of order $1/\mathscr{D}$, the tracer becomes vertically well-mixed, $c(\chi, y, \tau) = \bar{c}(\chi, \tau)$. Once the tracer concentration is independent of the depth, the nose acts as a no-flux boundary because the flux of tracer in and out the nose balances. The tracer distribution evolves with a half-Gaussian profile, as described earlier (corresponding to the top, grey zone in figure 4.1). The other case, in which the tracer is vertically homogenised before reaching the nose, corresponding to $\Gamma \gtrsim 1$ (i.e. a thinner aquifer) was discussed in §4.4.2 and is illustrated in figure 4.7g-4.7j. This regime corresponds to the yellow (leftmost) region in figure 4.1. Note that the horizontal axis in figure 4.1 is proportional to Γ^{-1}.

In the case that advection dominates as tracer enters the nose, the tracer in the high permeability half of the aquifer quickly enters the nose (see figure 4.8). If instead the tracer is vertically homogenised before interacting with the nose then the proportion of particles

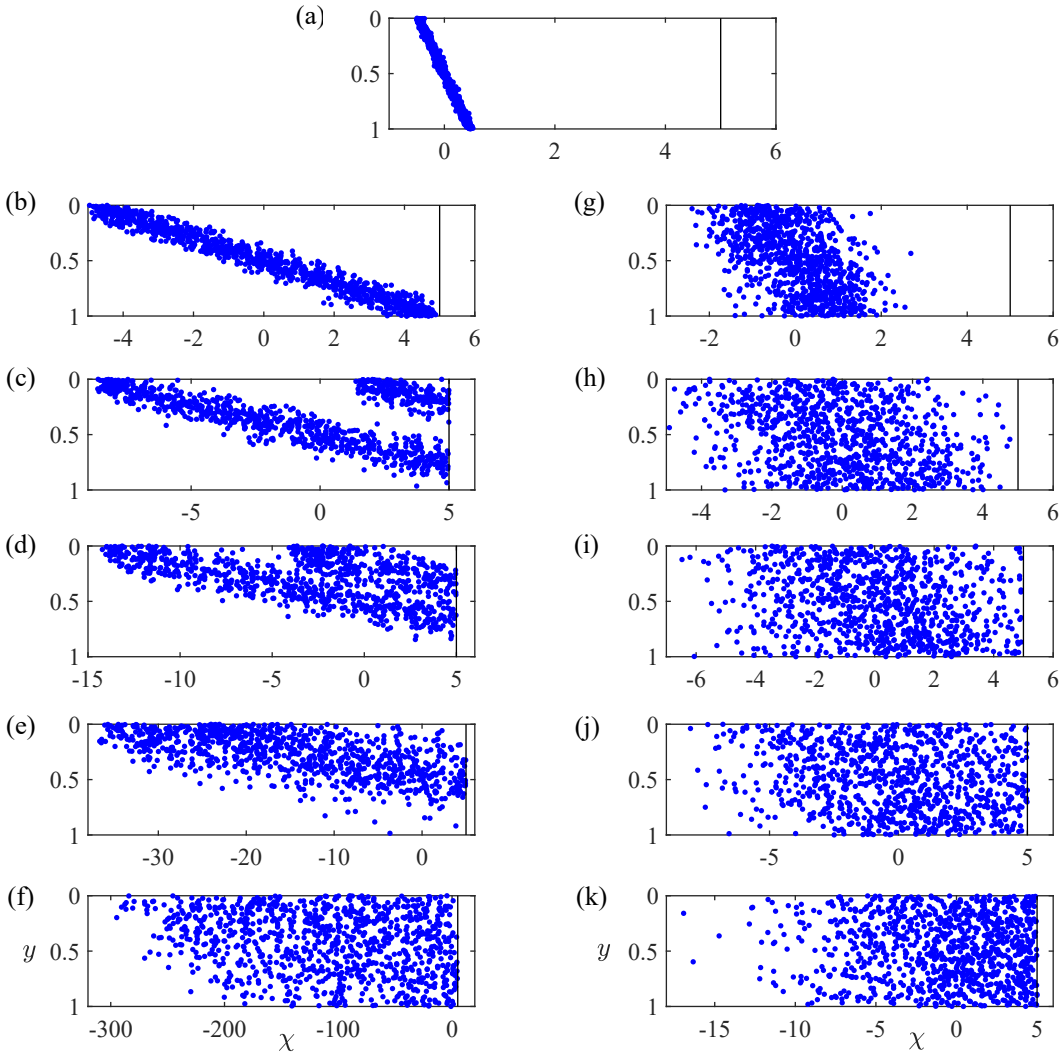

Fig. 4.7 Interaction between 1000 tracer particles and a nose of fixed extent at $\chi = 5$. (a) At early times, advection dominates and the tracer undergoes a shear. (b-e) The case in which advection continues to be the dominant dispersion mechanism when tracer nears the nose ($\Gamma \ll 1$). Tracer is reflected in the centreline by the nose owing to the recirculation in the nose. Subsequently it occupies the low permeability region and migrates backwards relative to the nose. (g-j) If the rate of diffusion is larger then tracer becomes vertically well-mixed before nearing the nose ($\Gamma \gtrsim 1$). (f, k) For any non-zero value of Γ, the tracer eventually becomes vertically well-mixed. The concentration becomes independent of depth and the nose acts as a no-flux boundary to the depth-integrated concentration, which leads to a half-Gaussian profile for the tracer concentration.

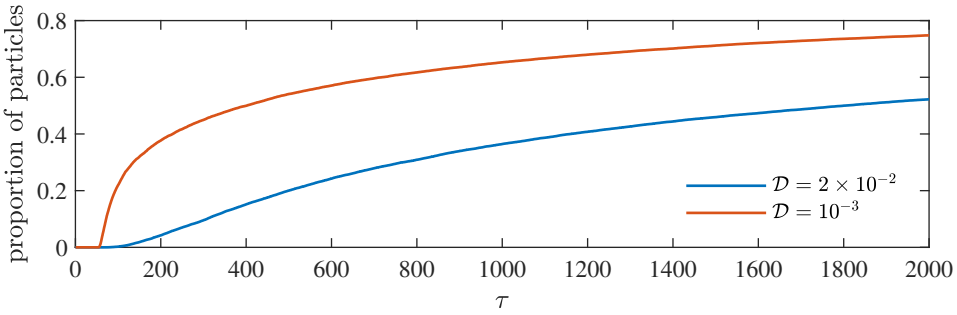

Fig. 4.8 Proportion of tracer particles that have transitioned through the nose at least once. We use a release distance (or time) of $l_R = 25$, a permeability gradient of $\Delta k = 1$ and two values for the diffusion coefficient $\mathscr{D} = 0.02$ and $\mathscr{D} = 0.001$ (corresponding to $\Gamma = 1$ and $\Gamma = 0.05$, respectively). In the case that $\mathscr{D} = 0.001$ (red line), advection dominates and the upper half of the tracer pulse in the high permeability zone quickly enters the nose. For stronger diffusion ($\mathscr{D} = 0.02$, blue line), the tracer becomes vertically homogenised before reaching the nose and the proportion of particles entering the nose increases much more slowly because only the leading edge of the tracer cloud reaches the nose.

that have been through the nose evolves more slowly because the concentration near the nose is small and most of the particles are far from the nose (compare figure 4.8 and figure 4.7).

In both regimes ($\Gamma \ll 1$ and $\Gamma \gtrsim 1$), the ultimate asymptotic behaviour is that the tracer concentration profile becomes depth-independent and evolves as a half-Gaussian. The time scale for the extent of the half-Gaussian is

$$\tau + \tau_1 - \tau_0 = \tau + \frac{l_R^2}{2\mathscr{D}_{\text{eff}}} - \frac{\lambda}{\mathscr{D}^2 \mathscr{D}_{\text{eff}}}, \tag{4.47}$$

regardless of whether the nose interaction occurs before or after homogenisation. Equation (4.47) can be rewritten in terms of Γ; the second and third terms are equal to

$$\tau_1 - \tau_0 = \frac{1}{8\mathscr{D}_{\text{eff}}}\left(\Gamma^2 - \Gamma_c^2\right), \tag{4.48}$$

where Γ_c is a numerical constant that depends on the permeability structure. For a linear permeability profile, $\Gamma_c = \sqrt{17/2520} \approx 0.082$. The time offset for the half-Gaussian, $\tau_1 - \tau_0$ represents the combination of the offset owing to the initial advection dominated regime (τ_0) and the offset owing to the interaction with the nose (τ_1). The former contribution is negative because the advection-driven spreading is slower than the shear dispersion at early times whilst the latter is positive as described above. The offsets balance each other for $\Gamma = \Gamma_c$. Smaller values of Γ correspond to advection dominating the dispersion for longer and the late-time extent is reduced. Similarly, for larger values of Γ, the transition to shear dispersion

is much faster and occurs before tracer reaches the nose and the interaction between the shear dispersion and the nose dominates leading to an increased late-time extent.

4.5 Release of a non-uniform pulse of tracer

In §4.4, we assumed that the tracer, released from $x = 0$ at $t = t_R$, was initially uniformly distributed over the thickness of the aquifer. We used this idealised initial condition to simplify the analysis and this enabled us to determine the behaviour of the dominant physical processes in the problem. However, in a heterogeneous aquifer, the initial distribution is unlikely to be uniform; more tracer is released in the higher permeability regions. The flux of tracer released at each height from a vertical line source is proportional to the permeability there. Therefore, the initial concentration of tracer at $x = 0$ is $c = k(y)$.

The details of the competition between advection and diffusion described in the previous section is unchanged. However, the mean position of the tracer is altered. When the initial vertical distribution was uniform, the centre of mass of tracer migrated at the mean flow velocity in the advection-dominated early time regime. In the case that the tracer concentration is initially $c = k(y)$, the centre of mass of tracer will migrate faster than the mean flow because there is more tracer initially in high permeability regions. For a linear shear (4.29), in the absence of diffusion, the centre of mass is at

$$\int_0^1 c(t = t_R)u(y)\tau \,\mathrm{d}y = \tau + \frac{\Delta k^2}{12}\tau. \tag{4.49}$$

The tracer subsequently becomes vertically well-mixed and travels at the mean flow velocity (assuming this occurs before the nose influences the spreading). For the release of a uniform pulse, ignoring the nose influence, the centre of mass of tracer is at $x = \tau$ during and after the advection-dominated regime. For the heterogeneous pulse, the centre of mass is at $x = \tau + m_1(\tau)$. The correction length, $m_1(\tau)$ arises from the extra velocity above the mean flow during the advection-dominated transition.

To calculate the correction length, m_1, we can use the analysis from §4.4. The along-aquifer integrated concentration, c_0 satisfies equation (4.16), which has general solution

$$c_0(y,\tau) = a_0 + \sum_{n=1}^{\infty} a_n \cos(n\pi y)\exp\left[-n^2\pi^2\mathscr{D}\tau\right]. \tag{4.50}$$

The initial condition, $c_0(y,0) = k(y)$ imposes $a_0 = 1$ and

$$\tilde{k}(y) = \sum_{n=1}^{\infty} a_n \cos(n\pi y). \tag{4.51}$$

The equation for the mean position (4.12) is

$$\frac{\mathrm{d}m_1}{\mathrm{d}\tau} = \sum_{n=1}^{\infty} \overline{a_n \cos(n\pi y) \exp\left[-n^2\pi^2\mathscr{D}\tau\right]\tilde{k}(y)}. \tag{4.52}$$

We integrate with respect to time and apply $m_1(0) = 0$ to obtain

$$m_1 = \sum_{n=1}^{\infty} \overline{\frac{a_n}{n^2\pi^2\mathscr{D}} \cos(n\pi y)\left\{1 - \exp\left[-n^2\pi^2\mathscr{D}t\right]\right\}\tilde{k}(y)}. \tag{4.53}$$

At times after $\tau \sim 1/\mathscr{D}$, we neglect the exponential terms. Then integrating by parts twice and substituting (4.51) for the coefficients yields the late-time expression

$$m_1(\tau) = \kappa/\mathscr{D} + E.S.T., \tag{4.54}$$

where $\kappa = \overline{\tilde{\psi}(y)^2}$ as defined earlier. This result confirms that the centre of mass of the tracer migrates faster than the mean flow until the tracer has vertically homogenised and this leads to an extra distance of $\kappa/\mathscr{D}$.

We can determine the time dependence of the position of the centre of mass for a linear permeability profile (4.29). We calculate $a_{2m+1} = -4\Delta k/[(2m+1)^2\pi^2]$ and $a_{2m} = 0$ from (4.51). The distance that the centre of mass is ahead of the mean flow is

$$m_1(\tau) = \frac{1}{\mathscr{D}} \sum_{n=1}^{\infty} \frac{8\Delta k^2}{(2m+1)^6\pi^6}\left\{1 - \exp[-(2m+1)^2\pi^2\mathscr{D}\tau]\right\}, \tag{4.55}$$

which converges to $\kappa/\mathscr{D} = \Delta k^2/(120\mathscr{D})$ as $\tau \to \infty$ as expected. The adjustment $m_1(\tau)$ is plotted in figure 4.9 for the case of a linear permeability profile with $\Delta k = 1$ and $\mathscr{D} = 0.002$. The mean from the numerical results, with two million particles, is plotted as a solid blue line and the first hundred terms of (4.55) are plotted with red dots showing excellent agreement.

We have found how the position of the centre of mass is advanced owing to the higher proportion of tracer in the high permeability region during the early-time transient in the case that the nose does not influence the migration during this period.

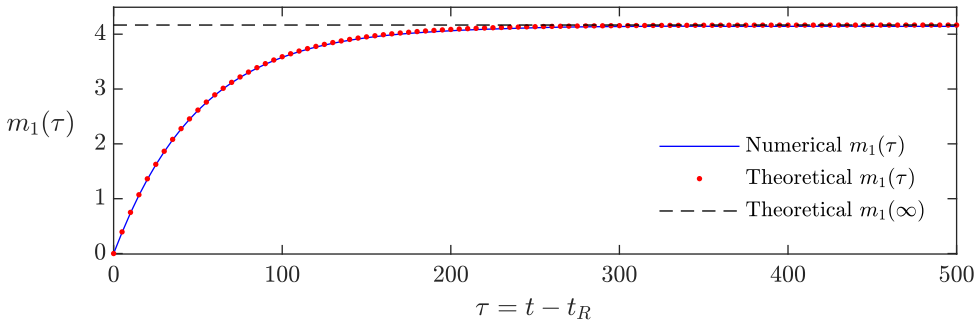

Fig. 4.9 Distance of the centre of mass ahead of the mean flow, $m_1(\tau)$ owing to the initial non-uniform concentration profile, $c_0(y,0) = k(y)$ in the case of a linear permeability profile with $\Delta k = 1$ and diffusion coefficient $\mathscr{D} = 0.002$. The mean position calculated from our numerical simulations (see §4.3) with two million particles is plotted as a blue line whilst the theoretical prediction from the first hundred terms of (4.55) is plotted as red dots. The black dashed line is the late-time limit $m_1 = \kappa/\mathscr{D}$.

4.6 Applications

We consider the release of tracer in two example aquifers of differing thickness and illustrate how this changes the processes that dominate the dispersion of tracer. In both cases we assume that the input fluid is sufficiently viscous that the interface advances with fixed shape. This may be the case in contexts such as enhanced oil recovery or geothermal power extraction in superheated reservoirs, although any phase change will further complicate the results [cf. 143].

We take the coefficient of molecular diffusion in a porous medium to be $D = 5 \times 10^{-9}\mathrm{m\,s}^{-2}$ [144]. We use a typical value for the injection velocity within the layer of $V_i = Q/(\phi H_0) = 2 \times 10^{-5}\mathrm{m\,s}^{-1}$. Shear dispersion becomes important at times when tracer is vertically homogenised, which corresponds to $T \sim H_0^2/D$.

First, we consider a layer with thickness of 10m. The timescale for vertical homogenisation is centuries. The advection owing to the shear flow associated with any permeability variation will dominate the dispersion of tracer in the months and years after its release. In figure 4.10a, the lateral standard deviation is plotted against time. In the two cases plotted, tracer is released one week and five weeks after the start of injection and we assume the layer has a linear permeability profile with $\Delta k = 1$. At early times after release, the extent of tracer grows linearly in time owing to the shear flow. At later times, the tracer in high permeability regions enters the nose and the tracer is reflected in the centreline ($y = 1/2$) as it interacts with the nose. This still leads to linear growth of the extent but the constant is altered. For a larger release time, the tracer is initially further behind the nose and the nose interaction

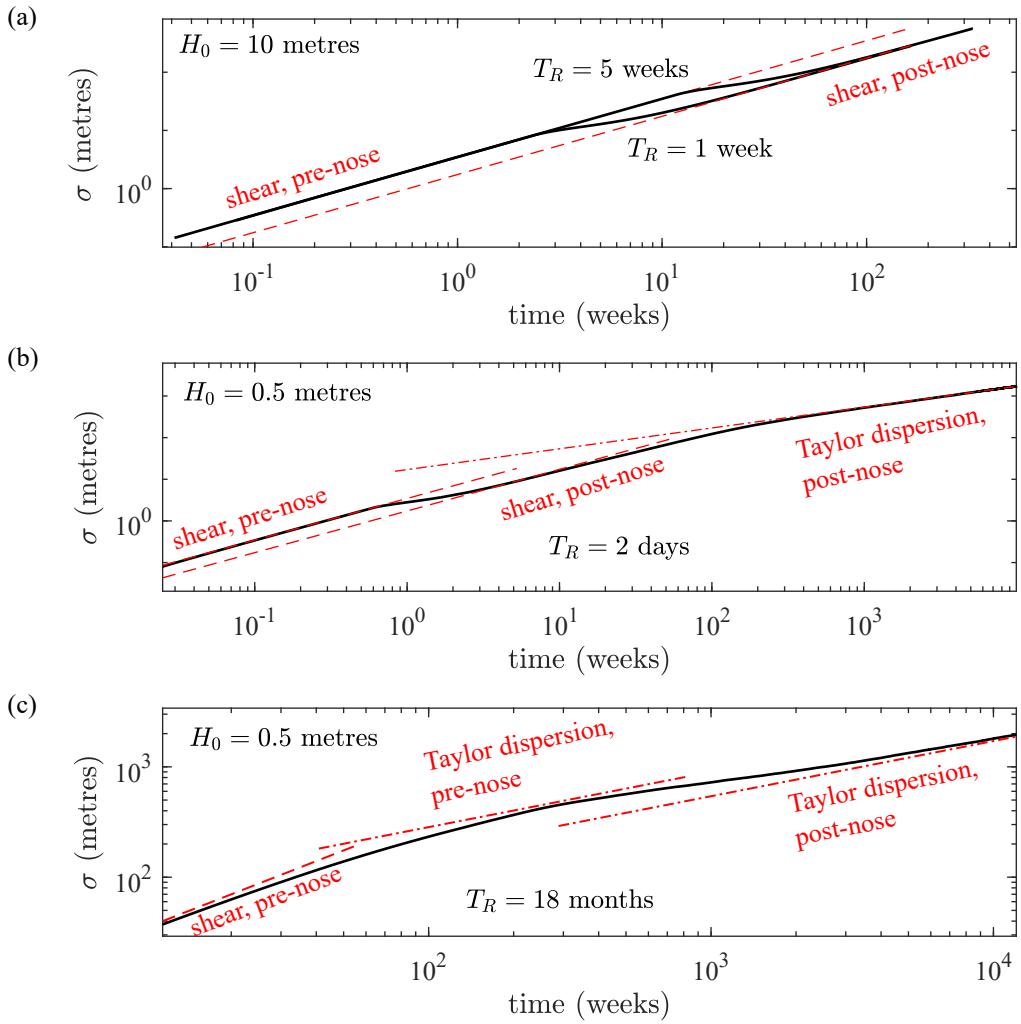

Fig. 4.10 Evolution of the lateral standard deviation of tracer (σ) as a function of time (solid black lines). (a) A 10m layer, (b, c) a 0.5m layer. Parameter values are given in the text and in both cases the injection velocity is $2 \times 10^{-5} \mathrm{m\,s}^{-1}$. In (a), the spreading is dominated by advection associated with the shear flow with $\sigma \sim T$. The coefficient changes as tracer interacts with the nose and is transported into lower permeability regions (indicated by the dashed red lines). Two release times are shown. Vertical homogenisation (and hence shear dispersion) does not occur until centuries have passed. (b) In a thinner layer, the early spreading is similar to the thicker layer and tracer reaches the nose. However, at later times (H_0^2/D), Taylor dispersion dominates and $\sigma \sim T^{1/2}$ (red dot-dashed line). The coefficient for the rate of this post-nose Taylor dispersion is given by equation (4.44). (c) For a much later release time in the thin layer, Taylor dispersion dominates before the interaction with the nose.

occurs at a later time. The role of diffusion is negligible in the case of a fixed nose in a 10m layer over the typical timescales of a project.

The permeable layer could have thickness as low as a few centimetres. If we consider a layer of thickness 0.5m then the timescale for vertical homogenisation of the tracer is of order

$$H_0^2/D = 5 \times 10^7 \mathrm{s} = 19 \text{ months}. \tag{4.56}$$

If the 0.5m layer has a linear permeability structure with $\Delta k = 1$, then the dimensional shear dispersion coefficient is

$$D_{\mathrm{eff}} = D + \frac{\kappa H_0^2 V_i^2 \Delta k^2}{D} = 1.7 \times 10^{-4} \mathrm{m\,s^{-2}}. \tag{4.57}$$

This is almost five orders of magnitude larger than the molecular diffusion coefficient.

We consider tracer released into this layer two days after the injection began. We suppose that the injection velocity in the thinner layer remains, $V_i = Q/(\phi H_0) = 2 \times 10^{-5} \mathrm{m\,s^{-1}}$. In figure 4.10b, we plot the standard deviation against time. At very early times, advection dominates and the extent grows in proportion to time as in the 10m layer. Tracer is then transported into lower permeability regions by the nose and there is slower linear growth. Subsequently, tracer becomes vertically homogenised and shear dispersion dominates the spreading. In this regime, the extent grows in proportion to $T^{1/2}$. The behaviour of the dispersion of tracer is substantially changed in layers of different thicknesses. In both examples, we assumed that the tracer release was vertically uniform. A vertical variation in the initial concentration alters the mean position by approximately 10 metres. We note that in the case of a very late release time, the tracer becomes vertically homogenised before the interaction with the nose (figure 4.10c).

In figure 4.11, the concentration profiles that would be observed at a well a distance 100 metres downstream from the injection well are shown for the cases discussed above. The transition from the shearing pre-nose regime to the shearing post-nose regime can be observed by comparing figure 4.11a and figure 4.11b. In this 10 metre thick layer, diffusion is unimportant. In the case that tracer is released a week after CO_2 injection begins (figure 4.11a), tracer in the high permeability regions reaches the nose and is transported into the low permeability regions. There is then a region near the nose in which the tracer concentration is doubled (cf. figure 4.7c). This region ends abruptly after about 12 weeks as can be observed. For a later release, there is no interaction with the nose and the concentration reduces in time as the tracer in low permeability regions slowly reaches the observation well.

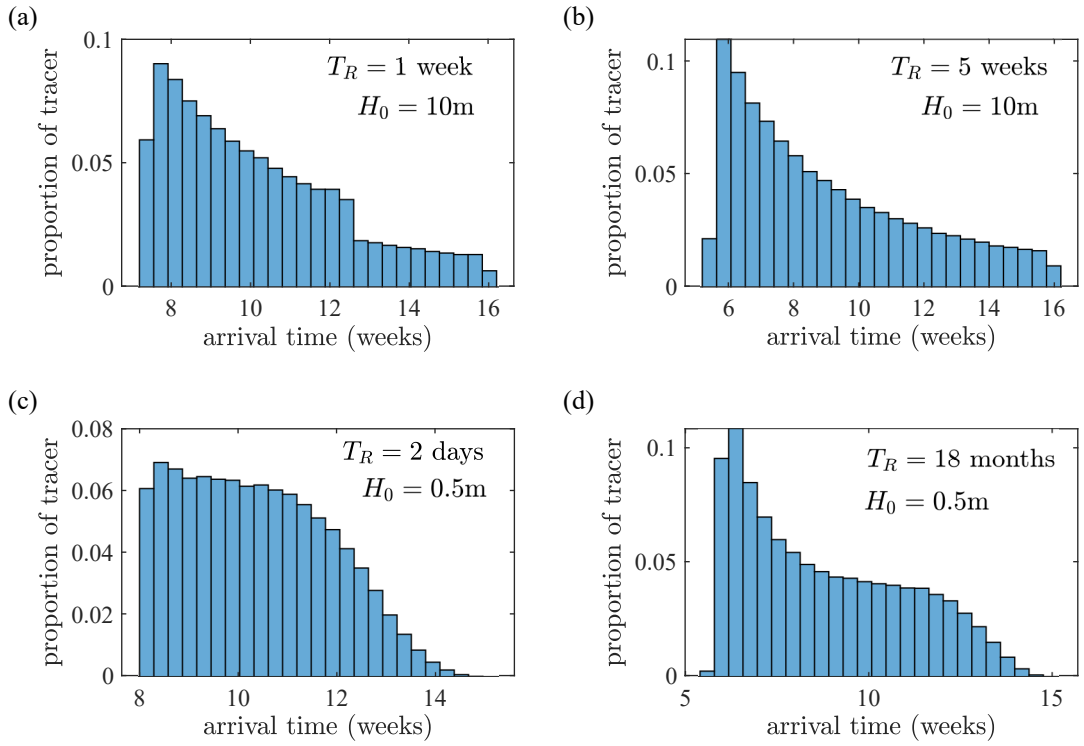

Fig. 4.11 Arrival times of tracer at an observation well that is 100m downstream for the cases considered in figure 4.10. The parameter values are given in the text. The arrival time is measured from the time at which tracer is released. (a, b) In the thick layer ($H_0 = 10$m) the role of diffusion is negligible and the tracer undergoes a shear. For an earlier release time, the tracer reaches the nose and is 'folded', which leads to a region in which the concentration is double the upstream concentration (cf. figure 4.7c) as seen in panel (a). With a later release time, the tracer has not interacted with the nose when it reaches the observation well. (c, d) In a thinner layer, cross-flow diffusion vertically homogenises the tracer. For an earlier release time, tracer interacts with the nose developing a half-Gaussian profile. The greatest concentration is at the front of the cloud of tracer, which coincides with the nose. For a later release time, the tracer has not interacted with the nose and the maximum concentration is not at the front of the tracer cloud.

The transition from the Taylor-dispersion pre-nose regime to the Taylor-dispersion post-nose regime can be observed by comparing figure 4.11c and figure 4.11d. In this 0.5 metre layer, cross-flow diffusion is important. For an early release, the half-Gaussian regime develops as tracer interacts with the nose and the highest concentration is at the front (figure 4.11c). For a much later release of tracer, the nose does not affect the dispersion and the maximum concentration is not at the front. Also, the arrival time (measured from the tracer release time) is much longer for earlier releases because the nose acts as a no-flux boundary slowing the dispersal of tracer towards the observation well (compare the axes in the two columns in figure 4.11). We have demonstrated that the different regimes analysed in this paper can lead to substantially different observed concentration profiles and hence understanding the dispersal mechanisms is key to correctly interpreting the results of tracer tests.

Finally, we justify our assumption that the extent of the fixed nose is negligible in comparison to the lateral extent of the tracer and hence the nose can be modelled as a vertical line of zero width. The lengthscale that tracer disperses in the shear dispersion regime over a year is $(2D_{\text{eff}}T)^{1/2} \sim 100$m. In the purely advective regime in an aquifer with vertically varying permeability, the lengthscale after a year is $\Delta k V_i T/\sqrt{12} = 180$m in the case that $\Delta k = 1$. The fixed nose has extent proportional to bH_0, where $b = U_B H_0/Q$ is the ratio of the buoyancy velocity to the injection velocity. Consider an aquifer with mean permeability $4 \times 10^{-13}\text{m}^2$, porosity $\phi = 0.2$, input fluid viscosity of 6×10^{-5}Pa s and density difference between the fluids of $300\text{kg}\,\text{m}^{-3}$. Then the buoyancy velocity is $U = 2 \times 10^{-5}\text{m}\,\text{s}^{-1}$ and $b = 5$ so that the nose extent is of order metres compared to the dispersive lengthscale over a year, which is hundreds of metres in the advection-dominated or shear dispersion regimes.

In this section, we have assumed that the permeability in the aquifer varies linearly with depth. This is a good first approximation for many real aquifers and both the qualitative and quantitative results we have obtained regarding the role of advection, diffusion, shear dispersion and the nose region apply generally to any permeability variation (see for example figure 4.4).

4.7 Conclusion

We have analysed the migration of tracer within a fluid injected into a confined aquifer initially saturated with a second fluid of different viscosity. The analysis focuses on the dispersion of tracer driven by the combination of a shear flow, which arises from permeability variations, molecular diffusion and interaction with the fixed-extent interface region. The

evolution of the tracer distribution is initially advection-controlled and the extent grows in proportion to $\Delta kV(T-T_R)$ owing to the shear, which has magnitude Δk (V is the injection velocity). At later times, of order H_0^2/D, cross-channel diffusion has vertically homogenised the tracer distribution leading to an enhanced dispersion coefficient with the lateral extent of tracer growing in proportion to $[2(D+\kappa V^2 H_0^2/D)(T-T_R)]^{1/2}$, where κ is a dimensionless constant, which is a function of the permeability structure.

We have shown how tracer interacts with the nose region of the flow in the case that it has fixed extent and travels at the mean injection velocity, which occurs provided the input fluid is sufficiently viscous relative to the ambient. Tracer may reach the nose during the advection-dominated regime or during the vertically homogenised regime. We have shown that in both cases the tracer distribution transitions from symmetric to asymmetric. The concentration distribution tends to a half-Gaussian, with the maximum concentration at the nose.

The initial release of tracer may not be vertically uniform but instead the concentration released at each height may be proportional to the permeability there. This alters the results because there is a transition in which the tracer migrates ahead of the mean flow since more tracer is released in higher permeability regions. We have quantified the extent of the distance advanced ahead of the mean flow and shown how this alters the interaction with the nose.

We have applied our results in the context of subsurface flows, demonstrating that, depending primarily on the thickness of the aquifer, the migration of tracer is controlled by advection in thicker layers whilst shear-dispersion is the dominant mechanism in thinner layers. The difference is important for accurately interpreting the results of tracer tests. In the case that advection dominates, the concentration observed at a production has a significant discontinuity if the tracer has interacted with the nose owing to the 'folding' associated with the nose. In a thinner aquifer, the concentration observed will increase and then decrease if the tracer has not yet interacted with the nose or will slowly decrease in time if the half-Gaussian regime has developed following interaction with the nose.

In the next chapter, we consider the case of a growing nose when the injected fluid is of relatively low viscosity.

Chapter 5

Shear dispersion in an intrusion with a growing nose in a porous medium

The material contained in this chapter has been accepted for publication in the *Journal of Fluid Mechanics*, under the title 'Shear dispersion in a porous medium. Part 2. An intrusion with a growing shape.' [80].

5.1 Introduction

CO_2 sequestration, which involves the injection and storage of CO_2 in deep saline aquifers, is a key tool for reducing industrial emissions. It is important to develop techniques to monitor where the CO_2 goes in the subsurface but this is a challenging proposition. Two approaches include (i) geophysical monitoring using seismic surveys [eg. 123] and (ii) the use of tracers within the CO_2, which are monitored by recording their arrival time at observation wells [94, 132]. Interpretation of tracer tests depends on understanding how tracer is carried by the flow. The results obtained from the tracer can provide data about the permeability structure, porosity and thickness of an aquifer and these can be used to make invaluable estimates of the CO_2 storage capacity of an aquifer [6, 81]. The injected CO_2 is of low viscosity relative to the ambient brine in the host aquifer [6]. The interface between the two fluids grows in time and tracer is carried into this growing interface region, which has a significant influence on the dispersion.

Interpreting tracer tests is challenging because of the many physical processes involved. These include small scale dispersion owing to molecular diffusion or the tortuous path taken by particles around the grains [124, 18, 40]. Secondly, the sedimentary rocks that make up porous reservoirs are often heterogeneous on the macroscale and this has a major impact on

fluid flow and hence tracer dispersion [2, 22, 112]. Finally, the immiscible displacement with an evolving interface between the relatively buoyant (or dense) injected fluid and the ambient fluid plays a key role in tracer transport. There has been much work on interface evolution but less on how this influences tracer transport. We investigate how a tracer migrates into the interface zone and study the dominant processes that control dispersion in this zone.

The migration of tracer in the case of a growing nose is characterised by the flow carrying tracer into continually thinner regions of the nose (see figure 5.1). In chapter 3, we examined the dispersal of a material line of tracer in an aquifer with vertically varying permeability in the case that diffusion is neglected and the migration of the tracer is assumed to be controlled by the advection of the buoyant fluid. We showed that the tracer enters the nose region and follows a complex path through the head of the flow.

In this chapter, we consider the dispersal of a finite-width pulse of tracer. When the pulse is in the growing nose, its extent increases in time as the fluid within the nose is vertically squashed and laterally stretched. In the absence of any diffusion, the volume of the pulse of tracer remains constant but its lateral extent increases owing to advection, even in a uniform aquifer (see figure 5.1a-5.1c). At late times, the lateral extent of the tracer is proportional to $t^{1/2}$. We show that until very late times, diffusion is insignificant in comparison to the stretching in the nose in dispersing the tracer. However, at late times, there is an interesting regime that occurs in which the processes of stretching and diffusion are both important. Each process acts to spread the tracer at the same rate but the diffusion dilutes the tracer into the surrounding fluid, which enhances the stretching and the late-time lateral extent is proportional to $(t\log t)^{1/2}$.

In the case that the aquifer has vertically varying permeability, the combination of a shear flow and cross-flow pore-scale dispersion can enhance the along-flow rate of dispersion. The effect is known as 'shear dispersion' and was first identified for Poiseuille flow in a tube [137, 5]. This phenomenon may arise in porous media owing to the combination of cross-aquifer heterogeneity, which creates a shear flow, and pore-scale dispersion [34, 144]. However, curiously the role of such shear dispersion diminishes as tracer migrates into continually thinner regions of the nose where it samples less of the cross-flow permeability gradient. At such times, the stretching dominates the spreading as in a uniform aquifer (see figure 5.1e-5.1h). However, the tracer extent in the stretching regime depends on the pre-stretching extent, which is sensitive to the early shearing. Thus heterogeneity can have an important influence even after tracer is in the thin regions of the nose.

This chapter is structured as follows. In §5.2, we introduce the migration of a tracer under advection and diffusion in the case of a growing nose. We consider the release of a vertically

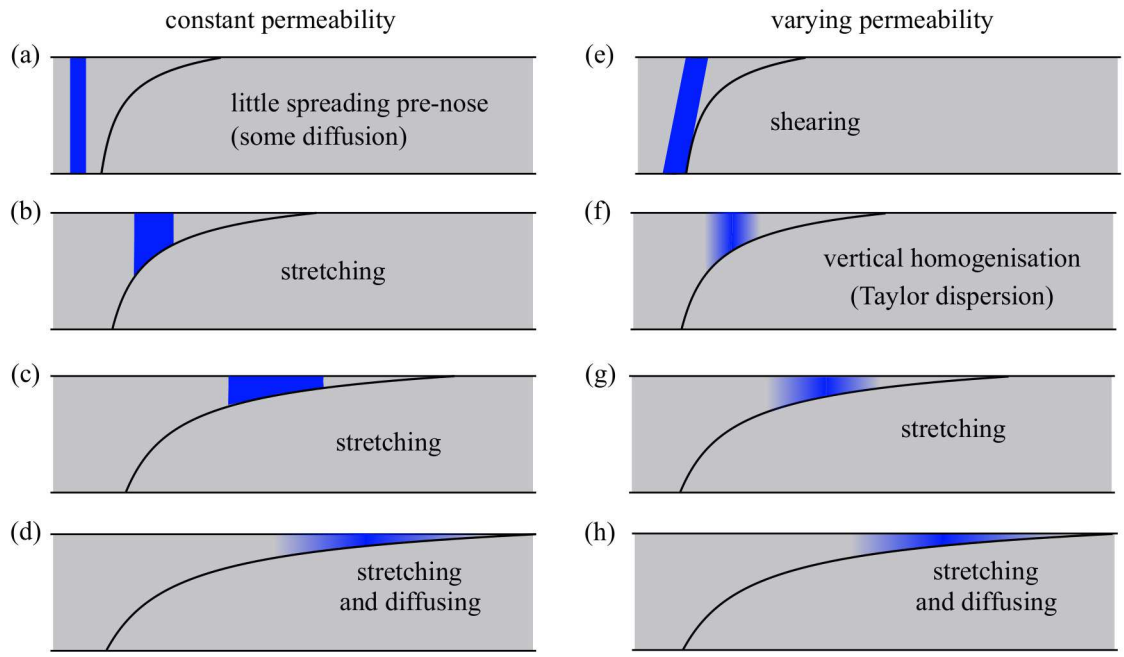

Fig. 5.1 Schematics of the regimes for the migration of tracer in a growing nose. (a-d) The spreading in an aquifer with constant permeability, studied in §5.3. A finite-width pulse disperses owing to the stretching from the growth of the nose. In chapter 3, we studied the migration of a zero-width material line. Until very late times, the stretching owing to the growth of the nose dominates. Subsequently, the combination of stretching and diffusion is important and the tracer is diluted. (e-h) Tracer diffusion in an aquifer with vertically varying permeability (§5.4). The shear is important before tracer becomes vertically homogenised. Subsequently, tracer occupies a thin region of the nose and behaves as if the permeability were constant. Taylor dispersion may play a role if the tracer becomes vertically homogenised before it is in very thin regions.

uniform pulse of tracer. We then study the case of a nose that grows in proportion to time t within a uniform aquifer in §5.3, corresponding to a low viscosity injectate, and find that tracer migrates into continually shallower regions of the nose where it is stretched owing to the growth of the nose. Next, we study the influence of permeability variations on the dispersion within the growing nose. This creates a shear flow, which leads to shear dispersion but as tracer migrates into thinner regions of the flow, the influence of the shear diminishes. However, the shearing has a strong influence on the lateral extent in the stretching regime. We conclude with some applications of the modelling in §5.5. For an analysis of how tracer migrates within a nose that grows in proportion to $t^{1/2}$, which occurs in the special case of equally viscous fluids in an aquifer of constant permeability, see Hinton and Woods [80].

5.2 Formulation

As in the previous chapter, we consider a passive tracer released into the input fluid and we use the same scalings to obtain the dimensionless diffusion coefficient,

$$\mathscr{D} = \frac{\phi D}{Q}. \tag{5.1}$$

The dimensionless advection-diffusion equation is

$$\frac{\partial c}{\partial t} + \frac{\partial (uc)}{\partial x} + \frac{\partial (vc)}{\partial y} = \mathscr{D}\nabla^2 c, \tag{5.2}$$

Since the flow is incompressible, $\boldsymbol{\nabla} \cdot \boldsymbol{u} = 0$, we can calculate the vertical velocity from the horizontal velocity,

$$v = -\int_0^y \frac{\partial u}{\partial x} \mathrm{d}y, \tag{5.3}$$

and the condition $v(y = 0) = 0$ as there is no flux across the upper boundary. The vertical velocity, v is small in comparison to the horizontal velocity, u because the interface is long and thin at late times. Thus, the assumption of hydrostatic pressure is valid provided that variations in the permeability are modest.

We assume a vertical line of nonreacting, nonadsorbing tracer is released into the current from the injection well at a time $t = t_R$, which is sufficiently long after the injection began so that the late-time regime has developed. The initial concentration of tracer is vertically uniform. We assume that the tracer is immiscible in the ambient fluid; in the context of CO_2 sequestration, MacMinn et al. [103] showed that the fraction of the CO_2 that dissolves

during the injection period is negligible because of the low solubility of CO_2 in water. We assume that the injection of fluid continues at a constant rate throughout the period in which we study the migration of tracer. The evolution of the interface and hence the flow field is significantly altered in the post-injection regime [68, 103]. The post-injection migration of tracer is beyond the scope of this thesis.

The migration of the tracer in a growing nose in a heterogeneous aquifer is complex. Many physical processes are involved including the shear flow associated with permeability variation, cross-flow diffusion, stream-wise diffusion and the interaction with the extending nose. We split the analysis in two. First, in §5.3, we consider the migration of tracer in a growing nose in a uniform aquifer. Then in §5.4, we develop the model to account for the shear associated with a vertically varying permeability.

5.3 Dispersion of a tracer pulse in a uniform aquifer

In this section, we study the dispersion of tracer in the case that the interface grows in proportion to time, t in an aquifer with constant permeability. This occurs when the injected fluid is less viscous than the ambient fluid ($m < 1$). We first consider the dispersion owing to the growth of the nose in the absence of diffusion in §5.3.1. Chapter 3 analysed the migration of a material line of tracer with zero thickness. We show that a pulse with finite thickness disperses within the nose owing to the differing velocities across the lateral extent of the pulse. Next, the role of diffusion is studied in §5.3.2.

5.3.1 Dispersion in the case of zero diffusion

The velocity in the nose of a uniform aquifer is given by (3.10),

$$u = \Big[x/(mt)\Big]^{1/2}. \tag{5.4}$$

We can use (5.4) to obtain the along-channel position of a particle,

$$x(t) = \left[\left(\frac{t}{m}\right)^{1/2} - a_0\right]^2 \tag{5.5}$$

where a_0 is a constant that depends on the initial position, which was determined in chapter 3. The expression for the particle position (5.5) demonstrates that the distance between two

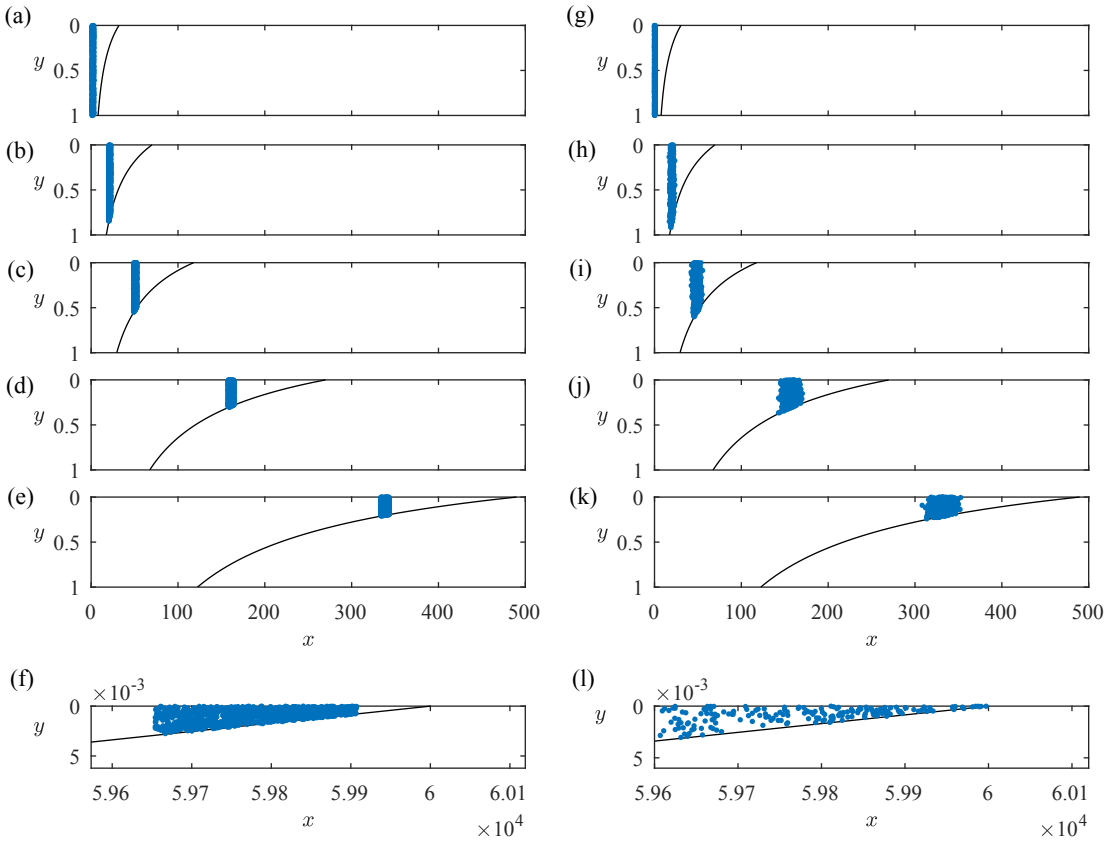

Fig. 5.2 The positions of 1000 particles migrating within the growing nose in a uniform aquifer in the case of zero diffusion ($\mathscr{D} = 0$, left-hand column) and the case $\mathscr{D} > 0$ (right-hand column). For details of the numerical technique, see §4.3. (a-e) Particles migrate into shallower regions of the nose and the lateral extent grows in proportion to $t^{1/2}$ owing to advection (see equation 5.7). We call this the 'stretching' regime. (f) With $\mathscr{D} = 0$, the volume of fluid ahead of the tracer is fixed and hence tracer never reaches the leading contact point. (g-k) Diffusion does not alter the qualitative behaviour of the tracer dispersion until very late times. (l) At much later times, tracer reaches the leading contact point (owing to the $t \log t$ dispersion), which acts as a no-flux boundary to the spreading. The tracer subsequently disperses in self-similar fashion with $x \sim (t \log t)^{1/2}$, owing to the combination of advection and diffusion, as described in section 5.3.

particles within the nose, δ, increases in proportion to $t^{1/2}$,

$$\delta = a_1 t^{1/2} + a_2, \tag{5.6}$$

where the constants, a_1 and a_2 depend on the initial positions of the particles. When a finite pulse of tracer with non-zero initial extent enters the nose region it will disperse longitudinally as shown in the left-hand column of figure 5.2. We call this growth within the nose the 'stretching' regime. The concentration of tracer is constant because there is no diffusion. Instead the longitudinal spreading arises from the vertical squashing and longitudinal stretching of the fluid in the growing nose.

If a finite pulse of tracer is released, beginning at $t = t_R$ and stopping and $t = t_R + \Delta t$, and $\Delta t \ll t_R$ then the tracer extent is a constant, Δt, before entering the nose and after entering the nose ($t > t_E$) the extent is

$$\Delta t \left\{ 1 + (1/m) \left[(t/t_E)^{1/2} - 1 \right] \right\}. \tag{5.7}$$

For large times, the extent grows in proportion to $l_0 (t/t_E)^{1/2}$ where l_0 is a constant that is proportional to the initial extent. We plot the lateral extent of the tracer for three release times with $m = 0.2$, $\Delta t = 0.5$ in figure 5.3a. For smaller release times, the tracer quickly enters the nose where it disperses. Hence for smaller release times, the tracer spends longer in the nose and thus disperses for longer as a proportion of its travel time and this appears as a higher effective dispersivity (see figure 5.3b and figure 5.3c). Finally, we recall that the distance between tracer and the leading contact point of the interface grows in proportion to $t^{1/2}$.

5.3.2 Role of diffusion in a uniform aquifer

In the previous section, we showed that the flow within the nose leads to the extent of tracer growing in proportion to $t^{1/2}$. Since this stretching of the flow acts at the same rate as diffusion we anticipate that the combination of stretching and diffusion could lead to an anomalous rate of diffusion and we show that this is the case. The diffusion acts to dilute the tracer concentration and spread tracer beyond the fluid it initially occupies. This diluted tracer distribution continues to be stretched and thus the combination of the two effects - diffusion and stretching - leads to a faster rate of spreading than owing to either process alone.

The distance between particles and the leading contact point grows in proportion to $t^{1/2}$ owing to the advection. In the absence of diffusion, tracer cannot reach the leading contact

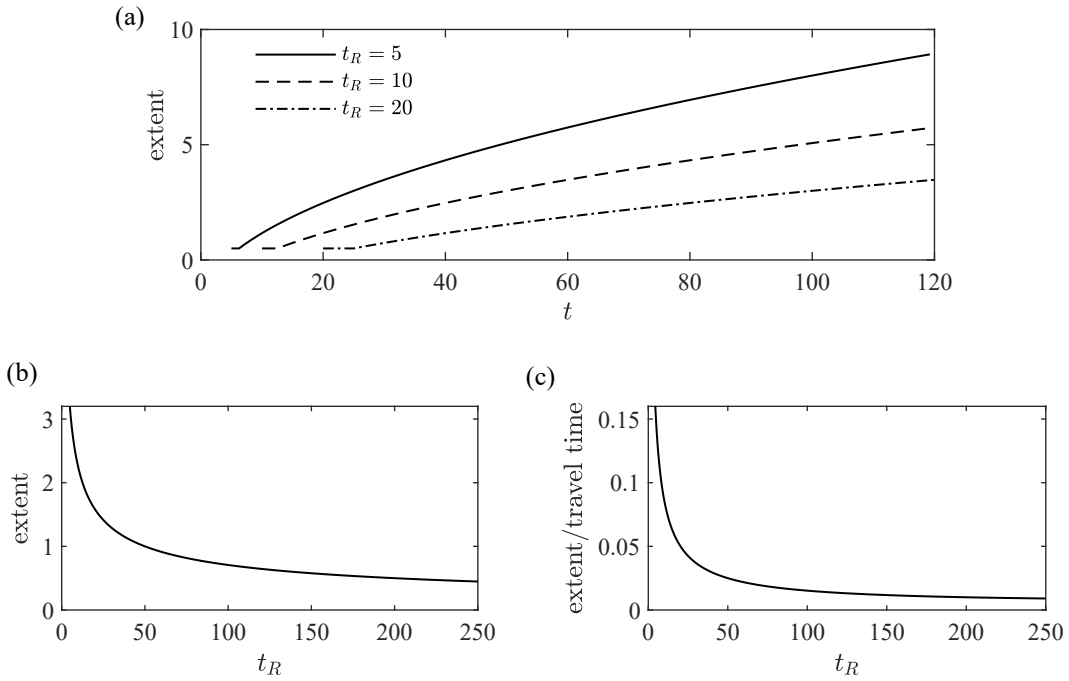

Fig. 5.3 The stretching of tracer owing to the growth of the nose region (zero diffusion). (a) The lateral extent of a pulse of tracer for three release times. Tracer is released during a time interval of $[t_R, t_R + \Delta t]$, we use $\Delta t = 0.5$ and $m = 0.2$. Initially the extent is constant (equal to the initial extent). Tracer subsequently enters the nose and disperses owing to the stretching. For larger release times, the tracer takes longer to enter the nose. (b) The lateral extent of tracer as observed at a well a distance $l = 50$ downstream, as a function of release time. The extent is large for small release times because tracer spends longer in the nose. For large t_R, the extent converges to $\Delta t = 0.5$ because tracer never enters the nose. (c) The extent divided by the time for the centre of mass to reach $L = 50$. This is a measure of the rate of dispersion. It converges to $\Delta t/L = 0.01$ as $t_R \to \infty$.

point (figure 5.2f). However, owing to the combination of stretching and diffusion, tracer disperses more quickly than $(\mathscr{D}t)^{1/2}$ and always reaches the leading contact point (figure 5.2l).

We can illustrate these effects more formally by including diffusion in the transport equation for the tracer concentration c, within the nose. First, we transform to the frame moving with the leading contact point, $z = x_0(t) - x$, in which the velocity is

$$w = \frac{z}{2t} + \mathscr{O}(z^2/t^2). \tag{5.8}$$

We can also obtain the flow thickness in the nose to leading order as a function of $z = t/m - x$ and t

$$h(z,t) = \frac{m^2}{2(1-m)}(z/t) + \mathscr{O}(z^2/t^2), \tag{5.9}$$

and we note that since tracer migrates into thinner regions of the nose, $z \ll t$ at late times. In the frame of the leading contact point, $z = t/m - x$, the advection-diffusion equation for the depth-integrated concentration, ch is

$$\frac{\partial(ch)}{\partial t} + \frac{\partial}{\partial z}\big(wch\big) = \mathscr{D}\frac{\partial}{\partial z}\left(h\frac{\partial c}{\partial z}\right), \tag{5.10}$$

where w is the velocity in the z frame (equation 5.8). The aquifer is vertically uniform and the flow velocity is independent of y. Therefore, we have neglected y derivatives (see figure 5.2).

We can rewrite equation (5.10) as

$$\frac{\partial(hc)}{\partial t} + w\frac{\partial(hc)}{\partial z} + hc\frac{\partial w}{\partial z} = \mathscr{D}\frac{\partial^2(hc)}{\partial z^2} - \mathscr{D}\frac{\partial}{\partial z}\left(c\frac{\partial h}{\partial z}\right). \tag{5.11}$$

At late times, the tracer is in the thinnest region of the nose and the distance between the tracer and the leading contact point grows much more slowly than the extent of the nose owing to mass conservation as the nose stretches out. Therefore, $z \ll t$ and we can use the leading order approximations $w = z/2t$ and $h = \text{const} \times (z/t)$ in the advection-diffusion equation (5.11) to obtain

$$\frac{\partial(hc)}{\partial t} + \frac{\partial}{\partial z}\left(\frac{z}{2t}hc\right) = \mathscr{D}\frac{\partial^2(hc)}{\partial z^2} - \mathscr{D}\frac{\partial}{\partial z}\left(\frac{hc}{z}\right). \tag{5.12}$$

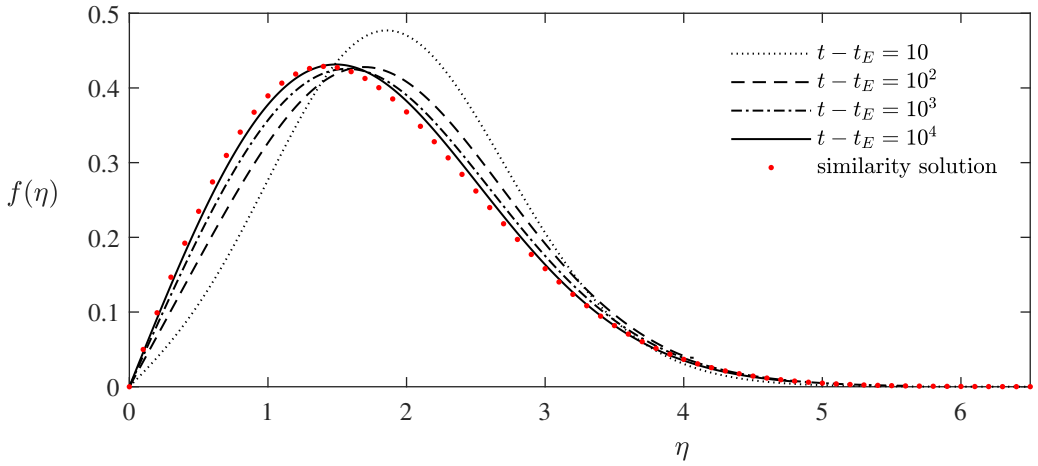

Fig. 5.4 Comparison of the similarity solution and the numerical solutions to equation (5.10) for the growing nose ($m < 1$). The results are shown in similarity coordinates with viscosity ratio $m = 0.5$, diffusion coefficient $\mathscr{D} = 1$, and tracer release time $t_R = 10$. The numerical results are shown at four times after tracer enters the nose. We chose $t_0 = 0.7$ to match the late-time numerical results with the similarity solution (5.17).

Conservation of mass may be expressed as

$$\int_0^\infty hc \, \mathrm{d}z = 1. \tag{5.13}$$

We anticipate that the combination of advection and diffusion both independently spreading at a rate proportional $t^{1/2}$ leads to a rate of dispersion asymptotically faster than $t^{1/2}$. Since the rate cannot be a higher power than that owing to diffusion and advection, we conjecture that $z \sim (t \log t)^{1/2}$. We seek a self-similar solution to equation (5.12) and mass conservation condition (5.13) with variables

$$hc = \frac{1}{[\mathscr{D}t \log(t/t_0)]^{1/2}} f(\eta), \qquad \eta = \frac{z}{[\mathscr{D}t \log(t/t_0)]^{1/2}}, \tag{5.14}$$

where t_0 is associated with the transition time to the similarity solution. It depends on the dispersion at earlier times as tracer migrates further into the nose. Equation (5.12) is recast as an ODE in terms of the similarity variables,

$$-\frac{1}{2}(\eta f)' = f'' - (f/\eta)', \tag{5.15}$$

with mass conservation (5.13) given by

$$\int_0^\infty f \,\mathrm{d}\eta = 1. \tag{5.16}$$

The solution is

$$f(\eta) = \frac{\eta}{2}\exp\left(\frac{-\eta^2}{4}\right). \tag{5.17}$$

The constant t_0 in (5.14) is calculated by comparing the similarity solution to the numerical results. In figure 5.4, we plot both the similarity solution (red dots) and the numerical solutions to the full advection-diffusion equation (5.10) at four times after tracer enters the nose. The numerical results were calculated using MATLAB$^{\mathrm{TM}}$'s PDE solver. With the choice $t_0 = 0.7$, the late-time numerical results show good agreement with the similarity solution.

We use the expression (5.17) to calculate the distance between the centre of mass of the tracer and the leading contact point. We find this to have value

$$\langle z\rangle = \left[\pi\mathscr{D}t\log(t/t_0)\right]^{1/2}. \tag{5.18}$$

This contrasts with the distance in the absence of diffusion which increases in proportion to $t^{1/2}$ (§3.2.3). However, we note that diffusion only plays a dominant role compared to the stretching owing to the growth of the nose when $\mathscr{D}\log t \gg 1$, which corresponds to very late times. Qualitatively, the dispersion is independent of whether there is any diffusion until very late times (compare the columns of figure 5.2). At times of order $\log t \sim 1/\mathscr{D}$, tracer begins to reach the leading contact point and our analysis here applies.

The along-channel standard deviation is

$$\left(\langle z^2\rangle - \langle z\rangle^2\right)^{1/2} = \left[(4-\pi)\mathscr{D}t\log(t/t_0)\right]^{1/2}, \tag{5.19}$$

which is an enhanced rate of dispersion relative to that resulting from diffusion in a constant flow field. Our assumption that the extent of the tracer increases much more slowly than the extent of the nose is self-consistent. Tracer occupies a continually thinner region of the nose near the leading contact point (see figure 5.2l).

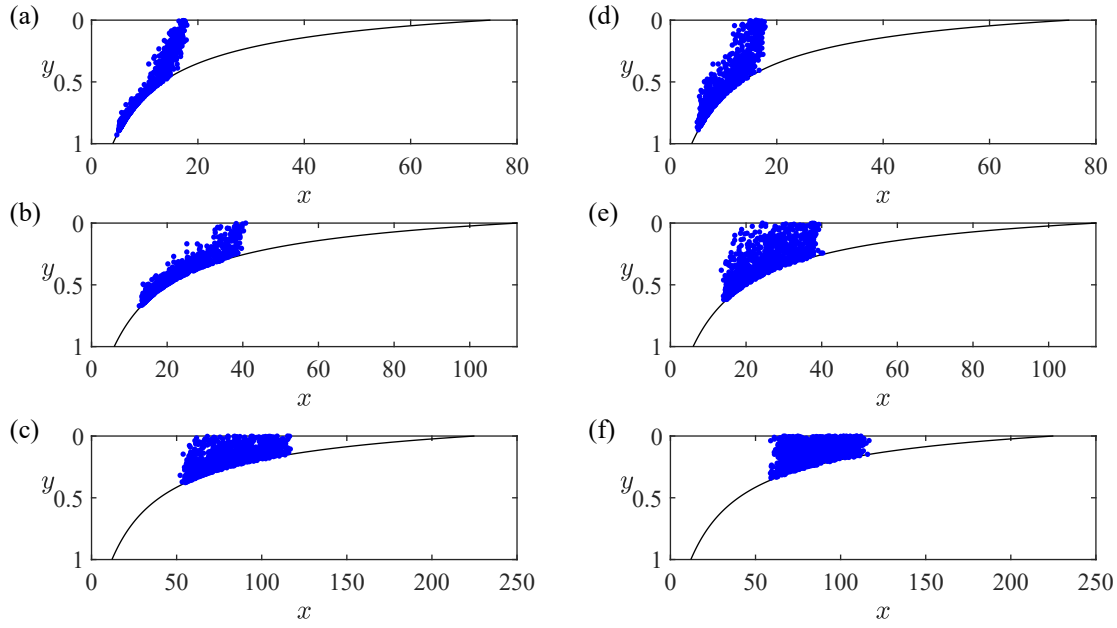

Fig. 5.5 The interaction of 1000 tracer particles with a growing nose, released as a vertically uniform pulse at $t_R = 10$ with a linear permeability variation with $\Delta k = -1$ and viscosity ratio, $m = 0.4$. For details of the numerical technique, see §4.3. (a-c) Positions of tracer at three times after release $t - t_R = 10, 20, 50$ for $\mathscr{D} = 0.001$. (d-f) Positions of tracer at three times after release $t - t_R = 10, 20, 50$ for $\mathscr{D} = 0.004$. The time for vertical homogenisation of the tracer is significantly reduced from $1/\mathscr{D}$ as tracer migrates into thin regions of the nose. The vertical homogenisation is slower with a lower diffusion coefficient. The extent of the tracer is increased with smaller $\mathscr{D}$ because the shear dispersion is inversely proportional to $\mathscr{D}$ (see figure 5.6).

5.4 Tracer dispersion in an aquifer with vertically varying permeability

We now develop our results to account for the migration of tracer in an aquifer in which the permeability varies vertically and the nose region of the current grows in proportion to time, t. This corresponds to a low viscosity input fluid relative to the ambient. The dispersion of tracer is influenced by four key processes: (i) the shear flow arising from the permeability variation; (ii) cross-flow diffusion, which homogenises the shear flow and leads to Taylor dispersion; (iii) the stretching of the tracer associated with the growth of the nose; (iv) streamwise diffusion. Our aim in the present section is to determine which combinations of these processes dominate at different times as tracer migrates into continually thinner regions of the growing nose.

Figure 5.5 shows the evolution of 1000 tracer particles at three times with (a-c) $\mathscr{D} = 0.001$ and with (d-f) $\mathscr{D} = 0.004$. We assume that the permeability varies linearly with the vertical coordinate,

$$k(y) = 1 + \Delta k(y - 1/2), \tag{5.20}$$

and in figure 5.5, we use $\Delta k = -1$. The panels demonstrate that at early times, the shear flow (advection) controls the dispersion. If tracer is in the nose at these times, the stretching owing to the growth of the nose is also significant. The tracer subsequently becomes vertically well-mixed and Taylor dispersion may become important. As tracer migrates into thinner regions of the nose, the role of Taylor dispersion diminishes. Eventually, the dispersion is as in a uniform aquifer and the anomalous $(t \log t)^{1/2}$ rate of dispersion, owing to the combination of stretching and streamwise diffusion, dominates. In the following subsections, we investigate each of these regimes in turn. We first consider the dispersion prior to the tracer becoming vertically homogenised in §5.4.1 and then consider the post-homogenised regime in §5.4.2.

Note that although we use a linear structure (5.20) for the permeability, the results in the present section apply to any non-uniform permeability variation.

5.4.1 Advection-controlled dispersion

The dispersion is initially controlled by molecular diffusion in the streamwise direction. However, this quickly becomes negligible in comparison to the shear flow arising from the permeability variation (see figure 5.5a). Before entering the nose, the tracer extent grows in proportion to time in this pre-homogenisation regime. Once tracer enters the nose, the stretching driven by the growth of the nose is important as well as the shear flow. These are both advective processes. As tracer migrates into thinner regions of the nose, it samples less of the permeability variation (see figure 5.5). Therefore, the spreading owing to the shear advection causes the extent of tracer to grow more slowly than t when tracer is in the nose. Eventually, tracer occupies regions of the nose in which $h \ll 1$ and the influence of the shear becomes negligible in comparison to the stretching owing to the growth of the nose. The dispersion becomes independent of any permeability gradient and the uniform stretching dominates (see §5.3).

Cross-aquifer diffusion becomes important at some time. This may occur (a) before tracer enters the nose, (b) after tracer enters the nose and whilst the shear is still important, or (c) after the tracer is in very thin regions where the shear is unimportant. The first situation was analysed in the previous chapter and tracer becomes homogenised at times of order $1/\mathscr{D}$.

After entering the nose, the homogenisation time is reduced because the vertical extent of the current is less than 1. In the third situation (c), the description of the dispersion in the present section applies until homogenisation at which point, the permeability gradient is unimportant and the late-time results for a uniform aquifer (§5.3) apply. In situation (c), Taylor dispersion never occurs because when the tracer is homogenised, the permeability gradient sampled by the tracer is negligible. In the next section, we investigate the second situation (b) in which homogenisation occurs after entry into the nose but before tracer is in very thin regions (as in figure 5.5).

5.4.2 Vertically-homogenised tracer

In this section, we study the influence of the permeability variation in tracer dispersion after vertical homogenisation. We investigate how long Taylor dispersion associated with the shear flow is an important mechanism. When the tracer is homogenised, the role of advection owing to the shear flow diminishes because the tracer does not remain in the high (or low) permeability regions but instead it samples the thickness of the flow. Taylor [137] showed that the combination of a shear flow and cross-flow diffusion leads to the streamwise extent of tracer growing in proportion to $t^{1/2}$ but with an enhanced, velocity-dependent, coefficient. The increase in the coefficient is proportional to

$$\frac{\Delta u^2 h^2}{\mathscr{D}}, \tag{5.21}$$

where Δu is the velocity difference across the flow and in the case of a linear permeability variation, $\Delta u = \Delta k h$.

In figure 5.6, the streamwise standard deviation of tracer is plotted for $\mathscr{D} = 0.001$ and $\mathscr{D} = 0.004$ and $\Delta k = -1$. The results are obtained from the numerical method. The situations correspond to those in figure 5.5. The extent of the tracer is larger for smaller values of $\mathscr{D}$ because the shear extends the tracer further, analogous to Taylor dispersion. The effect of altering $\mathscr{D}$ on the extent of the tracer is complicated because of the complex dependence of the current thickness, h, on $\mathscr{D}$ and the dispersion is sensitive to h (equation 5.21). At late times, the stretching in the nose dominates the dispersion and the extent grows in proportion to $t^{1/2}$. We found that decreasing $\mathscr{D}$ from 0.004 to 0.001 increased the extent by a factor of $k \approx 1.26$ at late times (see black line in figure 5.6). Decreased $\mathscr{D}$ leads to a multiplicative increase in the extent because cross-flow diffusion is slower. The case $\mathscr{D} = 0$, in which the tracer is never vertically homogenised, is included in figure 5.6 for comparison.

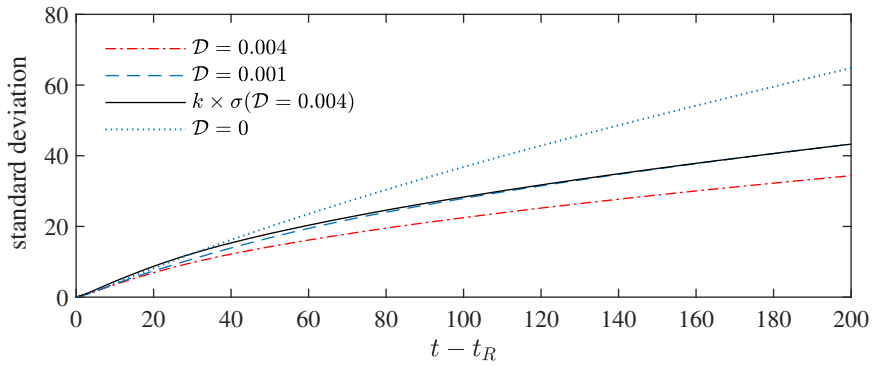

Fig. 5.6 Lateral standard deviation (σ) of the distribution of tracer obtained using the numerical method. Tracer is released as a vertically uniform pulse at $t_R = 10$ and there is a linear permeability variation in the aquifer with $\Delta k = -1$, viscosity ratio, $m = 0.4$. Two values of $\mathscr{D}$ (corresponding to the schematics in figure 5.5) and the case $\mathscr{D} = 0$ are shown. Initially, the dispersion is dominated by the shear and the extent increases in proportion to time, t. Once vertically homogenised, the extent grows through stretching which dominates the shear dispersion because tracer is in thin regions. The subsequent growth of the extent is $l_0(t/t_A)^{1/2}$ to leading order with the constant, t_A, corresponding to the time at which the stretching first dominates and l_0 is the extent at this time (cf. equation 5.7). This is illustrated by multiplying the $\mathscr{D} = 0.004$ standard deviation by $k \approx 1.26$ (continuous black line); it shows excellent agreement with $\mathscr{D} = 0.001$ at late times. In the limit $\mathscr{D} \to 0$, the tracer never becomes homogenised and the dispersion is controlled by advection owing to the shear, leading to different dispersion. In other words, diffusion acts to slow the dispersion via vertical homogenisation.

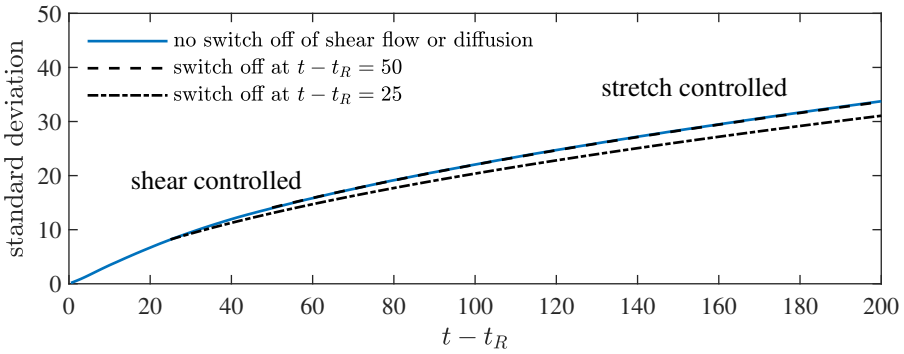

Fig. 5.7 Tracer extent for tracer released at $t_R = 10$ with a linear permeability profile ($\Delta k = -1$), diffusivity $\mathscr{D} = 0.004$ and viscosity ratio, $m = 0.4$. The solid blue line shows the lateral standard deviation of the tracer distribution. The black dashed line shows the standard deviation in the case that we 'switch off' the diffusion and the shear flow at a time $t - t_R = 50$ and use the depth-averaged horizontal velocity everywhere (the profile at this time is shown in figure 5.5f). The influence of the shear and shear dispersion is negligible compared to the stretching owing to the growth of the nose and hence the lines agree. For an earlier 'switch off' (black dotted-dashed line, $t - t_R = 25$), the tracer has not yet vertically homogenised and the shear flow and shear dispersion are still important so the lines diverge.

For non-zero diffusion, the influence of shear dispersion diminishes at later times because tracer occupies a small fraction of the aquifer (equation 5.21). The dispersion will become dominated by the stretching of the fluid in the nose driven by the growth of the nose.

We illustrate this in figure 5.7 by comparing the lateral standard deviation of tracer in the case of $\mathscr{D} = 0.004$ and a linear permeability profile (solid blue line) to the same system but with diffusion and the shear set to zero at $t - t_R = 50$ and $t - t_R = 25$. At such times, the diffusivity is set to zero, the tracer flow velocity is adjusted to its depth-averaged value at each location but the evolution of the interface is unchanged.

If we switch off early then the shear associated with the permeability gradient is still important and we underpredict the extent. If we switch off later then stretching dominates and we get the same answer as in the case of no switch off. The solid blue line and the black dashed line show excellent agreement because the influence of the permeability gradient and hence the shear is negligible at $t - t_R = 50$. However, for an earlier 'switch off' at $t - t_R = 25$, the tracer extent grows more slowly in the absence of shear and diffusion because the shear is still important at these earlier times. We can use figure 5.7 to calculate the time at which the stretching dominates and the aquifer behaves as if it were uniform. Note that the tracer distribution at $t - t_R = 50$ is shown in figure 5.5f; the tracer is vertically homogenised and in a thin region of the aquifer. The role of the shear flow and shear dispersion is negligible in comparison to the stretching.

Although the tracer dispersion is always dominated by stretching at late times, its extent is sensitive to the earlier shear-controlled spreading as shown in figure 5.7. This is because the extent of tracer in the stretching regime grows in proportion to $l_0(t/t_A)^{1/2}$ where l_0 is proportional to the lengthscale of the tracer extent prior to stretching and t_A is the time at which stretching first dominates (cf. equation 5.7). Early shearing enhances the lengthscale, l_0 faster than $t_A^{1/2}$ and hence alters the late-time extent of the tracer pulse despite the shearing becoming dominated by the stretching. This is demonstrated in figure 5.7.

The final regime for the evolution of the tracer distribution occurs at exponentially late times ($\log t \sim 1/\mathscr{D}$) when the combination of along-flow diffusion and stretching of the nose occurs and the extent grows in proportion to $(\mathscr{D}t\log t)^{1/2}$ as analysed in §5.3.

5.5 Application to CO_2 storage

We consider the implications of our results in the context of CO_2 storage. We demonstrate how the late-time dispersivity of tracer depends sensitively on the aquifer thickness and any heterogeneity. In a porous medium, we take the coefficient of diffusion of a tracer or solute to be [144]

$$D = 5\times10^{-9}\mathrm{m\,s^{-2}}. \tag{5.22}$$

We use the following typical values: a viscosity ratio of $m = 0.1$; a porosity of $\phi = 0.2$ and an injection flux of $Q = 4\times10^{-5}\mathrm{m^2\,s^{-1}}$ [24]. In a layer of thickness 10m, the interstitial injection velocity is $V_i = Q/(\phi H_0) = 2\times10^{-5}\mathrm{m\,s^{-1}}$, a unit of dimensionless time corresponds to approximately six days and the dimensionless diffusion coefficient is $\mathscr{D} = 2.5\times10^{-5}$. Tracer is released one month after the injection began and it is released for a week, which provides the initial length of the pulse.

In figure 5.8a, the ratio of the lateral standard deviation of the tracer to the along-flow position of the centre of mass of the tracer is plotted as a function of the location of the centre of mass for the 10m layer. The two cases of an aquifer with constant permeability and an aquifer with linear permeability structure with $\Delta k = -1$ are shown. The extent of the tracer pulse is larger at early times in the heterogeneous aquifer because of the early shearing. The extent is also larger at late times when the tracer has been vertically homogenised and the stretching dominates. This is because the tracer extent in the stretching regime is controlled by the pre-stretching length, which is significantly increased owing to the early shearing.

We also consider the dispersion of tracer in a thinner layer with $H_0 = 0.5$m. We suppose that the injection velocity, V_i, is as in the 10m aquifer. All other parameters are as before

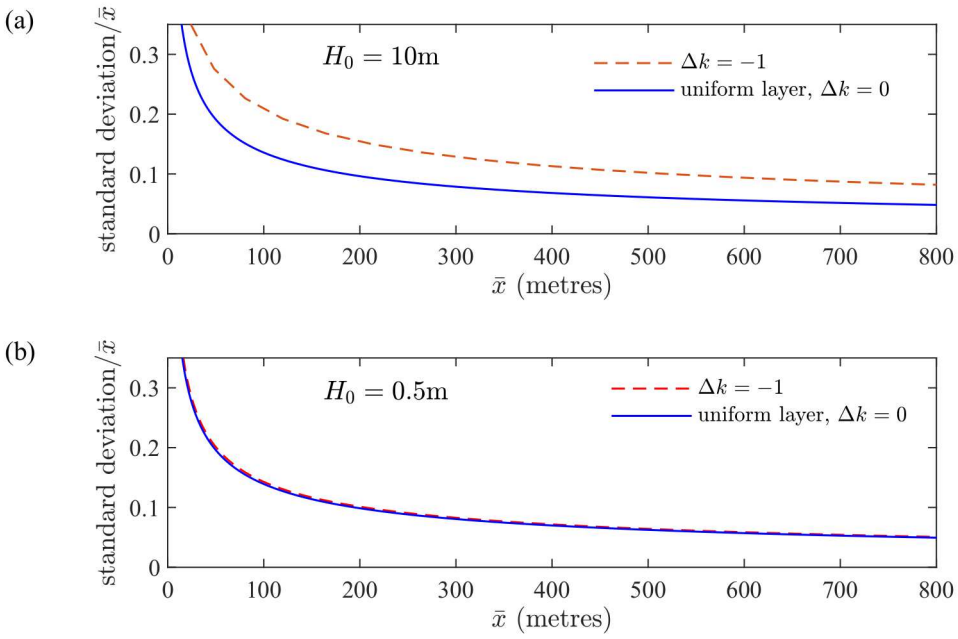

Fig. 5.8 Ratio of the lateral standard deviation of the tracer to the along-flow position of the centre of mass of the tracer as a function of the location of the centre of mass for a uniform aquifer and an aquifer with permeability that varies linearly with depth for two layers of different thicknesses: (a) $H_0 = 10$m and (b) $H_0 = 0.5$m. The injection velocity and the other parameters are the same for both layers. The heterogeneity is important in thicker layers but not thinner layers. The results are obtained from the numerical method.

and so the dimensionless diffusion coefficient is $\mathscr{D} = 5 \times 10^{-4}$. The dispersion of tracer within this layer is plotted in figure 5.8b for $\Delta k = 0$ and $\Delta k = -1$. In contrast to the thick layer, the influence of heterogeneity is negligible. This is because the time for the tracer to become vertically homogenised, and hence the time in which the shearing is important, is much shorter. The stretching extent is approximately independent of the heterogeneity.

These results have profound implications for tracer tests because they demonstrate that heterogeneity has a significant influence on the dispersion in thicker layers, even after tracer is in a thin region of the nose where the permeability is approximately uniform. In addition, the magnitude of this effect increases with layer thickness. In very thin layers the influence of heterogeneity diminishes. Models that treat the subsurface as vertically uniform will likely miss these subtleties and could lead to unrealistic interpretations of tracer tests.

We note that tracer tests last for months or years and the longitudinal diffusive regime in the nose, owing to the combination of stretching and diffusion, is not important at these times.

5.6 Conclusion

In this chapter we have studied the migration of tracer in the case that the injected fluid is less viscous than the ambient fluid in a uniform aquifer. The nose region grows in proportion to time, t. The flow speed within the growing nose varies in space and time and disperses particles at a rate proportional to $t^{1/2}$ (in the absence of diffusion). We call this novel behaviour the 'stretching' regime. This dispersion is the same rate as that owing to diffusion. The combination of stretching and diffusion within the growing nose leads to an enhanced, anomalous rate of longitudinal dispersion proportional to $(\mathscr{D}t\log t)^{1/2}$ at very late times.

In an aquifer with vertically varying permeability, the nose may still grow in proportion to time provided that the input fluid is not too viscous relative to the ambient. The evolution of the tracer distribution is initially advection-controlled and the extent grows in proportion to Δkt owing to the shear. At later times, cross-channel diffusion has vertically homogenised the tracer distribution and this leads to an enhanced dispersion coefficient owing to Taylor dispersion [137]. However, tracer migrates into continually thinner regions of the nose and the influence of Taylor dispersion becomes negligible as less of the permeability gradient is sampled by the tracer; the late-time migration of tracer is identical to that in a uniform aquifer but with an altered initial condition.

Our results are important for interpreting tracer tests used in CO_2 sequestration. We have shown that in a typical project, the role of diffusion is important only in homogenising

the tracer distribution when it is in a thin region of the nose. The influence of the shear is significant because it controls the extent of tracer in stretching regime. This effect is stronger in thicker layers because the shear acts for longer before vertical homogenisation.

Chapter 6

Interaction of viscous free-surface flows with topography

The material contained in this chapter has been published in the *Journal of Fluid Mechanics*, under the title 'Interaction of viscous free-surface flows with topography' [76].

6.1 Introduction

The interaction between viscous free-surface flows and topography has received considerable attention owing to its importance in a wide range of industrial and environmental contexts. These include the down-slope migration of lava flows, which develop when liquid magma erupts from a volcano [131, 27], ice flows over Greenland and Antarctica [122] and thin 'coating' flows in engine bearings, printing, painting and other manufacturing processes [84, 133, 96, 15].

In many of these applications, the fluid flow is influenced by a range of complex physics and this has engendered much research. As an example, modelling lava is particularly challenging because it is a complex fluid; as it cools, lava becomes more viscous and subsequently solidifies, and has a yield strength that varies across time and space [131, 54, 136]. Slow travelling ice is often modelled as a non-Newtonian viscous fluid using a power-law model [52, 90], whilst in thin coating flows over small obstacles such as adhered particles, surface tension plays a key role [61, 115, 93, 106, 23]. There have also been experiments to determine the role of inertia in thin flows over topography [117]. Many researchers simplify the flow physics by applying the lubrication approximation. Gaskell et al. [49] demonstrated that this is often a good approximation even when it does not strictly apply (for example in flow over steep topographies).

The present chapter is primarily motivated by how lava flows interact with topography and how this informs the design of barriers. We analyse how a steady downslope viscous flow is perturbed by topography and apply the results to inform optimal barrier construction. Larger topographical mounds can partition the flow and lead to 'safe' zones in their wake in which there is no fluid. Thus, along with determining the major features of the flow, a key aim of this chapter is to ascertain the dimensions and strength of a barrier necessary to protect a particular location from a lava flow. An increased understanding of how lava flows over topography is also critical for our ability to use volcanic deposits for paleoclimate reconstructions [44]. The present work may also be of interest in other areas, such as the glass industry, coating flows and glacier dynamics.

The chapter is structured as follows. In section 6.2, we adapt Lister's governing equation for downslope viscous flows to incorporate the influence of topographical variations [101]. This introduces dimensionless parameters that quantify the amplitude of the mound and the depth of the oncoming flow. We focus on the steady flow from a sustained source that develops at late times after the front has passed the topography and other transient effects have diminished. In section 6.3 we introduce a numerical scheme to simulate this steady problem. The results demonstrate that dry regions, in which there is no fluid, can occur for shallow flows past sufficiently large mounds.

To provide insights to the key physics of the problem, we first consider the simpler case of topography which varies only in the downslope direction in §6.4. In this case, dry regions cannot develop. Ponding, where the flow becomes much deeper than its steady upstream depth, occurs upstream of any locations at which the gradient of the topography points upwards relative to the downwards direction of gravity. We find asymptotic expressions for the depth in the ponded region.

In section 6.5, we examine flow around topography that varies in both down- and cross-slope directions and extend our asymptotic approach to the flow over and around an axisymmetric mound. The results show good agreement with our numerical simulations, providing both a useful validation of the numerical technique and significant insight into the dynamical controls of these flows. When the topography is everywhere coated by the fluid, there is mathematically an 'inner region' in which the flow is driven primarily by the topography and the downslope component of gravity, matched to an 'outer region' in which gradients of the hydrostatic pressure associated with the component of gravity normal to the slope become significant. The 'inner' expansion breaks down with the onset of dry regions. By reintroducing the diffusive slumping terms associated with the hydrostatic pressure gradients, we calculate the extent of the flow up the mound.

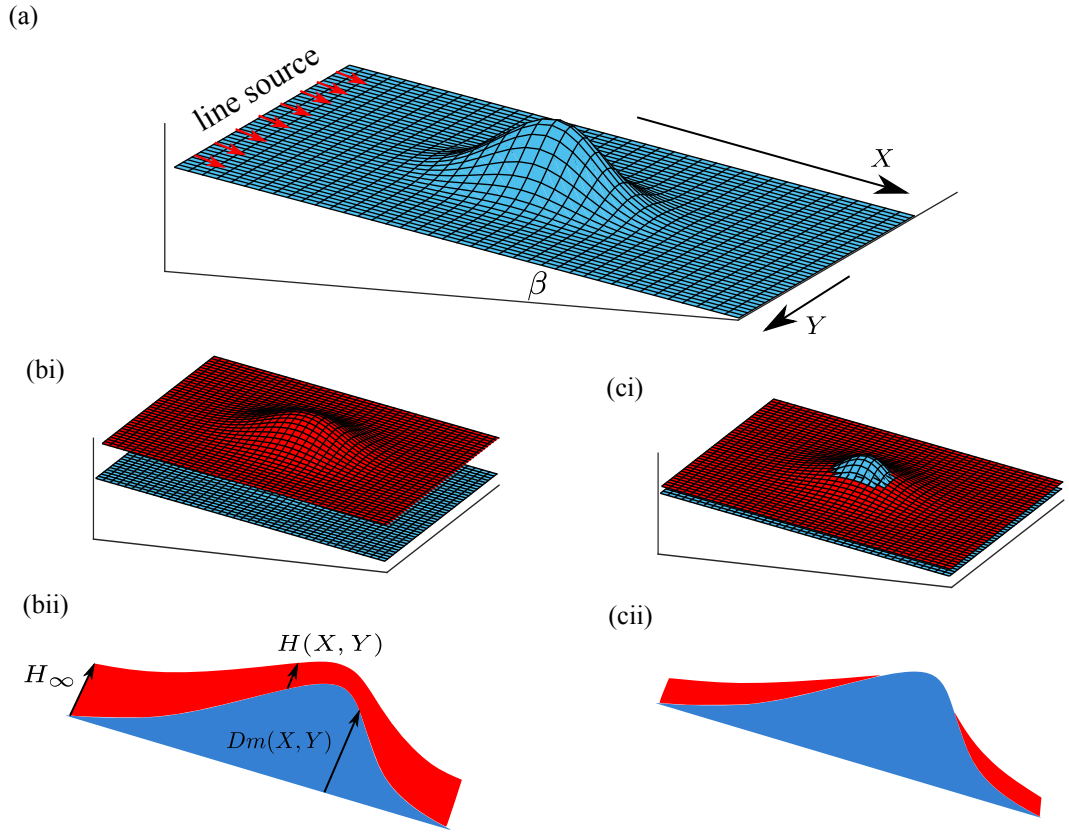

Fig. 6.1 Schematic diagrams showing the steady flow over mounds. The topography is shown in blue whilst the flow surface is shown in red. (a) An example slope topography. (bi) Flow over a mound in the case where there is no dry region, (bii) cross-section in the X direction along the line of symmetry. (ci) Flow around a mound in the case where there is a dry region at the top, (cii) cross-section in the X direction.

Finally, in order to apply the results to the problem of barrier construction, we consider a wide elliptical mound in section 6.6. Our asymptotic analysis can be used to determine the mound width and height and the upstream flow depth for which lava is diverted away from a downstream region. We also calculate an upper bound for the force exerted on the mound by the pond of lava.

6.2 Model

We consider the flow of a fluid of constant dynamic viscosity μ down a rigid inclined plane at an angle β to the horizontal. We denote the downslope coordinate by X, the cross-slope coordinate by Y, the normal distance above the inclined plane by Z and time by T. A mound of height, $Dm(X,Y)$ (with height scale D), is added to the plane (figure 6.1), where the

maximum value of m is 1. The thickness of the current is given by $H(X,Y,T)$. We assume that the flow is driven by gravity and resisted by viscous stresses and that the effects of both inertia and surface tension can be neglected (i.e. Reynolds number is sufficiently small and Bond numbers is sufficiently large). We further assume that the flow is 'shallow', meaning that its thickness, H, is much smaller than its characteristic lengthscale, L, parallel to the inclined plane. Continuity imposes that the component of velocity normal to the plane, W, is much smaller than the velocities in the X and Y directions by a factor of H/L. This simplification, known as lubrication theory, applies to many gravity-driven and pressure-driven viscous flows and flows in porous media [101, 89, 147, 81, 74]. The flow is assumed to be predominantly parallel to the inclined plane and the pressure within the liquid is hydrostatic to leading order [14],

$$P = P_0 + \Delta\rho g\big[H(X,Y) + Dm(X,Y) - Z\big]\cos\beta, \tag{6.1}$$

where $\Delta\rho$ is the density difference between the fluid and the ambient and P_0 is the ambient pressure, assumed constant. The fluid velocity in the X and Y directions is given by

$$U = \frac{\Delta\rho g}{2\mu} Z\big(Z-2H\big)\left[\Big(\frac{\partial H}{\partial X} + D\frac{\partial m}{\partial X}\Big)\cos\beta - \sin\beta\right], \tag{6.2}$$

$$V = \frac{\Delta\rho g}{2\mu} Z\big(Z-2H\big)\Big(\frac{\partial H}{\partial Y} + D\frac{\partial m}{\partial Y}\Big)\cos\beta, \tag{6.3}$$

respectively [101]. Local mass conservation is expressed by

$$\frac{\partial H}{\partial T} + \frac{\partial}{\partial X}\left(\int_0^H U\,\mathrm{d}Z\right) + \frac{\partial}{\partial Y}\left(\int_0^H V\,\mathrm{d}Z\right) = 0. \tag{6.4}$$

Then using our expressions for the velocities (equations 6.2 and 6.3), we obtain as the nonlinear partial differential equation governing the flow

$$\frac{\partial H}{\partial T} + \frac{\Delta\rho g\sin\beta}{3\mu}\frac{\partial H^3}{\partial X} = \frac{\Delta\rho g\cos\beta}{3\mu}\nabla\cdot\left[H^3\nabla\big(H+Dm\big)\right]. \tag{6.5}$$

We consider a line-source far upstream of the mound supplying a flux of Q per unit width. Nusselt [109] showed that after an initial transient and away from the contact line, the flow behind the front becomes steady and advances with constant depth [see also 101]

$$H_\infty = \left(\frac{3\mu Q}{\Delta\rho g\sin\beta}\right)^{1/3}. \tag{6.6}$$

We consider the interaction between this flow and mounds with length scale L measured parallel to the inclined plane and we assume that the channel is much wider than the mound so that it may be considered isolated. We note that the assumption of hydrostatic pressure (6.1) requires that the flow is shallow relative to the streamwise variation ($H_\infty \ll L$). In terms of the parameters in the problem, the Reynolds and Bond numbers are

$$Re = \frac{\Delta\rho U^2/L}{\mu U/H_\infty^2} = \frac{H_\infty^5 \Delta\rho^2 g}{L^2\mu^2}, \qquad Bo = \frac{\Delta\rho g L^2}{\gamma}, \tag{6.7}$$

where the velocity scale is $U \sim \Delta\rho g H_\infty^3/(\mu L)$ [see (6.2)] and γ is the coefficient of surface tension.

There are three length scales in the model: the mound amplitude, D; the mound's streamwise length scale, L; and the depth of the flow far upstream, H_∞. We introduce the following dimensionless variables

$$x = X/L, \quad y = Y/L, \quad z = Z/H_\infty, \quad t = QT/LH_\infty. \tag{6.8}$$

Using equation (6.5), we find the following governing equation for the dimensionless depth, $h(x,y,t)$,

$$\frac{\partial h}{\partial t} + \frac{\partial h^3}{\partial x} = \nabla\cdot\left[h^3\nabla\big(\mathcal{F}h + \mathcal{M}m\big)\right], \tag{6.9}$$

where

$$\mathcal{F} = \frac{H_\infty}{L\tan\beta} = \left[\frac{3\mu Q}{(\Delta\rho g\sin\beta)L^3\tan^3\beta}\right]^{1/3} \tag{6.10}$$

is a dimensionless proxy for the upstream flow depth. It quantifies the importance of the diffusive terms on the right-hand side of equation (6.9), associated with the gravity-driven slumping of the fluid, relative to the downslope advective term on the left-hand side of the same equation, associated with the gravity-driven flow down the plane. Also,

$$\mathcal{M} = \frac{D}{L\tan\beta}, \tag{6.11}$$

which is the ratio of the characteristic gradient of the mound, D/L, to the gradient of the inclined plane, $\tan\beta$. Because there are three length scales in the problem, it is fully defined by the two dimensionless parameters, $\mathcal{F}$ and $\mathcal{M}$.

To protect towns, barriers must be many hundreds of metres wide whilst the oncoming lava flows may have a depth of the order of metres. For a typical slope gradient of 10% to

20%, we find that $\mathcal{F} \ll 1$ and we focus our attention on this limit and investigate the effect of varying the mound height through the parameter $\mathcal{M}$.

We now describe the dimensionless mound topography, $m(x,y)$. We begin our analysis by assuming that the mound is axisymmetric, $m = m(r)$, where $r = \sqrt{x^2+y^2}$. The peak dimensional height of the mound is D and we take the origin in x, y coordinates to be at the peak of the mound, i.e. $m(0) = 1$. The mound height decays to zero away from the origin ($m \to 0$ as $r \to \infty$). In §6.3 and §6.5, we use $m = \exp(-r^2)$ but our analysis applies to a more general class of mounds. We generalise this in §6.6 to analyse non-axisymmetric mounds with elliptical contours.

Since we are interested, inter alia, in determining the shape of dry regions when they occur, we can simplify the governing equation by restricting our attention to the steady flow which occurs after the front of the current has passed the mound. In this case the governing equation is

$$\frac{\partial h^3}{\partial x} = \nabla \cdot \left[h^3 \nabla \big(\mathcal{F} h + \mathcal{M} m \big) \right]. \tag{6.12}$$

The term on the left-hand side is associated with the component of gravity in the downslope direction, while the right-hand side represents the motion due to the gradients of hydrostatic pressure. The right-hand side comprises two terms: the first is due to gradients of the flow thickness; while the second encodes the force due to the underlying topography.

To determine the boundary condition as $r \to \infty$, we note that sufficiently far away from the origin, the mound has negligible influence on the current and hence $H \to H_\infty$ from which we obtain

$$h \to 1 \qquad \text{as} \quad r \to \infty. \tag{6.13}$$

The dimensionless flow velocity is given by

$$\mathbf{u} = 3z(z/2 - h) \left[\nabla(\mathcal{F} h + \mathcal{M} m) - \mathbf{e}_x \right], \tag{6.14}$$

where $\mathbf{e}_x$ is the unit vector in the x direction.

One limitation of lubrication theory is that a retreating contact line cannot occur, for example at the upstream edge of a fixed volume of liquid flowing over inclined plane [101]. Instead, the theory suggests that receding regions are very slowly draining thin films. For the problem considered presently, this limitation is unimportant because dry regions can occur only in a region downstream of the mound into which liquid never flows, thus the contact line is nowhere receding.

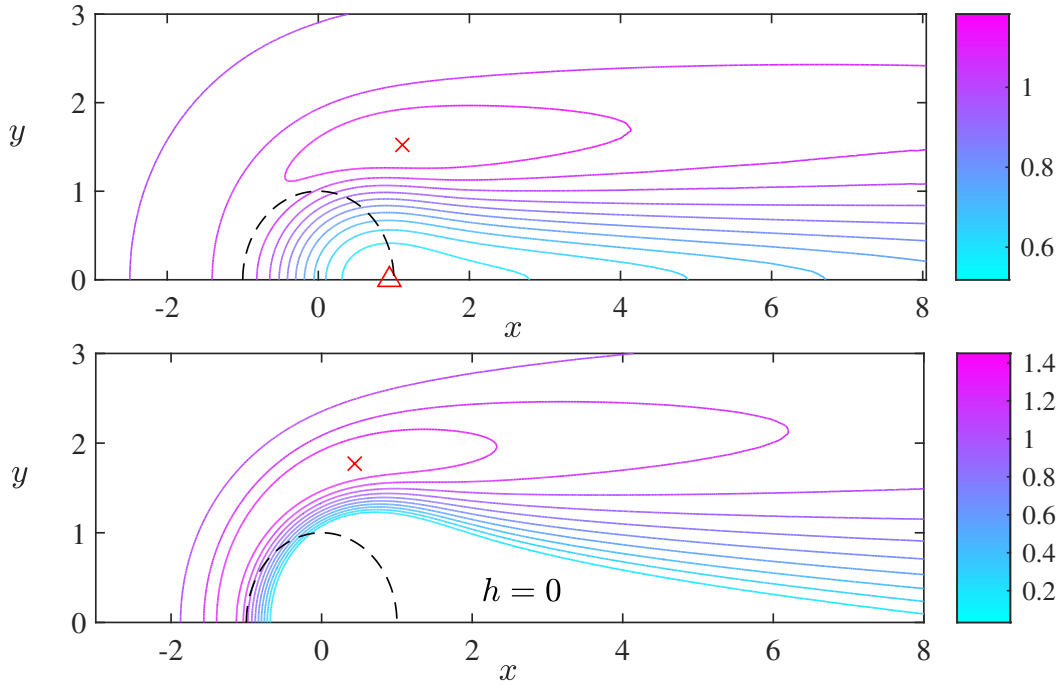

Fig. 6.2 Contour plots of the thickness of the steady flow above the topography of shape $m = \exp(-r^2)$ and of different dimensionless magnitudes, $\mathcal{M}$. (a) $\mathcal{F} = 0.1$ and $\mathcal{M} = 0.5$, the red cross marks the maximum thickness ($h = 1.183$) and the red triangle marks the minimum thickness ($h = 0.519$). (b) $\mathcal{F} = 0.1$ and $\mathcal{M} = 1.5$, the red cross marks the maximum thickness ($h = 1.463$) and there is a region in which $h = 0$. As the mound height is increased, dry regions occur. Note that the mound is centred at the origin of the (x,y) plane and the dashed line is the unit semicircle, which is a contour of the mound.

6.3 Numerical method

We used MATLAB's Partial Differential Equation Toolbox$^{\text{TM}}$ to solve the steady governing equation (6.12). The program uses a finite-element method and performs adaptive mesh generation.

The program operates as follows. The two-dimensional computational domain, Ω, is represented by a union of triangles (the mesh). The first step is to convert the strong form of the PDE (6.12) into an integral (weak form) by multiplying by a test function, v, and integrating over the domain. The weak form is discretized into the mesh elements of Ω (for an introduction to the finite element method, see Johnson [91]). The approximate solution is expressed as a linear combination of piecewise polynomial basis functions, which each have compact support corresponding to one of the triangles in the mesh. The weak form then simplifies to a finite system of algebraic equations for the coefficients in the linear

combination of basis functions. This system is solved to obtain an approximate solution to the governing equation.

The algorithm improves the accuracy of the solution by solving a sequence of problems using refined triangular meshes. The first mesh generation is specified by the user and we guess that $h = 1$ everywhere, which corresponds to neglecting the influence of the topography. Subsequent generations of triangular meshes are obtained by solving the PDE problem, computing an error estimate, selecting a set of triangles based on the error estimate and then refining the triangles (for example by dividing them in half along the longest edge). The solution is then recomputed. The loop continues until the triangle selection method selects no further triangles or until the maximum number of triangles is obtained.

The problem is symmetric about the centreline $y = 0$ so computational effort is reduced by using a half-domain. We solve the governing equation on the domain $0 < y < c$, $a < x < b$ (where $a < 0$) with boundary conditions described as follows. The upstream line source supplies constant flux so $h(x = a) = 1$. We allow 'free-flow' on the other three boundaries which corresponds to $\partial h/\partial n = 0$. For each pair $\mathcal{F}$, $\mathcal{M}$, we run our numerical technique on the domain $0 < y < 5$, $-5 < x < 5$ and subsequently increase the domain size by one unit in the y direction and the negative x direction and two units in the positive x direction. The numerical integration is performed on the new domain and the process is repeated until the flow thickness changes by at most 0.1% between iterations anywhere in the domain. For example, with $\mathcal{F} = 0.1$ and $\mathcal{M} = 0.5$, the final domain used was $a = -15$, $b = 25$ and $c = 15$. A contour plot of the thickness of the flow is shown in figure 6.2a. It was confirmed that the numerical results conserved mass by comparing the total downslope flux at various y cross-sections. The flux in the x direction across the width of the domain, $0 < y < c$, is

$$\int_0^c h^3 \left(1 - \mathcal{F}\frac{\partial h}{\partial x} - \mathcal{M}\frac{\partial m}{\partial x}\right) \mathrm{d}y. \tag{6.15}$$

This is computed at $x = 0$ and $x = 10$ from the numerical result for the flow depth and compared to the supplied flux which is equal to the width, c. The error between each of the fluxes was at most 0.2% for the final domain.

The minimum thickness of the current decreases as the mound height is increased through the parameter $\mathcal{M}$ or as the upstream flow depth is decreased through the parameter $\mathcal{F}$. For sufficiently large mounds, dry regions in which the flow depth vanishes ($h = 0$) can occur (see figure 6.2b). In the regime of very shallow upstream flow ($\mathcal{F} \ll 1$), the critical mound height beyond which dry regions occur is $\mathcal{M}_c \approx 1.17$ for $m = \exp(-r^2)$. This critical height is derived using asymptotic analysis in §6.5, where we also discuss its physical significance.

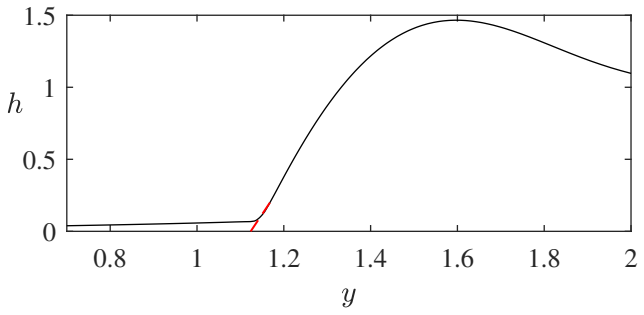

Fig. 6.3 The cross-section of the numerical solution to equation (6.16) with $\mathcal{F} = 0.1$ and $\mathcal{M} = 1.5$ along the line $x = 0$ is shown as a continuous black line. The dashed red line indicates the extrapolation used to obtain the location of the boundary of the dry zone.

The original numerical scheme was not effective when there were dry regions. The diffusive term in the partial differential equation (6.12) is $\nabla \cdot (h^3 \nabla h)$. The nonlinear diffusion coefficient is h^3, which is degenerate as $h \to 0$. There are large gradients in h near the dry regions and these are unable to be resolved by the numerical scheme and can lead to spurious and inadmissible regions of $h < 0$.

We therefore introduced a small source upstream of the mound to provide a 'virtual' thin film over the dry region to combat this difficulty. The governing equation is adjusted to

$$\frac{\partial h^3}{\partial x} = \nabla \cdot \left[h^3 \nabla \left(\mathcal{F} h + \mathcal{M} m \right) \right] + \varepsilon(x,y), \tag{6.16}$$

where $\varepsilon(x,y) = \varepsilon_0 \exp[-(x+1)^2 - y^2]$. The magnitude of the source, ε_0, was minimized subject to the constraint that the thin film coats the dry region. For figure 6.2b with $\mathcal{F} = 0.1$ and $\mathcal{M} = 1.5$, we used $\varepsilon_0 = 0.008$ (smaller ε_0 led to regions with $h < 0$ in the numerical results). The flow's thickness is everywhere $h > 0$ and the problem can be solved as described above. The edge of the dry region can be determined by analysing where the flow thickness increases from its approximately constant value in the thin film. The 'dry' region is coated in fluid owing to the 'virtual' source. Within the thin film of 'virtual' fluid, the depth is approximately constant but there are large gradients in h at the boundary of the film zone (figure 6.3). The large gradients provide the location of the boundary of the 'dry' region and we set $h = 0$ inside this region (see figure 6.2b). The boundary of the dry zone is determined from the numerical results along radial cross-sections in $x < 0$ and transverse cross-sections in $x > 0$. The prediction for $h = 0$ is obtained by linearly extrapolating the data at $h = 0.1$ and $h = 0.2$ along these cross-sections. The extrapolated line for the cross-section along $x = 0$ for $\mathcal{F} = 0.1$ and $\mathcal{M} = 1.5$ is plotted as a dashed red line in figure 6.3. We found

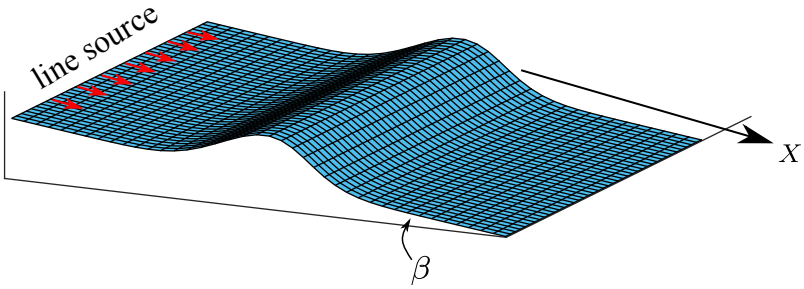

Fig. 6.4 Schematic diagram showing a 'one-dimensional' mound topography which varies only in the X direction.

that doubling the source magnitude from $\varepsilon_0 = 0.008$ to $\varepsilon_0 = 0.016$ reduced the area of the predicted dry zone by 1.5% and increased the maximum flow depth upstream by less than 0.2%. This suggests that the magnitude of the virtual film source has a negligible influence on the location of the dry zone obtained using the method described here.

We now compute the flow thickness for a wide range of two-dimensional topographies. Asymptotic analysis can help interpret the results of these computations, but before launching into this analysis it is helpful to study the one-dimensional case of flow over a mound which spans the channel in the y direction; $m = \exp(-x^2)$ (see figure 6.4). Although dry zones are not possible in this one-dimensional problem due to the imposition of a constant volume flux, this problem provides valuable insights into the important aspects of the problem.

6.4 Flow over one-dimensional mounds

For flow over a one-dimensional mound (as depicted in figure 6.4), the steady governing equation (6.12) simplifies to

$$\frac{\mathrm{d}h^3}{\mathrm{d}x} = \frac{\mathrm{d}}{\mathrm{d}x}\left[h^3\left(\mathcal{F}\frac{\mathrm{d}h}{\mathrm{d}x} + \mathcal{M}\frac{\mathrm{d}m}{\mathrm{d}x}\right)\right]. \tag{6.17}$$

Mass conservation demands that the flow must all go over the bump and hence dry regions cannot occur, in contrast to the two-dimensional problem in which the flow may be entirely deflected around the topography. Since the flow is steady, the downstream flux per unit width is constant everywhere and determined by the source injection. This condition can be written as

$$\int_0^h u(x,z)\,\mathrm{d}z = h^3\left(1 - \mathcal{F}\frac{\mathrm{d}h}{\mathrm{d}x} - \mathcal{M}\frac{\mathrm{d}m}{\mathrm{d}x}\right) = 1, \tag{6.18}$$

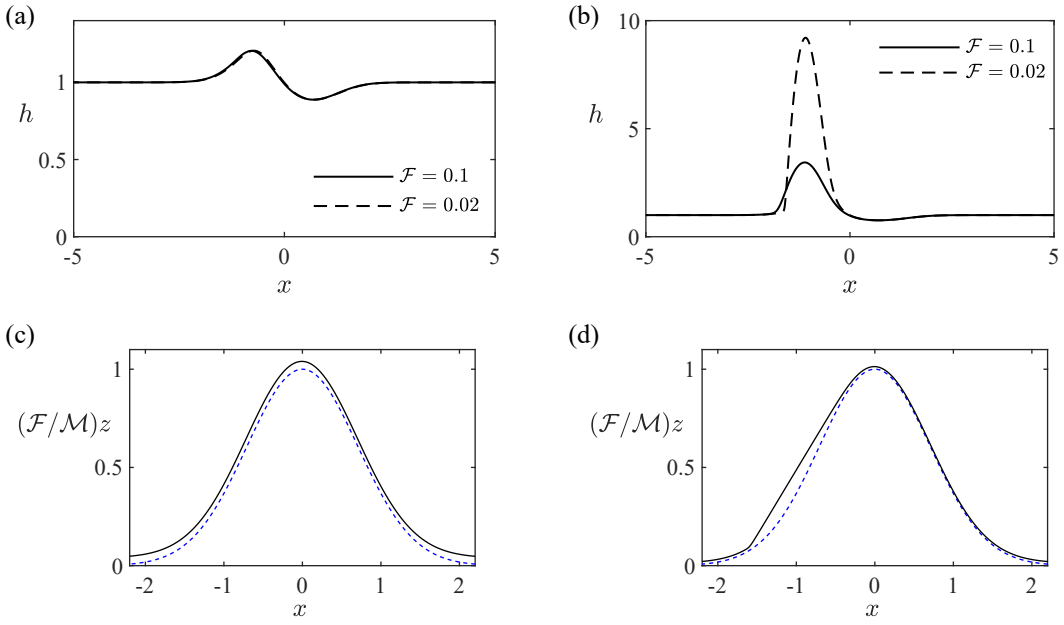

Fig. 6.5 The profiles of the steady flow over the one-dimensional mound, $m(x) = \exp(-x^2)$, as a function of streamwise distance, x. (a) Numerical solutions to equation (6.19) for $\mathcal{M} = 0.5$ and two shallow oncoming flows, $\mathcal{F} = 0.1$ and $\mathcal{F} = 0.02$. (b) Solutions for a larger mound, $\mathcal{M} = 1.5$. The solution is no longer independent of $\mathcal{F}$ to leading order. (c) The flow thickness relative to the height of the topography corresponding to $\mathcal{F} = 0.02$ in (a). The vertical axis has been scaled so that the mound height is unity. (d) The flow thickness relative to the topography corresponding to $\mathcal{F} = 0.02$ in (b). In both (c) and (d), the surface of the flow is plotted with a continuous line, while the mound is plotted with a dotted line. The fluid 'ponds' upstream of the mound; the flow surface is horizontal in coordinates parallel and perpendicular to the direction of gravity (see figure 6.6).

where u is the flow velocity, given by the x-component of equation (6.14). The condition (6.18) cannot be satisfied if $h = 0$ and hence requires that $h > 0$ everywhere in the steady flow over a one-dimensional mound; that is there are no dry regions possible.

We can integrate equation (6.17), or use the constant flux condition (6.18), to obtain the following first order differential equation for $h(x)$

$$h^3\left[1 - \mathcal{M}\frac{\mathrm{d}m}{\mathrm{d}x}\right] = 1 + \mathcal{F}h^3\frac{\mathrm{d}h}{\mathrm{d}x}. \tag{6.19}$$

The numerical solution of (6.19) depends upon the shape of the mounds, given by $m(x)$. We solve equation (6.19) together with the far-field boundary condition $h \to 1$ as $x \to \pm\infty$, which demands that the flow returns to its unperturbed steady-state far from the mound. In principle, we could impose the depth of the flow at some distant upstream location, $h(-\mathscr{L}) = 1$, where

$\mathscr{L}$ is positive and $\mathscr{L} \gg 1$. However, in this case numerical integration downstream generates numerical instability and exponential growth in $h(x)$. Instead, we impose the condition at a downstream location, $h(\mathscr{L}) = 1$, and then straightforwardly numerically integrate to upstream locations, ensuring that the computed solution does not depend upon the magnitude of $\mathscr{L}$. In figure 6.5 we have plotted our numerical results for some shallow flows ($\mathcal{F} \ll 1$). The numerical results exhibit a qualitative change in behaviour as $\mathcal{M}$ is increased past a critical value, $\mathcal{M}_c$, which will be determined below (see figure 6.5a where $\mathcal{M} = 0.5$ and figure 6.5b where $\mathcal{M} = 1.5$). For $\mathcal{M} > \mathcal{M}_c$, the flow develops a deep 'pond' of fluid upstream of the mound.

We illustrate the qualitative change in behaviour in figure 6.6. Increasing the mound height beyond a critical value, $\mathcal{M}_c$, leads to a region in which the topography is upslope (between x_1 and x_0 in figure 6.6b). The qualitative change in behaviour occurs at $\mathcal{M}_c$ because the current cannot flow up a slope, even with a very shallow gradient, until sufficient fluid has accumulated in a pond to overtop the highest part of the slope. This is because the flow is shallow and viscously controlled, with inertia playing only a negligible role.

The critical mound height, $\mathcal{M}_c$, corresponds to a mound at which the topography first becomes horizontal at a single point. This can be seen by noting that the gradient of the topography relative to gravity is given by (cf. equation 6.2)

$$(D/L)m'(x) - \tan\beta = -\tan\beta\left[1 - \mathcal{M}m'(x)\right]. \tag{6.20}$$

For the case $m = \exp(-x^2)$, the expression $1 - \mathcal{M}m'(x)$ is strictly positive provided that

$$\mathcal{M} < \mathcal{M}_c = (e/2)^{1/2} \approx 1.16\ldots \tag{6.21}$$

and hence there are no regions of upslope topography in this case. For $\mathcal{M} > \mathcal{M}_c$, the expression, $1 - \mathcal{M}m'(x)$, is negative in a region which we label $x_1 < x < x_0$ (see figure 6.6b).

Figure 6.5a suggests that for sufficiently small mound heights, $\mathcal{M}$, the flow thickness is of order unity throughout the domain in the regime $\mathcal{F} \ll 1$, because the motion is predominantly driven by the downslope component of gravity and the contribution due to the gradient of hydrostatic pressure is negligible. This motivates a regular expansion, $h_R(x)$, in terms of the small parameter $\mathcal{F}$

$$h \equiv h_R(x) = h_0(x) + \mathcal{F}h_1(x) + \cdots \tag{6.22}$$

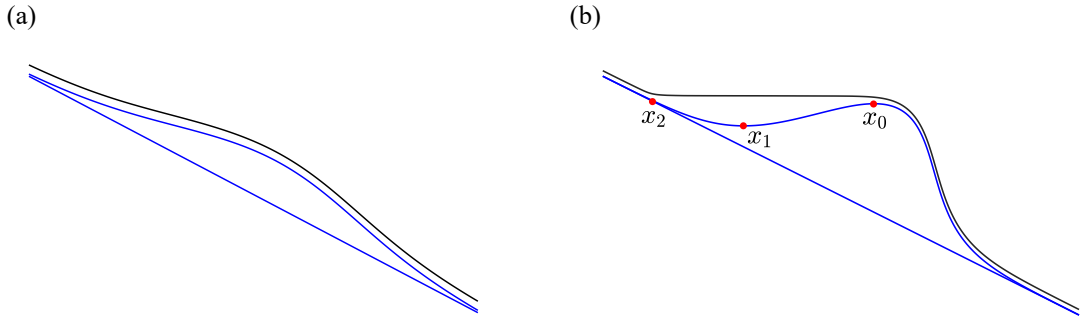

Fig. 6.6 Cartoons of the two flow regimes: (a) $\mathcal{M} < \mathcal{M}_c$ and (b) $\mathcal{M} > \mathcal{M}_c$. At the points x_1 and x_0, the topography is horizontal with an inflection point in between. The 'pond' rejoins the regular expansion at the upstream point x_2.

The governing equation (6.19) together with the far-field boundary condition $h \to 1$ can be used to determine

$$h_0 = \left[1 - \mathcal{M}m'(x)\right]^{-1/3}, \quad h_1 = \mathcal{M}m''(x)\left[1 - \mathcal{M}m'(x)\right]^{-8/3}/9, \tag{6.23}$$

and the first two terms in the expansion for h are

$$h \sim \left[1 - \mathcal{M}m'(x)\right]^{-1/3} + \mathcal{F}\mathcal{M}m''(x)\left[1 - \mathcal{M}m'(x)\right]^{-8/3}/9 + \cdots \tag{6.24}$$

This expansion is plotted as a red dashed line in figure 6.7a for $\mathcal{F} = 0.1$ and $\mathcal{M} = 0.5$. It shows excellent agreement with the numerical solution, which is plotted as a continuous black line. Equation 6.24 predicts that the flow thickness at leading order is independent of $\mathcal{F}$, which agrees with the numerical solutions in figure 6.5a.

Figure 6.7b illustrates that for a larger mound ($\mathcal{M} = 1.5$), there is a deep region in which our expansion (6.24) does not agree with the numerical results; this indicates that a different approach is required. The solution for $h_R(x)$ is invalid because it becomes singular if there is a solution to the equation

$$1 - \mathcal{M}m'(x) = 0 \tag{6.25}$$

For $\mathcal{M} > \mathcal{M}_c$, there are two (negative) solutions to (6.25), which we label $x_1 < x_0 < 0$ and (6.24) no longer provides a complete asymptotic solution for the depth of the fluid layer over the entire domain (see figure 6.6). Our expansion (6.24) is valid for $\mathcal{M} < \mathcal{M}_c$, and in this case the solution is accurately provided by (6.24), as illustrated by figure 6.5a. However, for larger mounds it is not asymptotic near x_0 and x_1; the second term in (6.24) is more singular than the first, and thus a new expansion is required.

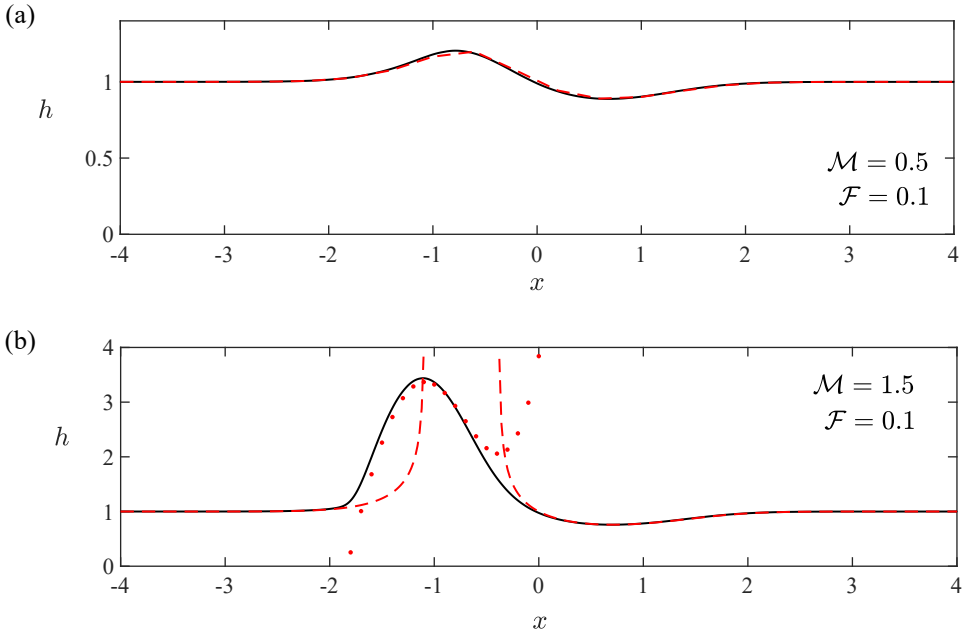

Fig. 6.7 The thickness of the flow as a function of streamwise distance, showing the comparison between the numerical solutions (continuous black lines) and asymptotic approximations found in section 6.4. (a) For the smaller mound regime ($\mathcal{M} = 0.5$), the $\mathcal{O}(1)$ expansion given by equation (6.24) and plotted as a red dashed line is accurate everywhere. (b) For a larger mound ($\mathcal{M} = 1.5$), the $\mathcal{O}(1)$ expansion is not valid in the large depth region and is in fact singular here. We plot the $\mathcal{O}(\mathcal{F}^{-1})$ expansion (equation 6.34) in red dots, noting that this is valid only within the ponded region and is matched to the regular expansion outside of this zone.

To determine the revised asymptotic form of the solution in the regime $\mathscr{M} > \mathcal{M}_c$, we return to the governing equation (6.19). We note that the regular asymptotic series (6.24) was derived on the basis that the gradient of the flow thickness was negligible. As the singular points of the regular series are approached (namely, $x = x_0$ and $x = x_1$), it is no longer the case that the gradients are negligible; instead they play a leading order role in the form of the solution. This motivates a different asymptotic expansion in the 'ponded' region, close to but upstream of the peak of the mound, within which the flow is relatively thick. In the ponded region we write

$$h \equiv h_p(x) = \mathcal{F}^{-1}\hat{h}_{-1} + \gamma(\mathcal{F})\hat{h}_0 + \cdots, \tag{6.26}$$

where $\gamma(\mathcal{F}) \ll \mathcal{F}^{-1}$ is to be determined. This form of solution is restricted to the ponded region; far-field boundary conditions may not be applied directly and instead the solution must be matched to the regular series, $h_R(x)$ at 'transition' zones close to $x = x_0$ and $x = x_2$ ($< x_1$), the latter of which is to be determined as part of the solution (see figure 6.6).

Substituting $h_p(x)$ into (6.19) and balancing terms of the same asymptotic order, we find that

$$\hat{h}_{-1} = x - \mathcal{M}m(x) + c_{-1} \qquad \text{and} \qquad \hat{h}_0 = c_0, \tag{6.27}$$

where c_{-1} and c_0 are constants to be determined.

First we match to the downstream form of the flow thickness by analysing the governing equation close to $x = x_0$. We introduce the following rescaled variables

$$x = x_0 + \left(\mathcal{F}^3/\mathscr{X}^4\right)^{1/7}\eta \qquad \text{and} \qquad h = (\mathcal{F}\mathscr{X})^{-1/7}H(\eta), \tag{6.28}$$

where $\mathscr{X} = -\mathcal{M}m''(x_0)$. The leading order terms in the governing equation in the regime $\mathcal{F} \ll 1$ are then given by

$$\eta = \frac{1}{H^3} + \frac{\mathrm{d}H}{\mathrm{d}\eta}. \tag{6.29}$$

Matching to the downstream regular expansion (6.24), we obtain

$$H \to \eta^{-1/3} + \tfrac{1}{9}\eta^{-8/3} \qquad \text{as} \qquad \eta \to \infty. \tag{6.30}$$

We note that the distinguished scalings of (6.28) are deduced by balancing the terms downstream (6.30). Numerically integrating (6.29), we find that

$$H \to \tfrac{1}{2}\eta^2 + 1.611\ldots \qquad \text{as} \qquad \eta \to -\infty, \tag{6.31}$$

and this condition must match the form of the solution in the ponded region. Thus evaluating (6.26) as $x \to x_0$ by substituting for x in terms of η given by (6.28), we find that

$$h_p \sim \mathcal{F}^{-1}\left[x_0 - \mathcal{M}m(x_0) + c_{-1}\right] + (\mathcal{F}\mathscr{X})^{-1/7}\,\eta^2 + \gamma(\mathcal{F})c_0 + \cdots. \tag{6.32}$$

Matching (6.31) and (6.32), we determine that $\gamma(\mathcal{F}) = \mathcal{F}^{-1/7}$ and that

$$c_{-1} = -x_0 + \mathcal{M}m(x_0) \qquad \text{and} \qquad c_0 = 1.611\left[-\mathcal{M}m''(x_0)\right]^{-1/7}. \tag{6.33}$$

In the ponded region, the asymptotic expansion is given by

$$h_p \sim \mathcal{F}^{-1}\left[x - x_0 + \mathcal{M}(m(x_0) - m(x))\right] + 1.611\mathcal{F}^{-1/7}\left[-\mathcal{M}m''(x_0)\right]^{-1/7} + \cdots \tag{6.34}$$

Upstream of the mound, the ponded zone re-joins a region that is modelled accurately by the regular expansion $h_R(x)$ around the location $x = x_2$. We introduce a rescaled independent variable in this zone to capture the transition in the solution between the ponded and regular asymptotic series. In this case the distinguished scaling is

$$x = x_2 + \mathcal{F}\xi \quad \text{and} \quad h = \hat{h}(\xi). \tag{6.35}$$

In terms of these variables the leading order terms in the governing equation become

$$1 - \mathcal{M}m'(x_2) = \frac{1}{\hat{h}^3} + \frac{\mathrm{d}\hat{h}}{\mathrm{d}\xi}. \tag{6.36}$$

The matching condition upstream is that the regular series is approached and thus $\hat{h} \to [1 - \mathcal{M}m'(x_2)]^{-1/3}$ as $\xi \to -\infty$. Substituting for x in the ponded expression (6.34) and evaluating this when $\xi \ll 1$, we find that

$$h_p = \mathcal{F}^{-1}\left[x_2 - \mathcal{M}m(x_2) + c_{-1}\right] + c_0\mathcal{F}^{-1/7} + \xi\left[1 - \mathcal{M}m'(x_2)\right] + \cdots. \tag{6.37}$$

Thus we deduce that

$$x_2 = x_0 + \mathcal{M}\left[m(x_2) - m(x_0)\right] + \mathcal{F}^{6/7}1.611\left[-\mathcal{M}m''(x_0)\right]^{-1/7} + \cdots. \tag{6.38}$$

This completes the asymptotic solution for the thickness of the flowing layer in the regime $\mathcal{F} \ll 1$. In figure 6.7b we show that it captures accurately the numerically computed behaviour for a particular parameter value.

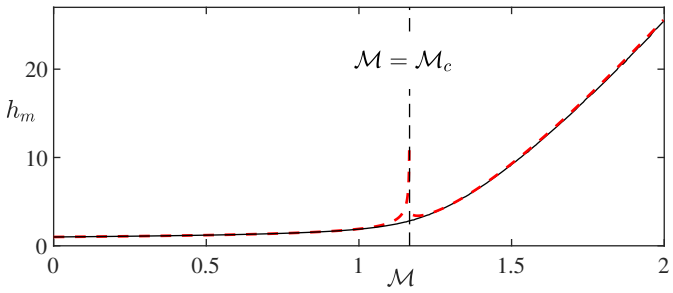

Fig. 6.8 Maximum flow thickness as a function of the dimensionless amplitude of the mound for $\mathcal{F} = 0.02$. The numerically calculated thickness is plotted as a continuous black line; the asymptotic prediction is plotted as a red dashed line.

We calculate numerically the maximum flow thickness that occurs as the fluid flows over the mound, h_m, as a function of the dimensionless amplitude of the mound, $\mathcal{M}$ (see figure 6.8), noting its weak dependence on $\mathcal{M}$ for values less than the critical value, $\mathcal{M}_c$, but its much stronger dependence for values in excess of the critical value. This quantity may also be evaluated directly from our asymptotic expansions for h_R and h_P. When $\mathcal{M} < \mathcal{M}_c$, the maximum depth occurs at $x_m (< 0)$ where $m''(x_m) = 0$ and $h_m = h_R(x_m)$; for $m(x) = \exp(-x^2)$ this means that $x_m = -1/\sqrt{2}$ and $h_m = (1 - \mathcal{M}/\mathcal{M}_c)^{-1/3}$.

When $\mathcal{M} > \mathcal{M}_c$, the maximum occurs at $x = x_1$, since this is where $\mathrm{d}h_p/\mathrm{d}x$ vanishes and so the maximum height is given by

$$h_m = \mathcal{F}^{-1}\Big\{x_1 - x_0 - \mathcal{M}\big[m(x_1) - m(x_0)\big]\Big\} + c_0\mathcal{F}^{-1/7}. \tag{6.39}$$

We have found two regimes for the flow over a one-dimensional mound in the case of a shallow upstream depth ($\mathcal{F} \ll 1$). For smaller mounds, the flow thickness is everywhere comparable to the upstream depth, but for mounds higher than a critical threshold ($\mathcal{M} > \mathcal{M}_c$), there is a region upstream of the mound in which the fluid 'ponds' much deeper than the upstream depth.

The critical dependence of the flow behaviour on the mound height will inform our study of two-dimensional mounds in the next section.

6.5 Flow over two-dimensional mounds

The governing equation for steady flow over a mound is given by (6.12) and in this section we analyse the motion when the mound varies both laterally and in the downslope direction. In contrast to one-dimensional mounds (§6.4), the flow in this scenario need not surmount

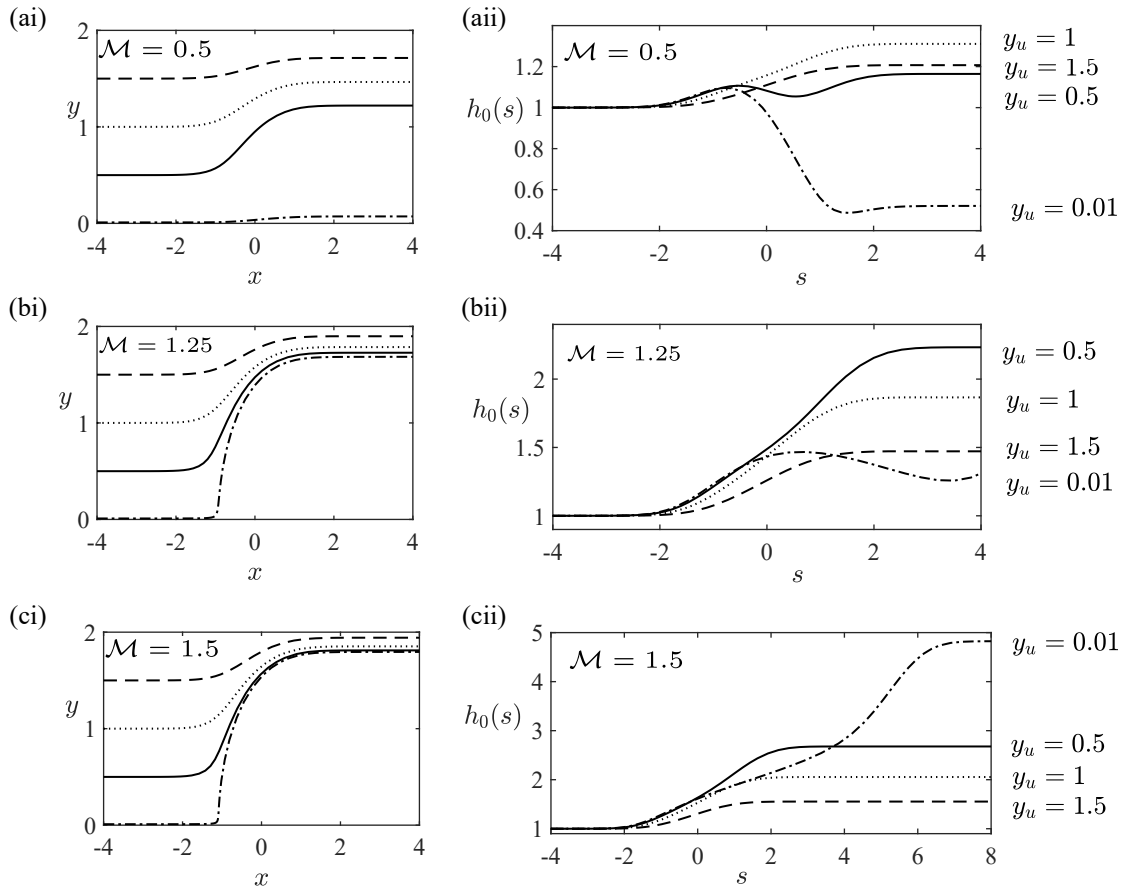

Fig. 6.9 The asymptotic solution for flow over a two-dimensional mound, $h_0(x,y)$, in the case that the diffusive slumping terms are neglected. The characteristics for equation (6.41) are plotted in the (x, y) plane for $\mathcal{M} = 0.5$ in (ai), for $\mathcal{M} = 1.25$ in (bi) and for $\mathcal{M} = 1.5$ in (ci) for four upstream cross-flow positions, y_u. The characteristics are parameterised by s (see equation 6.42). The leading order flow thickness, $h_0(s)$, is plotted along the four characteristics for $\mathcal{M} = 0.5$, $\mathcal{M} = 1.25$ and $\mathcal{M} = 1.5$ in (aii), (bii) and (cii) respectively.

the obstacle, but rather may be totally deflected around it. In this section we analyse the motion in the regime $\mathcal{F} \ll 1$ and $\mathcal{M} = \mathcal{O}(1)$ in which the flowing layer is much shallower than both the amplitude and streamwise extent of the mound.

We follow a similar analysis as for the one-dimensional problem (§6.4) to determine how the size of the mound controls the steady flow and in particular determine when the flow does not surmount the mound, leading to a dry region. Motivated by the numerical results shown in figure 6.2a, we seek a regular expansion for the flow thickness for smaller mounds in the form

$$h \equiv h_R = h_0 + \mathcal{F} h_1 + \cdots . \tag{6.40}$$

Then, at leading order, we find the first-order partial differential equation for h_0

$$\left[1-\mathcal{M}\frac{\partial m}{\partial x}\right]\frac{\partial h_0^3}{\partial x}-\mathcal{M}\frac{\partial m}{\partial y}\frac{\partial h_0^3}{\partial y}=\mathcal{M}h_0^3\nabla^2 m. \tag{6.41}$$

This equation neglects the diffusive slumping terms in the governing equation (6.12). We use the method of characteristics to find the following solution to (6.41)

$$\frac{\mathrm{d}x}{\mathrm{d}s}=1-\mathcal{M}\frac{\partial m}{\partial x},\quad \frac{\mathrm{d}y}{\mathrm{d}s}=-\mathcal{M}\frac{\partial m}{\partial y},\quad \frac{\mathrm{d}\log(h_0^3)}{\mathrm{d}s}=\mathcal{M}\nabla^2 m, \tag{6.42}$$

where s parameterises the characteristics. The characteristic projections in the (x, y) plane and the flow thickness, $h_0(s)$, along some of the characteristics are plotted in figure 6.9.

We observe that for $\mathcal{M}<\mathcal{M}_c$, $\mathrm{d}x/\mathrm{d}s$ is nowhere 0, where $\mathcal{M}_c=(e/2)^{1/2}$ [see (6.21)] takes the same critical value as found for the one-dimensional mound. It corresponds to the smallest mound for which there is a point at which the topography is horizontal relative to the direction of gravity. As in the one-dimensional problem, we anticipate a qualitative change in behaviour at $\mathcal{M}_c$ and begin our analysis by studying smaller mounds defined by $\mathcal{M}<\mathcal{M}_c$.

In the (x, y) plane, the shapes of the characteristic curves for equation (6.41) are given by

$$\frac{\mathrm{d}y}{\mathrm{d}x}=\frac{2\mathcal{M}ye^{-r^2}}{1+2\mathcal{M}xe^{-r^2}}, \tag{6.43}$$

where $r^2=x^2+y^2$ and $m=\exp(-r^2)$. The characteristics are plotted for $\mathcal{M}=0.5<\mathcal{M}_c$ in figure 6.10ai.

The depth far upstream of the mound is unity and we can numerically integrate the system (6.42) to obtain the leading order thickness, h_0. We plot a cross-section through the line of symmetry ($y=0$) of h_0 in figure 6.10aii.

Far downstream, the characteristic solution converges to a shape which is independent of x since $\mathrm{d}y/\mathrm{d}s$ and $\mathrm{d}h/\mathrm{d}s$ tend to zero; we denote

$$h_\infty(y)=\lim_{x\to\infty}h_0(x,y). \tag{6.44}$$

This far downstream shape is plotted in figure 6.10aiii, which illustrates that the thickness converges to 1 as $y\to\infty$ but not as $x\to\infty$.

The leading order thickness h_0 cannot be matched with the far-field condition, $h\to 1$ as $x\to\infty$, which suggests there is again an 'outer' region in which the diffusive slumping terms are important and our current asymptotic expansion, which neglects this cross-slope

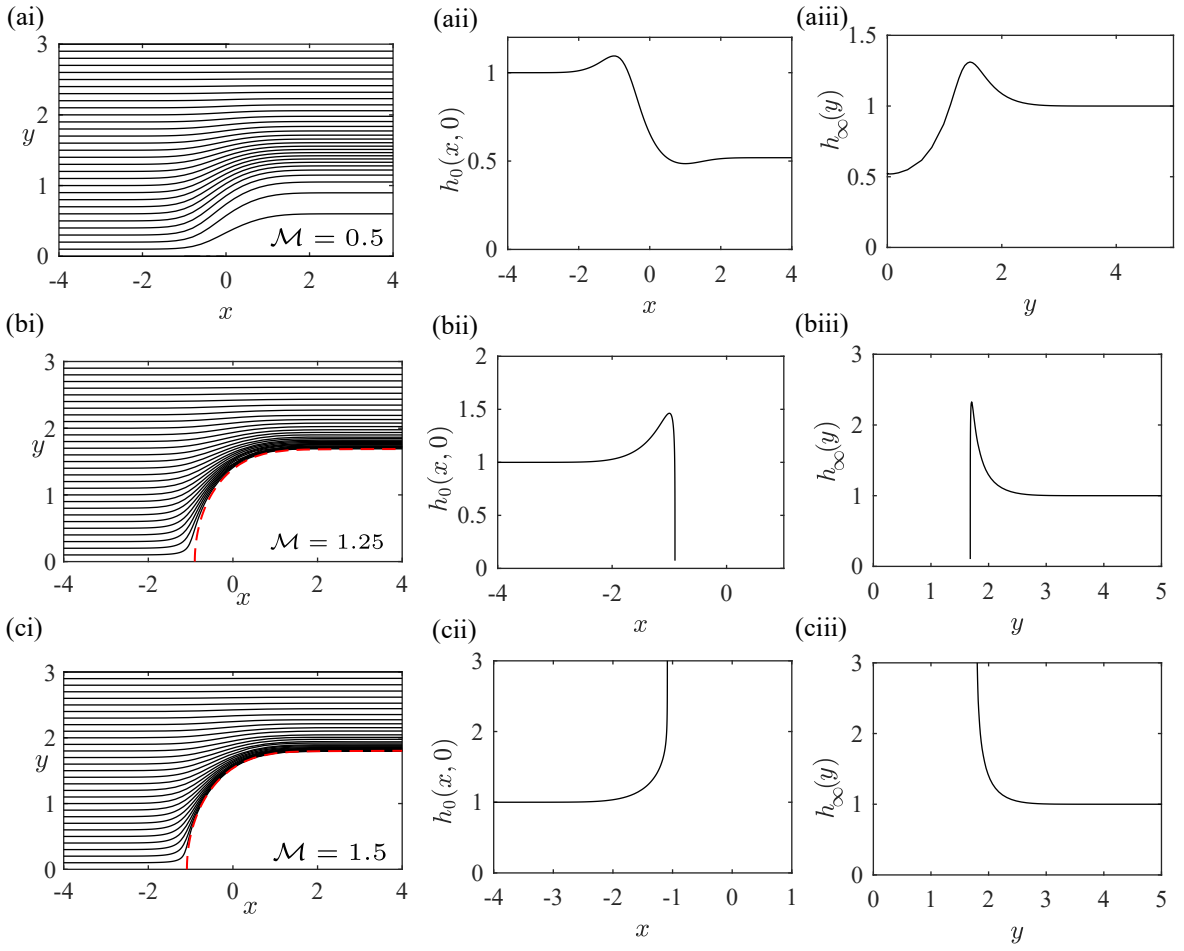

Fig. 6.10 The asymptotic solution for flow over a two-dimensional mound, $h_0(x,y)$, in the case that the diffusive slumping terms are neglected (see equation 6.41). The three rows correspond to different mound heights: $\mathcal{M} = 0.5$, 1.25 and 1.5. The characteristics are shown in the (x, y) plane in the first column. The red dashed lines in panel (bi) and (ci) show the boundary of the region that is not accessed by characteristics. The second column presents the thickness along the centreline, $y = 0$, predicted by the method of characteristics. Further downstream, the solution depends only on the cross-slope coordinate and this far downstream shape, $h_\infty(y)$ is plotted in the third column.

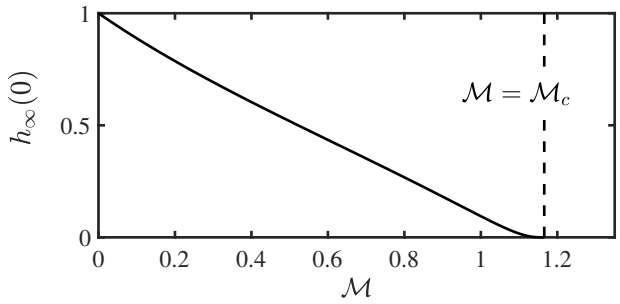

Fig. 6.11 Far downstream flow thickness over an axisymmetric mound along the line of symmetry ($y = 0$). The thickness is plotted as a function of the dimensionless mound amplitude, $\mathcal{M}$, according to the leading order expansion (6.41).

spreading, is not valid [see chapter 5 of 72]. This downstream region is analysed in subsection 6.5.1.

In figure 6.11, we plot the far downstream thickness on the line of symmetry, $h_\infty(0)$, as a function of the dimensionless mound amplitude, $\mathcal{M}$. The flow thickness over the highest parts of the mound decreases as the mound amplitude increases. However, there are no dry regions for $\mathcal{M} < \mathcal{M}_c$.

Figure 6.11 suggests that dry regions may occur for $\mathcal{M} > \mathcal{M}_c$. For such larger mounds, $\mathrm{d}x/\mathrm{d}s$ vanishes along the x axis at x_1, the more negative root of equation (6.25). The characteristic, which originates from (x_1, ε), where $\varepsilon > 0$ is arbitrarily small, is plotted as a red dashed line in figure 6.10bi and figure 6.10ci. This line bounds a region that is not accessed by the characteristics. We anticipate that dry regions may occur within the area not accessed by characteristics and this is corroborated by our numerical results (see figure 6.2). Figure 6.10bii shows that the flow thickness along the centreline vanishes. This vanishing thickness is propagated along the characteristics at the edge of the inaccessible region. In figure 6.10cii, the behaviour is different; the flow thickness becomes singular and this singularity is propagated along the bounding characteristics. We discuss the difference between these regimes later in this section.

We note that the characteristic projections (equation 6.42a and 6.42b) may be thought of as a phase plane. For $\mathcal{M} < \mathcal{M}_c$, there are no stationary points but for $\mathcal{M} > \mathcal{M}_c$, there are two stationary points at $(x_1, 0)$ and $(x_0, 0)$, where $x_1 < x_0$. The point $(x_1, 0)$ is at the edge of the inaccessible region and is the stationary point of interest. It is a saddle point with an unstable manifold in the y-direction and a stable manifold along the x axis, which can be seen in figure 6.10bi and figure 6.10ci. The point $(x_1, 0)$ is a saddle for all $\mathcal{M} > \mathcal{M}_c$ because m_{xx} is positive here and m_{yy} is negative.

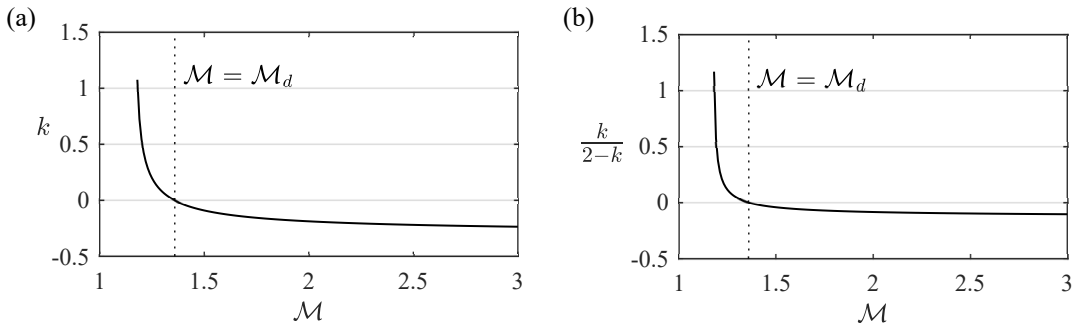

Fig. 6.12 (a) Exponent k [of $h_0 \sim (x_1 - x)^k$ as $x \to x_1$] as a function of the dimensionless mound amplitude, $\mathcal{M}$. (b) Exponent, $k/(2-k)$, of $\mathcal{F}$ in the flow depth ($h \sim \mathcal{F}^{k/(2-k)}$, equation 6.56) in the ponded region upstream of the mound.

To analyse behaviour at the edge of the inaccessible region, we consider the flow thickness along the line of symmetry $y = 0$ as the point $(x_1, 0)$ is approached. The characteristics from our asymptotic expansion, (6.40) and (6.41), indicate that the flow thickness along the centreline is given by

$$\frac{\mathrm{d}\log(h_0^3)}{\mathrm{d}x} = \frac{4\mathcal{M}(x^2-1)e^{-x^2}}{1+2\mathcal{M}xe^{-x^2}}. \tag{6.45}$$

As $x \to x_1$ the denominator tends to zero and the gradients in the flow thickness become very large (see figure 6.10bii and figure 6.10cii). Our asymptotic expansion breaks down here, similar to the behaviour in the one-dimensional problem (see §6.4).

The large x-gradients in the flow thickness, $(\partial h/\partial x)$ suggest that the downslope diffusive slumping term $\mathcal{F}\partial^2 h^4/\partial x^2$ needs to be reintroduced near the singularity. We consider this neighbourhood and approximate (6.45) to leading order by

$$\frac{\mathrm{d}\log(h_0^3)}{\mathrm{d}x} = \frac{2(x_1^2-1)}{(1-2x_1^2)(x-x_1)}. \tag{6.46}$$

Then, according to (6.45), near x_1, the leading order term, h_0 is proportional to $(x_1 - x)^k$, where

$$k = \frac{2(x_1^2-1)}{3(1-2x_1^2)}, \tag{6.47}$$

which, through x_1, is weakly dependent on $\mathcal{M}$ for $\mathcal{M} > 1.5$. The exponent k is plotted as a function of $\mathcal{M}$ in figure 6.12a. The plot demonstrates that $k < 2$ and that k changes sign as $\mathcal{M}$ is increased. Note that $x_1 < -1/2^{1/2}$ and hence k changes sign as x_1 crosses -1. In

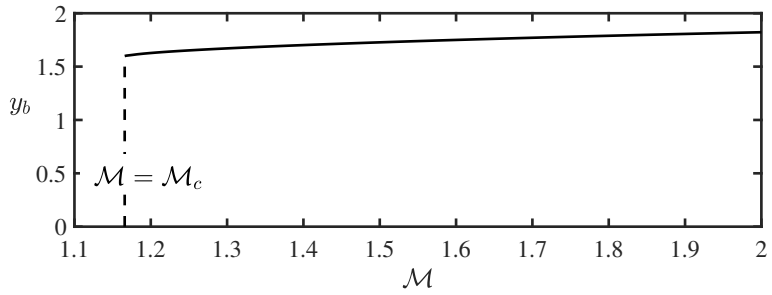

Fig. 6.13 The downstream width of the inaccessible region, y_b, as a function of the dimensionless amplitude of the mound, $\mathcal{M}$, for flow over the axisymmetric mound $m = \exp(-r^2)$.

terms of $\mathcal{M}$ this sign change corresponds to

$$k > 0 \quad \text{for } \mathcal{M} < \mathcal{M}_d = e/2 \approx 1.36, \tag{6.48a}$$

$$k < 0 \quad \text{for } \mathcal{M} > \mathcal{M}_d. \tag{6.48b}$$

Hence there is a change in behaviour at the secondary critical value, $\mathcal{M} = \mathcal{M}_d$. This can be observed by comparing figure 6.10bii, 6.10biii and 6.10cii, 6.10ciii; in the former, $\mathcal{M} = 1.25 < \mathcal{M}_d$, whilst in the latter, $\mathcal{M} = 1.5 > \mathcal{M}_d$. The regime change corresponds to a change in sign of the gradient of h_0 at the stagnation point, $(x_1, 0)$. The gradient is proportional to $\nabla^2 m = 4(r^2-1)e^{-r^2}$, which changes sign (for $y = 0$) as x_1 crosses 1.

The regime change also corresponds to the inaccessible region containing the unit circle. We deduce from (6.42) that the flow thickness, h_0 is monotonically increasing along characteristics that do not pass through the unit circle, which corresponds to the region in which the amplitude of the topography is greatest. Within the unit circle, the flow thickness is monotonically decreasing along characteristics (compare the $y_u = 0.01$ characteristics in figure 6.9bii and 6.9cii).

In figure 6.13, we demonstrate how the size of the inaccessible region for an exponential mound increases with $\mathcal{M}$ by plotting y_b, the far downstream deflection of the bounding characteristic [i.e. the solution of (6.42) for $y(s)$ as $s \to \infty$ given $y(0) = \varepsilon \ll 1$ and $x(0) = x_1$]. For $\mathcal{M} < \mathcal{M}_d$, some characteristics pass through the unit circle and hence h_0 is not everywhere monotonically increasing along characteristics. We note that y_b vanishes for $\mathcal{M} < \mathcal{M}_c$ because the mound is sufficiently small that the flow surmounts it and is not deflected around it.

The flow thickness far downstream of the mound, $h_\infty(y)$, does not vary monotonically with y if $\mathcal{M} < \mathcal{M}_d$, as illustrated, for example, by figure 6.10aiii and 6.10biii; instead it exhibits a maximum, h_m, which occurs at location y_m [defined by $h_\infty(y_m) = h_m$]. The

variation of h_m and y_m with the dimensionless mound size, $\mathcal{M}$, is plotted in figure 6.14, noting that for $\mathcal{M} > \mathcal{M}_d$ the downstream depth has become infinite at $y = y_b$ and that for $\mathcal{M} < \mathcal{M}_d$ both h_m and y_m increase monotonically with $\mathcal{M}$ due to the increased flow deflection around the mound.

To analyse the downslope diffusive term in a neighbourhood of x_1 along the symmetry axis ($y = 0$), we introduce the rescalings

$$x = x_1 + \mathcal{F}^{\alpha}\xi, \quad h = \mathcal{F}^{\alpha k}\tilde{h}, \tag{6.49}$$

where the scaling for h is motivated by the behaviour of the characteristic solution (6.46) and (6.47). Using the governing equation (6.12), we find that along the centreline $\tilde{h}$ satisfies

$$\frac{1}{4}\frac{\partial^2 \tilde{h}^4}{\partial \xi^2} + A_{\mathcal{M}}\xi\frac{\partial \tilde{h}^3}{\partial \xi} + B_{\mathcal{M}}\tilde{h}^3 = 0, \tag{6.50}$$

where we have chosen

$$\alpha = (2-k)^{-1}, \tag{6.51}$$

for a balance and

$$A_{\mathcal{M}} = \mathcal{M}\frac{\partial^2 m}{\partial x^2}\bigg|_{x=x_1,y=0}, \qquad B_{\mathcal{M}} = \mathcal{M}\nabla^2 m\bigg|_{x=x_1,y=0} \tag{6.52}$$

are constants. The boundary condition for (6.50) as $\xi \to -\infty$ is provided by the limiting behaviour of the characteristic solution along the centreline, given by (6.46). Writing this in terms of $\tilde{h}$ and ξ, we find that

$$\tilde{h} = C_{\mathcal{M}}(-\xi)^k, \tag{6.53}$$

where $C_{\mathcal{M}}$ is a constant that can be determined from the limit of the numerical solution to the characteristics as x_1 is approached. We solve for $\tilde{h}$ by assuming $\tilde{h}$ has compact support, shooting from $\tilde{h}(\xi_0) = 0$ and iterating to find ξ_0 by matching with the boundary condition (6.53) as $\xi \to -\infty$. To shoot from $\tilde{h} = 0$ we need two boundary conditions. Taking the limit of small $\tilde{h}$ in equation (6.50), we determine the behaviour near ξ_0 to be

$$\tilde{h} \sim A_{\mathcal{M}}\xi_0(\xi_0 - \xi). \tag{6.54}$$

This provides the two boundary conditions: the values of h and its first derivative at $\xi \approx \xi_0$. We plot the solution to equation (6.50) in figure 6.15 for $\mathcal{M} = 1.5$ as a red dashed line. The limiting behaviour, which we match to (given by equation 6.53) is plotted as a

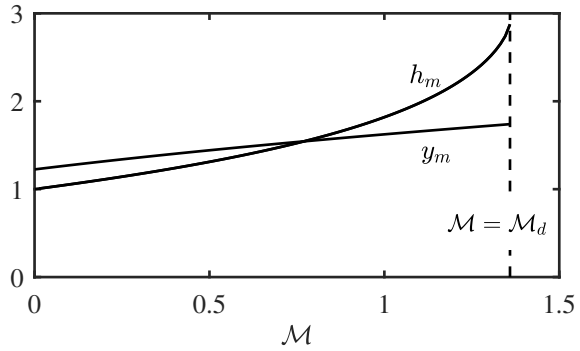

Fig. 6.14 Cross-slope location, y_m, and magnitude, h_m, of the maximum downstream flow thickness $h_\infty(y)$ as functions of $\mathcal{M}$ for flow over the axisymmetric mound, $m = \exp(-r^2)$.

black dotted line. Finally, we include a slice along the centreline of the numerical solution to the full governing equation with $\mathcal{F} = 0.05$ (continuous black line). The solution to equation (6.50) shows excellent agreement with the numerical slice in a neighbourhood of x_1. In particular, these results confirm that the downslope diffusive terms are crucial to the flow near x_1 but the cross-slope diffusive slumping which we have neglected is unimportant because the streamwise gradients are much larger than the lateral gradients.

Note that our analysis relies on the contact point where the depth is first zero occurring upstream of x_0 because the topography becomes downslope at x_0 in our simple mound. This corresponds to

$$x_1 + \mathcal{F}^{1/(2-k)}\xi_0 < x_0, \tag{6.55}$$

which is satisfied for sufficiently small $\mathcal{F}$. If the contact point extends beyond x_0 then there is no dry region because fluid has flowed over the 'steepest' slope of the topography. In this case the analysis above is rendered invalid because shooting from $h = 0$ at ξ_0 is incorrect. The inequality (6.55) can be used to determine the largest $\mathcal{F}$ for which dry regions occur for a given $\mathcal{M}$. We investigate this result for elliptical mounds in section 6.6.

In the one-dimensional problem (§6.4) we found that beyond the critical mound height, $\mathcal{M}_c$, ponding occurs and the flow thickness increases in proportion to the mound height. A regime change also occurs at this point in two dimensions because the topography becomes upslope and for the two-dimensional mound, this first occurs along the centreline, $y = 0$, where the mound slope is steepest. For a two-dimensional mound above the critical height, $\mathcal{M}_c$, the depth in a neighbourhood of x_1 is given by the scaling in (6.49),

$$h \sim \mathcal{F}^{k/(2-k)}. \tag{6.56}$$

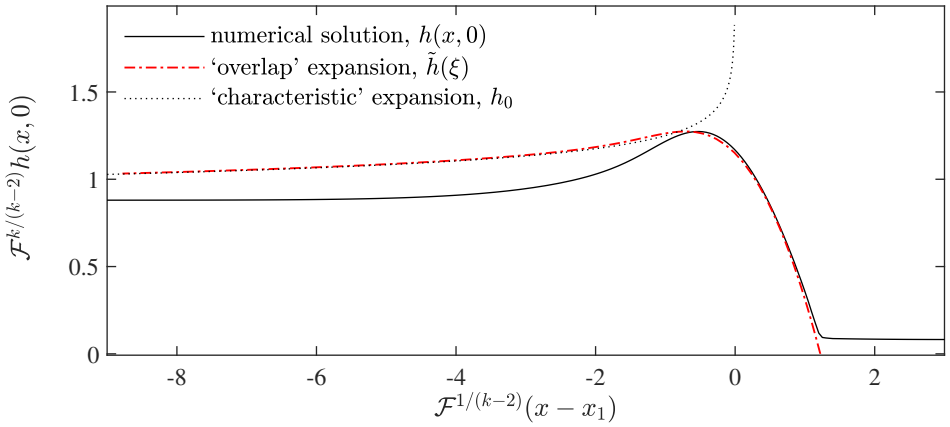

Fig. 6.15 The rescaled thickness of the fluid layer as a function of distance along the line of symmetry ($y = 0$) for $\mathcal{F} = 0.05$ and $\mathcal{M} = 1.5$ for flow over the axisymmetric mound, $m = \exp(-r^2)$. We plot the solution to (6.50) with initial condition (6.54) as a red dotted dashed line. The location of ξ_0 is chosen to match with the limit of the characteristic solution near x_1, which is plotted as a dashed black line. We include a slice along the centreline of the numerical solution from section 6.3, plotted as a continuous black line. It agrees well with the solution to equation (6.50) near x_1, the depth does not become zero at ξ_0 in the numerical solution because of the small virtual source.

The exponent of $\mathcal{F}$ changes sign as k changes sign. It is plotted as a function of $\mathcal{M}$ in figure 6.12b. For $\mathcal{M} < \mathcal{M}_d$, the exponent is positive and the depth of the flow is at most order 1. For a larger mound ($\mathcal{M} > \mathcal{M}_d$), the depth along the centreline near x_1 is of order $\mathcal{F}^{k/(2-k)}$, which grows as $\mathcal{F}$ becomes smaller. This corresponds to ponding upstream of the mound. The maximum flow thickness then occurs along $y = 0$, upstream of the mound, owing to this ponding. This is in contrast to the case of $\mathcal{M} < \mathcal{M}_d$ (see figure 6.14 and compare the two panels in figure 6.2). The ponding is much weaker than in the one-dimensional case and the mound height threshold at which it occurs is higher (for example, the exponent of $\mathcal{F}$ is $k/(2-k) \approx 0.04$ for $\mathcal{M} = 1.5$). This difference occurs because fluid is diverted away from the centreline and around the mound by the topography in the cross-slope direction, whereas in the one-dimensional problem, the pond has to grow until it overcomes the mound.

The flow thickness near $(x_1, 0)$ tends to zero and we anticipate that this dry edge is propagated by the characteristics as indicated in figure 6.10. Further downstream, the characteristics become parallel to the x axis and we anticipate that the y gradients are non-negligible here. Thus cross-slope diffusive slumping becomes important and this acts to 'close' the dry region downstream, which we investigate below.

6.5.1 Downstream 'outer' region

To leading order, the regular asymptotic expansion described above converges to a fixed shape in y far downstream, i.e. $h \to h_\infty(y)$ as $x \to \infty$ (see figure 6.10, right-hand column). Cross-channel diffusive slumping, which was neglected at leading order, smooths this shape so that the depth converges to unity everywhere distant from the mound. This motivates an 'outer' region, in which we rescale only the downstream coordinate x to incorporate the second-order derivative in y

$$x = \hat{x}/\mathcal{F}. \tag{6.57}$$

Then the leading order terms in (6.12) are

$$\frac{\partial h^3}{\partial \hat{x}} = \frac{1}{4}\frac{\partial^2 h^4}{\partial y^2}, \tag{6.58}$$

which represents a balance between downslope advection and cross-channel diffusive slumping. We use the far downstream shape of our 'inner' asymptotic solution, $h_\infty(y)$, (see figure 6.10aiii) as the 'initial' condition at $\hat{x} = 0$ to solve the nonlinear diffusion equation (6.58) numerically. The cross-slope shape converges to $h = 1$ everywhere, satisfying the far-field boundary condition.

In figure 6.16a, we compare this outer 'downstream' expansion (blue dotted-dashed line) to the numerical results from §6.3 (black continuous line) along the centreline, $y = 0$ for $\mathcal{M} = 0.5$. The inner 'characteristic' asymptotic expansion is included (red dashed line) to illustrate how it is accurate only upstream of the mound peak. In figure 6.16b, we compare the 'downstream' expansion with the numerical results in the cross-slope direction at two locations, demonstrating how the flow thickness returns to unity downstream.

For larger mounds in the domain $\mathcal{M} > \mathcal{M}_c$, the same technique can be applied to determine the downstream shape, but care must be taken in selecting the correct 'initial' condition for equation (6.58). The downstream limit of the characteristic solution for $\mathcal{M} > \mathcal{M}_c$ (figure 6.10biii and figure 6.10ciii) has large gradients and is not an accurate approximation to the true depth near $x = 0$ because the neglected diffusive terms are significant. The shapes in figure 6.10biii and figure 6.10ciii do not provide good initial conditions. Instead, we take a y cross-section of the numerical solution at $x = 0$ as the initial condition.

In figure 6.17, we compare the shape of the dry region predicted by the limiting characteristic and the shape of the dry region from the numerical results for $\mathcal{M} = 1.5$ and three values of $\mathcal{F}$. The importance of diffusive slumping is proportional to $\mathcal{F}$ and hence the closing of the dry region is faster for larger $\mathcal{F}$.

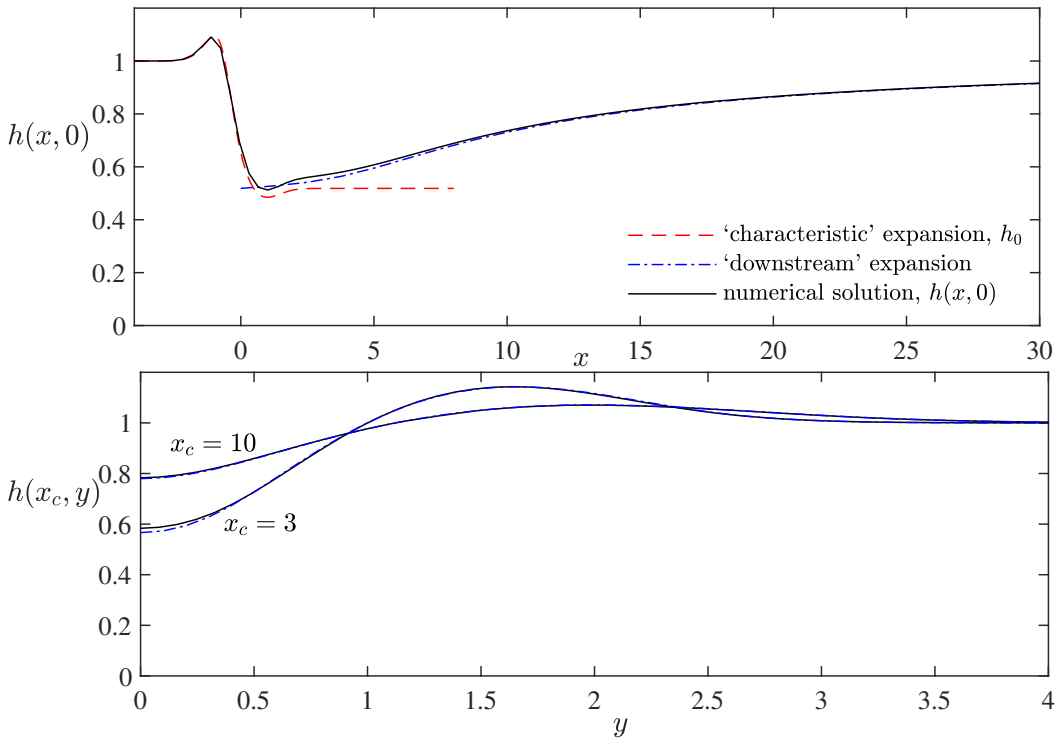

Fig. 6.16 (a) Flow thickness along the centreline, $h(x,0)$, as a function of streamwise distance. The cross-section of our numerical solution from section 6.3 for $\mathcal{F} = 0.08$, $\mathcal{M} = 0.5$ is plotted as a continuous black line. The asymptotic 'characteristic' expansion that neglected the diffusive slumping terms (equation 6.41) is plotted as a red dashed line and the 'downstream' expansion which balances the cross-slope slumping with the downslope advective term (see section 6.5.1) is plotted as a blue dashed-dotted line. (b) Flow thickness along cross-sections, $h(x_c,y)$, as a function of the cross-slope direction at various locations downslope from the mound, plotting the numerical solution (solid line) and the asymptotic solution (dot-dashed line).

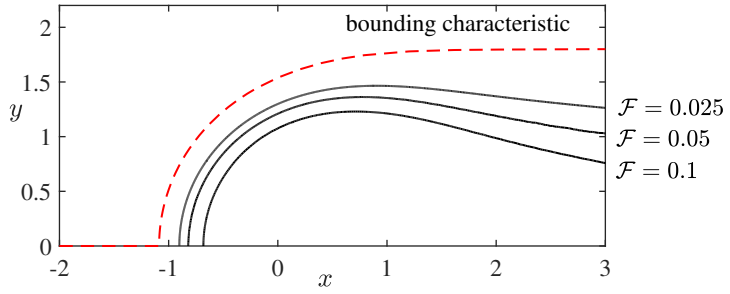

Fig. 6.17 Shape of the edge of the 'dry' region predicted by the characteristics (red dashed line) and the shape found from our numerical simulations for three values of $\mathcal{F}$, with $\mathcal{M} = 1.5$.

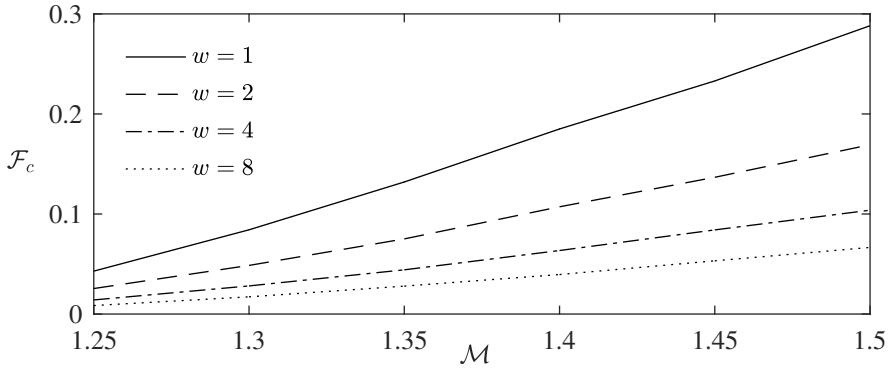

Fig. 6.18 The dimensionless upstream depth, $\mathcal{F}_c$ at which dry regions first occur as a function of dimensionless mound size, $\mathcal{M}$. For $\mathcal{M} > \mathcal{M}_c$ dry regions occur as the upstream flow depth ($\mathcal{F}$) tends to zero. We plot how small the flow depth must be for dry regions to occur for different nondimensional mound widths, w. The results are obtained from the inequality (6.55). Wider mounds should be built taller to defend against the same depth flow because the upstream ponding, which can overtop the mound, is enhanced.

6.5.2 Summary

We have found three regimes for a shallow oncoming flow ($\mathcal{F} \ll 1$) over an axisymmetric mound. For small mounds in which the slope is nowhere uphill ($\mathcal{M} < \mathcal{M}_c$), the flow goes over and around the mound and there are no dry regions. Mounds in the second regime, for which $\mathcal{M}_c < \mathcal{M} < \mathcal{M}_d$, give rise to dry regions. The flow thickness is order 1 with respect to $\mathcal{F}$ because sufficient flux of the fluid flows around the mound. For the larger mound regime, $\mathcal{M} > \mathcal{M}_d$, there is a dry region and the depth upstream of the mound increases as $\mathcal{F}^{k/(2-k)}$, with $k < 0$ [see (6.49)]. This weak dependence of the depth on $\mathcal{F}$ corresponds to the signature of ponding in two dimensions. We note that our analysis applies to any axisymmetric mound, although $\mathcal{M}_c$ and $\mathcal{M}_d$ may take different values. In the next section, we consider a more general class of mound.

6.6 Implications for barrier design

In this section we apply our analysis to inform efforts at designing barriers to protect towns and infrastructure from lava flows. To maximise the region downstream that is protected whilst minimising the overall size, barriers should be wider in the cross-flow direction than they are in the along-flow direction. This motivates considering mounds with elliptical contours; we suppose that the mound has cross-flow length scale W and along-flow length scale L. We use the same non-dimensionalisation as in §6.2 and consider an elliptical

Gaussian mound of profile

$$m(x,y) = \exp\left[-(x^2 + (y/w)^2)\right], \tag{6.59}$$

where $w = W/L$ is the aspect ratio of the elliptical contours of the mound. Note from (6.42) and (6.46) we deduce that this adjusts k to

$$k = \frac{2x_1^2 - 1 - w^{-2}}{3(1 - 2x_1^2)}. \tag{6.60}$$

The asymptotic analysis for an axisymmetric mound from section 6.5 can be repeated for an elliptical mound. We can use the inequality (6.55) to determine how shallow the upstream flow must be for dry regions to occur. We plot the critical value of $\mathcal{F}$ at which a dry region first occurs, $\mathcal{F}_c$, in figure 6.18 for an axisymmetric mound ($w = 1$) and three elliptical mounds. In the limit $w \to \infty$, the critical line tends to $\mathcal{F}_c = 0$. Thus, in this limit, the mound is overcome by the flow, and we recover the results of §6.4 for flow over a one-dimensional mound.

Figure 6.18 demonstrates that if a mound is widened but not heightened (i.e. w is increased and $\mathcal{M}$ held fixed), then the depths of flows which it defends against is reduced. In figure 6.19, contours of the flow thickness are plotted for $\mathcal{F} = 0.05$ and $\mathcal{M} = 1.4$ for different mound widths, w. In figure 6.19a, $w = 2$ and there is a dry region, whilst in figure 6.19b $w = 4$ and there is no dry region. The difference arises because the ponding upstream is stronger for a wider mound. The increased ponding can overtop the mound. This effect is crucial for informing barrier construction [for example in the Mt. Etna 2001 eruption, see 11].

We illustrate the importance of ponding by considering the necessary dimensions for an example Gaussian barrier which is 200 metres wide and has a streamwise length scale of 50 metres, on a slope with a gradient of 20%. To defend against a one metre high flow, the barrier would need to be 15 metres high. If instead the barrier was only 50 metres wide, then it would need to be about 13 metres high to provide a safe, dry region. These results approximately agree with the simulations of Chirico et al. [30], who suggested that barriers ought to be five to ten times the height of the average lava flow thickness.

6.6.1 Stress on mounds

We have used our results to suggest barrier dimensions but we can also calculate estimates of the force that barriers must withstand. A major engineering concern is that the lava pond

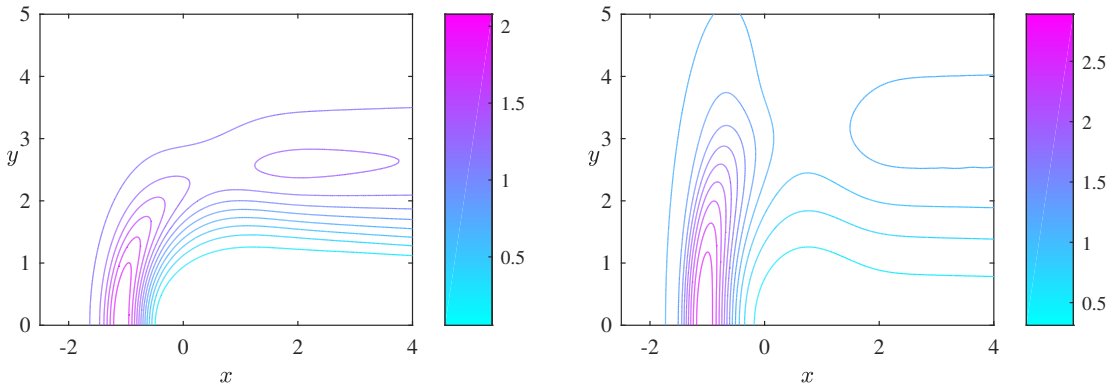

Fig. 6.19 Contour plots of the steady flow thickness above the topography in the case of an 'elliptical' mound with $\mathcal{F} = 0.05$ and $\mathcal{M} = 1.4$. (a) $w = 2$; there is a dry region with boundary given by the contour of least thickness. (b) $w = 4$; for a wider mound, the ponding effect is stronger and the flow overcomes the mound (cf. figure 6.18). Note the different scales for the thickness.

which can develop upstream of a barrier exerts a large force and can even rupture the barrier [107].

To obtain an upper bound on the force exerted by the pond, we consider a very wide mound ($w \gg 1$) which is on the verge of being overtopped by the oncoming flow. This situation is well approximated by the flow over a one-dimensional mound in which the flow thickness is much greater upstream of the mound than over the mound. Recall (see equation 6.34) that in the ponding region

$$h_p \sim \mathcal{F}^{-1}\left\{x - x_0 + \mathcal{M}\left[m(x_0) - m(x)\right]\right\} + \cdots \tag{6.61}$$

the flow surface is horizontal (perpendicular to the direction of gravity) and hence the velocity is approximately zero (cf. equation 6.14). Therefore, the leading order contribution to the stress comes from the weight of the fluid in the pond. This can be calculated by integrating the depth between x_2 and x_0 [where x_2 is calculated from (6.38) by assuming $\mathcal{F} = 0$]. The dimensional force per unit length in the downslope direction is given by

$$\rho g L H_\infty \sin\beta \int_{x_2}^{x_0} h_p \mathrm{d}x = \rho g L^2 f(\mathcal{M}) \tan\beta \sin\beta, \tag{6.62}$$

where

$$f(\mathcal{M}) = \mathcal{M}^2\left[m(x_0)^2 - m(x_2)^2\right]/2 - \mathcal{M}\int_{x_2}^{x_0} m(x)\mathrm{d}x. \tag{6.63}$$

This upper bound is independent of the upstream flow depth, H_∞, because it quantifies the stress exerted in the case of the deepest flow which does not overtop the mound. We note that we have neglected any extensional flow and the force calculated arises solely from the hydrostatic pressure.

Consider a mound barrier with $L = 50\text{m}$ and $\mathcal{M} = 1.5$ for which $f(\mathcal{M}) \approx 0.83$. We suppose the oncoming lava is two and a half times as dense as water and the slope is of gradient 0.25. With these parameters, (6.62) predicts that the maximum force per unit width exerted on the mound is $1.2 \times 10^7 \text{N}\,\text{m}^{-1}$.

6.7 Conclusion

In this chapter we have investigated theoretically the interaction between a fully-developed, free-surface flow of viscous fluid down an inclined plane with topographic features. Our results were derived on the basis that the flow is shallow, which in the context of this study requires that the flow thickness is much less than the downslope extent of the topographic feature. In this regime, the pressure is hydrostatic to leading order and we computed the steady flow around and over isolated mounds. This chapter was in part motivated by the need to inform the design and dimensioning of barriers that deflect lava flows away from built infrastructure. Our results were computed numerically and very often we employed asymptotic analysis to examine some of their key features.

A particular feature of our study has been the ways in which the mound causes a significant perturbation to the oncoming flow through deflecting its passage around the barrier, the development of 'dry' zones in the downslope wake of the barrier or by the establishment of upstream, ponded regions within which the thickness of the flow is enhanced. We showed that a key discriminant of when the flow became significantly affected by the topography was when there are uphill regions. In such circumstances we showed for one-dimensional obstacles, namely those that do not vary with the lateral coordinate, that the flow develops a pond upstream as it deepens to overtop the barrier. However, for axisymmetric mounds, the flow may be deflected around the obstacle rather than just overtopping it, potentially leading to downslope dry zones into which the fluid does not flow. The existence and dimensions of the dry zones are controlled by the amplitude of the mound. Flow around non-axisymmetric mounds featured the same phenomena, although as the mound became wider, the deflection of the flow was reduced, ponding was enhanced, and the dry zone was potentially eradicated.

In future studies, it would be interesting to analyse further controls on the interactions with topography that emerge if the flowing material exhibit some of the non-Newtonian

rheology associated with lava flows. The application of our results to field data from real lava flows is another area of our concern. A key challenge is determining how the crust formation at the front of a lava flow influences the shape of the 'safe' zone downstream of an obstruction.

Chapter 7

Viscous free-surface flows past cylinders

The material contained in this chapter has been submitted to *Physical Review Fluids*, under the title 'Viscous free-surface flows past cylinders' [Hinton et al.].

7.1 Introduction

The interaction between a free-surface viscous flow and immobile obstructions on an inclined plane occurs in many industrial and environmental contexts. It is often important to quantify the stress that is exerted on an obstruction and determine how the free-surface is perturbed. These flows are dominated by different forces depending on the lengthscale and shape of the obstruction, and the properties of the fluid. A common feature in many applications is that the flow is thin relative to the longitudinal lengthscale and so the lubrication approximation may be applied [14].

In the present chapter, we consider the interaction of free-surface viscous flow with cylindrical obstructions that are oriented with their axis perpendicular to the inclined plane and which are of a sufficient height that the flow does not surmount them (see figure 7.1). The motivation of the work is, in part, to inform the construction of barriers used to divert lava flows, which can cause enormous damage to homes and infrastructure [12].

The motion of a viscous Newtonian liquid down an inclined plane from either point or line sources is well-studied and it has been shown that a steady flow arises from a line source delivering a constant volume flux of liquid [130, 101]. The interaction of this steady flow with a topographical mound was the subject of the previous chapter. It was shown, and analysed quantitatively, that smaller mounds are surmounted by the flow whilst larger mounds lead to dry regions in which there is no liquid and a build-up of liquid in a pond upstream of the mound [see also the investigation of the lava field at Marcath volcano, 145].

The present chapter, investigating the interaction of a downslope viscous flow with cylindrical obstructions, pertains to lava barriers that are steeper and taller than those considered in chapter 6. Free-surface flows are often described by highly nonlinear partial differential equations and as such much of the previous work is primarily numerical or experimental [for a review, see 3]. In this chapter, we derive asymptotic results that show excellent agreement with our computational results and provide both a simplified quantification of the flow depth and insight into the dominant physics. Since part of the aim of the present work is to inform barrier construction, we quantify how the flow depth increases upstream of a cylinder to determine how tall an obstruction must be to prevent overtopping; we also make estimates of the force exerted on the obstruction. The results are calculated numerically and through explicit analytical expressions that result from our asymptotic analysis.

Additionally, our results have important applications to the study of the interaction between lava and trees. As an example, observations of 'lava-trees' post-eruption may be used to determine properties of the lava flow [29]. It has been shown that forests slow the advance of a lava flow and lead to build up of lava upstream [20]. Our results demonstrate similar phenomena.

The chapter is structured as follows. In section 7.2, we formulate the lubrication model for a free-surface viscous flow past a cylindrical obstruction, adapting the model from the previous chapter. We identify a single parameter, $\mathcal{F}$, which is a dimensionless proxy for the upstream flow depth relative to the width of the cylinder. We then present a numerical scheme and results for the steady flow depth. These demonstrate that for sufficiently wide obstructions ($\mathcal{F} \ll 1$), the depth increases significantly upstream of the cylinder and there are dry regions with no liquid downstream of the cylinder. For relatively narrow obstructions, the perturbation to the upstream flow depth is small.

In section 7.4, we determine an asymptotic approximation for the case of flows past a relatively narrow circular cylinder, corresponding to the regime $\mathcal{F} \gg 1$. In section 7.5, we consider the other regime of relatively wide cylinders ($\mathcal{F} \ll 1$) and show that the depth increases by a factor proportional to $\mathcal{F}^{-1/4}$ to leading order. Laboratory experiments are presented in section 7.6 and these corroborate our theory. Finally, in the last two sections, we study how the flow is perturbed upstream of a relatively wide square cylinder (7.7) and a relatively wide wedge (7.8). The three shapes of cylinder analysed in this study (sections 7.5, 7.7 and 7.8) have different behaviour in the upstream flow depth. This is associated with the different curvatures at the upstream point of the obstruction; for a circle the curvature is finite, for a square it vanishes whilst a wedge has infinite curvature at the vertex.

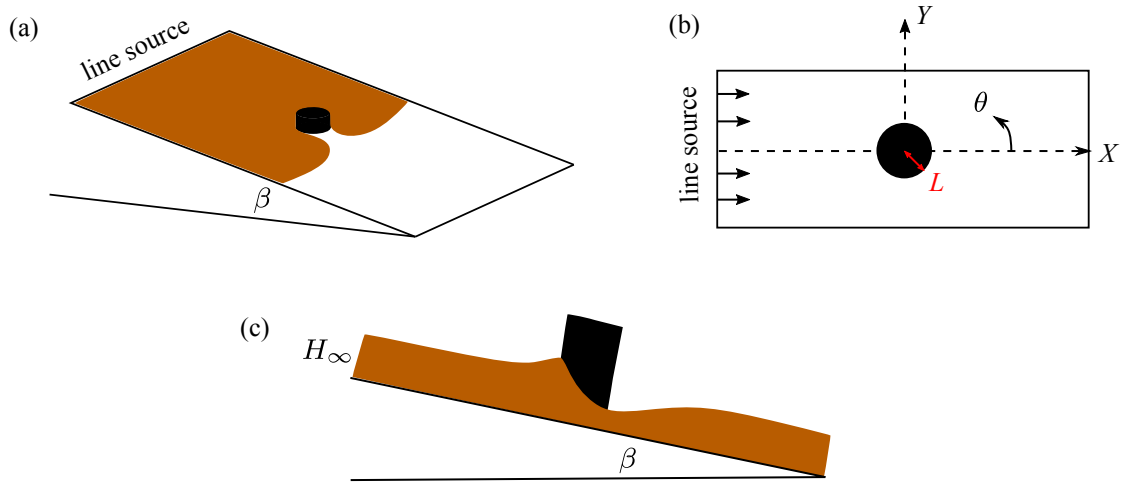

Fig. 7.1 (a) Schematic for viscous flow down an inclined plane at an angle, β, to the horizontal, past a cylinder from a line source. (b) Bird's eye view of the setup. The cylinder has radius L, the X axis is in the downslope direction and the Y axis is in the cross-slope direction. (c) Side view of the flow showing the far upstream thickness, H_∞, and the perturbation owing to the cylinder.

7.2 Formulation

We adapt the model from §6.2 to the case of a cylindrical obstruction.

We restrict our attention to cylindrical obstructions that are sufficiently high that they pierce the free-surface and there is no overtopping during the ensuing motion. The overtopping of topographical mounds was part of the consideration of the previous chapter. We use the following dimensionless variables

$$x = X/L, \quad y = Y/L, \quad h = H/H_\infty, \tag{7.1}$$

where H_∞ is the upstream flow depth (6.6) and L is the cylinder radius. Using equation (6.5), we find the following governing equation for the steady dimensionless depth, $h(x,y)$,

$$\frac{\partial h^3}{\partial x} = \mathcal{F}\left[\frac{\partial}{\partial x}\left(h^3\frac{\partial h}{\partial x}\right) + \frac{\partial}{\partial y}\left(h^3\frac{\partial h}{\partial y}\right)\right], \tag{7.2}$$

where the dimensionless parameter,

$$\mathcal{F} = \frac{H_\infty}{L\tan\beta} = \left[\frac{3\mu Q}{(\Delta\rho g\sin\beta)L^3\tan^3\beta}\right]^{1/3} \tag{7.3}$$

is the ratio of downslope to lateral pressure gradients. It quantifies the importance of the diffusive terms on the right-hand side of (7.2), associated with the gravity-driven slumping of the liquid, relative to the downslope advective term on the left-hand side of (7.2), associated with the gravity-driven flow down the plane. The dimensionless velocity is given by

$$\mathbf{u} = \frac{3}{2} z(2h-z)\left(1 - \mathcal{F}\frac{\partial h}{\partial x}, -\mathcal{F}\frac{\partial h}{\partial y}\right). \tag{7.4}$$

This parabolic velocity profile is typical of flows governed by a simple balance between viscous stresses and a uniform driving force (in this case gravity).

We begin the analysis by considering circular cylinders of radius L, centred on the origin. In dimensionless polar coordinates, with $x = r\cos\theta$, $y = r\sin\theta$ and the cylinder lies within $r < 1$, the steady governing equation for the motion ($r > 1$) is given by

$$\cos\theta \frac{\partial h^3}{\partial r} - \frac{\sin\theta}{r}\frac{\partial h^3}{\partial \theta} = \tfrac{1}{4}\mathcal{F}\nabla^2 h^4. \tag{7.5}$$

In this coordinate system the components of the velocity in the radial and azimuthal directions are

$$u_r = \frac{3}{2} z(2h-z)\left[\cos\theta - \mathcal{F}\frac{\partial h}{\partial r}\right], \tag{7.6}$$

$$u_\theta = \frac{3}{2} z(2h-z)\left[-\sin\theta - \frac{\mathcal{F}}{r}\frac{\partial h}{\partial \theta}\right], \tag{7.7}$$

respsectively. We impose a no-flux boundary condition at the edge of the obstruction, $\mathbf{u}\cdot\mathbf{n} = 0$, where $\mathbf{n}$ is the outward pointing normal, which becomes

$$h^3\left(\mathcal{F}\frac{\partial h}{\partial r} - \cos\theta\right) = 0 \quad \text{on} \quad r = 1. \tag{7.8}$$

We require that the flow depth returns to its unperturbed value far from the cylinder,

$$h \to 1 \quad \text{as} \quad r \to \infty. \tag{7.9}$$

Finally, we allow free-slip on the obstruction in accordance with the leading order lubrication model. Under our assumption of shallow flow ($H_\infty/L \ll 1$), the X and Y viscous stress terms, $\mu\partial^2 U/\partial X^2$ and $\mu\partial^2 U/\partial Y^2$ are neglected in the momentum equation. The order of the problem is therefore suppressed and the no-slip boundary condition on the cylinder

cannot be imposed. There is an inner region near the cylinder where the second order X and Y derivatives of the velocity become important. Our model neglects this region, which has been shown to occupy $R-L \sim H_\infty$ [for a detailed analysis of the inner region and the matching with the outer lubrication flow, see 138, 10]. In addition, if small inertial terms are reintroduced into the problem then the Z component of the velocity is non-zero in this region and there are secondary flows associated with the no-slip boundary, which we also neglect [138, 10, 36, 35]. In the case of relatively narrow obstructions, analysed in section 7.4, the region in which secondary flow is important may occupy much or all of the 'inner' region of the asymptotic analysis of our lubrication model.

7.3 Numerical method

We used MATLAB's Partial Differential Equation Toolbox$^{\text{TM}}$ to solve the steady governing equation (7.5), following the method of §6.3. We solve the governing equation on the domain $0 < y < c$, $a < x < b$ (where $a < 0$), with the unit semicircle in $y > 0$, centred at the origin, removed (see figure 7.2a). Since the problem is symmetric about the centreline $y = 0$ we solve the governing equation in $y \geq 0$ to reduce computational effort.

The boundary conditions on the domain are as follows. The upstream line source supplies constant flux; thus $h(x = a) = 1$. We impose a no-flux condition into the cylinder boundary, which is given by equation (7.8). We allow 'free-flow' on the other boundaries ($y = c$ and $x = b$), which corresponds to $\partial h/\partial n = 0$. For each value of $\mathcal{F}$, we run our numerical technique on an initial domain and subsequently increase the domain size until the flow depth varies by at most 0.1% upon extending the domain by a single unit in any direction. In the case that $\mathcal{F} = 0.1$, we used $a = -10$, $b = 40$ and $c = 10$. Typically, we use approximately 100,000 elements. We found that increasing this to 200,000 elements led to a change in the flow depth of at most 0.1% at any location. Contour plots of the thickness of the flow for three values of $\mathcal{F}$ are shown in figure 7.2.

For large $\mathcal{F}$, the diffusive terms in the governing equation (7.5) dominate and the perturbation to the flow depth due to the cylinder is small, as illustrated in figure 7.2a. The minimum thickness of the current (at $x = 1$, $y = 0$) decreases as $\mathcal{F}$ is decreased, corresponding to a relatively wider cylinder, steeper slope or shallower current (or a combination of these). For $\mathcal{F} = 1$, the minimum thickness is approximately half of the far upstream flow thickness (figure 7.2b). For sufficiently small $\mathcal{F}$, dry zones in which the flow depth vanishes ($h = 0$) can occur (see figure 7.2c).

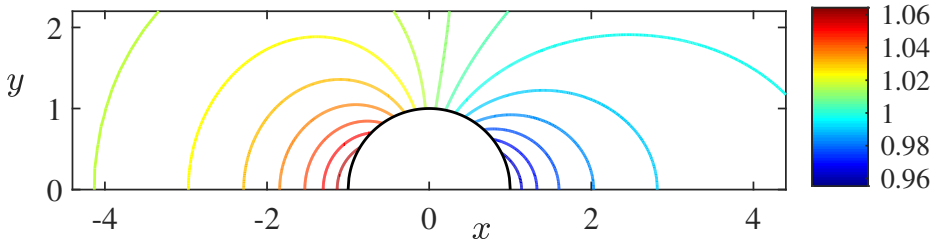

(a) $\mathcal{F} = 20$ (diffusive terms dominate advective terms).

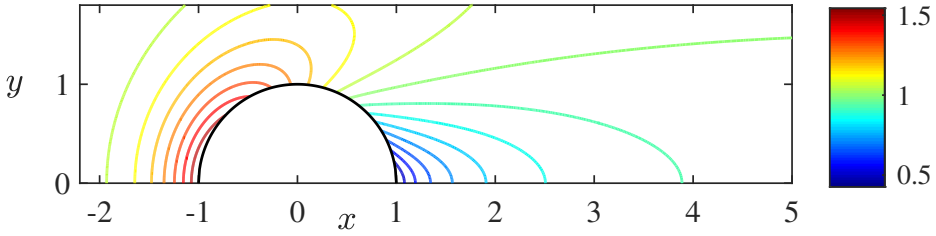

(b) $\mathcal{F} = 1$ (diffusive terms and advective terms are comparable and both are important).

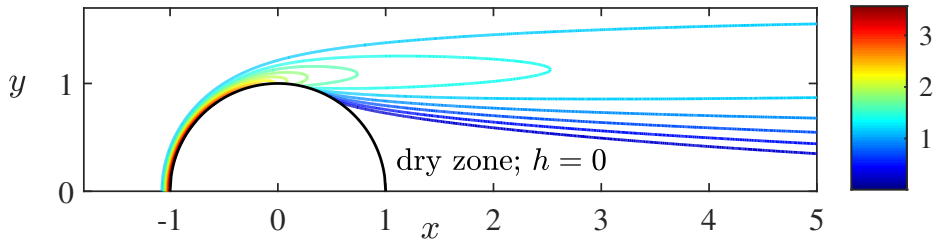

(c) $\mathcal{F} = 0.025$ (advective terms dominate the diffusive terms).

Fig. 7.2 Contour plot of the thickness of the steady flow around a cylinder with dimensionless radius $r = 1$ for three values of the flow parameter, $\mathcal{F}$.

The original numerical scheme was not effective when there were dry regions (cf. §6.3). To overcome this, we introduced a small source at the downstream edge of the cylinder, $r = 1$, $0 < \theta < \pi/2$, to provide a 'virtual' thin film over the dry region. It is analogous to radially 'squirting' a very small amount of fluid from the cylinder. The boundary condition on the cylinder (7.8) is then adjusted to

$$h^3\left(\cos\theta - \mathcal{F}\frac{\partial h}{\partial r}\right) = \varepsilon \qquad \text{on} \qquad r = 1, \quad 0 < \theta < \pi/2. \tag{7.10}$$

The magnitude of the source, ε, was minimized subject to the constraint that the thin film coats the dry region (and consequently the thickness of the flow everywhere satisfies $h > 0$). At such values of ε, the flow thickness becomes independent of ε away from the dry zone. The edge of the dry region can be determined by analysing where the flow thickness steeply increases from its approximately constant value in the thin film. We apply the method of §6.3 to obtain the boundary of the dry region, using cross-sections in the y direction. Typically, we use $\varepsilon = 10^{-6}$. We found that doubling the value of ε to 2×10^{-6} reduced the area of the dry region by less than 1%.

We computed the flow thickness for a wide range of values of the parameter, $0.025 \leq \mathcal{F} \leq 40$. In the following sections, we use asymptotic analysis to interpret the results.

7.4 Flows past narrow circular cylinders ($\mathcal{F} \gg 1$)

For $\mathcal{F} \gg 1$, the flow remains attached to the cylinder, i.e. there are no dry regions downstream. The increase in depth upstream of the cylinder is small relative to the far upstream depth (see figure 7.2a). This motivates seeking an expansion for h in the case $\mathcal{F} \gg 1$, about the far-field depth, $h = 1$, of the form

$$h = 1 + \mathcal{F}^{-1}h_1 + \mathcal{F}^{-2}h_2 + \cdots \tag{7.11}$$

To $\mathcal{O}(1)$, equation (7.5) is

$$\nabla^2 h_1 = 0, \tag{7.12}$$

subject to boundary conditions (7.8, 7.9)

$$\frac{\partial h_1}{\partial r} = \cos\theta \quad \text{at } r = 1, \tag{7.13a}$$

$$h_1 \to 0 \quad \text{as } r \to \infty. \tag{7.13b}$$

We seek a separable solution in r and θ, which satisfies the boundary conditions and obtain

$$h_1 = -r^{-1}\cos\theta. \tag{7.14}$$

To $\mathscr{O}(\mathcal{F}^{-1})$, equation (7.5) is

$$\nabla^2 h_2 = 3\cos\theta\frac{\partial h_1}{\partial r} - 3\frac{\sin\theta}{r}\frac{\partial h_1}{\partial\theta} - \frac{3}{2}\nabla^2 h_1^2. \tag{7.15}$$

We substitute our expression (7.14) for h_1, which yields

$$\nabla^2 h_2 = 3r^{-2}\cos 2\theta - 3r^{-4}. \tag{7.16}$$

The boundary conditions for h_2 are

$$\frac{\partial h_2}{\partial r} = 0 \quad \text{at } r = 1, \tag{7.17a}$$

$$h_2 \to 0 \quad \text{as } r \to \infty. \tag{7.17b}$$

The general solution to equation (7.16) is

$$h_2 = A_0\log(r) + B_0 + \sum_{n=1}^{\infty}\left(A_n r^n + B_n r^{-n}\right)\left[C_n\cos n\theta + D_n\sin n\theta\right] - \frac{3}{4}\cos 2\theta - \frac{3}{4}r^{-2}, \tag{7.18}$$

where A_n, B_n, C_n and D_n are constants to be determined. The last two terms represent the complementary function arising from the right-hand side of (7.16). We impose $A_n = 0$ (for $n \geq 1$) because h_2 cannot grow algebraically in the far-field if it is to match with $h_2 \to 0$ as $r \to \infty$. Applying the boundary condition at $r = 1$ (equation 7.17a), we find $A_0 = -3/2$ and $B_n = 0$ (for $n \geq 1$) and obtain

$$h_2 = -\frac{3}{2}\log(r) + B_0 - \frac{3}{4}\cos 2\theta - \frac{3}{4}r^{-2}. \tag{7.19}$$

It is not possible to apply the boundary condition as $r \to \infty$ (equation 7.17b) because $A_0 \neq 0$ and hence $h_2 \sim \log r$.

Instead, in the regime $\mathcal{F} \gg 1$, the solution forms two asymptotic regions close to and far from the cylinder. When the radial distance is $\mathscr{O}(\mathcal{F})$, the advective terms, on the left-hand side of (7.5), are comparable with the diffusive terms. The problem is therefore singular and its asymptotic approximation comprises an 'inner' region close to the cylinder which is matched to an 'outer' region far from it [for further details of this general idea, see chapter 5

of 72]. There is an analogy here with the resolution of Stokes' paradox for low Reynolds number flow past a cylinder, obtained by Proudman and Pearson [118], where an outer region is introduced to account for inertia.

Next, we seek an asymptotic expansion for the depth in the outer region where the advective and diffusive terms balance.

7.4.1 Outer region

The distinguished limit for the outer region of equation (7.5) occurs when we rescale r with $\mathcal{F}$ by

$$r = \mathcal{F}\hat{r}, \tag{7.20}$$

where $\hat{r}$ is order 1, and we define $\hat{x} = \hat{r}\cos\theta$ and $\hat{y} = \hat{r}\sin\theta$. The governing equation (7.5) in the rescaled coordinates is

$$\frac{\partial h^3}{\partial \hat{x}} = \left[\frac{\partial}{\partial \hat{x}}\left(h^3\frac{\partial h}{\partial \hat{x}}\right) + \frac{\partial}{\partial \hat{y}}\left(h^3\frac{\partial h}{\partial \hat{y}}\right)\right]. \tag{7.21}$$

Since $h \to 1$ as $\hat{r} \to \infty$, we seek an outer expansion of the form $h = 1 + \delta(\mathcal{F})\hat{h}$, where $\delta(\mathcal{F}) \ll 1$ is to be determined as part of the matching procedure. The leading order equation for $\hat{h}$ is

$$3\frac{\partial \hat{h}}{\partial \hat{x}} = \nabla^2\hat{h}, \tag{7.22}$$

which is linear. By letting $\hat{h} = \phi(\hat{r},\theta)e^{3\hat{x}/2}$, (7.22) is transformed into a more familiar equation for $\phi(\hat{r},\theta)$ [see chapter 5 of Ref 72]

$$(\nabla^2 - 9/4)\phi = 0. \tag{7.23}$$

Note that the boundary condition in the far field for ϕ is that it decays faster than $e^{-3\hat{x}/2}$ in order that $\hat{h} \to 0$ as $\hat{r} \to \infty$. Equation (7.23) has separable solutions of the form

$$\phi = \left[a_m\cos(m\theta) + b_m\sin(m\theta)\right]\Phi(\hat{r}), \tag{7.24}$$

where a_m and b_m are constants and Φ satisfies

$$\hat{r}^2\Phi'' + \hat{r}\Phi' - (9/4)\hat{r}^2\Phi - m^2\Phi = 0. \tag{7.25}$$

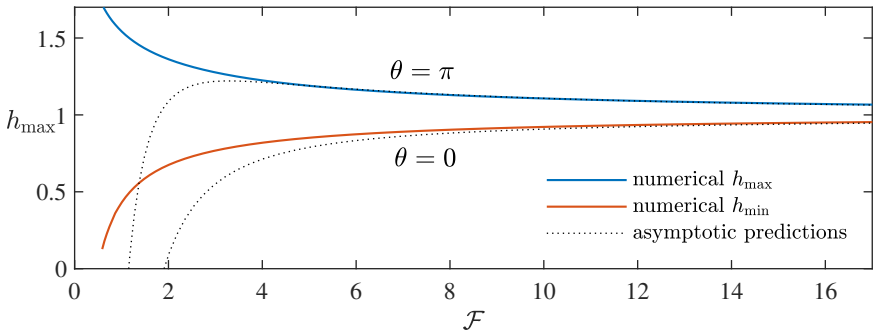

Fig. 7.3 The maximum (blue solid line) and minimum (red solid line) depths, calculated from our numerical technique, for steady flow past a cylinder as functions of the parameter $\mathcal{F}$. The deepest point is always at the stagnation point on the upstream boundary at $\theta = \pi$, whilst the shallowest point is on the downstream boundary at $\theta = 0$. The asymptotic predictions for the two extrema, calculated from equation (7.39), are plotted as black dotted lines, which show excellent agreement for $\mathcal{F} \gg 1$.

The general solution for Φ is

$$\Phi = c_m I_m\left(3\hat{r}/2\right) + d_m K_m\left(3\hat{r}/2\right), \tag{7.26}$$

where I_m and K_m are modified Bessel functions of the first and second kind, respectively [1] and c_m and d_m are constants. The function I_m grows as $\hat{r} \to \infty$, which imposes $c_m = 0$. We note that for $\hat{r} \gg 1$

$$K_m\left(3\hat{r}/2\right) \sim \sqrt{\frac{\pi}{3\hat{r}}} e^{-3\hat{r}/2}, \tag{7.27}$$

which implies that $\hat{h} \sim \hat{r}^{-1/2} \to 0$ as $\hat{r} \to \infty$, as required. Finally, since the flow is symmetric about the x axis, the coefficients of the $\sin(m\theta)$ terms in equation (7.24) vanish; $b_m = 0$. Putting this together, we obtain the following expression for the outer expansion

$$h = 1 + \delta(\mathcal{F})\hat{h} = 1 + \delta(\mathcal{F}) \sum_{m=0}^{\infty} a_m \cos(m\theta) K_m\left(3\hat{r}/2\right) e^{3\hat{x}/2}. \tag{7.28}$$

7.4.2 Matching

In this subsection, we match the inner solution as $r \to \infty$ with the outer solution as $\hat{r} \to 0$ to determine the correct form of the two expansions. We recall that the inner expansion is

$$h = 1 - \frac{\cos\theta}{r\mathcal{F}} + \mathcal{F}^{-2}\left[B_0 - \frac{3}{2}\log(r) - \frac{3}{4}\cos 2\theta - \frac{3}{4}r^{-2}\right]. \tag{7.29}$$

We match using an intermediate variable,

$$\rho = r\mathcal{F}^{-\alpha} = \hat{r}\mathcal{F}^{1-\alpha} \tag{7.30}$$

with ρ fixed as $\mathcal{F} \to \infty$ and α between 0 and 1. In terms of the intermediate variable, the inner expansion is

$$h = 1 - \mathcal{F}^{-\alpha-1}\rho^{-1}\cos\theta + \mathcal{F}^{-2}\left[B_0 - (3/2)\log(\mathcal{F}^{\alpha}\rho) - (3/4)\cos 2\theta - \frac{3}{4}\mathcal{F}^{-2\alpha}\rho^{-2}\right] + \ldots \tag{7.31}$$

The behaviour of the modified Bessel functions, K_m, which occur in the outer expansion, as $\hat{r} \to 0$ is given by,

$$K_0\left(3\hat{r}/2\right) \sim -\log(3\hat{r}/4) - \gamma, \qquad K_m\left(3\hat{r}/2\right) \sim [(m-1)!/2]\left(3\hat{r}/4\right)^{-m} \tag{7.32}$$

where $\gamma \approx 0.577$ is the Euler constant. In terms of the intermediate variable, the behaviour is $K_m \sim \rho^{-m}\mathcal{F}^{m(1-\alpha)}$. The size of the terms in the sum in the outer expansion (7.28) increases with m and these cannot all be matched to the inner expansion (7.31). We hence determine that $a_m = 0$ for $m \geq 2$. The outer expansion in the intermediate region is

$$h = 1 + \delta\left[-a_0\gamma - a_0\log\left(3\mathcal{F}^{\alpha-1}\rho/4\right) + (2/3)\mathcal{F}^{1-\alpha}a_1\rho^{-1}\cos\theta\right]\left[1 + (3/2)\mathcal{F}^{\alpha-1}\rho\cos\theta\right]. \tag{7.33}$$

The leading order term of both inner and outer expansions is 1 and the next term in the inner expansion (7.31) is $\mathcal{O}\left(\mathcal{F}^{-1-\alpha}\right)$. The second order term in the outer expansion (7.33) arises from K_1 and is $\mathcal{O}\left(\delta\mathcal{F}^{1-\alpha}\right)$. To match the two expansions we therefore choose

$$\delta = \mathcal{F}^{-2}. \tag{7.34}$$

To $\mathcal{O}(\mathcal{F}^{-1-\alpha})$, matching implies that

$$a_1 = -3/2. \tag{7.35}$$

To $\mathcal{O}(\mathcal{F}^{-2})$, we find that

$$-a_0\log(\tfrac{3}{4}) - \gamma a_0 - a_0\log(\rho) - a_0(\alpha-1)\log(\mathcal{F}) + \tfrac{a_1}{2} = B_0 - \tfrac{3}{2}\alpha\log(\mathcal{F}) - \tfrac{3}{2}\log(\rho). \tag{7.36}$$

Comparing $\log\rho$ terms and constant terms, we obtain

$$a_0 = \frac{3}{2}, \quad B_0 = -\frac{3}{2}\log\left(\frac{3}{4\mathcal{F}}\right) - \frac{3\gamma}{2} - \frac{3}{4}, \tag{7.37}$$

respectively. The inner and outer expansions are now fully determined up to order $\mathcal{F}^{-2}$. The outer expansion is

$$h = 1 + (3/2)\mathcal{F}^{-2}\left[K_0\left(3\hat{r}/2\right) - \cos\theta K_1\left(3\hat{r}/2\right)\right]e^{(3\hat{r}\cos\theta)/2}. \tag{7.38}$$

The inner expansion is

$$h = 1 - \frac{\cos(\theta)}{\mathcal{F}r} - \frac{3}{4\mathcal{F}^2}\left[2\log\left(\frac{3r}{4\mathcal{F}}\right) + 2\gamma + 2\cos^2(\theta) + r^{-2}\right]. \tag{7.39}$$

We use (7.39) to evaluate the flow depth attained on the cylinder ($r = 1$) at the upstream stagnation point ($\theta = \pi$) and the downstream point ($\theta = 0$), which give the maximum and minimum perturbations to the depth of the flow, respectively, in the regime $\mathcal{F} \gg 1$,

$$h_{\max} = h(1,\pi) = 1 + \frac{1}{\mathcal{F}} - \frac{3}{4\mathcal{F}^2}\left[2\log\left(\frac{3}{4\mathcal{F}}\right) + 2\gamma + 3\right] \tag{7.40}$$

$$h_{\min} = h(1,0) = 1 - \frac{1}{\mathcal{F}} - \frac{3}{4\mathcal{F}^2}\left[2\log\left(\frac{3}{4\mathcal{F}}\right) + 2\gamma + 3\right]. \tag{7.41}$$

In figure 7.3, we compare these predictions with the maximum and minimum flow thicknesses from the numerical solution of the governing equation (7.5). There is excellent agreement in the regime $\mathcal{F} \gg 1$.

We have obtained the asymptotic approximations for the flow depth in the inner region in which r is order 1 (equation 7.39) and the outer region in which r is order $\mathcal{F}$ (equation 7.38). By adding these approximations and subtracting the common terms in the matching region, we can obtain the following composite expansion

$$h_{\text{com}} = 1 - 3\mathcal{F}^{-2}/(4r^2) + (3/2)\mathcal{F}^{-2}\left\{K_0\left[3r/(2\mathcal{F})\right] - \cos\theta K_1\left[3r/(2\mathcal{F})\right]\right\}e^{(3r\cos\theta)/(2\mathcal{F})}, \tag{7.42}$$

which is an excellent approximation for all r (see figure 7.4). The composite asymptotic solution accurately captures the numerical results.

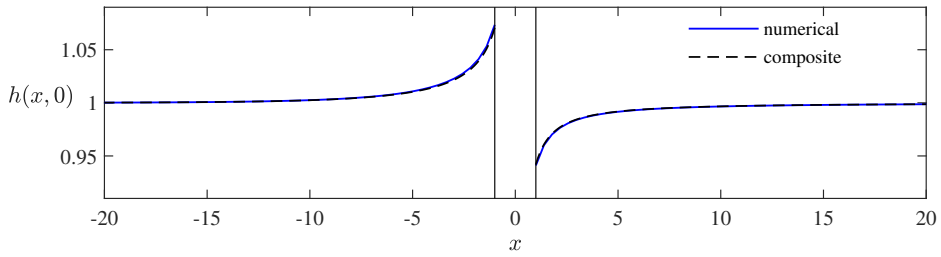

(a) The depth of fluid along the centreline.

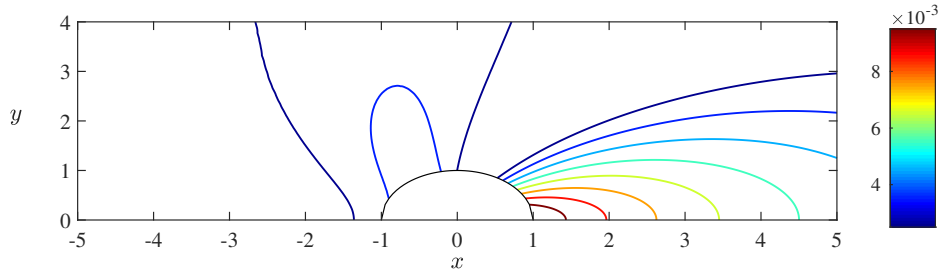

(b) Contours of the absolute error.

Fig. 7.4 Comparison between the composite expansion (7.42) and the numerical results for $\mathcal{F} = 15$. (a) The depth of fluid along the centreline of the steady flow past a cylinder as a function of the downstream distance, x, for $\mathcal{F} = 15$. The composite expansion (7.42) shows excellent agreement with our numerical simulations. (b) Contours of the absolute difference between the numerical result and the composite expansion for the flow thickness. The error does not exceed 1.1% of the upstream flow depth.

The approximations found in this section are effective (and show good agreement with the numerical results) provided that $\mathcal{F} \gtrapprox 5$ (see figure 7.3).

7.4.3 Force exerted on the cylinder

In many practical applications, it is important to estimate the force exerted by the flow on the cylinder. We use our asymptotic approximations to calculate this force in the regime $\mathcal{F} \gg 1$. The force consists of a hydrostatic component arising from the pressure and a dynamic component associated with gradients in the flow velocity. The lubrication model neglects the no-slip boundary condition on the cylinder wall and so our predictions for the flow velocity near $r = 1$ will not be correct. We therefore ignore the dynamic component and calculate the dimensional force owing to the pressure,

$$\int_0^{2\pi} \int_0^{H(L,\theta)} -P\cos\theta L \,\mathrm{d}\theta \,\mathrm{d}Z, \tag{7.43}$$

where P is the dimensional hydrostatic pressure at the cylinder boundary, $P = \Delta\rho g H_\infty \cos\beta\,(h - z)$, from which we obtain

$$\int_0^{2\pi} \int_0^{H} -P\cos\theta L \,\mathrm{d}\theta \,\mathrm{d}Z = \pi \mathcal{F}^{-1} \Delta\rho g H_\infty^2 L \cos\beta, \tag{7.44}$$

to leading order, where we have used the inner expansion (7.39) for the flow depth.

7.5 Flows past wide circular cylinders ($\mathcal{F} \ll 1$)

In this section, we study the regime $\mathcal{F} \ll 1$, corresponding to a steep slope relative to the ratio of the far upstream depth to the cylinder radius. Figure 7.2c, a contour plot of the numerical results for $\mathcal{F} = 0.025$, illustrates that in this regime of flow past a relatively wide cylinder, dry zones in which there is no fluid occur downstream of the cylinder. Figure 7.2c also illustrates how the flow accumulates in a small but deep region upstream of the cylinder, within which the flow depth is considerably enhanced as a result of its deflection. For the case plotted in figure 7.2c, the maximum flow depth is 3.57 when $\mathcal{F} = 0.025$. We apply asymptotic methods to interpret the structure of the flow in the deep upstream region. We introduce an inner asymptotic region close to $r = 1$, writing

$$r = 1 + \mathcal{F}^a s \qquad \text{and} \qquad h = \mathcal{F}^b \mathscr{H}. \tag{7.45}$$

We balance the leading order terms in the governing equation (7.5); $\cos\theta\partial h^3/\partial r \sim \mathcal{F}\partial^2 h^4/\partial r^2$, which leads to the requirement that

$$b = a - 1. \tag{7.46}$$

The governing equation in the inner region can be written in terms of s and $\mathscr{H}$ as

$$\cos\theta\frac{\partial \mathscr{H}^3}{\partial s} - \frac{\mathcal{F}^a \sin\theta}{1+\mathcal{F}^a s}\frac{\partial \mathscr{H}^3}{\partial \theta} = \frac{1}{4}\left[\frac{\partial^2 \mathscr{H}^4}{\partial s^2} + \frac{\mathcal{F}^a}{1+\mathcal{F}^a s}\frac{\partial \mathscr{H}^4}{\partial s} + \frac{\mathcal{F}^{2a}}{(1+\mathcal{F}^a s)^2}\frac{\partial^2 \mathscr{H}^4}{\partial \theta^2}\right]. \tag{7.47}$$

The boundary condition (7.8) at the edge of the cylinder ($s = 0$) is

$$\cos\theta - \frac{\partial \mathscr{H}}{\partial s} = 0 \quad \text{or} \quad \mathscr{H} = 0. \tag{7.48}$$

The form of equation (7.47) suggests the following expansion for $\mathscr{H}$,

$$\mathscr{H} = \mathscr{H}_0 + \mathcal{F}^a \mathscr{H}_1 + \ldots \tag{7.49}$$

To leading order, we obtain

$$\cos\theta\frac{\partial \mathscr{H}_0^3}{\partial s} = \frac{1}{4}\frac{\partial^2 \mathscr{H}_0^4}{\partial s^2}. \tag{7.50}$$

Integrating twice and applying the boundary condition (7.48), we obtain the linear profile

$$\mathscr{H}_0 = s\cos\theta + G(\theta), \tag{7.51}$$

where $G(\theta)$ is an arbitrary function, which is to be determined. Equation (7.51) implies that to leading order the flow depth is horizontal, forming a 'pond' upstream of the cylinder. It has previously been shown that a pond of viscous fluid develops upstream of a mound of sufficient amplitude (chapter 6) and upstream of an injection source [see figure 3 of Ref 101].

The governing equation (7.47) to $\mathscr{O}(\mathcal{F}^a)$ is

$$\cos\theta\frac{\partial}{\partial s}\left(3\mathscr{H}_0^2\mathscr{H}_1\right) - \sin\theta\frac{\partial \mathscr{H}_0^3}{\partial \theta} = \frac{1}{4}\frac{\partial}{\partial s}\left(\mathscr{H}_0^4\right) + \frac{\partial^2}{\partial s^2}\left(\mathscr{H}_0^3\mathscr{H}_1\right) \tag{7.52}$$

with boundary condition $\partial\mathscr{H}_1/\partial s = 0$ at $s = 0$. The solution, in terms of $\mathscr{H}_0$, is

$$\mathscr{H}_1 = k_{-2}(\theta)\mathscr{H}_0^{-2} + k_0(\theta) + k_1(\theta)\mathscr{H}_0 + k_2(\theta)\mathscr{H}_0^2, \tag{7.53}$$

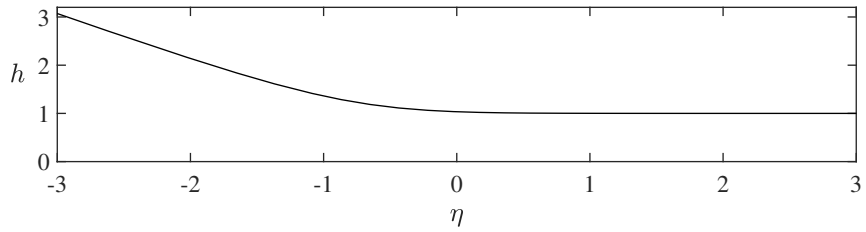

Fig. 7.5 Flow depth in the interior region of our asymptotic analysis, according to equation (7.62).

where $k_0(\theta)$ is an arbitrary function arising from integration and

$$k_{-2}(\theta) = -\frac{1}{8\cos\theta}\frac{\mathrm{d}}{\mathrm{d}\theta}\left(G^4\tan\theta\right), \tag{7.54}$$

$$k_1(\theta) = -\frac{G\tan^2\theta + G'\tan\theta}{\cos\theta}, \tag{7.55}$$

$$k_2(\theta) = \frac{3\tan^2\theta - 1}{8\cos\theta}. \tag{7.56}$$

When $\mathscr{H}_0$ vanishes, the series becomes non-asymptotic. We denote this location as

$$s = s_*(\theta) = \frac{-G(\theta)}{\cos\theta}. \tag{7.57}$$

Also, the leading order behaviour for the depth (7.51) does not satisfy the boundary condition $h \to 1$ as $r \to \infty$. Hence, near s_*, we must introduce an interior region in order to match the inner expansion to a far-field expansion in which $h \to 1$. To capture the behaviour in this region, we write

$$s = s_* + \mathcal{F}^c\eta, \tag{7.58}$$

where c is another exponent to be determined.

The behaviour of the leading order function near the interior region is $\mathscr{H}_0 = \mathcal{F}^c\eta\cos\theta$ and for $|s - s^*| \ll 1$,

$$\mathscr{H}_1 \sim k_{-2}(\theta)\mathscr{H}_0^{-2} = \frac{k_{-2}(\theta)}{\mathcal{F}^{2c}\eta^2\cos^2\theta}. \tag{7.59}$$

In the interior region, the first two terms in the expansion for the depth are

$$h = \mathcal{F}^b\mathscr{H}_0 + \mathcal{F}^{b+a}\mathscr{H}_1 = \mathcal{F}^{b+c}\eta\cos\theta + \mathcal{F}^{b+a-2c}k_{-2}(\theta)/(\eta\cos\theta)^2 + \ldots \tag{7.60}$$

and this must be the behaviour as $\eta \to -\infty$. Conversely as $\eta \to \infty$, we must find that $h \to 1$. Thus we can determine that $b + c = 0$ and $b + a - 2c = 0$. By combining these conditions

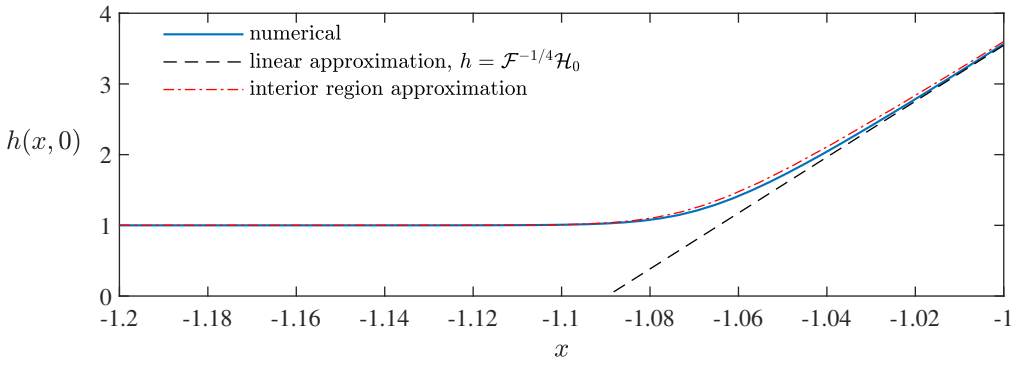

Fig. 7.6 Depth along the centreline for the steady flow past a cylinder as a function of distance, x, with $\mathcal{F} = 0.025$. The depth from our numerical simulations (solid blue line) is compared to the 'inner' approximation (black dashed line, equation 7.70), which varies linearly with x, and is very close to the 'interior' approximation (red dot-dashed line), the solution to equation (7.62), which is plotted in figure 7.5.

with equation (7.46), we obtain the exponents,

$$a = 3/4, \qquad b = -1/4, \qquad c = 1/4. \tag{7.61}$$

The leading order governing partial differential equation in the interior region is

$$\cos\theta \frac{\partial h^3}{\partial \eta} = \frac{1}{4}\frac{\partial^2 h^4}{\partial \eta^2}, \tag{7.62}$$

with boundary conditions

$$h \to 1 \quad \text{as} \quad \eta \to \infty. \tag{7.63}$$

$$h \to \eta\cos\theta + \frac{k_{-2}(\theta)}{\eta^2\cos^2\theta} \quad \text{as} \quad \eta \to -\infty. \tag{7.64}$$

We integrate the interior governing equation (7.62) to obtain

$$\cos\theta(h^3 - 1) = h^3\frac{\partial h}{\partial \eta}, \tag{7.65}$$

where we have used the condition (7.63). We calculated the solution to equation (7.65), with boundary condition (7.64), numerically and it is shown in figure 7.5. As $\eta \to -\infty$, $h \to \eta\cos\theta$, which leads to

$$\frac{\partial h}{\partial \eta} = \cos\theta\left(1 - h^{-3}\right) \sim \cos\theta\left[1 - (\eta\cos\theta)^{-3}\right] \tag{7.66}$$

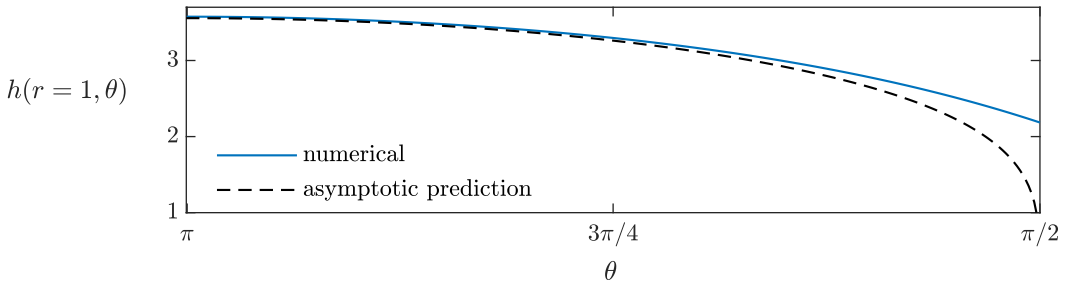

Fig. 7.7 Flow thickness on the upstream cylinder boundary, $h(1,\theta)$, as a function of polar angle θ for $\mathcal{F}=0.025$. The numerically calculated flow thickness (solid curve) is compared to the asymptotic approximation, $h(1,\theta)=\mathcal{F}^{-1/4}G(\theta)$, equation (7.72) (dashed curve).

as $\eta\to-\infty$. We can compare this to (7.64) to obtain

$$k_{-2}(\theta)=1/2. \tag{7.67}$$

Then (7.54) provides a differential equation for $G(\theta)$, which upon integrating becomes

$$G^4\tan\theta=-4\sin\theta+K. \tag{7.68}$$

The function $G(\theta)$ is bounded at $\theta=\pi$ so $K=0$. The solution is

$$G=(-4\cos\theta)^{1/4}, \tag{7.69}$$

for $\pi/2<\theta<3\pi/2$. Note that $G(\pi)=\sqrt{2}$ and $G(\pi/2)=0$. Upstream of the cylinder, near $r=1$, the depth to leading order varies linearly with radial distance, given by

$$h=\mathcal{F}^{-1/4}\mathscr{H}_0=2^{1/2}\mathcal{F}^{-1/4}(-\cos\theta)^{1/4}+\mathcal{F}^{-1}\cos\theta(r-1), \tag{7.70}$$

which we compare to the numerical results along the line of symmetry (the $x<0$ axis along which $\theta=\pi$) in figure 7.6. We also plot the interior approximation, given by the solution to equation (7.65), as a red dot-dashed line. The asymptotic approximations accurately capture the behaviour.

To leading order, the free surface is horizontal in a region of lengthscale $\mathcal{F}^{3/4}$ upstream of the cylinder and there is a pond of nearly stationary fluid there. Correspondingly, the radial velocity (7.6) is zero to leading order in this region, whilst the azimuthal velocity is (7.7)

$$u_\theta=\frac{3}{2}z(2h-z)\big[-r^{-1}\sin\theta+\mathscr{O}(\mathcal{F}^{3/4})\big]. \tag{7.71}$$

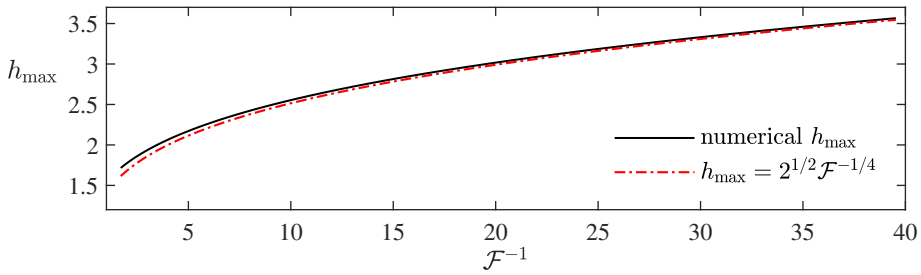

Fig. 7.8 The maximum depth, for steady flow past a cylinder as a function of $\mathcal{F}^{-1}$. The deepest point is always at the stagnation point on the upstream boundary at $\theta = \pi$. The results from our numerical technique (solid black line) compare very closely to the leading order prediction of equation (7.72) and there is particularly good agreement for $\mathcal{F} \ll 1$.

On the boundary of the cylinder ($r = 1$) we find that the flow thickness is

$$h = \mathcal{F}^{-1/4} G(\theta), \tag{7.72}$$

which is compared to the numerical results in figure 7.7. We note that there is very good agreement between the numerical and asymptotic result close to the upstream stagnation point ($\theta = \pi$), but as the edge of the cylinder is approached ($\theta = \pi/2$), the agreement declines, indicating that a different asymptotic balance arises in that zone (see subsection 7.5.1).

The maximum flow thickness is attained at the upstream stagnation point, $(r, \theta) = (1, \pi)$, and is given by

$$h_{\max} = \mathcal{F}^{-1/4} 2^{1/2} \tag{7.73}$$

This leading order prediction for the maximum flow thickness shows good agreement with the numerical results for $\mathcal{F} \ll 1$ (see figure 7.8).

To obtain the second order term in the maximum flow depth,

$$h_{\max} = \mathcal{F}^{-1/4} \mathscr{H}_0(s = 0, \theta = \pi) + \mathcal{F}^{1/2} \mathscr{H}_1(s = 0, \theta = \pi) + \ldots \tag{7.74}$$

requires determining $k_0(\pi)$ (see equation 7.53). This is achieved by matching at higher order in the interior region and we provide details in appendix A. We obtain $k_0(\pi) = -17/40$ and the improved approximation for the maximum flow depth is

$$h_{\max} = \mathcal{F}^{-1/4} 2^{1/2} + \mathcal{F}^{1/2}(3/40) + \ldots \tag{7.75}$$

In figure 7.9, we compare this improved approximation with the numerical results and include the asymptotic predictions for the maximum flow depth from §7.4 (for $\mathcal{F} \gg 1$). The

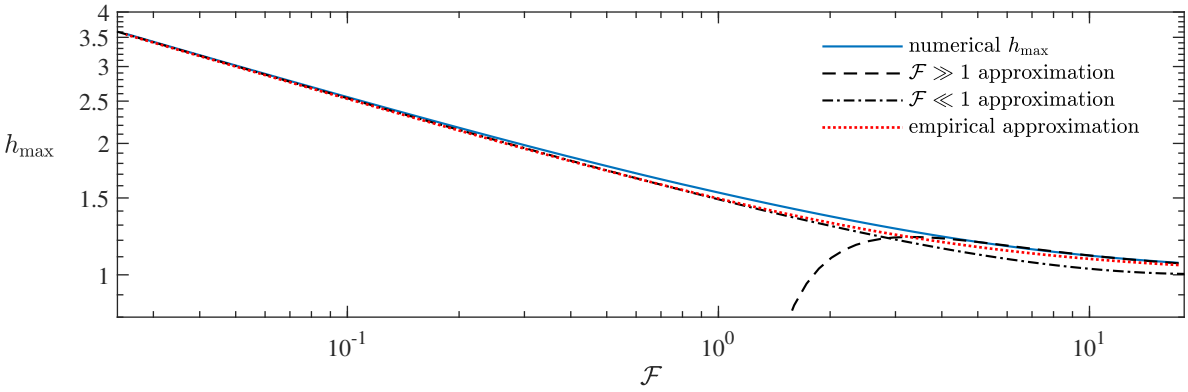

Fig. 7.9 The maximum thickness for steady flow past a cylinder as a function of $\mathcal{F}$. The numerical results are compared to our asymptotic predictions for the two regimes; $\mathcal{F} \ll 1$ (equation 7.75) and $\mathcal{F} \gg 1$ (equation 7.40). We also include our empirical approximation (7.76) as a dotted red line.

empirical expression

$$h_{\max} = \left(1 + 4\mathcal{F}^{-1}\right)^{1/4}, \tag{7.76}$$

agrees with the small $\mathcal{F}$ expansion (7.75) to leading order in the regime $\mathcal{F} \ll 1$ and agrees with the large $\mathcal{F}$ expansion (7.40) to order $\mathcal{F}^{-1}$ in the regime $\mathcal{F} \gg 1$. Indeed, the simple expression (7.76) accurately captures the behaviour of the maximum flow depth for all $\mathcal{F}$ (see figure 7.9). The error between (7.76) and the numerical results for the maximum depth never exceeds 3.5%.

7.5.1 The behaviour of the flow depth near $\theta = \pi/2$

The asymptotic expression for the depth of the fluid layer on the upslope side of the circular cylinder (7.70) loses its validity as $\theta \to \pi/2$. This corresponds to the widest cross-slope extent of the circular cylinder, and it is evident that the leading order asymptotic expression (in the regime $\mathcal{F} \ll 1$) is no longer an accurate representation of the dynamics (see figure 7.7, for example, close to $\theta = \pi/2$). Instead there is a new distinguished scaling for the depth of the fluid, and associated with it, a spatial region within which it applies, that matches onto the upslope form. We may construct these new scales by writing $\theta = \pi/2 + \hat{\phi}$ and $r = 1 + \hat{R}$ and analysing the balances and matching conditions when $\hat{\phi} \ll 1$ and $\hat{R} \ll 1$.

In the governing equation we require that advective terms in the radial and angular directions are of comparable magnitude. Therefore we balance $-\hat{\phi}\partial h^3/\partial \hat{R}$ with $\partial h^3/\partial \hat{\phi}$. For matching to the leading order expression upslope (7.70) and close to the stagnation point at $\theta = \pi$, we require that $h \to F^{-1/4}[-F^{-3/4}\hat{\phi}\hat{R} + (4\hat{\phi})^{1/4}]$ and the distinguished scaling

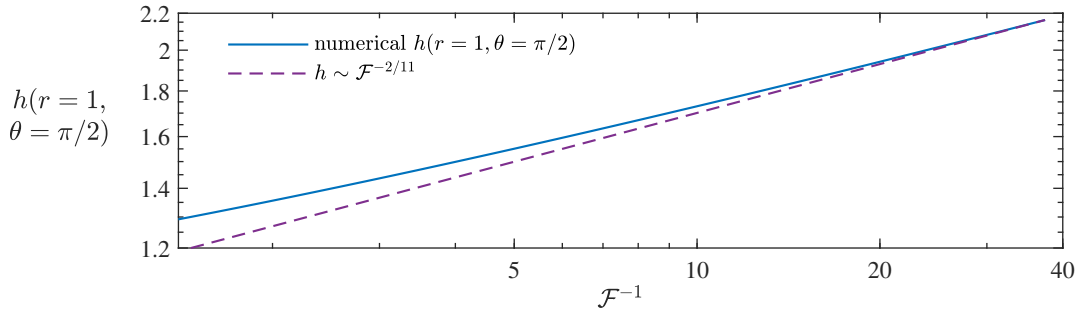

Fig. 7.10 The flow thickness at $(r,\theta) = (1,\pi/2)$ for steady flow past a cylinder as a function of $\mathcal{F}$. The numerical results follow the $h \sim \mathcal{F}^{-2/11}$ prediction from our asymptotic analysis for $\mathcal{F} \ll 1$ (see equation 7.77).

demands that both terms for this matching expression are the same order of magnitude. Thus in the region close to $\theta = \pi/2$, we deduce that

$$\hat{\phi} = \mathscr{O}\left(\mathcal{F}^{3/11}\right), \qquad \hat{R} = \mathscr{O}\left(\mathcal{F}^{6/11}\right) \qquad \text{and} \qquad h = \mathscr{O}\left(\mathcal{F}^{-2/11}\right). \tag{7.77}$$

We demonstrate the validity of this scaling by plotting $h(1,\pi/2)$ as a function of $\mathcal{F}$ in figure 7.10.

7.5.2 Force exerted on the cylinder

For the regime of a wide cylinder, $\mathcal{F} \ll 1$, we assume that $H_\infty/L \ll 1$ as well as $\mathcal{F} \ll 1$ so that the force on the cylinder is dominated by the hydrostatic pressure associated with the pond of liquid that builds upstream of the cylinder. Thus, to leading order, the dimensional normal stress is

$$\sigma_{RR}\cos\theta = -\Delta\rho g(H-Z)\cos\beta\cos\theta. \tag{7.78}$$

We integrate this over the upstream boundary of the cylinder and by considering symmetry about the centreline, we find the dimensional force exerted on the cylinder to be

$$2L\int_{\pi/2}^{\pi}\int_0^H \sigma_{RR}\cos\theta\,\mathrm{d}Z\,\mathrm{d}\theta = \mathcal{F}^{-1/2}\Delta\rho g H_\infty^2 L\cos\beta\int_{\pi/2}^{\pi} G(\theta)^2\cos\theta\,\mathrm{d}\theta \tag{7.79}$$

$$= 1.865\mathcal{F}^{-1/2}\Delta\rho g H_\infty^2 L\cos\beta. \tag{7.80}$$

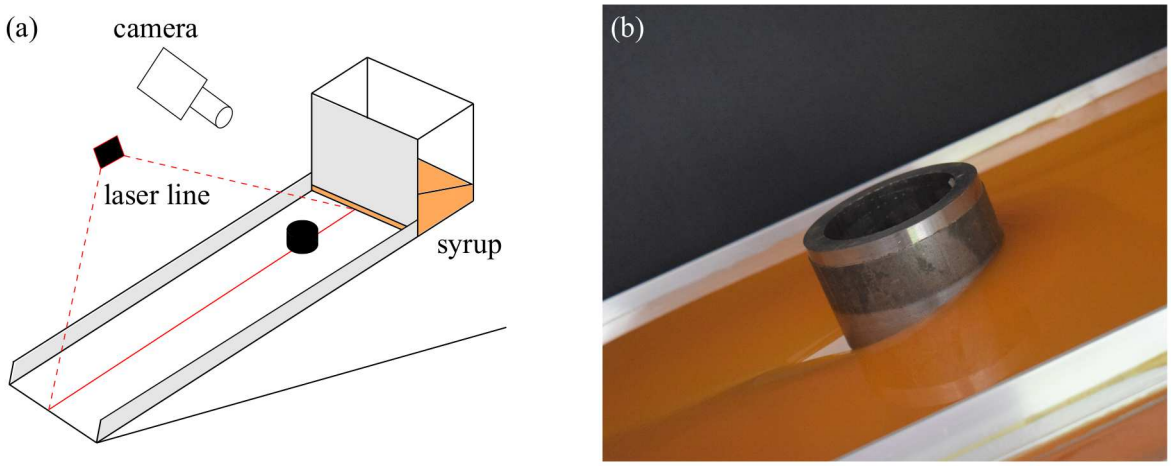

Fig. 7.11 (a) Schematic of the experimental setup. A constantly maintained head of syrup supplies constant flux. (b) Photograph of the steady syrup flow past the cylinder, illustrating the increase in flow depth upstream of the cylinder, the sharp decrease in flow depth around the cylinder and the dry region downstream.

7.6 Laboratory experiments

We carried out a series of laboratory experiments on an inclined slope of width 30cm and length 120cm in the downslope direction (see figure 7.11a). Golden syrup was released from a lock gate behind which a fixed depth of syrup was maintained by hand to provide a constant head. The downslope flow from a constant-flux line source evolved into a steady current with constant thickness, H_∞.

A cylinder was held fixed in the centre of the slope and we measured the flow thickness, H_∞, far upstream of the cylinder. After a sufficiently long period, the flow past the cylinder became steady. We observed that the far upstream, constant thickness flow is perturbed in a neighbourhood of the cylinder. The flow deepened upstream and became shallower downstream of the cylinder (see figure 7.11b).

The minimum and maximum thicknesses of the steady flow occur at the edge of the cylinder, at the most downstream and most upstream points respectively. We performed a series of experiments in which we varied the inclination of the plane, the radius of the cylinder and the source flux per unit width. We measured the far upstream, minimum and maximum thicknesses using a laser line following a technique that has previously been used for measuring the thickness of a free surface [70, 37] and a deformed elastic sheet [113, 7]. A laser line was directed onto black paper laid on the tank base and photographed. The image could then be compared to later images of the laser shining onto syrup flowing down the tank

Angle (degrees)	cylinder radius R (mm)	flow thickness H_∞ (mm)	parameter $\mathcal{F}$	experimental max. $h_{\max}$ (dimensionless)	experimental min. $h_{\min}$ (dimensionless)
5.0	24	15	7.14	1.2	0.85
3.5	48	13.2	4.50	1.72	0.61
5.0	24	7.9	3.76	1.28	0.77
3.5	48	9.8	3.34	1.22	0.57
10.0	24	7.4	1.75	1.38	0.53
14.6	24	8.5	1.36	1.63	0.43
13.0	24	5.5	0.99	1.7	0
14.6	24	6	0.96	1.71	0.38
15.0	24	6	0.93	1.56	0.32
10.0	40.5	6.5	0.91	1.61	0
20.0	24	7.9	0.90	1.64	0
20.0	40.5	11	0.75	1.68	0
23.1	40.5	12.1	0.70	1.64	0
23.1	40.5	8	0.47	1.76	0

Table 7.1 Experimental results of the minimum and maximum flow thicknesses.

to determine the flow thickness. The laser is directed to illuminate the centreline of the tank. This technique required the syrup to be opaque, which was achieved by adding a few drops of magnolia paint to the syrup. The mixture was tested in a rheometer to confirm that it was still Newtonian, with viscosity 89.6 ± 0.1 Pa s at room temperature. We note that the results presented below for the dimensionless flow depth, $h = H/H_\infty$, do not require knowledge of the viscosity of the fluid. We require only the flow depth $H(X,Y)$ and the far upstream flow depth H_∞ (which is dependent on the viscosity) to be measured, as well as the slope angle and cylinder radius. Thus, although changes in the laboratory temperature from experiment to experiment can have a strong effect on the viscosity of the syrup, they do not lead to errors in the experimental data for the dimensionless flow depth.

7.6.1 Results

Our results are shown in table 7.1. The minimum and maximum flow thicknesses are compared to our numerical results in figure 7.12. The flow thickness of the syrup along the centreline upstream of the cylinder determined using the laser line technique is compared to our numerical results in figure 7.13 for three values of $\mathcal{F}$. The flow thickness is obtained to a precision of 0.1 mm, which is associated with the resolution of the camera.

One major source of random error is variations in the depth of the reservoir of fluid behind the lock gate. The flux provided by the reservoir is proportional to the hydrostatic

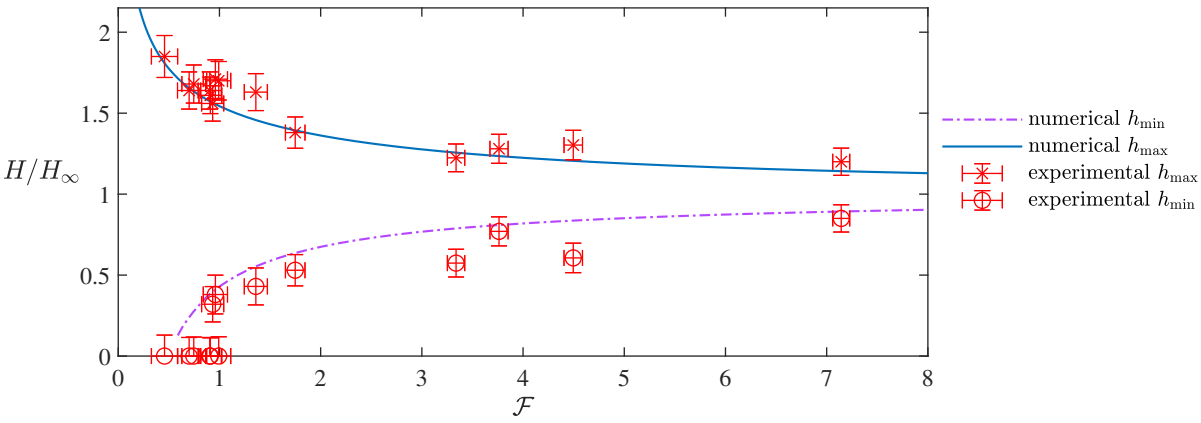

Fig. 7.12 Comparison of the experimental and theoretical results (calculated numerically) for the maximum and minimum flow thicknesses. Zero minimum flow thickness corresponds to a dry zone downstream of the cylinder in which there is no syrup.

head, which is $\rho g H_R$, where H_R is the reservoir depth. The flow thickness in the channel, H_∞ is proportional to the cube root of the delivered flux and hence $H_\infty \sim H_R^{1/3}$ (cf. equation 6.6). Time-lapse photography showed that the reservoir depth varied by up to 20% over a single experiment. This suggests that errors in the measured flow depth, $h = H/H_\infty$, and the flow parameter, $\mathcal{F} = H_\infty/(L\tan\beta)$, are up to approximately 7%.

In general the experiments showed a slightly larger increase in flow thickness upstream of the cylinder compared to the theory. This may be because the theory neglects the no-slip condition at the cylinder wall, which will slow the flow here and lead to an increased build-up of liquid upstream.

The small discrepancy could also be caused by surface tension, which was neglected in the model (see section 7.2). At room temperature, the density of the syrup is $1400\,\mathrm{kg\,m^{-3}}$ and we take its surface tension coefficient to be $\sigma = 0.08\mathrm{Nm}^{-1}$ [from Ref 102]. With these values, the capillary length and Bond number are

$$l_c = \sqrt{\frac{\sigma}{\Delta\rho g}} = 2.4\mathrm{mm}, \qquad Bo = \frac{\Delta\rho g L^2}{\sigma} = 280, \tag{7.81}$$

where we have used a streamwise lengthscale $L = 40\mathrm{mm}$, which is the radius of the larger cylinder used in the experiments. These values suggest that the influence of surface tension is negligible upstream of the cylinder, except perhaps in a region very close to the cylinder and the contact line if a dry region forms.

The numerical results predict that a dry region in which $h = 0$ occurs downstream of the cylinder only when $\mathcal{F} < 0.47$. However, the experimental results often have a dry region for

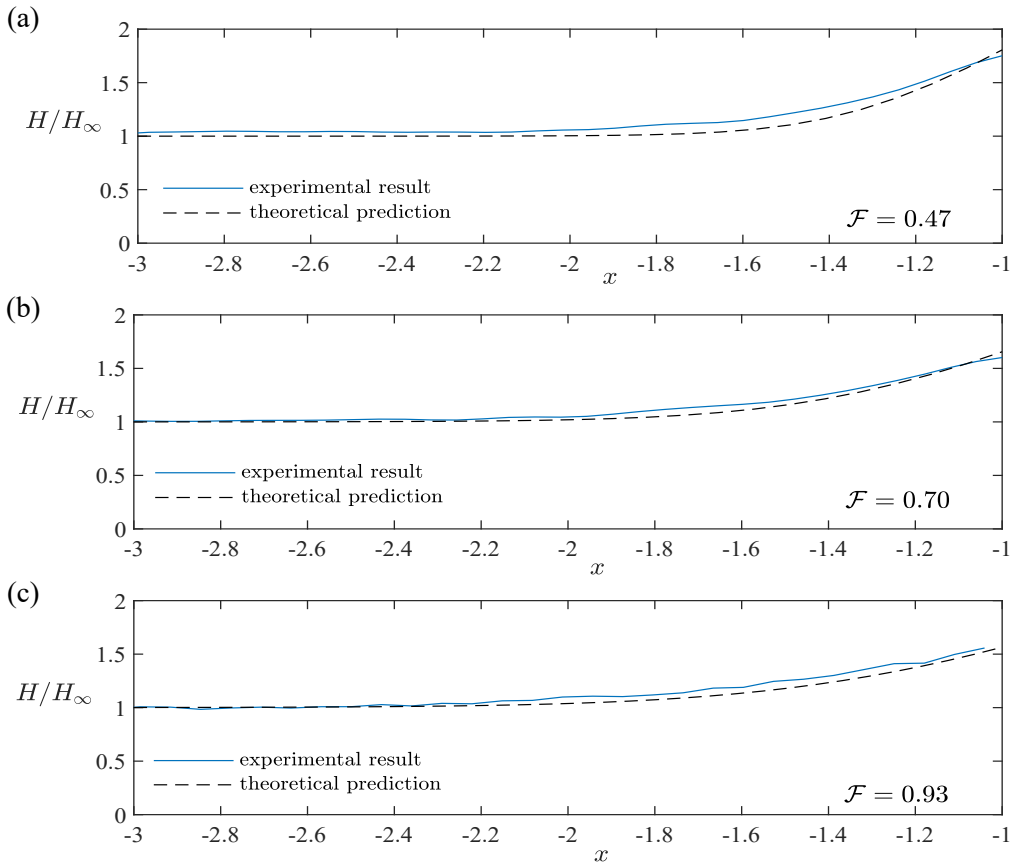

Fig. 7.13 Flow depth along the centreline as a function of dimensionless distance, x, upstream of the cylinder for three values of the flow parameter, $\mathcal{F}$. The experimental results (solid line) obtained from the laser line technique show very good agreement with our theoretical predictions (dashed lines), calculated using the numerical scheme described in section 7.3.

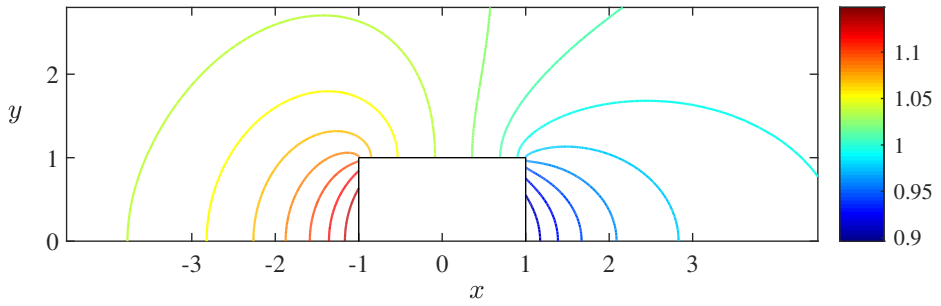

(a) $\mathcal{F} = 10$.

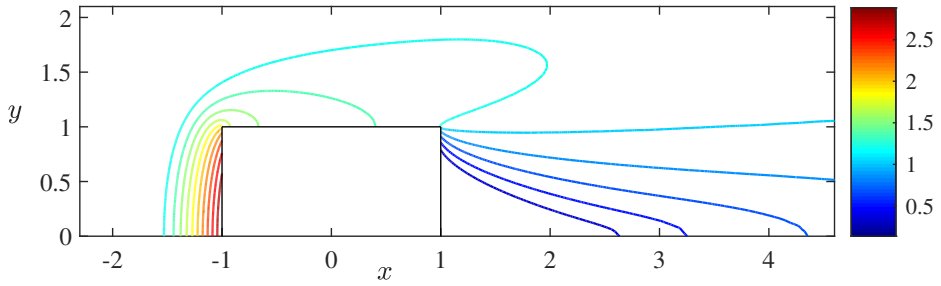

(b) $\mathcal{F} = 0.25$.

Fig. 7.14 Flow past a square with (a) $\mathcal{F} = 10$ and (b) $\mathcal{F} = 0.25$. The two panels have different axes to capture the region of interest. Note that the flow remains attached to the square in both cases and there is no dry region for these values of $\mathcal{F}$.

values of $\mathcal{F}$ larger than this (i.e. $h_{\min} = 0$; see figure 7.12). This discrepancy is most likely due to contact angle effects at the edge of the dry region. The associated force resists the spreading of the thin syrup film and this is not accounted for in the model. The difference may also be due to the no-slip condition being neglected, which resists syrup flowing around the downstream side of the cylinder. Alternatively, it may be a result of very slow temporal convergence to the steady state downstream of the cylinder and that the experimental runs had not fully attained their steady-state.

7.7 Flow past square cylinders

In this section, we analyse steady free-surface viscous flow past a square cylinder, of side length $2L$. The dimensionless governing equation is given by (7.2), while boundary conditions enforce $\mathbf{u} \cdot \mathbf{n} = 0$ on the surface of the square and $h \to 1$ as $|\mathbf{x}| \to \infty$. The square is centred on the origin and its upstream boundary is at $x = -1$ (see figure 7.14). We adapt our numerical technique for this geometry and in the case that there are dry regions downstream of the square, we add a small source on the downstream boundary at $x = 1$ (see section 7.3). Contour

plots of the numerical results for $\mathcal{F} = 10$ and $\mathcal{F} = 0.25$ are shown in figure 7.14. In the regime $\mathcal{F} \gg 1$, there is a small perturbation to the flow depth (figure 7.14a) and the behaviour is broadly similar to that for flow past a circular cylinder in the same regime. In particular the perturbation to the flow depth is approximately antisymmetric in $x = 0$. The behaviour in the regime of flow past a relatively wide cylinder of square cross-section ($\mathcal{F} \ll 1$) is however significantly different from the circular cylinders analysed in section 7.5 for different shaped cross-sections. Henceforth in the present section, we restrict our attention to the regime $\mathcal{F} \ll 1$.

In section 7.5, we quantified the increase in flow depth upstream of a wide circular cylinder ($\mathcal{F} \ll 1$) using asymptotic analysis. We found a ponded region in which the flow depth is horizontal. In the present section, we determine the leading order expressions for the depth and shape of the ponded region upstream of a square cylinder by balancing the volume flux in the pond rather than repeating the asymptotic analysis of §7.5, although such an expansion with 'inner', 'interior' and 'outer' regions may be constructed and is necessary to extend the results beyond their leading order form. Importantly, we find that the depth within the pond upstream of a square cylinder has a different scaling in its dependence on $\mathcal{F}$ from the case of a circular cylinder.

The no-flux condition at the upstream boundary is

$$1 - \mathcal{F}\frac{\partial h}{\partial x} = 0 \quad \text{at} \quad x = 0, \qquad \text{provided } h \neq 0. \tag{7.82}$$

We also require that the flow depth returns to its unperturbed value far from the square,

$$h \to 1 \quad \text{as} \quad x \to -\infty. \tag{7.83}$$

The liquid within the ponded region just upstream of the square has the following depth (cf. equation 7.51)

$$h_p = \mathcal{F}^{-1}(1 + x) + G_s(y), \tag{7.84}$$

where the prefactor, $\mathcal{F}^{-1}$ is chosen to satisfy the boundary condition at $x = -1$ (7.82) and $G_s(y)$ represents the flow depth on $x = -1$ and is to be determined. The edge of the pond, where the flow depth returns to order unity, is given by the solution to $h_p = 0$, which is

$$x_u(y) = -1 - \mathcal{F}G_s(y). \tag{7.85}$$

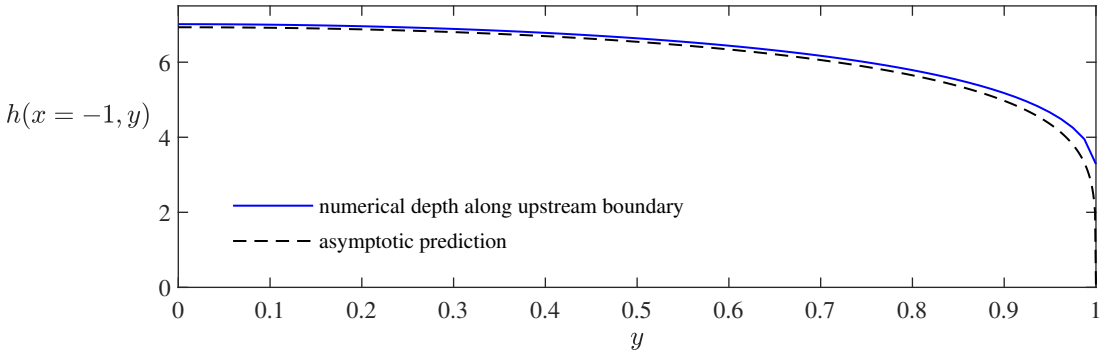

Fig. 7.15 Flow depth as a function of position along the upstream boundary of the rectangle for $\mathcal{F} = 0.025$. The asymptotic prediction is $h = \mathcal{F}^{-2/5}G(y)$ where the function $G(y)$ is given by equation (7.88).

The flux into the pond from upstream, between $y = 0$ and $y = \mathscr{Y}$, is simply $\mathscr{Y}$. The flux out of this region of the pond is the integral of the cross-slope flux from $x = x_u(\mathscr{Y})$ to $x = -1$ at $y = \mathscr{Y}$ (since there is no flux across $y = 0$). In steady state, we balance these fluxes, which yields

$$\mathscr{Y} = \int_{x=x_u(\mathscr{Y})}^{x=-1} -\mathcal{F}h_p^3 \frac{\partial h_p}{\partial y}\mathrm{d}x. \tag{7.86}$$

Then using $G_s'(0) = 0$, owing to symmetry, we obtain

$$G_s(y) = 10^{1/5}\mathcal{F}^{-2/5}(a_0 - y^2)^{1/5}, \tag{7.87}$$

where a_0 is a constant of integration. Near the cross-stream edge of the square (at $y = 1$, $x = -1$), the pond ends and the flow depth is no longer of order $\mathcal{F}^{-2/5}$. Thus we find $a_0 = 1$. The flow depth along the upstream wall at $x = -1$ is

$$h = \mathcal{F}^{-2/5}10^{1/5}(1 - y^2)^{1/5}. \tag{7.88}$$

Along the upstream wall, the numerically calculated flow thickness is compared to this asymptotic prediction (7.88) in figure 7.15. The asymptotic scaling for the flow depth in the pond is $h \sim \mathcal{F}^{-2/5}$ and the extent of the pond upstream is $x_u \sim \mathcal{F}^{3/5}$. Notably these are different from the circular cylinder (cf. 7.61).

The maximum depth occurs at $y = 0$, $x = -1$ and is

$$h_{\max} = 10^{1/5}\mathcal{F}^{-2/5}, \tag{7.89}$$

which shows good agreement with numerical results for small $\mathcal{F}$ (see figure 7.16).

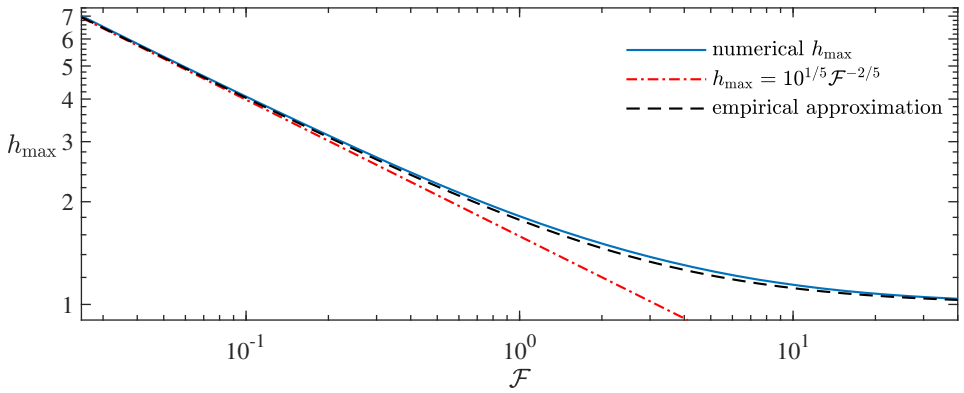

Fig. 7.16 Maximum thickness for flow past a square as a function of the dimensionless flow parameter, $\mathcal{F}$. The asymptotic prediction is $h_{\max} = 10^{1/5}\mathcal{F}^{-2/5}$, equation (7.89) and is accurate for $\mathcal{F} \ll 1$. The empirical approximation is quite accurate for all $\mathcal{F}$ and is given by equation (7.90).

The increase in flow depth upstream of the square (7.89) has a different scaling to that for a circular cylinder (7.73). The flow depth increases more significantly for a square because the wall is perpendicular to the oncoming flow. Also, the curvature at the upstream boundary of the square is zero whereas the curvature of a circle is finite. In the next section, we consider how the flow depth increases upstream of a wedge, which has infinite curvature at its upstream vertex.

For a circular cylinder, we obtained an empirical approximation (7.76) for the maximum flow depth, which was accurate for all $\mathcal{F}$. For a square cylinder, the expression

$$h_{\max} = \left(1 + 10^{1/2}\mathcal{F}^{-1}\right)^{2/5} \tag{7.90}$$

agrees to leading order with the small $\mathcal{F}$ approximation (7.89) in the regime $\mathcal{F} \ll 1$. Although we have not established the expansion for the depth in the regime $\mathcal{F} \gg 1$, the expression (7.90) provides an excellent approximation to the numerical results for all $\mathcal{F}$ as shown in figure 7.16. The error between the approximation (7.90) and the numerical results never exceeds 3.5%.

The results in this section pertain to the flow depth upstream of a square but the analysis is independent of the streamwise length of the square. Thus, the results apply more generally to rectangular cylinders.

Finally, we calculate the force exerted on the cylinder. We assume that the dominant contribution is from the weight of the liquid in the pond (as was the case for a circular

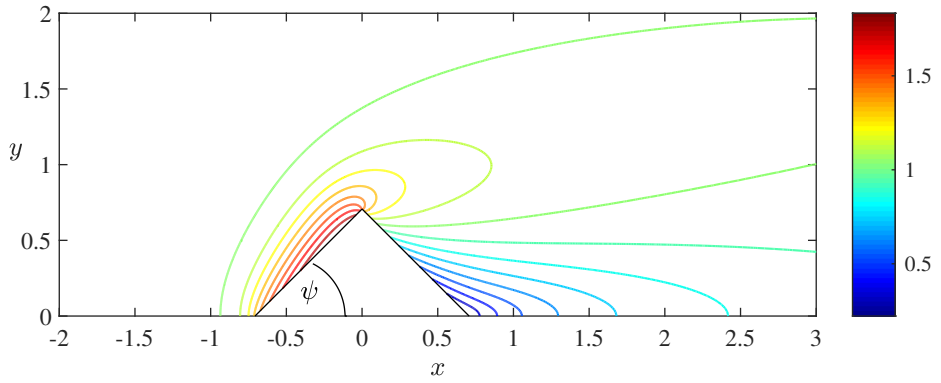

Fig. 7.17 Flow past a rhombus with $\mathcal{F} = 0.25$. The angle between the upstream boundary and the centreline is $\psi = \pi/4$. The rhombus sides have dimensionless length of unity. There is no dry region for $\mathcal{F} = 0.25$.

cylinder, see section 7.5.2). The force exerted is

$$2\int_0^L \int_0^H P\,\mathrm{d}Z\,\mathrm{d}Y = 2.05\mathcal{F}^{-4/5}\Delta\rho g H_\infty^2 L\cos\beta, \tag{7.91}$$

which is higher order with respect to $\mathcal{F}$ when compared to the force exerted on a circular cylinder [cf. equation (7.79)].

7.8 Flow past a wide wedge ($\mathcal{F} \ll 1$)

In this section, we consider steady free-surface viscous flow past a cylinder with rhombus cross section. Each side of the rhombus has length L. The dimensionless setup is shown in figure 7.17; the rhombus is centred at the origin and the angle between the upstream boundary and the centreline is denoted by ψ.

The dimensionless governing equation is as before (7.2). We adapt our numerical technique for this geometry and in the case that there are dry regions, we add a small source on the downstream boundary of the rhombus (see section 7.3). A contour plot of the numerical result for $\mathcal{F} = 0.25$ is shown in figure 7.17. We note that when $\mathcal{F} \ll 1$, the flow forms a relatively deep pond on the upstream boundary of the rhombus. However, unlike the previous cases, the maximum depth is not located at the furthest upstream position on the symmetry axis. Instead as shown in figures 7.17 and 7.18, the fluid depth increases with distance from the apex along the upstream boundary.

As in the previous section for flow past a square, we balance the flux in the pond region to quantify the increase in flow depth upstream of the obstruction in the case of a wide

obstruction, $\mathcal{F} \ll 1$. We do not consider the regime of a relatively narrow wedge ($\mathcal{F} \gg 1$) as it leads to a small perturbation in the flow depth and this was studied for a circular cylinder in section 7.4.

We begin by rotating the coordinates,

$$x' = (x + \cos\psi)\cos\psi + y\sin\psi,$$
$$y' = -x\sin\psi + y\cos\psi.$$

In the new coordinates, the upstream wall lies along $0 < x' < 1$, $y' = \cos\psi\sin\psi$ and the governing equation becomes

$$\cos\psi\frac{\partial h^3}{\partial x'} - \sin\psi\frac{\partial h^3}{\partial y'} = \mathcal{F}\left[\frac{\partial}{\partial x'}\left(h^3\frac{\partial h}{\partial x'}\right) + \frac{\partial}{\partial y'}\left(h^3\frac{\partial h}{\partial y'}\right)\right]. \tag{7.92}$$

The no-flux condition on the upstream wall is

$$\mathcal{F}\frac{\partial h}{\partial y'} + \sin\psi = 0 \quad \text{at} \quad y' = \cos\psi\sin\psi, \qquad \text{provided } h \neq 0. \tag{7.93}$$

We also require that the flow depth returns to its unperturbed value far from the obstacle,

$$h \to 1 \quad \text{as} \quad y' \to \infty. \tag{7.94}$$

There is a pond region near the upstream boundaries of the obstacle in which the depth is given by (cf. equation 7.84)

$$h_p = -\mathcal{F}^{-1}\sin\psi(y' - \cos\psi\sin\psi) + G_w(x'), \tag{7.95}$$

where the prefactor, $\mathcal{F}^{-1}$ is chosen to satisfy the boundary condition at $y' = \cos\psi\sin\psi$ and $G_w(x')$ represents the flow depth on the wall and is to be determined. The flux into the pond from upstream, between $x' = 0$ and $x' = \mathscr{X}$, is simply $\mathscr{X}\sin\psi$. The flux out of this region of the pond is the integral of the flux in the x' direction, which is $h_p^3\cos\psi$ to leading order, where the component associated with the diffusive slumping is neglected as it is lower order. In steady state, we balance these fluxes as in section 7.7 to obtain the function

$$G_w(x') = \mathcal{F}^{-1/4}\left(\frac{4x'\sin^2\psi}{\cos\psi}\right)^{1/4}. \tag{7.96}$$

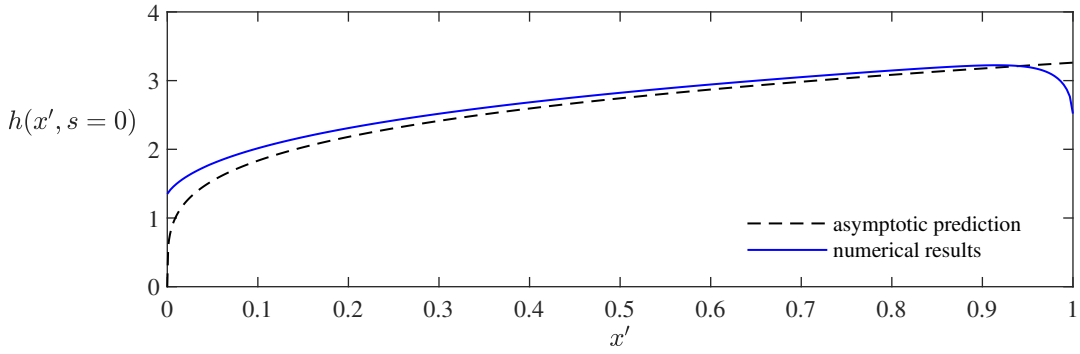

Fig. 7.18 Flow depth along the upstream wall of a rhombus for $\mathcal{F} = 0.025$ and $\psi = \pi/4$. The agreement between the numerical results and asymptotic prediction declines near $x' = 1$ as discussed in the text.

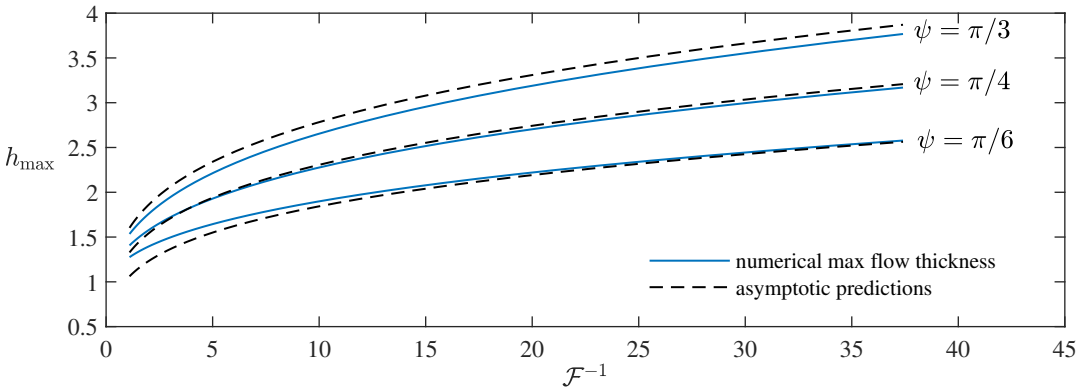

Fig. 7.19 Maximum flow depth as a function of the flow parameter, $\mathcal{F}$, for three wedge angles. The asymptotic prediction is given in equation (7.97).

The extent of the pond is order $\mathcal{F}^{3/4}$. Interestingly these scalings are identical to those found for a circular cylinder (7.61), but differ from the square cylinder. The difference is discussed further in the next section.

Along the wedge ($y' = \cos\psi \sin\psi$) we compare the numerically calculated flow thickness to the asymptotic result in figure 7.18 for $\psi = \pi/4$ and $\mathcal{F} = 0.025$. The agreement is good away from the edges of the wedge wall ($x' = 0$ and $x' = 1$). The asymptotic approximation is relatively poor near $x' = 1$ because it does not account for the diffusive slumping of liquid past this vertex. The size of this error increases with the angle ψ because more liquid accumulates near $x' = 1$.

From (7.95) and (7.96), the maximum depth is at the end of the wedge, $x' = 1$, $y' = \cos\psi \sin\psi$ and is

$$h_{\max} = \left(\frac{4\sin^2\psi}{\cos\psi}\right)^{1/4} \mathcal{F}^{-1/4}. \tag{7.97}$$

This shows good agreement with numerical results for small $\mathcal{F}$ and small ψ (see figure 7.19). The asymptotic approximation for the maximum thickness is not as good for blunter wedges (larger ψ) because the maximum thickness occurs further from $x' = 1$ owing to the importance of the diffusive slumping and advective terms at $x' = 1$ discussed earlier (see figure 7.18). Also, in the limit $\psi \to \pi/2$, the upstream wall is perpendicular to the oncoming flow and the flow depth scaling changes to $h \sim \mathcal{F}^{-2/5}$ (see section 7.7).

It is straightforward to repeat the calculation for the force exerted by the hydrostatic pressure on the obstruction from the previous cases of flow past a wide circular and square cylinder (equations 7.79 and 7.91). We obtain the force to be

$$(4/3)\frac{\sin\psi}{(\cos\psi)^{1/2}}\mathcal{F}^{-1/2}\Delta\rho g H_\infty^2 L\cos\beta. \tag{7.98}$$

7.9 Discussion and conclusion

We have studied the deflection of a steady free-surface viscous flow on an inclined plane by a cylinder oriented perpendicular to the plane. The flow depth is typically increased upstream of a circular or square cylinder with the maximum flow depth occurring on the cylinder boundary at the upstream stagnation point, $\theta = \pi$. There is a decrease in flow depth downstream of the cylinder and the minimum flow depth occurs on the cylinder boundary at $\theta = 0$.

The magnitude of the perturbation to the flow depth is dependent upon a single dimensionless parameter, $\mathcal{F} = H_\infty/(L\tan\beta)$, which is the upstream flow depth divided by the product of the cylinder radius and the slope gradient (for non-circular cross-sections, L is a representative lengthscale). For large $\mathcal{F}$, the perturbation is small. When $\mathcal{F} \ll 1$, however, the flow depth increases significantly upstream of the cylinder and dry regions in which there is no liquid occur downstream of the cylinder. We have also identified that the relatively deep region upstream of the cylinder is a pond of liquid with a horizontal free surface and the liquid is nearly stationary there. We have presented a numerical method that accurately determines the steady flow thickness past cylinders for a variety of cross-sections and a wide range of values of $\mathcal{F}$. The results demonstrate that the perturbation to the flow thickness is approximately antisymmetric about $x = 0$ in the case of relatively narrow obstructions ($\mathcal{F} \gg 1$). For much wider obstructions ($\mathcal{F} \ll 1$), the numerical method enables the shape of the downstream dry region to be determined and illustrates the ponding upstream of the cylinder.

In the case of a circular cylinder, we have employed asymptotic analysis to exposit the behaviour of the flow in the regimes of wide ($\mathcal{F} \ll 1$) and narrow ($\mathcal{F} \gg 1$) obstructions. For a narrow cylinder, we have obtained a composite asymptotic approximation for the depth, which is accurate everywhere. For wide cylinders, we have quantified the significant increase in depth upstream of the cylinder in the ponded region. We have also found a simple empirical expression, $h_{\max} = (1 + 4\mathcal{F}^{-1})^{1/4}$, which provides an excellent approximation for the maximum flow depth for any value of $\mathcal{F}$.

We have extended the flow analysis to wide cylinders with square and wedge-shaped cross-section, which also have upstream ponds. The scaling for the flow depth upstream of a square cylinder is larger than for wedge and circular cylinders. The difference between the scaling for the flow depth is associated with the curvature of the upstream boundary of the obstruction. In the case of positive curvature on the upstream boundary (e.g. a wedge or circle), the flux into the pond is balanced by the a component of gravity in the downslope direction. In the case of vanishing curvature (e.g. a square), there is no downslope flow out of the pond and the flux into the pond is balanced by the flux acting in the cross-slope direction associated with gradients of hydrostatic pressure. This flux is much smaller, for a fixed value of the flow depth, than the downslope flux in the regime of small $\mathcal{F}$ and so the pond has a greater depth. We have also shown that for a wedge-shaped obstruction, the maximum flow depth occurs along the upstream wedge wall away from the stagnation point, in contrast to the square and circular cylinders. In the case of negative curvature (i.e. a concave obstruction), the scaling for the depth will be the same as the square cylinder because the oncoming flux is balanced by the cross-slope flux in the pond.

We also report new laboratory experiments with circular cylinders for a variety of slope angles, cylinder radii and oncoming flow thicknesses. The minimum and maximum thickness and the thickness along the centreline of the steady flow have been obtained with a laser line. The results show very good agreement with our theoretical predictions and confirm the existence of dry regions downstream of wider obstructions.

This chapter was motivated by the need to inform the design of large-scale barriers that divert lava flows. The regime of a wide obstruction pertains to this context. The dry regions that occur downstream of obstructions provide safe zones for people, infrastructure and homes. However, barrier construction should also consider that the obstruction must be higher than the flow and able to withstand the force arising from the lava.

We have applied our asymptotic analysis to obtain approximations of the maximum flow depth on obstructions and demonstrated how this depends on the oncoming flow depth and the shape of the obstruction. We have also calculated the force exerted on an obstruction

by the pond of liquid upstream. For example, although a square obstruction may have a much larger dry region (thus protecting a greater area) than a circular obstruction, the square obstruction must be higher because it leads to a stronger increase in flow depth upstream. The square obstruction must also be able to withstand a much greater force.

Chapter 8

Conclusion

In this section, we discuss conclusions from this thesis in §8.1 and important further work in §8.2

8.1 Conclusions

We have analysed the injection of buoyant fluid into a confined aquifer in which the permeability varies vertically. We have derived a model for the evolution of the interface between the two fluids for a general permeability structure. The model was integrated numerically, which demonstrated that at late times the role buoyancy plays is negligible and the interface evolves in a self-similar fashion with the extent growing in proportion to time. The combination of a viscosity contrast between the injected and ambient fluids and a cross-aquifer permeability variation leads to regimes in which the interface consists of both growing regions and fixed regions. This type of interface does not occur in a uniform porous medium. We have delineated the different regimes in the case of a linear permeability structure. Our parameter space shows that the classic solution for equally viscous fluids in a uniform aquifer in which the interface advances with constant velocity and extends with length proportional to $t^{1/2}$ is singular and unstable to small changes in the permeability profile. Applying our results to the problem of carbon storage, we have shown that cross-aquifer permeability differences can significantly influence the volume of CO_2 that can be stored in an aquifer. In particular, it is preferable to store CO_2 in aquifers in which the permeability decreases towards the top because the viscous finger at the top of the aquifer is suppressed and the plume is more localised thus accessing a higher fraction of the pore space.

We have shown that the migration of tracer within these currents is complex even when the aquifer is vertically uniform and molecular diffusion and pore-scale dispersion are neglected.

If the nose region grows in time then tracer migrates into continually thinner regions in a uniform aquifer because the growing nose is continually supplied by fluid from upstream. When the formation has a vertical gradient of permeability, we have found three regimes for the evolution of the tracer in a growing nose; the tracer can continue to migrate into progressively shallower regions of the nose indefinitely; the tracer can enter the nose, and then circulate through the nose, so that it then reverses relative to the interface and drops out of the nose; finally, tracer may converge to a region within the nose. We have found parameter values which delineate these different regimes and explored the transitions between them. The combination of a shear flow and a fixed-shape, shock-like interface also leads to novel results. Fluid in the high permeability regions travels faster than the interface, this fluid enters the nose and subsequently migrates out of the nose via the low permeability region. The longitudinal extent of the tracer then grows in proportion to t, rather than $\sqrt{t}$ which would be expected if small-scale dispersion or diffusion dominated.

At later times, or in thinner aquifers, molecular diffusion acts to vertically homogenise the tracer distribution as it is sheared. This leads to an enhanced longitudinal rate of dispersion and the lateral extent grows in proportion to $\sqrt{t}$ [137]. Prior to interacting with the nose, tracer spreads symmetrically with its concentration distribution evolving as a Gaussian. A fixed nose acts as a no-flux boundary to the tracer migration. The distribution transitions to a half-Gaussian with the maximum concentration at the nose of the current. The initial release of tracer may not be vertically uniform but instead the concentration released at each height may be proportional to the permeability there. This alters the results because there is a transition, prior to the vertical homogenisation, in which the tracer migrates ahead of the mean flow since more tracer is released in higher permeability regions. In the context of subsurface flows, the migration of tracer is controlled by advection in thicker layers whilst shear-dispersion is the dominant mechanism in thinner layers. The difference is important for accurately interpreting the results of tracer tests (see section 8.2).

The dispersion of tracer within a growing nose in the case that diffusion is important is more complex still because of the many dispersive processes. The growth of the nose leads to squashing and stretching of the fluid and we have shown that this causes the extent of a pulse of tracer to grow in proportion to $t^{1/2}$. Diffusion acts at the same rate and dilutes the tracer into the surrounding fluid, which is subsequently stretched by the flow. The combination of the diffusion and advection (stretching) within the nose leads to an anomolous rate of dispersion with the tracer extent growing in proportion to $(t \log t)^{1/2}$. In the case that the aquifer is not uniform, the tracer is sheared prior to entering the nose. Taylor dispersion may also be important at intermediate times but its influence diminishes as tracer migrates

into thin regions. However, the early-time shearing leads to a longer tracer extent when the stretching of the nose dominates the dispersion. Thus the stretching pulse has a larger extent at late times in heterogeneous layers, even though tracer has migrated into thin regions where it samples only a fraction of the permeability contrast. These results suggest that Fickian dispersion may not be the key mechanism of dispersion of tracer in carbon dioxide storage. Instead the nose evolution dominates and this could lead to tracer test results being misinterpreted.

8.1.1 Lava flows

We have modelled lava as an isothermal viscous Newtonian fluid in order to understand how it interacts with different barrier designs. We have computed the steady flow around topographic mounds and shown that larger mounds deflect the flow leading to a dry region (or 'safe' zone). We showed that a key discriminant of when the flow became significantly affected by the topography was when its gradient points upwards (i.e. $\nabla m.\mathbf{g} < 0$, where $\mathbf{g}$ is gravitational acceleration). With a mound that is wider in the cross-slope direction, the deflection of the flow was reduced and hence the ponding was enhanced. The deeper flow may then overtop the mound and the dry zone is potentially eradicated. This suggests that wider mounds, which are needed to protect large areas, need to be built higher to prevent overtopping.

We next studied the interaction of free-surface viscous flows with surface-piercing cylinders. The magnitude of the perturbation to the flow depth is dependent upon a single dimensionless parameter, $\mathcal{F} = H_\infty/(L\tan\beta)$, which is the upstream flow depth divided by the product of the cylinder radius and the slope gradient. For large $\mathcal{F}$, the perturbation is small. When $\mathcal{F} \ll 1$, however, the flow depth increases significantly upstream of the cylinder and 'dry' regions in which there is no fluid occur downstream of the cylinder. Ponding of nearly stationary fluid upstream occurs for wider cylinders, analogous to the case of topographical mounds and we have confirmed this experimentally. The depth of the pond and location of the maximum flow thickness is sensitive to the cross-sectional shape of the cylinder. In particular, the pond depth is controlled by the curvature of the upstream boundary of the cylinder. Square cylinders lead to deeper ponds because the fluid is dissipated only by gradients in the hydrostatic pressure, which is weaker for a fixed flow thickness as compared to the gravity-driven flow down the plane. Our study was motivated by the need to inform the construction of barriers that divert lava flows and we have calculated how high and wide barriers need to be and the stress they must withstand to protect a given area.

8.2 Further work

In chapter 2, the model assumes that the injected buoyant fluid always lies above the denser ambient fluid, which is valid at low injection rates because buoyancy dominates any permeability variations that lead to non-uniform flow speed. However, for high injection rates and in aquifers with permeability that increases strongly with depth, it is possible that the buoyant injectate will spread along the base of the aquifer. The interface is unstable to Rayleigh-Taylor fingers because the buoyant fluid is underneath the dense fluid. It would be valuable to determine the flow rates, viscosity ratios and permeability gradients at which such permeability-driven flows occur. The injection speed required in the case of two discrete layers of different permeability has been investigated experimentally by Huppert et al. [88] and further work could involve extending their results to more general permeability variations.

The long-term success of CO_2 storage projects relies upon permanently trapping the CO_2 and this occurs primarily through dissolution into the ambient brine and capillary trapping in the pore throats [103]. These two effects play a dominant role in the dynamics after injection stops. Previous work on residual capillary trapping has focused on the role of the viscosity ratio and confinement [67, 92]. These works are invaluable in estimating the runout distance of the CO_2 and hence the safe volume that can be injected. However, Hesse et al. [67] notes that the estimates may be sensitive to permeability variations within a layer and an important piece of future work is to apply the model from chapter 2 to the problem of capillary trapping [78].

The interaction between tracer and the different nose regimes that can occur is complex and there are many possible regimes for the dispersion of tracer in these flows. This creates significant challenges for determine unique results from observations of tracer arrival times. A valuable extension would be to use our present forward model to determine the range of possible realisations of the tracer distribution that can occur given a small uncertainty in one of the aquifer parameters such as the magnitude of the permeability variation.

The model presented for lava flows in chapters 6 and 7 provides conservative bounds on the shape of the safe zone downstream of a barrier. Lava solidifies and its viscosity reduces as it cools and both of these effects act to slow the advance of the current into dry regions leading to a larger dry zone than those that we predicted. Additional experiments with a solidifying fluid such as hot wax or a fluid with a yield stress would be a useful complement to the present work. Our results have significant implications for civil defence authorities in regions of volcanic hazard and there is important work to be done in elucidating the key

aspects of barrier design that should be adopted. It would also be interesting to study the interaction between free-surface viscous flows and the downstream side of barriers [77].

References

[1] Abramowitz, M. and Stegun, I. A. (1965). *Handbook of mathematical functions with formulas, graphs and mathematical tables*. Dover books on intermediate and advanced mathematics. Dover.

[2] Adams, E. and Gelhar, L. W. (1992). Field Study of Dispersion in a Heterogeneous Aquifer Analysis of Hydraulic Conductivity. *Water Resources*, 28(12):3309–3324.

[3] Aksel, N. and Schörner, M. (2018). Films over topography: From creeping flow to linear stability, theory, and experiments, a review. *Acta Mechanica*, 229(4):1453–1482.

[4] Ancey, C. (2009). The design of avalanche protection dams: recent practical and theoretical developments. Brussels, European Communities. 195pp. ISBN 978-92-79-08885-8. *Journal of Glaciology*, 55(192):753–754.

[5] Aris, R. (1956). On the dispersion of a solute in a fluid flowing through a tube. *Proceedings of the Royal Society of London. Series A. Mathematical and Physical Sciences*, 235(1200):67–77.

[6] Bachu, S. (2015). Review of CO2 storage efficiency in deep saline aquifers. *International Journal of Greenhouse Gas Control*, 40:188–202.

[7] Ball, T. V. and Neufeld, J. A. (2018). Static and dynamic fluid-driven fracturing of adhered elastica. *Phys. Rev. Fluids*, 3:074101.

[8] Balmforth, N. J., Burbidge, A. S., Craster, R. V., Salzig, J., and Shen, A. (2000). Viscoplastic models of isothermal lava domes. *Journal of Fluid Mechanics*, 403:37–65.

[9] Balmforth, N. J., Craster, R. V., and Sassi, R. (2002). Shallow viscoplastic flow on an inclined plane. *Journal of Fluid Mechanics*, 470:1–29.

[10] Balsa, T. F. (1998). Secondary flow in a Hele-Shaw cell. *Journal of Fluid Mechanics*, 372:25–44.

[11] Barberi, F., Brondi, F., Carapezza, M., Cavarra, L., and Murgia, C. (2003). Earthen barriers to control lava flows in the 2001 eruption of Mt. Etna. *Journal of Volcanology and Geothermal Research*, 123(1-2):231–243.

[12] Barberi, F. and Carapezza, M. L. (2013). *The Control of Lava Flows at Mt. Etna*. American Geophysical Union (AGU).

[13] Barenblatt, G. I. (1996). *Scaling, Self-similarity, and Intermediate Asymptotics*. Cambridge University Press.

[14] Batchelor, G. K. (1965). *An introduction to fluid dynamics*. Cambridge University Press.

[15] Baxter, S. J., Power, H., Cliffe, K. A., and Hibberd, S. (2009). Three-dimensional thin film flow over and around an obstacle on an inclined plane. *Physics of Fluids*, 21(3):032102.

[16] Bear, J. (1961). Some experiments in dispersion. *Journal of Geophysical Research*, 66(8):2455–2467.

[17] Bear, J. (1971). *Dynamics of flow in porous media*. Elsevier.

[18] Berkowitz, B., Kosakowski, G., Margolin, G., and Scher, H. (2001). Application of Continuous Time Random Walk Theory to Tracer Test Measurements in Fractured and Heterogeneous Porous Media. *Ground Water*, 39(4):593–604.

[19] Berkowitz, B., Scher, H., and Silliman, S. E. (2000). Anomalous transport in laboratory-scale, heterogeneous porous media. *Water Resources Research*, 36(1):149–158.

[20] Bernabeu, N., Saramito, P., and Harris, A. (2018). Laminar shallow viscoplastic fluid flowing through an array of vertical obstacles. *Journal of Non-Newtonian Fluid Mechanics*, 257:59–70.

[21] Bickle, M. J. (2009). Geological carbon storage. *Nature Geoscience*, 2(12):815–818.

[22] Bjorlykke, K. (1993). Fluid flow in sedimentary basins. *Sedimentary Geology*, 86(1-2):137–158.

[23] Blyth, M. G. and Pozrikidis, C. (2006). Film flow down an inclined plane over a three-dimensional obstacle. *Physics of Fluids*, 18(5):052104.

[24] Boait, F. C., White, N. J., Bickle, M. J., Chadwick, R. A., Neufeld, J. A., and Huppert, H. E. (2012). Spatial and temporal evolution of injected CO2 at the Sleipner Field, North Sea. *Journal of Geophysical Research: Solid Earth*, 117(3):1–21.

[25] Boggs, J. M., Young, S. C., Beard, L. M., Gelhar, L. W., Rehfeldt, K. R., and Adams, E. E. (1992). Field study of dispersion in a heterogeneous aquifer: 1. Overview and site description. *Water Resources Research*, 28(12):3281–3291.

[26] Carman, P. C. (1939). Permeability of saturated sands, soils and clays. *The Journal of Agricultural Science*, 29:262.

[27] Cashman, K. V., Kerr, R. C., and Griffiths, R. W. (2006). A laboratory model of surface crust formation and disruption on lava flows through non-uniform channels. *Bulletin of Volcanology*, 68(7-8):753–770.

[28] Celia, M. A., Bachu, S., Nordbotten, J. M., and Bandilla, K. W. (2015). Status of CO2 storage in deep saline aquifers with emphasis on modeling approaches and practical simulations. *Water Resources Research*, 51(9):6846–6892.

[29] Chevrel, M. O., Harris, A., Ajas, A., Biren, J., Gurioli, L., and Calabrò, L. (2019). Investigating physical and thermal interactions between lava and trees: the case of Kīlauea's July 1974 flow. *Bulletin of Volcanology*, 81(2):6.

[30] Chirico, G. D., Favalli, M., Papale, P., Boschi, E., Pareschi, M. T., and Mamou-Mani, A. (2009). Lava flow hazard at Nyiragongo Volcano, DRC. *Bulletin of Volcanology*, 71(4):375–387.

[31] Colombrita, R. (1984). Methodology for the construction of earth barriers to divert lava flows: the Mt. Etna 1983 eruption. *Bulletin Volcanologique*, 47(4):1009–1038.

[32] Cui, X. and Gray, J. (2013). Gravity-driven granular free-surface flow around a circular cylinder. *Journal of Fluid Mechanics*, 720:314–337.

[33] Dagan, G. (1984). Solute transport in heterogeneous porous formations. *Journal of Fluid Mechanics*, 145:151–177.

[34] Dagan, G. (2012). *Flow and transport in porous formations*. Springer Science & Business Media.

[35] Dalwadi, M. P., Chapman, S. J., Oliver, J. M., and Waters, S. L. (2018). The effect of weak inertia in rotating high-aspect-ratio vessel bioreactors. *Journal of Fluid Mechanics*, 835:674–720.

[36] Dalwadi, M. P., Chapman, S. J., Waters, S. L., and Oliver, J. M. (2016). On the boundary layer structure near a highly permeable porous interface. *Journal of Fluid Mechanics*, 798:88–139.

[37] Dauck, T.-F., Box, F., Gell, L., Neufeld, J. A., and Lister, J. R. (2019). Shock formation in two-layer equal-density viscous gravity currents. *Journal of Fluid Mechanics*, 863:730–756.

[38] De Josselin De Jong, G. (1958). Longitudinal and transverse diffusion in granular deposits. *Eos, Transactions American Geophysical Union*, 39(1):67–74.

[39] Debbabi, Y., Jackson, M. D., Hampson, G. J., and Salinas, P. (2018). Impact of the Buoyancy–Viscous Force Balance on Two-Phase Flow in Layered Porous Media. *Transport in Porous Media*, 124(1):263–287.

[40] Dentz, M., Icardi, M., and Hidalgo, J. J. (2017). Mechanisms of Dispersion in a Porous Medium. *Journal of Fluid Mechanics*, 841:851–882.

[41] Dietterich, H. R., Cashman, K. V., Rust, A. C., and Lev, E. (2015). Diverting lava flows in the lab. *Nature Geoscience*, 8(7):494–496.

[42] Dullien, F. A. L. (2012). *Porous media: fluid transport and pore structure*. Academic press.

[43] Eames, I. and Bush, J. W. M. (1999). Longitudinal dispersion by bodies fixed in a potential flow. *Proceedings of the Royal Society A. Mathematical, Physical and Engineering Sciences*, 445(1990):3665–3686.

[44] Edwards, B. R., Karson, J., Wysocki, R., Lev, E., Bindeman, I., and Kueppers, U. (2013). Insights on lava–ice/snow interactions from large-scale basaltic melt experiments. *Geology*, 41(8):851–854.

[45] Erban, R. and Chapman, S. J. (2007). Reactive boundary conditions for stochastic simulations of reaction–diffusion processes. *Physical Biology*, 4(1):16–28.

[46] Farcas, A. and Woods, A. W. (2016). Buoyancy-driven dispersion in a layered porous rock. *Journal of Fluid Mechanics*, 767:226–239.

[47] Fayers, F. J., Blunt, M. J., and Christie, M. A. (1992). Comparisons of Empirical Viscous-Fingering Models and Their Calibration for Heterogeneous Problems. *Society of Petroleum Engineers*, 7(02):195–203.

[48] Fujita, E., Hidaka, M., Goto, A., and Umino, S. (2009). Simulations of measures to control lava flows. *Bulletin of Volcanology*, 71(4):401–408.

[49] Gaskell, P. H., Jimack, P. K., Sellier, M., Thompson, H. M., and Wilson, M. C. T. (2004). Gravity-driven flow of continuous thin liquid films on non-porous substrates with topography. *Journal of Fluid Mechanics*, (509):253–280.

[50] Gelhar, L. W., Gutjahr, A. L., and Naff, R. L. (1979). Stochastic analysis of macrodispersion in a stratified aquifer. *Water Resources Research*, 15(6):1387–1397.

[51] Gelhar, L. W., Welty, C., and Rehfeldt, K. R. (1992). A Critical Review of Data on Field-Scale Dispersin in Aquifers. *Water Resources Research*, 28(7):1955–1974.

[52] Glenn, J. W. (1955). The creep of polycrystalline ice. *Proceedings of the Royal Society of London A: Mathematical, Physical and Engineering Sciences*, 228(1175):519–538.

[53] Golding, M. J., Neufeld, J. A., Hesse, M. A., and Huppert, H. E. (2011). Two-phase gravity currents in porous media. *Journal of Fluid Mechanics*, 678:248–270.

[54] Griffiths, R. W. (2001). The Dynamics of Lava Flows. *Annu. Rev. Fluid Mech*, WP01/05(1):4–25.

[55] Gunn, I. and Woods, A. W. (2011). On the flow of buoyant fluid injected into a confined, inclined aquifer. *Journal of Fluid Mechanics*, 672:109–129.

[56] Guo, B., Bandilla, K., Nordbottten, J., Keilegavlen, E., and Doster, F. (2016a). A multiscale multilayer vertically integrated model with vertical dynamic for CO2 sequestration in layered geological formations. *Water Resources Research*, 52:6490–6505.

[57] Guo, B., Zheng, Z., Bandilla, K. W., Celia, M. A., and Stone, H. A. (2016b). Flow regime analysis for geologic CO2 sequestration and other subsurface fluid injections. *International Journal of Greenhouse Gas Control*, 53:284–291.

[58] Györe, D., Stuart, F. M., Gilfillan, S. M. V., and Waldron, S. (2015). Tracing injected CO2 in the Cranfield enhanced oil recovery field (MS, USA) using He, Ne and Ar isotopes. *International Journal of Greenhouse Gas Control*, 42:554–561.

[59] Hákonardóttir, K. M. and Hogg, A. J. (2005). Oblique shocks in rapid granular flows. *Physics of Fluids*, 17(7):077101.

[60] Hákonardóttir, K. M., Hogg, A. J., Batey, J., and Woods, A. W. (2003). Flying avalanches. *Geophysical Research Letters*, 30(23).

[61] Hansen, E. B. (1986). Free surface Stokes flow over an obstacle. In *Boundary Elements VIII*, pages 783–792. Springer.

[62] Hayes, M., O'Brien, S., and Lammers, J. (2000). Green's function for steady flow over a small two-dimensional topography. *Physics of Fluids*, 12(11):2845–2858.

[63] Heining, C. and Aksel, N. (2009). Bottom reconstruction in thin-film flow over topography: Steady solution and linear stability. *Physics of Fluids*, 21(8):083605.

[64] Heining, C., Sellier, M., and Aksel, N. (2012). The inverse problem in creeping film flows. *Acta Mechanica*, 223(4):841–847.

[65] Hess, K. M., Wolf, S. H., and Celia, M. A. (1992). Large scale natural gradient tracer test in sand and gravel, Cape Cod, Massachusetts: 3. Hydraulic conductivity variability and calculated macrodispersivities. *Water Resources Research*, 28(8):2011–2027.

[66] Hesse, M., Tchelepi, H. A., and Orr, F. M. (2006). Scaling Analysis of the Migration of CO2 in Saline Aquifers. *Society of Petroleum Engineers*.

[67] Hesse, M. A., Orr, F. M., and Tchelepi, H. (2008). Gravity currents with residual trapping. *Journal of Fluid Mechanics*, 611:35–60.

[68] Hesse, M. A., Tchelepi, H. A., Cantwel, B. J., and Orr, F. M. (2007). Gravity currents in horizontal porous layers: transition from early to late self-similarity. *Journal of Fluid Mechanics*, 577(1):363–383.

[69] Hesse, M. A. and Woods, A. W. (2010). Buoyant dispersal of CO2 during geological storage. *Geophysical Research Letters*, 37.

[70] Hewitt, D. R. and Balmforth, N. J. (2013). Thixotropic gravity currents. *Journal of Fluid Mechanics*, 727:56–82.

[71] Higham, D. J. (2001). An algorithmic introduction to numerical simulation of stochastic differential equations. *SIAM review*, 43(3):525–546.

[72] Hinch, E. J. (1991). *Perturbation methods.* Cambridge texts in applied mathematics. Cambridge University Press, Cambridge.

[73] Hinton, E. and Woods, A. W. (2018a). Modelling the evolution of a CO2 plume and injected tracers in an aquifer with variable permeability. In *14th Greenhouse Gas Control Technologies Conference Melbourne*, pages 21–26.

[74] Hinton, E. M. (2020). Axisymmetric viscous flow between two horizontal plates. *Physics of Fluids*, 32(6):063104.

[Hinton et al.] Hinton, E. M., Hogg, A. J., and Huppert, H. E. Viscous free-surface flows past cylinders. submitted.

[76] Hinton, E. M., Hogg, A. J., and Huppert, H. E. (2019). Interaction of viscous free-surface flows with topography. *Journal of Fluid Mechanics*, 876:912–938.

[77] Hinton, E. M., Hogg, A. J., and Huppert, H. E. (2020). Shallow free-surface Stokes flow around a corner. *Philosophical Transactions of the Royal Society A*, 378(20190515).

[78] Hinton, E. M. and Woods, A. W. Residual trapping in vertically heterogeneous aquifers. submitted.

[79] Hinton, E. M. and Woods, A. W. Shear dispersion in a porous medium. Part 1. An intrusion with a steady shape. accepted.

[80] Hinton, E. M. and Woods, A. W. Shear dispersion in a porous medium. Part 2. An intrusion with a growing shape. accepted.

[81] Hinton, E. M. and Woods, A. W. (2018b). Buoyancy-driven flow in a confined aquifer with a vertical gradient of permeability. *Journal of Fluid Mechanics*, 848:411–429.

[82] Hinton, E. M. and Woods, A. W. (2019). The effect of vertically varying permeability on tracer dispersion. *Journal of Fluid Mechanics*, 860:384–407.

[83] Hogg, A. J., Hinton, E., and Huppert, H. E. (2019). The deflection of lava flows around obstacles and topography. In *AGU Fall Meeting 2019*. AGU.

[84] Huppert, H. E. (1982a). Flow and instability of a viscous current down a slope. *Nature*, 300(5891):427–429.

[85] Huppert, H. E. (1982b). The propagation of two-dimensional and axisymmetric viscous gravity currents over a rigid horizontal surface. *Journal of Fluid Mechanics*, 121:43–58.

[86] Huppert, H. E. (2006). Gravity currents: a personal perspective. *Journal of Fluid Mechanics*, 554:299–322.

[87] Huppert, H. E. and Neufeld, J. A. (2014). The Fluid Mechanics of Carbon Dioxide Sequestration. *Annual Review of Fluid Mechanics*, 46(1):255–272.

[88] Huppert, H. E., Neufeld, J. A., and Strandkvist, C. (2013). The competition between gravity and flow focusing in two-layered porous media. *Journal of Fluid Mechanics*, 720:5–14.

[89] Huppert, H. E. and Woods, A. W. (1995). Gravity-driven flows in porous layers. *Journal of Fluid Mechanics*, 292:55–69.

[90] Hutter, K. (1982). Dynamics of Glaciers. pages 245–256.

[91] Johnson, C. (2012). *Numerical solution of partial differential equations by the finite element method*. Courier Corporation.

[92] Juanes, R., MacMinn, C. W., and Szulczewski, M. L. (2010). The footprint of the CO2 plume during carbon dioxide storage in saline aquifers: Storage efficiency for capillary trapping at the basin scale. *Transport in Porous Media*, 82(1):19–30.

[93] Kalliadasis, S., Bielarz, C., and Homsy, G. (2000). Steady free-surface thin film flows over topography. *Physics of Fluids*, 12(8):1889–1898.

[94] Kampman, N., Bickle, M. J., Maskell, A., Chapman, H. J., Evans, J. P., Purser, G., Zhou, Z., Schaller, M. F., Gattacceca, J. C., Bertier, P., Chen, F., Turchyn, A. V., Assayag, N., Rochelle, C., Ballentine, C. J., and Busch, A. (2014). Drilling and sampling a natural CO2 reservoir: Implications for fluid flow and CO2-fluid-rock reactions during CO2 migration through the overburden. *Chemical Geology*, 369:51–82.

[95] Kerr, R. C., Griffiths, R. W., and Cashman, K. V. (2006). Formation of channelized lava flows on an unconfined slope. *Journal of Geophysical Research: Solid Earth*, 111(10):1–13.

[96] Kistler, S. F. and Schweizer, P. M. (1997). *Liquid film coating: scientific principles and their technological implications*. Springer.

[97] Kurganov, A. and Tadmor, E. (2000). New High-Resolution Central Schemes for Nonlinear Conservation Laws and Convection Diffusion Equations. *Journal of Computational Physics*, 160(1):241–282.

[98] Lajeunesse, E., Martin, J., Rakotomalala, N., Salin, D., and Yortsos, Y. C. (1999). Miscible displacement in a Hele-Shaw cell at High Rates. 398:299–319.

[99] Lake, L. W. (1989). *Enhanced Oil Recovery*. Prentice Hall.

[100] Lee, Y., Thompson, H., and Gaskell, P. (2007). An efficient adaptive multigrid algorithm for predicting thin film flow on surfaces containing localised topographic features. *Computers & fluids*, 36(5):838–855.

[101] Lister, J. R. (1992). Viscous flows down an inclined plane from point and line sources. *Journal of Fluid Mechanics*, 242:631–653.

[102] Llewellin, E., Mader, H., and Wilson, S. (2002). The rheology of a bubbly liquid. *Proceedings of the Royal Society of London. Series A: Mathematical, Physical and Engineering Sciences*, 458(2020):987–1016.

[103] MacMinn, C., Szulczewski, M., and Juanes, R. (2011). CO2 migration in saline aquifers. Part 2. Capillary and solubility trapping. *J. Fluid Mech.*, 688:321–351.

[104] Malamataris, N. and Bontozoglou, V. (1999). Computer aided analysis of viscous film flow along an inclined wavy wall. *Journal of Computational Physics*, 154(2):372–392.

[105] Mathieson, A., Midgely, J., Wright, I., Saoula, N., and Ringrose, P. (2011). In Salah CO2 storage JIP: CO2 sequestration monitoring and verification technologies applied at Krechba, Algeria. *Energy Procedia*, 4:3596–3603.

[106] Mazouchi, A. and Homsy, G. (2001). Free surface Stokes flow over topography. *Physics of Fluids*, 13(10):2751–2761.

[107] Moore, H. J. (1982). A geologic evaluation of proposed lava diversion barriers for the NOAA Mauna Loa Observatory Mauna Loa Volcano, Hawaii. *(U.S. Geol. Surv. Open-File Report 82-314*, pages 1–26.

[108] Neufeld, J. A., Hesse, M. A., Riaz, A., Hallworth, M. A., Tchelepi, H. A., and Huppert, H. E. (2010). Convective dissolution of carbon dioxide in saline aquifers. *Geophysical Research Letters*, 37(22):2–6.

[109] Nusselt, W. (1916). Die Oberflachenkondensation des Wasserdamphes. *VDI-Zs*, 60:541.

[110] Paster, A., Bolster, D., and Benson, D. A. (2013). Particle tracking and the diffusion-reaction equation. *Water Resources Research*, 49(1):1–6.

[111] Pegler, S. S., Huppert, H. E., and Neufeld, J. A. (2014). Fluid injection into a confined porous layer. *Journal of Fluid Mechanics*, 745:592–620.

[112] Phillips, O. M. (2009). Geological Fluid Dynamics. In *Sub-surface Flow and Reactions*. Cambridge University Press.

[113] Pihler-Puzović, D., Juel, A., Peng, G. G., Lister, J. R., and Heil, M. (2015). Displacement flows under elastic membranes. Part 1. Experiments and direct numerical simulations. *Journal of Fluid Mechanics*, 784:487–511.

[114] Pozrikidis, C. (1988). The flow of a liquid film along a periodic wall. *Journal of Fluid Mechanics*, 188:275–300.

[115] Pozrikidis, C. and Thoroddsen, S. T. (1991). The deformation of a liquid film flowing down an inclined plane wall over a small particle arrested on the wall. *Physics of Fluids A: Fluid Dynamics*, 3(11):2546–2558.

[116] Pritchard, D., Woods, A. W., and Hogg, A. J. (2001). On the slow draining of a gravity current moving through a layered permeable medium. *Journal of Fluid Mechanics*, 444:23–47.

[117] Pritchard, W. G., Scott, L. R., and Tavener, S. J. (1992). Numerical and asymptotic methods for certain viscous free-surface flows. *Philosophical Transactions of the Royal Society of London. Series A: Physical and Engineering Sciences*, 340(1656):1–45.

[118] Proudman, I. and Pearson, J. R. A. (1957). Expansions at small Reynolds numbers for the flow past a sphere and a circular cylinder. *Journal of Fluid Mechanics*, 2(3):237–262.

[119] Pruess, K., García, J., Kovscek, T., Oldenburg, C., Rutqvist, J., Steefel, C., and Xu, T. (2004). Code intercomparison builds confidence in numerical simulation models for geologic disposal of CO2. *Energy*, 29(9-10):1431–1444.

[120] Pyles, D. R., Straub, K. M., and Stammer, J. G. (2013). Spatial variations in the composition of turbidites due to hydrodynamic fractionation. *Geophysical Research Letters*, 40(15):3919–3923.

[121] Riaz, A., Hesse, M., Tchelepi, H. A., and Orr, F. M. (2006). Onset of convection in a gravitationally unstable diffusive boundary layer in porous media. *Journal of Fluid Mechanics*, 548:87–111.

[122] Rignot, E., Mouginot, J., and Scheuchl, B. (2011). Ice Flow of the Antarctic Ice Sheet. *Science*, 333(6048):1427–1430.

[123] Ringrose, P. S., Mathieson, A. S., Wright, I. W., Selama, F., Hansen, O., Bissell, R., Saoula, N., and Midgley, J. (2013). The In Salah CO2 storage project: lessons learned and knowledge transfer. *Energy Procedia*, 37:6226–6236.

[124] Saffman, P. G. (1959). A theory of dispersion in a porous medium. *J. Fluid Mech.*, 6(3):321–349.

[125] Saffman, P. G. and Taylor, G. I. (1958). The penetration of a fluid into a porous medium or Hele-Shaw cell containing a more viscous liquid. *Proceedings of the Royal Society of London A: Mathematical, Physical and Engineering Sciences*, 245(1242):312–329.

[126] Schörner, M., Reck, D., and Aksel, N. (2016). Stability phenomena far beyond the nusselt flow–revealed by experimental asymptotics. *Physics of Fluids*, 28(2):022102.

[127] Scifoni, S., Coltelli, M., Marsella, M., Proietti, C., Napoleoni, Q., Vicari, A., and Del Negro, C. (2010). Mitigation of lava flow invasion hazard through optimized barrier configuration aided by numerical simulation: The case of the 2001 Etna eruption. *Journal of Volcanology and Geothermal Research*, 192(1-2):16–26.

[128] Sellier, M. (2015). Modelling the wetting of a solid occlusion by a liquid film. *International Journal of Multiphase Flow*, 71:66–73.

[129] Sellier, M., Lee, Y., Thompson, H., and Gaskell, P. (2009). Thin film flow on surfaces containing arbitrary occlusions. *Computers & Fluids*, 38(1):171–182.

[130] Smith, P. C. (1973). A similarity solution for slow viscous flow down an inclined plane. *Journal of Fluid Mechanics*, 58(2):275–288.

[131] Sparks, R., Pinkerton, H., and Hulme, G. (1976). Classification and formation of lava levees on Mount Etna, Sicily. *Geology*, 4(5):269–271.

[132] Stalker, L., Boreham, C., Underschultz, J., Freifeld, B., Perkins, E., Schacht, U., and Sharma, S. (2015). Application of tracers to measure, monitor and verify breakthrough of sequestered CO2 at the CO2CRC Otway Project, Victoria, Australia. *Chemical Geology*, 399:2–19.

[133] Stillwagon, L. E. and Larson, R. G. (1988). Fundamentals of topographic substrate leveling. *Journal of Applied Physics*, 63(11):5251–5258.

[134] Sudicky, E. A. (1986). A natural gradient experiment on solute transport in a sand aquifer: Spatial variability of hydraulic conductivity and its role in the dispersion process. *Water Resources Research*, 22(13):2069–2082.

[135] Taghavi, S. M., Seon, T., Martinez, D. M., and Frigaard, I. A. (2009). Buoyancy-dominated displacement flows in near-horizontal channels: the viscous limit. *Journal of Fluid Mechanics*, 639:1–35.

[136] Takagi, D. and Huppert, H. E. (2010). Initial advance of long lava flows in open channels. *Journal of Volcanology and Geothermal Research*, 195(2-4):121–126.

[137] Taylor, G. I. (1953). Dispersion of soluble matter in solvent flowing slowly through a tube. *Proceedings of the Royal Society of London*, 219:186–203.

[138] Thompson, B. (1968). Secondary flow in a Hele-Shaw cell. *Journal of Fluid Mechanics*, 31(2):379–395.

[139] Unwin, J., Wells, G. N., and Woods, A. W. (2016). CO 2 dissolution in a background hydrological flow. *Journal of Fluid Mechanics*, 789:768–784.

[140] Vasco, D. W., Rucci, A., Ferretti, A., Novali, F., Bissell, R. C., Ringrose, P. S., Mathieson, A. S., and Wright, I. W. (2010). Satellite-based measurements of surface deformation reveal fluid flow associated with the geological storage of carbon dioxide. *Geophysical Research Letters*, 37(3).

[141] Walker, R. G. (1975). Generalized facies models for resedimented conglomerates of turbidite association. *Geological Society of America Bulletin*, 86(6):737–748.

[142] Williams, R. and Moore, J. (1983). Man Against Volcano : The Eruption on Heimaey, Vestmennaeyjar, Iceland. *Report USGS General Interest Publication*, pages 1–26.

[143] Woods, A. W. (1999). Liquid and vapor flow in superheated rock. *Annual Review of Fluid Mechanics*, 31(1):171–199.

[144] Woods, A. W. (2014). *Flow in Porous Rocks: Energy and Environmental Applications*. Cambridge University Press.

[145] Younger, Z. P., Valentine, G. A., and Gregg, T. K. (2019). 'A'ā lava emplacement and the significance of rafted pyroclastic material: Marcath volcano (Nevada, USA). *Bulletin of Volcanology*, 81(9):50.

[146] Zheng, Z., Guo, B., Christov, I. C., Celia, M. A., and Stone, H. A. (2015a). Flow regimes for fluid injection into a confined porous medium. *Journal of Fluid Mechanics*, 767(2015):881–909.

[147] Zheng, Z., Rongy, L., and Stone, H. A. (2015b). Viscous fluid injection into a confined channel. *Physics of Fluids*, 27(6):062105.

Appendix A

Matching at higher order to determine $k_0(\theta)$

In chapter 7, we found an asymptotic approximation for the flow thickness upstream of a circular cylinder in the regime of a wide cylinder ($\mathcal{F} \ll 1$). The maximum flow thickness occurs at $\theta = \pi$, $r = 1$ and we found that the second order contribution to this thickness included $k_0(\pi)$, which was undetermined. In this Appendix, we match through the interior region at higher order to obtain an ordinary differential equation for $k_0(\theta)$, which we use to determine $k_0(\pi)$.

In the inner region, in which $r = 1 + \mathcal{F}^{3/4}s$, we found in §7.5 that the asymptotic approximation for the depth takes the form

$$h = \mathcal{F}^{-1/4}\mathscr{H}_0 + \mathcal{F}^{1/2}\mathscr{H}_1 + \mathcal{F}^{5/4}\mathscr{H}_2 + \cdots \tag{A.1}$$

and by substituting into the governing equation (7.47), we obtain

$$\mathscr{H}_0 = s\cos\theta + G(\theta), \tag{A.2}$$

$$\mathscr{H}_1 = k_{-2}(\theta)\mathscr{H}_0^{-2} + k_0(\theta) + k_1(\theta)\mathscr{H}_0 + k_2(\theta)\mathscr{H}_0^2, \tag{A.3}$$

$$\mathscr{H}_2 = l_{-5}(\theta)\mathscr{H}_0^{-5} + l_{-3}(\theta)\mathscr{H}_0^{-3} + l_{-2}(\theta)\mathscr{H}_0^{-2} + \cdots, \tag{A.4}$$

where $k_0(\theta)$ is to be determined and the other $k_i(\theta)$ are given in equations (7.54a-c). With $G(\theta)$ known (**??**), these functions may be simplified to

$$k_{-2}(\theta) = 1/2, \tag{A.5}$$

$$k_1(\theta) = \frac{-3\sin^2\theta}{4\cos^3\theta} G(\theta), \tag{A.6}$$

$$k_2(\theta) = \frac{3\tan^2\theta - 1}{8\cos\theta}. \tag{A.7}$$

Finally, the functions in $\mathscr{H}_2$ are found to be

$$l_{-5}(\theta) = -3/10, \tag{A.8}$$

$$l_{-3}(\theta) = -k_0(\theta), \tag{A.9}$$

$$l_{-2}(\theta) = \big[-2\cos\theta\big]^{-1}\left[\big(k_0 G^3\tan\theta\big)' + (17/20)G + (51/16)G\tan^2\theta + (11/80)G\tan^4\theta\right], \tag{A.10}$$

where in the last line we have suppressed the argument in $k_0(\theta)$ and $G(\theta)$ for brevity and $'$ denotes the derivative with respect to θ.

In §7.5, we found an interior layer near $s = s^* = -G(\theta)/\cos\theta$, in which the thickness is order unity and we defined the coordinate

$$\eta = \mathcal{F}^{-1/4}\frac{G(\theta)}{\cos\theta} + \mathcal{F}^{-1}(r-1). \tag{A.11}$$

Within this region, we transform from (r,θ) to (η,θ) coordinates and the governing equation (7.47) is recast as

$$\cos\theta\frac{\partial h^3}{\partial\eta} - \mathcal{F}^{3/4}(3/4)\tan^2\theta G(\theta)\frac{\partial h^3}{\partial\eta} = \frac{\partial^2 h^4/4}{\partial\eta^2} + \mathscr{O}(\mathcal{F}). \tag{A.12}$$

As $\eta\to-\infty$, the thickness $h(\eta,\theta)$ is required to match with the approximation in which $s = \mathscr{O}(1)$ (equation A.1). We substitute for r in equation (A.1) to obtain

$$\begin{aligned} h \sim \eta\cos\theta + (1/2)(\eta\cos\theta)^{-2} - (3/10)(\eta\cos\theta)^{-5} \\ + \mathcal{F}^{1/2}k_0(\theta)\big[1-(\eta\cos\theta)^{-3}\big] \\ + \mathcal{F}^{3/4}\big[k_1(\theta)\eta\cos\theta + l_{-2}(\theta)(\eta\cos\theta)^{-2}\big]. \end{aligned} \tag{A.13}$$

Thus, the expansion for h in the interior layer takes the following form

$$h = h_0 + \mathcal{F}^{1/2} h_{1/2} + \mathcal{F}^{3/4} h_{3/4} + \cdots \tag{A.14}$$

Substituting this expression into equation (A.12), we obtain at $\mathcal{O}(\mathcal{F}^{3/4})$,

$$\cos\theta \frac{\partial}{\partial \eta}\left(3h_0^2 h_{3/4}\right) - \frac{3}{4}\tan^2\theta G(\theta)\frac{\partial h_0^3}{\partial \eta} = \frac{\partial^2}{\partial \eta^2}\left(h_0^3 h_{3/4}\right). \tag{A.15}$$

Away from the cylinder, the depth returns to its unperturbed value and hence $h_0 \to 1$ and $h_{3/4} \to 0$ as $\eta \to \infty$. We integrate equation (A.15) and apply this boundary condition to obtain

$$\frac{\partial h_{3/4}}{\partial \eta} = -\frac{3}{4}\tan^2\theta G(\theta)\left(1 - h_0^{-3}\right) + \frac{3h_{3/4}}{h_0}\left(\cos\theta - \frac{\partial h_0}{\partial \eta}\right). \tag{A.16}$$

We apply our expressions for h_0 and $h_{3/4}$ as $\eta \to -\infty$ (equation A.13) and compare the coefficients of η^{-3} to obtain

$$-2\cos\theta l_{-2}(\theta) = -(3/4)G(\theta)\tan^2\theta. \tag{A.17}$$

On substituting for $l_{-2}(\theta)$ from (A.10), this is a first-order ordinary differential equation for $k_0(\theta)$ and by analysing the behaviour near $\theta = \pi$, we find that

$$k_0(\pi) = -17/40. \tag{A.18}$$